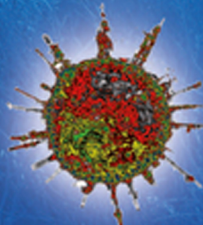
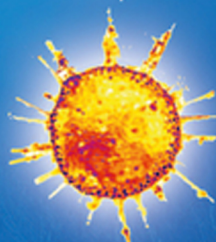
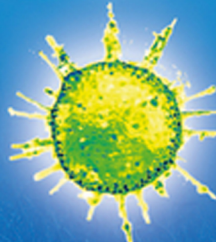
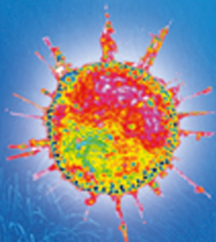
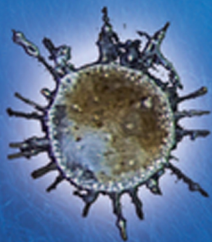
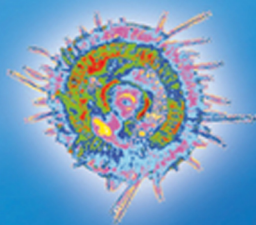
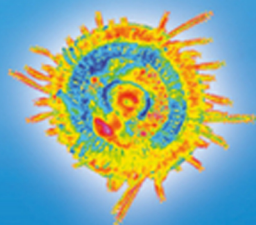
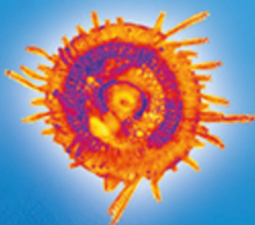
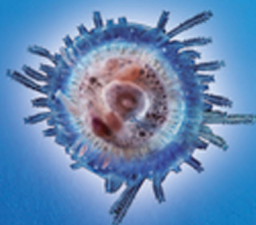
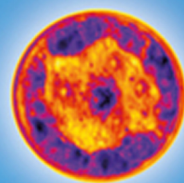
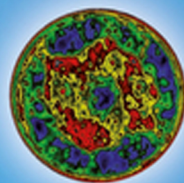
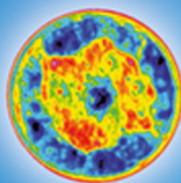
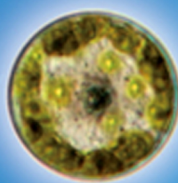
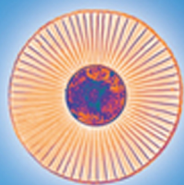
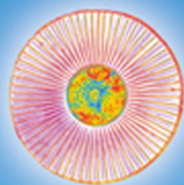
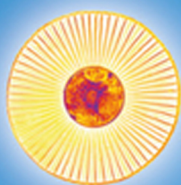
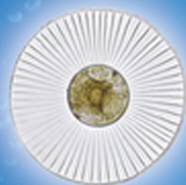


# Imaging Marine Life

Modern Imaging Techniques in Marine Biology

Edited by Emmanuel G. Reynaud



**TARA**  
**OCEANS**

**WILEY** Blackwell



*Edited by*  
*Emmanuel G. Reynaud*

**Imaging Marine Life**

## ***Related Titles***

Speight, M., Henderson, P.

### **Marine Ecology-Concepts and Applications**

2010

Print ISBN: 978-1-444-33545-3,  
also available as digital format

Kubitscheck, U. (ed.)

### **Fluorescence Microscopy From Principles to Biological Applications**

2013

Print ISBN: 978-3-527-32922-9,  
also available as digital format

Eleftheriou, A. (ed.)

### **Methods for Study of Marine Benthos**

4th Edition

2013

Print ISBN: 978-0-470-67086-6,  
also available as digital format

Miller, C., Wheeler, P.

### **Biological Oceanography**

2nd Edition

2012

Print ISBN: 978-1-444-33301-5,  
also available as digital format

### **Biotechnology Journal**

[www.biotechnology-journal.com](http://www.biotechnology-journal.com)



*Edited by Emmanuel G. Reynaud*

## **Imaging Marine Life**

Macrophotography and Microscopy Approaches for  
Marine Biology

**WILEY** Blackwell

## The Editor

**Dr. Emmanuel G. Reynaud**

School of Biology & Environmental Science  
Science Centre West  
University College Dublin  
Belfield  
Dublin 4  
Ireland

## Cover

Plankton organisms (diatoms (rows 1–2), hydroid (row 3) and radiolarian (row 4) can be imaged using different techniques and different image processing schemes. The cover shows four different organisms: *Planktoniella sol* (Schütt, 1892; Marquesas Archipelago, Tara Oceans), *Coscinodiscus* sp. (Azores islands, Tara Oceans), *Porpita porpita* (Linnaeus, 1758; North Pacific Ocean; Luis Gutierrez-Heredia, Tara Oceans) and a radiolarian (*Actinomma* sp.; Mediterranean Sea, Tara Oceans). All original colour images were converted to 8-bit then processed using different Look up Tables (LUT) to highlight specific characteristics using NIH Image]. Background underwater scene © adimas, fotolia.com

**Limit of Liability/Disclaimer of Warranty:** While the publisher and author have used their best efforts in preparing this book, they make no representations or warranties with respect to the accuracy or completeness of the contents of this book and specifically disclaim any implied warranties of merchantability or fitness for a particular purpose. No warranty can be created or extended by sales representatives or written sales materials. The Advice and strategies contained herein may not be suitable for your situation. You should consult with a professional where appropriate. Neither the publisher nor authors shall be liable for any loss of profit or any other commercial damages, including but not limited to special, incidental, consequential, or other damages.

**Library of Congress Card No.:** applied for

## British Library Cataloguing-in-Publication Data

A catalogue record for this book is available from the British Library.

## Bibliographic information published by the Deutsche Nationalbibliothek

The Deutsche Nationalbibliothek lists this publication in the Deutsche Nationalbibliografie; detailed bibliographic data are available on the Internet at <<http://dnb.d-nb.de>>.

© 2014 Wiley-VCH Verlag GmbH & Co. KGaA, Boschstr. 12, 69469 Weinheim, Germany

Wiley-Blackwell is an imprint of John Wiley & Sons, formed by the merger of Wiley's global Scientific, Technical, and Medical business with Blackwell Publishing.

All rights reserved (including those of translation into other languages). No part of this book may be reproduced in any form – by photoprinting, microfilm, or any other means – nor transmitted or translated into a machine language without written permission from the publishers. Registered names, trademarks, etc. used in this book, even when not specifically marked as such, are not to be considered unprotected by law.

**Print ISBN:** 978-3-527-32744-7

**ePDF ISBN:** 978-3-527-66420-7

**ePub ISBN:** 978-3-527-67542-5

**Mobi ISBN:** 978-3-527-67543-2

**oBook ISBN:** 978-3-527-67541-8

**Cover Design** Adam Design, Weinheim, Germany

**Typesetting** Laserwords Private Limited, Chennai, India

**Printing and Binding** Markono Print Media Pte Ltd, Singapore

Printed on acid-free paper.

## Contents

**Preface** XIII

**List of Contributors** XVII

<b>1</b>	<b>Under the Eye of Neptune: An Historical Perspective of Marine Creature Imagery</b>	<b>3</b>
	<i>Emmanuel G. Reynaud</i>	
1.1	Introduction	3
1.2	Ancient Uses of the Oceans	5
1.2.1	Seafarers	5
1.2.2	The Mediterranean Sea: the cradle of marine biology	6
1.2.2.1	Aristotle and Pliny the Elder, the Founding Fathers	6
1.2.2.2	Understanding the Oceans	7
1.3	From Neptune to Animalcules	8
1.3.1	Age of European Discovery and Exploration	8
1.3.2	Voyages of Exploration and finally Science	9
1.3.3	A Glimpse at the Invisible	9
1.4	The Birth of Oceanography (The Nineteenth Century)	10
1.4.1	Drawing the Jellyfish	10
1.4.2	The H.M.S. Challenger Expedition	11
1.4.3	Stations and Institutions	14
1.5	The Twentieth Century: Institutions and moving images	15
1.5.1	New tools – new images:	15
1.5.2	Jean Painleve	16
1.5.3	The Writers and the Explorers	16
1.5.4	The Future	18
1.6	Time Line of Ocean Imagery	18
	Further Reading	20
	Basic Texts	20
	Source Books	20
	Ships and Expeditions	21
	Institutions	21

<b>2</b>	<b>New Solutions in Underwater Imaging and Vision Systems</b>	<b>23</b>
	<i>Francisco Bonin-Font, Antoni Burguera, and Gabriel Oliver</i>	
2.1	Introduction	23
2.2	Underwater Optical Image Formation	25
2.3	Illumination Techniques	27
2.3.1	Illumination Sources	27
2.3.2	Selection of the Light Source Position	28
2.3.3	Illuminating Systems	30
2.4	Laser-Based Techniques	32
2.4.1	Laser Range-Gating (LRG) Methods	32
2.4.2	Laser Line Scan (LLS) Methods	33
2.4.3	Scattered Light Rejection Using Modulation/Demodulation Techniques	33
2.5	Underwater Imaging Infrastructures	34
2.6	Image Improvement via Polarization	35
2.6.1	Extended Range Using Polarization	36
2.6.2	Housing	36
2.6.3	Experimental Evaluation	37
2.7	A Vision System for Underwater Applications	39
2.7.1	The Fugu Vision System	40
2.8	Conclusion	42
	Acknowledgements	44
	References	44
<b>3</b>	<b>Holographic Microscopy of Marine Organisms</b>	<b>49</b>
	<i>Stefan K. Jericho, Manfred H. Jericho, and Hans J. Kreuzer</i>	
3.1	Introduction	49
3.2	Advantages of Holographic Microscopy	50
3.3	Past Attempts to Image Microplankton	51
3.4	Point Source Digital In-Line Holographic Microscopy	54
3.4.1	Instruments	55
3.4.2	Image Reconstruction	56
3.4.3	Image Examples	58
3.4.4	Resolution	60
3.4.5	Volume Imaging Challenges	63
3.5	Future Outlook	64
	References	65
<b>4</b>	<b>Confocal Laser Scanning Microscopy – Detailed Three-Dimensional Morphological Imaging of Marine Organisms</b>	<b>69</b>
	<i>Jan Michels</i>	
4.1	Introduction	69
4.2	Technical and Methodological Aspects of Confocal Laser Scanning Microscopy	69

- 4.3 Prerequisites for Generating High-Quality Confocal Laser Scanning Micrographs 73
- 4.4 Using Autofluorescences for Detailed Three-Dimensional Morphological Imaging 76
- 4.5 Application of Fluorescence Dyes 80
- 4.6 Surface Topography Analyses 85
- 4.7 Future Perspectives 88
- Acknowledgements 89
- References 89

## 5 **Optical Projection Tomography** 93

*Karl Gaff, Luke McCormac Parker, Dee Lawlor, and Emmanuel G. Reynaud*

- 5.1 Introduction 93
- 5.2 What Is Optical Projection Tomography? 94
  - 5.2.1 Assembly of an OPT System 98
    - 5.2.1.1 Detection Unit 98
    - 5.2.1.2 Illumination Units 98
    - 5.2.1.3 Sample Manipulation Unit 98
  - 5.2.2 Illumination Sources 99
  - 5.2.3 System Capabilities and Limitations 99
- 5.3 Comparison with Other 3D Microscopy Techniques 100
  - 5.3.1 Confocal Microscopy 101
  - 5.3.2 Two-Photon Microscopy 102
- 5.4 Sample Preparation 102
- 5.5 Image Processing and Analysis 104
- 5.6 Marine Biology Applications 104
- Acknowledgments 108
- References 108

## 6 **Electron Microscopy Techniques for Imaging Marine Phytoplankton** 111

*Gustaaf Hallegraeff*

- 6.1 Introduction 111
- 6.2 Collecting and Processing Specimens 112
- 6.3 Light Microscopy 113
- 6.4 Sediment Cyst Surveys 113
- 6.5 Transmission Electron Microscopy 114
- 6.6 Scanning Electron Microscopy 116
- Acknowledgements 121
- References 121



<b>7</b>	<b>Looking Inside Marine Organisms with Magnetic Resonance and X-ray Imaging</b>	<b>123</b>
	<i>Irene Zanette, Gheylen Daghfous, Timm Weitkamp, Brigitte Gillet, Dominique Adriaens, Max Langer, Peter Cloetens, Lukas Helfen, Alberto Bravin, Françoise Peyrin, Tilo Baumbach, Jean-Michel Dischler, Denis Van Loo, Tomas Praet, Marie Poirier-Quinot, and Renaud Boistel</i>	
7.1	Introduction	123
7.2	Magnetic Resonance Imaging	124
7.2.1	Experimental Setup	124
7.2.2	Hardware Improvements	128
7.2.3	Contrast	128
7.2.4	Applications	129
7.2.4.1	Anatomical MRI	129
7.2.4.2	Functional MRI	129
7.2.4.3	Diffusion Tensor Imaging or Diffusion MRI (DTI)	129
7.2.4.4	MEMRI or Manganese-Enhanced Magnetic Resonance Imaging	131
7.3	X-Ray Microtomography	132
7.3.1	Sources	133
7.3.1.1	Laboratory-Based Setups	133
7.3.1.2	Synchrotron-Based Setups	135
7.3.2	Sample Stage	138
7.3.3	Detector	138
7.3.4	Forward Problem (Contrast Formation)	140
7.3.5	Tomographic Reconstruction	142
7.3.5.1	2D Filtered Back-Projection	142
7.3.5.2	Image Quality and Artifacts	144
7.3.5.3	3D Image Reconstruction	145
7.4	Synchrotron laminography	146
7.4.1	Introduction	146
7.4.2	Image Reconstruction	149
7.4.3	Example Applications	151
7.5	Absorption Imaging	151
7.5.1	Natural Contrast	151
7.5.2	Staining Contrast	152
7.6	Phase-Contrast Imaging	155
7.6.1	Introduction	155
7.6.2	Free-Space Propagation Methods (Holotomography)	157
7.6.3	Analyzer-Based Imaging	160
7.6.3.1	Applications	161
7.6.4	X-Ray Grating Interferometry	162
7.6.4.1	Introduction	162
7.6.4.2	Performance Characteristics and Applications	165
7.7	Applications (Post-treatment)	166
7.7.1	Segmentation – Visualization Methods	166



9.2.1	Shutter Speed	213
9.2.2	Aperture	215
9.2.3	ISO Value	215
9.2.4	Depth of Field (DoF)	216
9.2.5	Camera Settings	217
9.2.6	What Is a Good Exposure?	217
9.3	Using Flashes	220
9.3.1	Controlling Exposure	220
9.3.2	Positioning and Shaping the Light	220
9.4	Equipment	222
9.4.1	Camera	222
9.4.2	Lenses	222
9.4.3	Flashes	223
9.4.4	Flash Accessories and Lighting Gear	224
9.4.5	Aquarium Setup	224
9.4.6	Other Accessories	225
9.5	Macro Photography of Marine Life	226
9.5.1	Setting up the Camera	226
9.5.2	Positioning the Flashes	227
9.5.2.1	Lighting Small Animals	227
9.5.2.2	Lighting Bigger Animals	228
9.5.2.3	Water Quality	228
9.6	After the Photographic Shoot	228
9.6.1	File Formats	229
9.6.2	Post-processing Workflow	230
9.6.3	Selecting Images	231
9.7	Animal Care	232
9.7.1	Collecting	232
9.7.2	Handling and Imaging	232
	Acknowledgements	233
	References	233
<b>10</b>	<b>Automated Image Processing in Marine Biology</b>	<b>235</b>
	<i>Robert T. Kelly, Maureen A. Williams, and Emmanuel G. Reynaud</i>	
10.1	Introduction	235
10.2	Methods of Planktonic Community Analysis	236
10.2.1	General Methods	236
10.2.2	Semi-automated Options	237
10.3	Semi-automated Planktonic Community Analysis	238
10.3.1	Work Flow of Analysis	238
10.3.1.1	Sample Collection	239
10.3.1.2	Image Capture	239
10.3.1.3	Importation and Segmentation	240
10.3.1.4	Classifier Generation	241

10.3.1.5	Classification	243
10.4	Future Directions	245
10.5	Conclusion	245
	References	246
	<b>Index</b>	<b>249</b>





## Preface

The Earth, the Blue planet, is so called because its larger biotope is a vast and deep intertwined blue expanse of salted oceans and seas. The water is filled with billions of organisms which are mainly invisible to the naked eye. These life forms have allowed us to breathe and to conquer the lands. They are our ancestors, our stones, our oils, our food or the food of our food . . . and they may hold the key to our future in these troubled times of climate change.

The idea for this book germinated during an oceanographic survey in the Mediterranean Sea where, as a cell biologist coming out of a high ranked institute of fundamental research, I realized that many imaging techniques including 3D microscopy techniques were not easily available to marine biologists. I came back eager to share my knowledge with this large and amazing scientific community. Many of my friends responded positively and shared the burden of tracking any application of advanced imaging methods in marine biology and I would like to thank them all, in particular Renaud Boistel, who managed a huge crowd of co-authors to give us a wonderful chapter on X-ray related imaging techniques, Stephan Jericho and his colleagues for their patience, Gustaaf Hallegraeff who shared his long-standing experience of Electron Microscopy techniques applied to planktonic species, and finally my students who took some of the burden of collecting information and writing.

This book is not an encyclopaedia of all imaging techniques applied in marine biology. We made a choice and two main factors influenced our choices: three-dimension and promises.

First, water is always a three-dimensional medium that governs marine organisms: their shapes and forms but also, surely, their physiology. And so there is a crucial need to obtain three-dimensional views as this opens ways to deeper approaches: taxonomy, cell biology and *in vivo* biochemistry, fields well established in the medical world. Secondly, because there are so many imaging techniques out there, we had to make choices for this first edition, so we decided to drop the well-established techniques: light microscopy, cytometry . . . and promote less appreciated techniques or emerging ones that often give us a better three-dimensional view of the creatures of the oceans (Optical Projection Tomography, Light Sheet Microscopy etc.) and we made a big effort to make them available.

We believe that these techniques can be highly beneficial to the marine biology community.

However, we provide some basic skills to enable the reader to photograph larger organisms (Chapter IX) and a historical perspective of ocean imagery (Chapter I) as a reminder of where we are coming from to enlighten the path of where we go...

This book is an introduction to marine biology imaging methods suitable not only for students wishing to pursue marine biology but also for established researchers eager to extend their knowledge of imaging methods that may improve their current or future research.

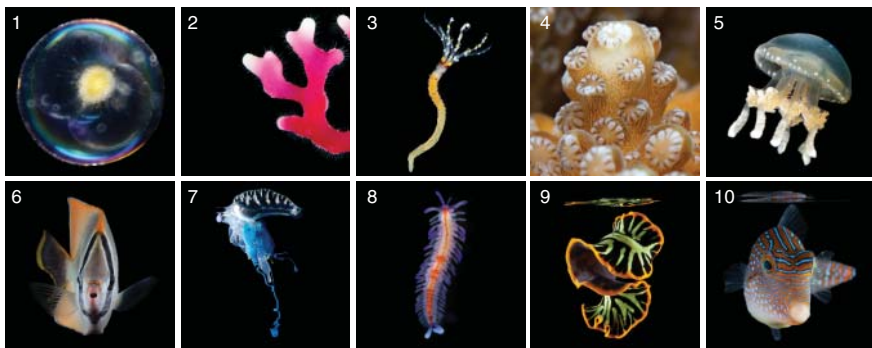
This first book, specifically-designed for the marine biology field, is work in progress. We hope you will find it informative and your feedback is welcome to improve our common knowledge.

*Swim long and image well!*  
*Emmanuel G. Reynaud*



Kahi Kai ('one sea' in Hawaiian) is a project born in Hawai'i. Kahi Kai stands for a unique ocean representing all oceans of our planet, which contain an amazing and mostly unknown biodiversity. The mission of Kahi Kai is to raise awareness about our ocean legacy and to appeal to our shared responsibility to preserve the fascinating, mysterious, and highly endangered marine world ([www.kahikai.org](http://www.kahikai.org)).

Some of the sea creature portraits featured as chapter openers were taken during the Tara Oceans expedition and are currently part of an itinerant exhibition that can be seen in 2013/2014 in French cultural centers and embassies throughout the world.



(1) *Noctiluca* sp. (Sea Sparkle) - Dinoflagellate, (2) - *Distichopora* sp. (Lace Coral) - Cnidarian, (3) *Sabel - lastarte* sp. (Sabellid worm) - Annelid, (4) *Acropora* sp. (Staghorn coral) - Cnidarian, (5) - *Mastigias* sp. (Lagoon jellyfish) - Cnidarian, (6) *Chaetodon trifascialis* (Chevron butterflyfish) - Vertebrate, (7) *Physalia physalis* (Portugese man o' war) - Cnidarian, (8) *Myrianida* sp. - Annelid, (9) *Pseudoceros dimidiatus* (Divided flatworm) - Platyhelminth, (10) *Canthigaster papua* (Papuan toby) - Vertebrate.

Photo credits: Kahi Kai - (1) Noan le Bescot, (2, 5, 6, 7, 9, 10) Eric Röttinger, (3, 4, 8) Aldine Amiel, (1, 2, 4, 6, 10) Tara Oceans.



## List of Contributors

### ***Dominique Adriaens***

Ghent University  
Evolutionary Morphology of  
Vertebrates & Zoology Museum  
K.L. Ledeganckstraat 35  
9000 Ghent  
Belgium

### ***Aldine Amiel***

Kahi Kai (non-profit organization)  
1996 Avenue Poincaré  
06360 Eze-sur-mer  
France

*and*

Université de Nice-Sophia-  
Antipolis/INSERM/CNRS  
Institute for Research on Cancer  
and Aging  
28 Avenue de Valombrese  
06107 Nice  
France

### ***Tilo Baumbach***

Karlsruhe Institute of Technology  
Institute for Photon Science and  
Synchrotron Radiation/ANKA  
Kaiserstraße 12  
76131 Karlsruhe  
Germany

### ***Renaud Boistel***

IPHEP/CNRS  
UMR 7262  
UFR SFA Université de Poitiers  
6 rue Michel Brunet  
86022 Poitiers  
France

### ***Francisco Bonin-Font***

University of the Balearic Islands  
Escola Politècnica Superior,  
Systems, Robotics and Vision  
Group  
Ctra.Valldemossa km 7.5  
07122 Palma de Mallorca  
Spain

### ***Alberto Bravin***

ESRF  
6 Rue Jules Horowitz  
38043 Grenoble, Cedex 9  
France

### ***Antoni Burguera***

University of the Balearic Islands  
Escola Politècnica Superior,  
Systems, Robotics and Vision  
Group  
Ctra.Valldemossa km 7.5  
07122 Palma de Mallorca  
Spain



**Jérémie Capoulade**

European Molecular Biology  
Laboratory  
Cell Biology and Biophysics Unit  
Meyerhofstraße 1  
69117 Heidelberg  
Germany

*and*

Developmental Biology Institute  
of Marseille-Luminy (IBDML)  
UMR 7288 CNRS/Aix-Marseille  
University  
Campus de Luminy  
Case 907  
13288 Marseille, Cedex 9  
France

**Peter Cloetens**

ESRF  
6 Rue Jules Horowitz  
38043 Grenoble, Cedex 9  
France

**Gheyleen Daghfous**

Groupe de Recherche sur le  
Système Nerveux Central  
Département de Physiologie  
Université de Montréal  
H3C 3J7 Montréal  
Québec  
Canada

**Jean-Michel Dischler**

ICUBE  
UMR CNRS-UDS 7357  
(Laboratoire des sciences de  
l'ingénieur, de l'informatique et  
de l'imagerie)  
300 bd Sébastien Brant  
BP 10413  
F-67412 Illkirch Cedex  
France

**Karl Gaff**

School of Biology &  
Environmental Science  
Science Centre West  
University College Dublin  
Belfield  
Dublin 4  
Ireland

**Brigitte Gillet**

Université Paris-Sud (Paris XI)  
IR4M CNRS (UMR 8081)  
Bâtiment 104 & 220  
91405 Orsay  
France

**Gustaaf Hallegraef**

University of Tasmania  
Institute for Marine and Antarctic  
Studies  
Private Bag 55 Hobart  
Tasmania, 7001  
Australia

**Lukas Helfen**

Karlsruhe Institute of Technology  
Institute for Photon Science and  
Synchrotron Radiation/ANKA  
Kaiserstraße 12  
76131 Karlsruhe  
Germany

*and*

ESRF  
6 Rue Jules Horowitz  
38043 Grenoble, Cedex 9  
France

**Manfred H. Jericho**

Dalhousie University  
Department of Physics and  
Atmospheric Science  
Halifax  
NS B3H 3J5  
Canada

**Stefan K. Jericho**

Dalhousie University  
Department of Physics and  
Atmospheric Science  
Halifax  
NS B3H 3J5  
Canada

**Robert T. Kelly**

School of Biology &  
Environmental Science  
Science Centre West  
University College Dublin  
Belfield  
Dublin 4  
Ireland

**Hans J. Kreuzer**

Dalhousie University  
Department of Physics and  
Atmospheric Science  
Halifax  
NS B3H 3J5  
Canada

**Max Langer**

Université de Lyon  
INSA Lyon, CREATIS  
INSERM U1044  
CNRS UMR 5220  
20 avenue Albert Einstein  
69621 Villeurbanne Cedex  
France

and

ESRF  
6 Rue Jules Horowitz  
38043 Grenoble, Cedex 9  
France

**Dee Lawlor**

School of Biology &  
Environmental Science  
Science Centre West  
University College Dublin  
Belfield  
Dublin 4  
Ireland

**Luke McCormac Parker**

School of Biology &  
Environmental Science  
Science Centre West  
University College Dublin  
Belfield  
Dublin 4  
Ireland

**Jan Michels**

Christian-Albrechts-Universität  
zu Kiel  
Department of Functional  
Morphology and Biomechanics,  
Institute of Zoology  
Am Botanischen Garten 1-9  
24118 Kiel  
Germany

and

GEOMAR Helmholtz Centre for  
Ocean Research Kiel  
Biological Oceanography  
Düsternbrooker Weg 20  
24105 Kiel  
Germany

**Gabriel Oliver**

University of the Balearic Islands  
Escola Politècnica Superior,  
Systems, Robotics and Vision  
Group  
Ctra.Valldemossa km 7.5  
07122 Palma de Mallorca  
Spain

**Mattias Ormestad**

Kahi Kai (non-profit organization)  
1996 Avenue Poincaré  
06360 Eze-sur-mer  
France

*and*

SciLifeLab Stockholm  
Karolinska Institutet Science Park  
Tomtebodavägen 23B  
171 65 Solna  
Sweden

**Françoise Peyrin**

Université de Lyon  
INSA Lyon, CREATIS  
INSERM U1044  
CNRS UMR 5220  
20 avenue Albert Einstein  
69621 Villeurbanne Cedex  
France

*and*

ESRF  
6 Rue Jules Horowitz  
38043 Grenoble, Cedex 9  
France

**Marie Poirier-Quinot**

Université Paris-Sud (Paris XI)  
IR4M CNRS (UMR 8081)  
Bâtiment 104 & 220  
91405 Orsay  
France

**Tomas Praet**

Ghent University  
bioMMeda, Institute Biomedical  
Technology  
De Pintelaan 185  
9000 Ghent  
Belgium

**Eric Röttinger**

Kahi Kai (non-profit organization)  
1996 Avenue Poincaré  
06360 Eze-sur-mer  
France

*and*

Université de Nice-Sophia-  
Antipolis/INSERM/CNRS  
Institute for Research on Cancer  
and Aging  
28 Avenue de Valombrose  
06107 Nice  
France

**Emmanuel G. Reynaud**

School of Biology &  
Environmental Science  
Science Centre West  
University College Dublin  
Belfield  
Dublin 4  
Ireland

**Denis Van Loo**

Ghent University  
Department of Physics and  
Astronomy  
Proeftuinstraat 86  
9000 Ghent  
Belgium

**Malte Wachsmuth**

European Molecular Biology  
Laboratory  
Cell Biology and Biophysics Unit  
Meyerhofstraße 1  
69117 Heidelberg  
Germany

**Timm Weitkamp**

Synchrotron SOLEIL  
L'Orme des Merisiers  
Saint-Aubin  
91190 Gif-sur-Yvette  
France

**Maureen A. Williams**

School of Biology &  
Environmental Science  
Science Centre West  
University College Dublin  
Belfield  
Dublin 4  
Ireland

**Irene Zanette**

Department of Physics (E17)  
Technische Universität München  
James-Franck-Straße  
85748 Garching  
Germany









## 1

## Under the Eye of Neptune: An Historical Perspective of Marine Creature Imagery

Emmanuel G. Reynaud

### Abstract

The ocean may have been filled by meteorites bringing water to Earth but its creatures were drawn by men. Sea shells were eaten in caves, dolphins drawn on cave walls. For a long time, though, its surface was the only visible thing, a glittering mirror for the human soul where Gods and Monsters fought over submerged empires, pulling down Atlantis and raising volcanic spires with thunder and smoke. Once the smoke had cleared and man learned to fish then dive, the marvels of the sea appeared and glittered even thousands of meters deep, revealing a magnificent world beyond our imagination. From the jellyfish's ballet to intricate glass houses of radiolarians, this introductory chapter presents a concise history of how man images the invisible oceanic world. Copyright © 2013 John Wiley & Sons, Ltd.

## 1.1

### Introduction

Black and dark was the Universe. Then, the Big Bang lit everything, making energy flow, and amongst the billions of particles thrown across space was our planet, a tiny ball of orange fire. No blue, no green, no life. With time and changes, perhaps meteorite showers, water appeared on Earth and built up the marine world, or at least a place like an ocean, 4.6 billion years ago.

Many theories have been proposed, discussed, discarded, and buried about the origin of life; often the ocean or marine environment is a component of the magical mix that gave rise to the chance for life on our planet. Cells appeared, close to deep sea volcanoes, or perhaps it was in rock pools; in a shallow bay stromatolites used the blazing sun's energy to create food sources and deposits that mark the origin and began the continents. Life expanded and thrived in these early oceans but there was no one to record the creatures that inhabited it. Only bones and stones give us a glimpse of these creatures and for many millions of years there were no eyes to see them, and no arm and digits to draw them or to build cameras to picture this

massive world up to 12 km deep and spanning 70% of our Earth, from the frozen lands of Antarctica to blooming coral reefs.

Oceans covered the globe and currents carried organisms, continents emerged, and shades of green would have been seen from outer space. Blue was no longer the only color: brown, green, gray, and shades of sand were turning our world into a magnificent rainbow. Fishes grew limbs and left this ever moving world packed with predators, and along this line of evolution came the mammals. They took over the world and even the oceans with the biggest of all those left alive: the whales.

They developed and, eventually, stood up to look at the world around them, trying to understand it. They started to draw and we can witness dolphins jumping out of the water (Figure 1.1) painted on rock faces. These are the first known images of an ocean creature painted by men, probably 30 to 10 000 years ago. They imaged marine life on rock faces with natural pigments, a beautiful first attempt to approach the Great Blue Beyond.

One of the most magnificent examples is L'Abri Poisson located in the valley of the Gorge d'Enfer, on the right bank of the Vézère River near Les Eyzies-de-Tayac. It was discovered in 1892 by Paul Girod, and dates from the Aurignacian (about 47,000 to 27,000 years). This salmon, 1.05 m long, is etched and carved in low relief on the ceiling of the vault, enhanced with red pigment. And it has been carved with such accuracy that its attitude can be seen as a characteristic of a male exhausted by spawning. This is one of the only ten Paleolithic cave art fish known.

Other examples of marine animals can be found in the Sierra de Guadalupe cave (Mulegé in Baja California, Mexico), Cueva de la Pileta cave (province of Málaga (Spain) or Misool (West Papua, Indonesia (Figure 1.1)).

Those fish drawings receive their origins from human's desire to feed, clothe, and equip themselves with useful implements. According to Michael Barton, a



**Figure 1.1** Prehistoric rock art, Misool, West Papua, Indonesia. In the Misool area there are several sites decorated with extensive rock art or paintings. The paintings are thought to be between 3000 and 5000 years old and feature dolphins, fishes, whales,

dugong, hands, abstract figures, and what may be representations of “Matuto,” a half-man, half-lizard hero, or god. The sites are on sections of limestone cliff. © Matthew Oldfield 2009.

prominent ichthyologist and professor at Centre College, “the earliest ichthyologists were hunters and gatherers who had learned how to obtain the most useful fish, where to obtain them in abundance and at what times they might be the most available”.

Fish were not the only marine organisms used by the first humans of the Upper Palaeolithic but never painted; molluscs or rather their remains: shells. They were certainly used as food source, raw material, ornaments, containers or even currency.

## 1.2

### Ancient Uses of the Oceans

For many years, the marine world was not only a source of food (fishes, shellfishes) but also, and mainly, a surface to move upon, a liquid pathway to new territories. But this dangerous blue world was deep and dark, feared as the house of Gods and Monsters able to swallow boats and seafarers in a single gulp.

#### 1.2.1

##### Seafarers

Knowing your environment and mastering it was a major leap in human activity. Early seafaring activity have been recorded in Sicily and Cyprus and dated to the Upper Palaeolithic period (30,000 to 11,000 years ago) but the Phoenicians are the most established sea-faring community (1,200BC) using the stars for their oceanic voyages. But Europe and the Mediterranean sea were not the birth place of human maritime activity.

About 30 000 years ago, human cultures along the western coastline of the Pacific Ocean – in the area between what is now Australia and China – started to migrate eastward across the great expanse of the Pacific Ocean. We are not sure exactly why the migrations started, but tribal wars, disease epidemics, the search for food, or natural disasters, such as large volcanic eruptions and earthquakes, may have been factors.

Over about 25 000 years, these people, called *the Polynesians*, eventually colonized the islands of the south and western Pacific, from New Guinea in the west to Fiji, and Samoa in the middle. They then moved onward to Tahiti and, finally, to Easter Island in the eastern south Pacific. How did the Polynesians manage to travel across thousands of miles of ocean without compasses, sextants, clocks, or other tools of modern navigation? Their migration was truly one of the great achievements of early seafaring cultures, and it marks the start of oceanographic observations by people who lived in harmony with the ocean. The Polynesians were very observant. They noted the directions that waves came from and how they affected or rocked their canoes. They had a keen sense of ocean currents and variations in bird and sea life in different places in the Pacific. They also were among the first people to use astronomical observations of the stars to help them navigate across the ocean.

They made the earliest form of navigational or oceanographic map, called *stick charts*. These were made of pieces of bamboo or other wood that were tied together. The locations of islands were often marked with shells or knots, and curved pieces of wood represented the bending of ocean waves around the islands and the way waves rocked their canoes. Polynesians handed down their lore of the sea in both the oral and stick-map traditions.

We can suppose that they also recorded their world and discovery and a few petroglyphs of fishes and canoes can be found on Nuku Hiva, Marquesas Archipelago, France.

### 1.2.2

#### The Mediterranean Sea: the cradle of marine biology

The references to the sea and its mysteries are myriad in Greek civilization, in particular in *The Iliad* and *The Odyssey*. However, in those two books about ancient history the sea is seen as the territory of Gods or as a means of moving from one point to the next and as providing food. Early Mediterranean civilizations, including the Greeks, have passed down many myths that include gods and goddesses who ruled over nature, such as Poseidon and his son Triton. Many Mediterranean legends, such as Jason and the Argonauts, also involved adventures on large and dangerous seas.

About 2900 years ago, the Greeks began to venture outside the Mediterranean, past the Straits of Gibraltar at the western end of the Mediterranean Sea. This narrow channel separates Europe from Africa, and the Mediterranean from the Atlantic Ocean. Just outside of the Straits of Gibraltar, early Greek sailors noticed a strong current running from north to south. Because the sailors had only seen currents in rivers, they thought that this great body of water on the other side of the Straits was an extremely big river. The Greek word for river was *okeano*, which is the root of our word for ocean.

#### 1.2.2.1 Aristotle and Pliny the Elder, the Founding Fathers

**Birth of Natural History Observation** With the Greek world came the Academy, a world of knowledge, teaching, and exchange. A pupil of Plato, Aristotle, was the first to make specific comments on sea life. He had collected and referenced a vast number of species, including echinoderms, molluscs, and fishes, and he wrote the founding book of biology: “Animal stories.”

In 344 BC, he went to the neighboring island of Lesbos, at Mytilene, to visit one of his colleagues from the Academy, the philosopher and naturalist – another student of Plato–Theophrastus (371–287 BC). They studied together the botany and the zoology of the island and also the creatures from the sea, or Thalassa, around it. Aristotle found on this island his second school, for almost two years. In 343 BC, he went back to Macedonia, invited by King Philippe II (359–336 BC), to

become the preceptor of his son, the future Alexander the Great (336–323 BC). He was then appointed head of the Royal Academy of Macedonia.

In 346 BC, Aristotle went to Atarneus with Xenocrates (ca. 396–314) and Theophrastus (ca. 372–288) and moved to the little harbor of Assos (the Turkish village of Berhamkale). Here he pursued further his biological research and started to observe marine life. He was the first to recognize that cetaceans were mammals and that those marine vertebrates were oviparous or viviparous. He described many forms of marine life and deduced gill function. He was the first zoologist and also the first to establish a classification of life forms. He mentioned nearly 400 species. He divided them in two groups: the ones that have blood (*Enhoema*), more precisely red blood, the vertebrates, and the ones without: the invertebrates (*Anhoema*). Amongst the marine organisms described by Aristotle we find fishes and cetaceans and also the *malacostraca* (crustacean, crabs, etc.) as well as the Ostreioda (oysters) and the Mollusca: squids and octopus. The texts that have survived about biology, anatomy, and physiology seem to indicate that Aristotle performed dissections and probably drew them. But we have no record of the way zoology and marine biology was taught in the famous school of Alexandria during the Ptolemaic dynasty where the pupils of Aristotle further pursued his work.

Interestingly, he also discussed tides and thought that there were due to the compression of lower sea water by surface waters. This error was later corrected by the Roman Pliny the Elder (v 23–79 BC), another father of zoology and marine biology, in his “Natural Stories.” He described these regular movements of the sea water (twice a day) as being caused by the Sun and the Moon. He observed two tides a day and, to quote, “In between two moon risings, the sea raises twice and ‘gone’ twice in a 24 hour period” and he pointed out that the tides were never at the same time the following day.

As he was the first to pass on his observations to us, Aristotle is considered to be the father of marine biology and zoology, even though he did not leave any drawings, only description of his observations.

During the Roman Empire we only find zoological observations from Pliny, Solinus, and the agronomical writers. However, Pliny the Elder was mainly a “collector” of stories that he bound together in his “Natural Stories;” he does not provide much new knowledge. The only images of ocean creatures passed on to us are large fishes, dolphins in mosaics in the middle of Monsters, Gods, and Mermaids.

### 1.2.2.2 Understanding the Oceans

**Early Science and Technology** The oceans were a dangerous place to be and the lack of a reference point on this ever changing blue surface made it difficult to navigate. The Egyptians and the Phoenicians mainly used coastal navigation to conquer the Mediterranean Sea. Finally, the Greeks extended the range of their journey towards Gibraltar and in 325 BC Pytheas sailed from Greece to Iceland and following the North Star he observed latitude, correcting Aristotle. He also proposed that the tides were caused by the Moon. His followers, like Eratosthanes,

calculated the circumference of the Earth. Aristarchus independently calculated the diameter of the Earth from observations of the elevation of the Sun at noon at two locations along a north–south line between Greece and Egypt. Those first invisible reference lines using the stars made it possible to draw maps and Ptolemy, in 127–151 AD, produced the first world atlas, including the Pacific and Indian Oceans; he also showed the world as a globe. At the other side of the planet, the Polynesians developed advanced maps or stick maps that display key islands but mainly ocean currents that helped them to move great distances.

Finally, Hellenistic Greece developed coastal markers and lighthouses as navigational aids, one of which, the Pharos (lighthouse) of Alexandria, was one of the Seven Wonders of the Ancient World. They also probably established ways of accurately measuring time so as to be able to precisely determine latitude. However, such discoveries were only ways of using the surface of the ocean – the life striving in the ocean lay hidden under the waves, drifting with the Gods: Oceanus, Tethys, the nymph Eurynome, and the giant Ophion.

### 1.3

#### From Neptune to Animalcules

Poseidon and his daughter Charybdis were replaced by Neptune as the Roman Empire conquered the world, including the European coast lines. The desire to explore and to rule pushed ahead mainly on roads and oceans. Then there came trade and legends of gold and spices so far away by foot that European explorers turned to the sea to find faster trade routes to cities in Asia and Europe. Prince Henry the Navigator of Portugal (1420) recognized the oceans' importance to trade and commerce and he established the first school of navigation.

#### 1.3.1

##### Age of European Discovery and Exploration

The fifteenth century saw Bartholomew Dias (1486) and then Vasco de Gama (1498) sailed around Africa and into the Indian Ocean while Columbus sailed the Atlantic and (re)discovered the Americas, becoming the first European to sail westward across the Atlantic Ocean and return home. Ponce de Leon “discovered” (for the European) the Pacific Ocean. Finally, the ultimate goal of circumnavigating the Earth was achieved by the Portuguese Ferdinand Magellan (1520) and later by Sir Francis Drake (1580).

It was not until the sixteenth century that zoology become a major subject of research and one of the earliest researchers was probably Guillaume Rondelet, known also as *Rondeletus*, in Montpellier who also, like Aristotle, performed dissection and explored not only fishes but also sea urchins and crabs. In 1556, he published “The Complete Story of Fish.”



### 1.3.2

#### Voyages of Exploration and finally Science

In the early 1700s, several European countries sought to expand their empires and discover new lands for raw materials, colonies or trade, and for spices from the East Indies, which they believed would help cure the Plague. They launched expeditions to survey faraway lands across the Atlantic, Pacific, and Indian Oceans, and in doing so also explored the Arctic and Antarctic Oceans. But only the lands were concerned and the oceans were merely a roadway to move from one land to another to claim them for their king, queen and other empires. The only sailors concerned about the sea creatures were the whalers.

But in 1768, James Cook, on board the HMS *Endeavour* is sent to Tahiti on a scientific mission: to observe a rare eclipse caused by the interposition of Venus between Earth and the Sun. Passed through Cape Horn; he made his astronomical observations in June 1769. The British captain then took possession of the archipelago which he gives the name of the Society Islands, in honor of the Geographical Society of London which send him to Tahiti. Over 10 years, Cook led three world-encircling expeditions and mapped many countries, including Australia, New Zealand, and the Hawaiian Islands. He was an expert seaman, navigator, and scientist who made keen observations wherever he went.

James Cook was not only an explorer. His travels have marked the end of the Great Discoveries and have allowed significant progress in the knowledge of the Pacific Ocean, with the hydrographic surveys and thoroughness of this great observations and reports. His expeditions were a huge success in Europe, which became fascinated with the stories of Cook, published along with remarkable maps and drawings. Louis XVI, during the Franco-English war, ordered to befriend him. The Anglo-French competition, hosted by Bougainville and La Perouse, facilitated the expansion of geographical knowledge of the Pacific. James Cook began the era of scientific exploration.

### 1.3.3

#### A Glimpse at the Invisible

The eighteenth century was not only a time of expedition but also of a major breakthrough for the future of biology. The magnifying power of segments of glass spheres was known to the Assyrians before the time of Christ; during the second century AD, Claudius Ptolemy, an astronomer, mathematician, and geographer at Alexandria, wrote a treatise on optics in which he discussed the phenomena of magnification and refraction as related to such lenses and to glass spheres filled with water. Despite this knowledge, however, glass lenses were not used extensively until around 1300, when an anonymous person invented spectacles for the improvement of vision. This invention aroused curiosity concerning the ability of lenses to magnify. In Holland in 1673, Anton Van Leeuwenhoek prepared quality lenses so that he could better examine garments. However, his insatiable curiosity led him to built one of the first microscope and use these lenses to examine many

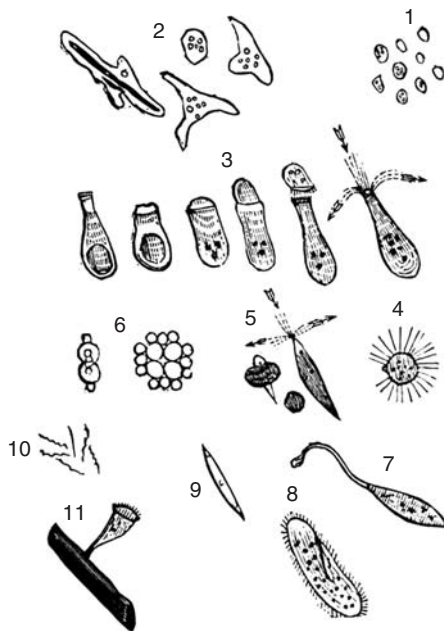


**Figure 1.2** Antonie van Leeuwenhoek “Animalcules.” The first pictures ever drawn of planktonic species defined by Antonie van Leeuwenhoek as “animalcules” or very tiny animals, which will become ciliates, algae, *Paramecium*, and so on.

biological items, including pond water. What he discovered in the water was a microscopic world of life. He described moving “animalcules,” later described by Christiaan Huygens in 1678 as *paramecium* (Figure 1.2). He described rotifers, *Euglena* and *Spirogyra* and paved the way to the use of microscope in biology and the extensive description of the invisible life in each drop of fresh or sea water.

## 1.4

### The Birth of Oceanography (The Nineteenth Century)

#### 1.4.1

##### Drawing the Jellyfish

Nicolas Baudin in the *Geographe* and Emmanuel Hamelin on the *Naturalist* left Le Havre on October 19, 1800 for what will be called the Baudin expedition (1800–1804). Francois Peron (1775–1810), a French naturalist and physicist, aboard the *Geographe*, alongside the artist Charles-Alexandre Lesueur (1778–1846). Only a few scientists and crew members survive dysentery, fevers, deprivation and navigation in the southern storms. The journey ends at Port Jackson the 20th of June 1802. But before, the *Geographe* had to leave hurriedly King Island to escape a storm, and left Peron and Lesueur behind. They will be collected twelve days later by

an English ship. The return of the expedition, March 25, 1804 in Lorient, takes place in the utmost discretion, politics and rivalries in Europe monopolizing Napoleon. But the expedition brought a hundred unknown live animals to Europe (presented to the Empress Josephine) and nearly 100,000 samples. Of these, more than 2,500 new species were described for the first time, Peron included in a rational and logical classification of high modernity. Also, Charles-Alexandre Lesueur realized the most vivid paintings based on live animals of jellyfishes, siphonophores and other fishes. Those were the first accurate depictions of those nearly invisible species, decades before Forbes, Agassiz or Haeckel books on the subject but the Napoleon wars and the political situation obscured their beauty and the expedition reports were greatly ignored.

#### 1.4.2

#### The H.M.S. Challenger Expedition

The nineteenth century was an important time for the development of marine biology. However, the oceans were still mainly treated as a motorway where the priority was to establish safer and faster routes for good transports. The only experienced sailors exploring unknown territories for economical reason were the whalers. Those “biologists” by needs observed the whale behaviors, charted new routes and brought back astonishing legends such as the depth to which those animals could dive far below the scientifically approved limits of life in the deep oceans. Those observations and their books were used by Americans and well as British Admiralty to improve their charts. For example, Matthew Fontaine Maury, (1806–1873) the American father of modern oceanography, compiled analyses of wind and current logs, and published maps of wind and current patterns. He wrote the first oceanography textbook in 1855, “The Physical Geography of the Sea”.

On the other side of the Atlantic, the Voyage of HMS *Beagle* (1831–1836) with Charles Darwin led to the publication of “The Origin of Species” but brought little to the history of marine biology apart from the theory of coral reefs formation.

In 1852, the United States Navy Department decide to conduct a naval and commercial survey of those parts of Bering Straits, the North Pacific Ocean and the China Seas frequented by American whaling ships and by trading vessels in their routes between the United States and China. This was an economical expedition but Captain Cadwallader Ringgold was placed in command of the expedition, which departed from Norfolk, Virginia, in June 1853. And William Stimpson was appointed Chief Zoologist alongside naturalists such as Alfred H. Ames, Assistant Naturalist, and Charles Wright, Botanist. From 1853 to 1856, they collected an extensive natural history collections were made. For nine years after the completion of the expedition, Stimpson utilized the facilities of the Smithsonian Institution while preparing a report based on the collections gathered during the expedition. While at the Smithsonian, he also helped classify and name specimens which the Smithsonian had been collecting. This great collection, including all the manuscripts being prepared by Stimpson, was destroyed in the Chicago fire of 1871, an event from which Stimpson never fully recovered.

Those expedition reports were largely ignored by the European and mainly British scientists. Their main concern in oceanography was the “Azoic theory”. Edward Forbes, a distinguished British naturalist sailed with the British Survey on the HMS *Beacon*, charting the waters of the Mediterranean and Aegean Sea, where he was able to dredge for samples from the deepest waters examined to date based on European records ignoring American dredging in the North Pacific and the whaler tales. After these explorations, he developed his theory that below 300 fathoms (~600 meters) the mysterious dark depths of the seas was a lifeless area and he named this the Azoic (lifeless) zone. His theory was accepted by the public but not by his colleagues such as Charles Wyville-Thomson who followed him in the Edinburgh Chair of Zoology.

C. Wyville Thomson and W.B. Carpenter started large oceanographic cruises (HMS *Lightning* and HMS *Porcupine*) and started to falsify the “Azoic theory” bringing animals from below the Forbes 300 fathoms line with their dredges. These discoveries persuaded the British government to launch a worldwide expedition to explore the ocean depths not only because they wish to disprove Forbes theory but also because another important economical endeavour was a stake: the telegraph.

The *Challenger* Expedition (1872–1876) – sponsored by the Royal Society and Royal Navy – left Portsmouth, England, just before Christmas 1872. The ship had many different types of samplers to grab rocks or mud from the ocean floor, and nets to capture animals from different levels in the ocean. It was the first expedition organized specifically to gather data on a wide range of ocean features, including ocean temperatures, seawater chemistry, currents, marine life, and the geology of the seafloor. The H.M.S. *Challenger* also had different winches – mechanical engines used to lower and hoist sounding lines to measure how deep the ocean was. At each sampling station, the crew lowered trawls, nets, and other samplers to different depths, from the surface to the seafloor, and then pulled them back on board loaded with animals or rocks. This British Navy corvette (a small warship), was converted into the first dedicated oceanographic ship with its own laboratories, microscopes, and other scientific equipment onboard (Figure 1.3). The expedition was led by British naturalist John Murray and Scottish naturalist Charles Wyville Thompson.

H.M.S. *Challenger* first traveled south from England to the South Atlantic, and then around the Cape of Good Hope at the southern tip of Africa (Table 1.1). It then headed across the wide and very rough seas of the southern Indian Ocean, crossing the Antarctic Circle, and then went on to Australia and New Zealand. The expedition then headed north to the Hawaiian Islands, and then south again around Cape Horn, at the southern tip of South America where the Pacific and Atlantic Oceans meet. After more exploration in the Atlantic, they returned to England in May of 1876.

It visited all of the world oceans, except the Arctic, covering 127,000 km. Scientists on board studied the physical conditions of the deep ocean, the chemical composition of seawater, the physical and chemical characteristics of the seafloor deposits, and the distribution of organic life at all water depths. As part of the

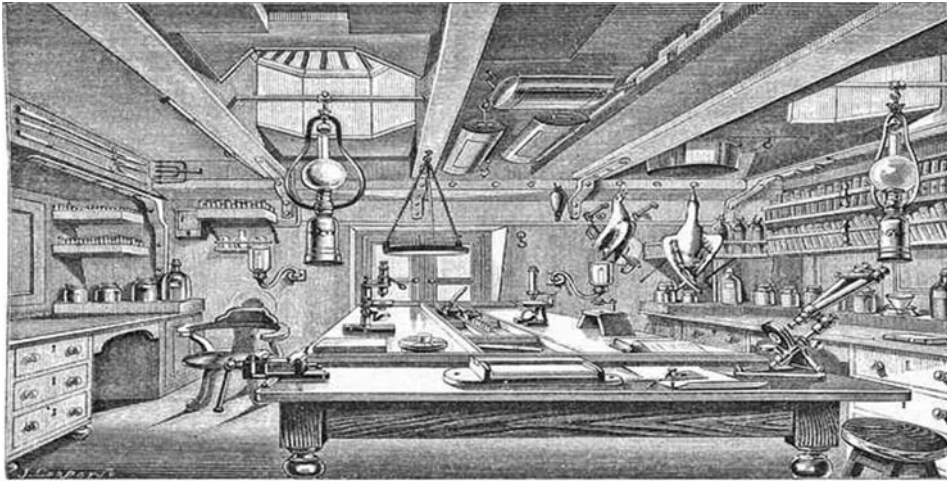


FIG. 1.—The Natural History Work-room.

**Figure 1.3** *H.M.S. Challenger* biological laboratory – This is a drawing of the first embarked biological laboratory to dissect, image, and analyze freshly collected planktonic and marine species – it would take 30 years to fully record and publish the results.

**Table 1.1** Some facts about the *H.M.S. Challenger* Expedition.

Expedition crew	243
Scientists	6
Duration of expedition	4 years
Distance sailed	127 000 km (68 890 miles)
Number of sampling stations	362
Number of depth soundings made	492
Number of dredges taken	133
Number of new species of animals and plants discovered	4700

cruise, scientists measured the water depth of the Marianas Trench (8185 m); some 4717 new marine species were netted and classified.

The expedition also tested and disproved Haeckel's *Bathysius theory* (primordial slime) (Figure 1.4). Even though, Ernst Haeckel worked extensively on the samples brought back by the *Challenger* Expedition and will draw them to great length showcasing to the world new planktonic unicellular species: radiolarian, acantharian . . . Those marvelous illustrations and drawing made by Ernst Haeckel were used by Leopold and his son Rudolf Blaschka to create the unique marine glass invertebrate models displayed across Europe in Museums and used in many universities to teach marine biology and influence the new generation of biologists and microscopists (Figure 1.4). The later publication of his book “*Art Forms of Nature*” will influence artists of the Art Nouveau movement introducing the planktonic life forms in the general public. Rene Binet, a French painter and architect, studied extensively the works of Ernst Haeckel and his study of Haeckel's lithographs of



**Figure 1.4** Blaschka glass jellyfish – Leopold and Rudolf Blaschka designed a unique way to display in a full three-dimensional manner marine invertebrate such as jellyfishes, ctenophores, and microscopical planktonic organism (radiolarians). Courtesy of Francis Latreille.

radiolaria culminated in the design for his Monumental Gate, located on the Place de la Concorde, at the Eastern entrance of the World Fair held in Paris in 1900. The design was heavily based on one radiolaria illustration alone – the *Cyrtoida Pterocanium trilobum*.

Most of all, the *Challenger* Expedition encouraged other countries to take an interest in the oceans and to mount their own expeditions such as the ones led by Prince Albert I of Monaco (Expeditions *Princesse Alice* I and II, *Hirondelle* I and II), who founded the Oceanographic Institute, which was later led by Jacques Cousteau. Prince Albert of Monaco led several expeditions and also developed an extensive knowledge of currents and collected maps. His institute knowledge of currents proved valuable during World War I as it allows military officials to predict how explosive mines would drift in the ocean and where they would land as in the twentieth century the oceans turn into battlefields.

The German Empire was not left out of the Ocean Race for Knowledge and led two important expeditions: 1889 – National Expedition and 1898–1899 - *Valdivia* expedition.

#### 1.4.3

##### Stations and Institutions

But one major step forward was the establishment of stations and institutions that will foster marine biology imagery and progress.

The College de France founded the first ever marine stations in Concarneau in 1859 which later extended to Roscoff on the northwest of France. Originally established for the cultivation of marine species, such as Dover sole, because of its location near marine estuaries with a variety of marine life, it evolves towards research on molecular biology, biochemistry, and environmental studies.

A few years late, the Stazione Zoologica was founded in 1872 by the German zoologist Anton Dohrn (1840–1909), a former student of Ernst Haeckel. Dohrn thought of the Napoli institute as a pilot centre of a worldwide network of research

facilities for studies in marine biology. He envisioned a railroad system where scientists could stop, collect material, make observations and conduct experiments, before moving to the next 'station': therefore the name "Stazione (=Station)".

At Woods Hole (USA) in 1888, the Marine Biological Laboratory (MBL) was established by Alpheus Hyatt, a student of Harvard naturalist Louis Agassiz who had established the first seaside school of natural history on an island near Woods Hole. MBL was designed as a summer program for the study of the biology of marine life for the purpose of basic research and education. The Woods Hole Oceanographic Institute was created in 1930 in response to the National Academy of Science's call for "the share of the United States of America in a worldwide program of oceanographic research". An independent biological laboratory was established in San Diego in 1903 by University of California professor Dr. William E. Ritter, which became part of the University of California in 1912 and was named the Scripps Institution of Oceanography after its benefactors. The MBL was also the first oceanographic institution to build the first oceanographic research vessel: "*Atlantis*" specifically for interdisciplinary research in marine biology, marine geology and physical oceanography. From 1931 to 1966, the "A-boat" made 299 cruises and covered 700,000 miles, doing all types of ocean science.

Interestingly the same year: 1888, a marine biological laboratory was established in Plymouth, England. This laboratory was established by the Marine Biological Association of the United Kingdom.

Finally, the Monaco's Oceanographic Museum and Laboratory opened in 1906 and was followed by an extensive network of stations across the Globe.

## 1.5

### The Twentieth Century: Institutions and moving images

The twentieth century was a century of wars and technological developments. One of them, the sonar gave images of the ocean sea floor based on acoustic measurement. The possibilities to observe the marine creatures in their habitat rather than in specimen jar even at great depth was another important step especially when using moving images or video.

#### 1.5.1

##### New tools – new images:

Technology brought the study of marine biology to new heights. In 1934 William Beebe (1877–1962) and Otis Barton descended 923 m/3,028 ft below the surface off the coast of Bermuda in a bathysphere designed and funded by Barton. This depth record was not broken until 1948 when Barton made a bathysphere dive to 1,372 m/4,500 ft. During the interim, Beebe was able to observe deep sea life in its own environment rather than in a specimen jar. Although he was criticized for failing to publish results in professional journals, his vivid descriptions of the bathysphere dives in the books he published inspired some of today's greatest oceanographers and marine biologists.



In 1960, a descent was made to 10,916 m/35,813 ft in the Challenger Deep of the Marianna trench – the deepest known point in the oceans, 10,924 m/35,838 ft deep at its maximum, near 11° 22'N 142° 36'E – about 200 miles southwest of Guam. The dive was made in the bathyscape “The Trieste” built by Auguste Piccard, his son Swiss explorer Jean Ernest-Jean Piccard and U.S. Navy Lieutenant Don Walsh. The descent took almost five hours and the two men spent barely twenty minutes on the ocean floor before undertaking the 3 hour 15 minutes way up.

Several technological developments allowed the marine biologists to record images *in situ* but also with better resolution (microscopes) and allowed the publications of pictures, photographs and videos. Remotely Operated Vehicle (ROV) and the development during the Second World War of scuba diving brought men further into the oceans as well as the establishment of ocean observatories, permanent stations connected to shore with optical cable.

### 1.5.2

#### Jean Painlevé

Jean Painlevé (1902–1989) was raised by his aunt, Mary, widow and sister of Paul Painlevé, after his mother, Marguerite Petit de Villeneuve is carried by puerperal fever shortly after his birth. He was not the best at school and skipped classes to go to the Zoo where he helps the guardian to care for animals. He managed to attend the Lycée Louis Le Grand, Paris and began studying medicine in 1921. Two years later, he slams the door in the face of Professor Delbet after a disagreement over the treatment of hydrocephalus patients that he estimated a cruel treatment. He turned to biology and begins to attend the Station Biologique de Roscoff where he met Alexander Calder and the surrealist movement. He also started to experiment with cameras and from 1927 he spent all his time making documentaries whose subject is the world of marine animals, shrimp, octopus, sea urchins and other shellfish. Between 1928 and 1930, he shot a dozen films, including several for the general public: “The Octopus”, “The Urchin”, “The Hermit Crab”, “Crab and Shrimp”, “Caprelles and Pantopodes” and “Hyas and Sténorinques”. Some of those films were presented in Paris and the press was very generous but also artists such as Fernand Léger or Marc Chagall. One of his movies “The SeaHorse” was distributed by Pathé and established Jean Painlevé as an artist but also the first scientific filmmaker and a movie maker of marine organisms. Painlevé, through film, wanted to show the bustling life of the underwater world to the “unsuspecting public”. He realized more than 200 films and inspired not only artists but also scientists the ever expanding use of cinema and videos in marine biology.

### 1.5.3

#### The Writers and the Explorers

The twentieth century was a time of media and communication that reached out and gave the unique opportunity to show to the public the oceans and its creatures



with books, novels than movies, TV series and online pages. Some people are well-known for their dedication to the marine world.

Rachel Carson (1907–1964) was a scientist and writer who brought the wonders of the sea to people with her lyrical writings and observations about the sea. Although she was a biologist for the US Fish and Wildlife Service, she devoted her spare time to translating science into writings that would infect the reader with her sense of wonder and respect for nature. She published a book in 1941 titled “*Under the Sea-Wind*.” These publications described the sea and the life within it from a scientist’s point of view, but in the words of a naturalist. In 1951, she published “*The Sea Around Us*” a prize-winning bestseller on the history of the sea.

Dr. Robert Ballard (1942–), a deep-sea explorer, may be best known for finding the Titanic, and helping James Cameron, using technologies he helped to develop, including the *Argo/Jason* remotely operated vehicles and the technology that transmits video images from the deep sea. His earlier deep sea explorations led to the first discovery of hydrothermal vents during an exploration in a manned submersible of the Mid-Ocean Ridge. Ballard spent 30 years working on the use of manned submersibles. Ballard has devoted a great deal of time to furthering the field of deep sea exploration. He created a distance-learning program with more than one million students enrolled, taught by more than 30,000 science teachers worldwide.

Jacques Cousteau (1910–1997) was determined to safely breathe compressed air underwater in order to lengthen dive times. His work with Emile Gagnan ultimately led to the invention of the regulator which releases compressed air to divers “on demand” (as opposed to a continuous flow). The combination of the Cousteau-Gagnan regulator with compressed air tanks allowed Cousteau the freedom to film underwater, and by 1950 he had produced the Academy Award winning “*The Silent World*.” By the 1970s he was bringing the underwater realm into millions of homes with his PBS series “*Cousteau Odyssey*.” Cousteau’s television documentaries won 40 Emmy Awards. Like other oceanography pioneers, Cousteau was criticized for his lack of scientific credentials; however his legacy fostered a greater knowledge and understanding of the devastation caused by threats to ocean health such as pollution of marine resources and resource exploitation.

Dr. Hans Hass (1919–2013), the Cousteau’s Austrian counterpart, also helped introduce the wonders of the underwater world to the public. Hass and his wife Lotte were both passionate about underwater exploration and protection of the marine environment, and together they produced numerous documentaries and wrote a variety of books on their underwater experiences. During his career as an underwater explorer, Hass also made significant contributions to diving technology. He invented one of the first underwater flash cameras and contributed to the development of the Dräger oxygen rebreather which he and Lotte used in 1942 to film “*Men Amongst Sharks*” and continued to use on diving expeditions aboard their research vessel “*Xarifa*” in the Red Sea and Caribbean. Hass is also known as one of the first humans to interact with a sperm whale underwater which helped him become a pioneer in the study of marine animal behavior.

#### 1.5.4

#### The Future

Today, the possibilities for ocean exploration and imaging are nearly infinite. In addition to scuba diving, fast computers, remotely-operated vehicles (ROVs), deep sea submersibles, reinforced diving suits, and satellites, other technologies are also being developed. In spite of ongoing technological advances, it is estimated that only 5% of the oceans have been explored. Surprisingly, we know more about the moon than we do the ocean. Many new discoveries await us as we use new instruments and deep submergence vehicles to explore the “inner space” in the twenty-first century.

In future, oceanographers want to go beyond learning about what is down there in the ocean to learning about what is going on down there. They want to observe oceans processes that change over days, weeks, seasons, years, or decades. However, it is difficult and expensive to send research ships back to the same site for repeat measurements. Sometimes rough seas and stormy weather make it impossible to send ships to certain parts of the oceans at certain times.

Consequently, oceanographers are launching a new era of ocean exploration. They want to establish long-term ocean floor observatories with arrays of sensors and instruments that make continuous measurements of various ocean properties and events. Data from the observatories will be sent to shore-based laboratories via submerged fiber-optic cables or via cables linked to moored buoys that can transmit data via satellite. The data can then be made available via the Internet.

Oceanographers will, in future, use different types of ROVs and AUVs that can “fly” in the oceans or along the seafloor, collecting measurements. The data can be downloaded when the AUVs surface, or when they dock at an underwater docking site. Oceanographers are also developing instrumented buoys moored thousands of miles from shore, and free-floating drifting instruments that can transmit data to scientists in their laboratories using satellites and the Internet.

### 1.6

#### Time Line of Ocean Imagery

- **30,000 BC (Upper Paleolithic Period):** Cave painting and carving of fishes and marine mammals in Europe and South East Asia
- **30,000 BC – 3,000 BC:** Polynesians then Mediterranean civilizations sailed the oceans and master currents, star guided navigations and named the Great Salted River, *okeanos*.
- **384 BC – 322 BC:** Aristotle, Greek philosopher and polymath wrote the first treaty of marine zoology.
- **323 BC – 32 BC:** Hellenistic Period. Marine mammals such as dolphins and fishes are represented in mosaics, vases but also in sculpture as gods mounts. Greek sailors further extended Thalassa limits.

- **27 BC–AD 476:** Roman Empire. Marine mammals such as dolphins and fishes are represented in mosaics, vases but also in sculpture as gods mounts.
- **1507–1566:** Gulielmus Rondelet wrote *libri de piscibus marinis*, whose works are almost entirely limited to Mediterranean and European fishes.
- **1530:** The first longitude is established but it will not be until 1737 and John Harrison that the first precise marine chronometer will appear.
- **1632–1723:** Antonie Philips van Leeuwenhoek: He described and draw for the first time “animalcules” found in a drop of water (rotifers, *euglena*, *spirogyra*).
- **1728–1779:** **James Cook:** The famous British explorer is well-known for his extensive voyages of discovery for the British Navy. He introduce the presence of scientists onboard expedition vessels who defined the modern day study of marine biology.
- **1842:** Darwin publishes *The Structure and Distribution of Coral Reefs*, in which he suggests that coral atolls are the final stage in the subsidence and erosion of volcanic islands.
- **1843:** Edward Forbes (1815–1854), after sailing on the HMS *Beacon* in the Mediterranean, develops the Azoic theory (no life deeper than 300 f = 1800 ft). This is the first marine scientific hypothesis! It started a 20-year debate on the presence of the lifeless (azoic) zone.
- **1857:** Charles Darwin (1809–1881) – Voyage of the HMS *Beagle*: circumnavigated the world; theory of coral reef subsidence (drilling in the Enewetak atoll partially confirmed the hypothesis); barnacle classification.
- **1859:** The first oceanographic station is established at Concarneau in France.
- **1868–1869:** Wyville Thomson dredges from HMS *Lightning* and *Porcupine* and discovers life as deep as 2400 fathoms, exploding forever Edward Forbes’ theory of a lifeless (azoic) zone below 300 fathoms.
- **1872–1876:** The *Challenger* Expedition circumnavigates the globe in the first great oceanographic expedition. Research is conducted on salinity, density, and temperature of sea water as well as ocean currents, sediment, and metrology. Hundreds of new species are discovered and underwater mountain chains documented. Modern oceanography is based on this research. The British *Challenger* expedition was led by Sir Wyville Thomson, who died before all of the results are compiled. Sir John Murray finished the great work, publishing 50 volumes of the *Challenger’s* results and discoveries.
- **1872:** The Stazione Zoological was founded in by the German zoologist Anton Dohrn (1840–1909)
- **1888:** Marine Biological Laboratory (MBL) was established by Alpheus Hyatt, a student of Harvard naturalist Louis Agassiz at Woods Hole (USA).
- **1888:** The Marine Biological Association of the United Kingdom established the marine biological laboratory Plymouth, England.
- **1890–1898:** First Austrian–Hungarian deep sea expedition on board the ship SMS *Pola* led by Franz Steindachner in the eastern Mediterranean and the Red Sea.

- **1898–1899:** First German deep sea expedition on board the ship *SMS Valdivia* led by Carl Chun; found many new species from depths greater than 4000 m (13000 ft) in the southern Atlantic Ocean.
- **1906:** Establishment of the Monaco's Oceanographic Museum and Laboratory
- **1930:** Jean Painleve shot the first movies of marine organisms
- **1930:** William Beebe and Otis Barton are the first humans to reach the Deep Sea when diving in the so-called Bathysphere, made from steel. They reach a depth of 435 m (1430 ft), where they observed jellyfish and shrimp.
- **1930:** Establishment of the Woods Hole Oceanographic Institute and build the “*Atlantis*” the first oceanographic vessel dedicated specifically for interdisciplinary research in marine biology, marine geology and physical oceanography.
- **1934:** Edward Beebe is lowered in a tethered bathyscaph to a depth of 3028 ft, marking the advent of manned exploration of the sea. William Beebe dives in his *bathysphere* to a depth of 908 m on 14 August 1934. He is the first to observe firsthand life at great depth.
- **1942:** Hans Hass film and present the movie: “*Men Amongst Sharks*”
- **1950:** Jacques Cousteau produced the Academy Award winning “*The Silent World*.”
- **1960:** Bathyscaph Trieste dives to what was believed to be the deepest point in the Mariana Trench: a depth of 10 915 m was observed. Since then, in 1998, a Japanese research vessel measured 10 938 m in the same area. The trench was first sounded by *H.M.S. Challenger* in 1875, and again by *H.M.S. Challenger II* in 1951.
- **1970:** Jacques Cousteau brings the underwater realm into millions of homes with his PBS series “*Cousteau Odyssey*.”

## Further Reading

### Basic Texts

- Deacon, M. (1997) *Scientists and the Sea 1650–1900: A Study of Marine Science*. Aldershot, UK, Brookfield, VT: Ashgate, 2d edn, pp. 459
- McConnell, A. (1982) *No Sea Too Deep: The History of Oceanographic Instruments* (Bristol: A. Hilger), pp. 162.
- Mills, E.L. (1989) *Biological Oceanography: An Early History, 1870–1960*. (Ithaca, NY: Cornell University Press, pp. 378.

### Source Books

- Deacon, M.B. (ed.) (1978) *Oceanography, Concepts and History*. Benchmark Papers in Geology, Vol. 35, Stroudsburg, PA: Dowden, Hutchinson & Ross, pp. 394.

- Deacon, G.E.R. and Deacon, M.B. (eds) (1982) *Modern Concepts of Oceanography*. Benchmark Papers in Geology, Vol. 61, Stroudsburg, PA: Hutchinson & Ross, pp. 385.
- Idyll, C.P. (ed.) (1969) *The Science of the Sea: A History of Oceanography*, New York: T.Y. Crowell, pp. 280.
- Murray, J. (1885) in *Report on the Scientific Results of the Voyage of H.M.S. Challenger During the Years 1873–1876*, Narrative, vol. I First Part, London: John Murray, pp. xxxi–liv.
- Murray, J. (1912) in *The Depths of the Ocean*, J. Murray, J. Hjort (eds), London: Macmillan, pp. 1–21.
- Schott, W. (1987) *Early German Oceanographic Institutions, Expeditions and*

- Oceanographers, Hamburg: Deutsches Hydrographisches Institut, pp. 50.
- Thomasson, E.M. (ed.) (1981) *Study of the Sea: The Development of Marine Research under the Auspices of the International Council for the Exploration of the Sea*, Farnham: Fishing News Books, pp. 253.
- Vaughan, T.W., et al. (eds) (1937) *International Aspects of Oceanography: Oceanographic Data and Provisions for Oceanographic Research*, Washington, DC, National Academy of Sciences, pp. 225.

### Ships and Expeditions

- de Buen, R. (1934) *Liste Chronologique des Croisieres Oceanographiques: Manuel pour les Observations Oceanographiques a la Mer-Commission Internationale pour l'Exploration Scientifique de la Mer Mediterranee I*, Venezia: C. Ferrari, pp. 73.
- Estok, R. and Boykin, R.E. (1976) *A Union List of Oceanographic Expeditions Including Results of Some Major Cruise Reports*, College Station: Texas A&M University Libraries, pp. 138.
- Guberlet, M.L. (1964) *Explorers of the Sea: Famous Oceanographic Expeditions*, New York: Ronald Press, pp. 226.
- Rice, A.L. (1986) *British Oceanographic Vessels, 1800–1950*, London: Ray Society, pp. 193.
- Schlee, S. (1978) *On Almost Any Wind: The Saga of the Oceanographic Research Vessel Atlantis*, Ithaca, NY: Cornell University Press, pp. 301.
- Wust, G. (1964) The major deep-sea expeditions and research vessels, 1873–1960, a contribution to the history of oceanography, *Prog. Oceanogr.* 2, 1–52.
- (2003) Archaeological Evidence for the Emergence of Language, Symbolism, and Music: An alternative Multidisciplinary Perspective, *Journal of World Prehistory* 17 (1), 1–51.
- Limburg, P.R. (1979) *Oceanographic Institutions: Science Studies the Sea*, New York: Elsevier/Nelson Books, pp. 265.
- Metz, C.B. (ed.) (1985) *The Naples Zoological Station and the Marine Biological Laboratory: One Hundred Years of Biology*, Biological Bulletin, vol. 168 Supplement, The Marine Biological Laboratory, pp. 1–207.
- Pinsell, M.I. (1981) *150 Years of Service on the Seas: A Pictorial History of the U.S. Naval Oceanographic Office from 1830 to 1980*, vol. 1 (1830–1946), Washington, DC, Department of the Navy, Oceanographic Office, pp. 233.
- Raitt, H. and Moulton, B. (1967) *Scripps Institution of Oceanography: First Fifty Years*, San Diego, CA: Ward Ritchie Press, pp. 217.
- Revelle, R. (1980) in *Oceanography: The Past* (eds M. Sears and D. Merriman), New York, Heidelberg, Berlin: Springer-Verlag, pp. 10–24.
- Sahrhage, D. (1982) 80 Jahre Deutsche wissenschaftliche kommission fur Meeresforschung. *Meeresforschung* 29, 197–207.
- Schott, W. (1987) *Early German Oceanographic Institutions, Expeditions and Oceanographers*, Hamburg: Deutsches Hydrographisches Institut, pp. 50.
- Shor, E.N. (1978) *Scripps Institution of Oceanography: Probing the Oceans 1936 to 1976*, San Diego: Tofua Press, pp. 502.
- Southward, A.J. and Roberts, E.K. (1987) One hundred years of marine research at Plymouth. *J. Mar. Biol. Assoc. U.K.* 67, 465–506.

### Institutions

- D'Errico, F., Henshilwood, C., Lawson, G., Vanhaeren, M., Tillier, A.M., Soressi, M., Bresson, F., Maureille, B., Nowell, A., Lakarra, J., Bacwell, L. and Julien, M.





## 2

## New Solutions in Underwater Imaging and Vision Systems

*Francisco Bonin-Font, Antoni Burguera, and Gabriel Oliver*

### Abstract

Underwater vehicles, with autonomous capabilities, are becoming increasingly available to assist or replace divers and remotely guided vehicles used for ocean exploration or for the maintenance of submerged installations. Traditionally, autonomous underwater vehicles have used acoustic sensors to perceive the environment or to navigate. However, although images of marine objects can be distorted by the seawater, optical imaging systems can clearly benefit many underwater robots. The European project Trident aims to develop a new multipurpose autonomous underwater platform, usable for exploration and intervention and with diverse scientific, industrial, and rescue applications. One of the main tasks included in Trident is the incorporation of an imaging infrastructure to run some of the projected functionalities: surveying, scene recognition, object identification, and station keeping. When a vision system for an underwater vehicle has to be designed, some specific characteristics of the image formation in sub-sea conditions should be taken into account. This chapter first presents an extensive survey of components, techniques, and methods used to build underwater vision systems. In particular the following are reviewed: characteristics of images formed underwater, some light source solutions, a list of relevant vision-based equipment and systems, as well as some methods for improving the image. Finally, a new imaging system developed in the context of the Trident project is described.

### 2.1

#### Introduction

Thanks to the latest technological advances, the submarine world is more accessible for exploration, scientific research, and industrial activity. Sampling the oceans has traditionally been carried out from ships and using divers, but nowadays, unmanned underwater vehicles play a very important role in the sub-sea exploration.

ROVs (remotely operated vehicles) have been used for several decades in many submarine tasks, but recently, AUVs (autonomous underwater vehicles)

have emerged as a suitable alternative to ROVs or divers, especially for highly repetitive tasks, in hazardous environments or for long missions. Currently AUVs are being used for various tasks, such as surveying, mine countermeasures, inspection, and maintenance of underwater infrastructures and wreck search and localization. Because they are untethered and self-powered, AUVs offer a significant independence from surface support ships and weather conditions. This can notably reduce the operational costs and the complexity of the required human and material resources, in comparison to operations conducted with tethered ROVs.

Detailed analyses of underwater autonomous robots shows that range sensors, such as acoustics or laser, have been traditionally used. However, visual sensors are emerging as good alternatives or complements to range sensors because of the low cost of the cameras, the richness of the data provided, and the better spatial and temporal resolution. Obviously, the type of sensors used to perceive the environment determines the final capabilities of the robot. Water presents limitations to almost all types of physical waves, so the sensing equipment must be designed to overcome these problems. In particular, owing to the interaction between water and electromagnetic waves, sub-sea images can suffer from several disruptive effects that need to be taken into account during the light-gathering process: namely, light attenuation and scattering, refraction, non-uniform lighting and shadows, and color filtering. Additional problems are created by suspended particles or the abundance of marine life surrounding the target of interest. Some techniques specifically designed to overcome these problems include the use of specialized illumination systems, filters, ultra-sensitive and wide-spectrum cameras, or multi-camera configurations (Kocak *et al.*, 2008). Other authors have shown how appropriately modeling the physical process of image formation, including information from the radiant source, the nature of the surface of scene objects or the imaging hardware, can improve the performance of some visual algorithms (Singh, Howland, and Pizarro, 2004; Negahdaripour, 1998; Ortiz and Oliver, 2010).

Ultrasounds are not affected by underwater optical-imaging problems, but sonar provides information at a relatively slower rate and less resolution. Laser light is affected by all the problems associated with using light as listed above, and although various techniques can ameliorate some of these, laser-based systems are still expensive.

Although the quality of images in subaquatic environments is strongly limited by the water and the illumination conditions, under certain situations optical cameras offer definite advantages over other sensors. Imaging platforms are not really appropriate in large scale deployments of AUVs or in open waters where it can be difficult to see the seabed, natural or man-made structures, or other reference points. However, for surveying or intervention applications, where the vehicle can navigate close to the bottom or it has to stay near the object that has to be manipulated, the use of cameras can certainly be a convenient option. Images taken at the pertinent distance to the target with a suitable illuminating infrastructure, can supply the robot with visual data of sufficient quality. Three examples of applications where cameras play an important role in the achievement of the desired task are: (i) visual mosaicking approaches attempt to overcome the difficulty of underwater visual



perception by aligning short range images of the sea bottom to compose a 2D or 3D reconstruction of larger areas (Campos, Garcia, and Nicosevici, 2011), (ii) visual station keeping approaches are used to maintain the robot in a predefined pose in front of the object of interest, usually when a manipulation task is being performed (van der Zwaan, Bernardino, and Santos-Victor, 2002), and (iii) some underwater visual localization techniques that detect and track visual features from images of the sea bottom, computing, afterwards, spatial transformations to estimate the robot motion (Botelho, Drews, and Leivas, 2008).

In this context, the European project Trident (2010–2013) has coped with the challenge of developing a system that combines the facilities of exploration, localization, and manipulation, and of performing complex tasks with minimal operator intervention. The generic mission proposed in the project consists of two phases: exploration and manipulation. Both main tasks are highly supported by a new visual infrastructure, developed by the Systems, Robotics, and Vision Group at the University of the Balearic Islands and designed to work with different underwater platforms. This visual system is dedicated to several functions, namely: seabed data collection for later mosaicking, object recognition, scene characterization and identification, visual docking to the support ship, and station keeping or odometry. The AUV Girona-500 (Ribas *et al.*, 2012) is being used to support part of the experiments and can be endowed with different new manipulators to permit intervention capabilities. The Girona-500 vehicle was developed as part of a Spanish project and designed as a reconfigurable system formed by three torpedo-shaped hulls that house the equipment and computers that manage the different functions of the robot.

This chapter now focuses on two main issues:

- 1) A review of present underwater imaging systems, paying special attention to available cameras, to the distorting effects of seawater, to different possibilities for illuminating the environment, and to possible techniques to improve the quality of the images based on the use of polarized light. Moreover, a list of underwater installations and submarine vehicles equipped with imaging infrastructures, recently developed and commercially available has been included as a record of previous applications.
- 2) A description of the aforementioned new vision system, called *Fugu*. As will be described in later sections, Fugu consists of a watertight cylinder containing a computer, some additional electronic cards and several internal sensors. The system interacts with two stereo cameras. Stereo images are processed in the same system to provide online the information required to other parts of the robot.

## 2.2

### Underwater Optical Image Formation

When electromagnetic waves propagate in a sub-aquatic medium they interact with water molecules and with dissolved and particulate matter. As a consequence,

the distance this radiation travels in the underwater environment is dramatically reduced compared to air. A general exposition of this situation from a physical point of view can be found in Gordon (1994) and Mobley (1994). A detailed analysis regarding the underwater light propagation problem, focused on computer vision and its applications in robotics is presented in Ortiz (1998) and Horgan and Toal (2009), respectively. Among all the optical issues known, refraction, scattering, and absorption seem to play a more significant role in underwater optical image formation and computer vision and they are described below.

Underwater cameras are housed in watertight enclosures including a depth rated lens. Before reaching the sensitive area of the camera, refraction causes the light rays coming from the scene to bend as they pass from water to glass and then from glass to air. Refraction modifies the apparent size and position of objects. This effect combined with imperfections of the housing system, including lens defects and misalignments, lead to nonlinear image distortion that must be compensated with a proper calibration process.

When a photon hits a particle suspended in the water its original path is deflected. Depending on the angle the light ray is deviated, this phenomenon is known as *forward scatter* or *backscatter*. Forward scatter occurs when the angle of deflection is small, resulting in image blurring and contrast reduction. Backscatter occurs when part of the light sent by the source is reflected to the camera before reaching the object to be illuminated. Backscatter may cause bright points in the image, which are usually known as *marine snow*. However, the main problem with backscatter, also referred to as *veiling light*, is that it can highly reduce the image contrast, causing serious problems in underwater imaging systems. The general term for this problem, which also appears in other media than water, is path radiance. Figure 2.1 illustrates the effects of backscatter, forward scatter, and refraction.

Both backscatter and forward scatter depend on the volume of illuminated water inside the camera's field of view. In general, this means that the negative effects of scatter in underwater imaging increase with the distance from the camera to the

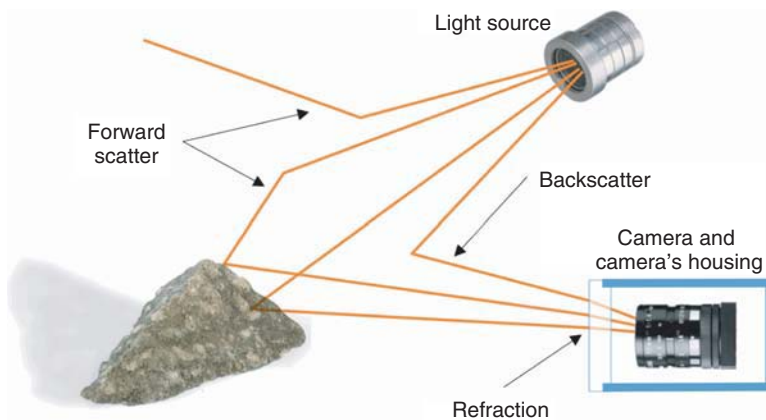


**Figure 2.1** Example of backscatter, forward scatter, and refraction.

object to be viewed. Moreover, as will be explained later, some veiling and snow effect reduction can be obtained by increasing the distance from the light source to the camera in an opportune way.

Absorption causes the electromagnetic waves traversing water to be quickly attenuated. Furthermore, the spectral components of light are differentially absorbed. Thus, in clear water long wavelength (red light) is lost first. In turbid waters, or in places with high concentration of plankton red light may be better transmitted than blue light. As a consequence, two problems arise that have important consequences for optical imaging and computer vision systems. First, the use of artificial lighting is needed in most cases and dramatically limits the distance at which objects are perceived. Second, the natural colors are distorted and the perception of the scene can be altered.

The overall effects of absorption, scatter, and other phenomena not described here, such as fluorescence, produce an attenuation of light. The attenuation factor depends on the specific characteristics of the water, the dissolved components and the particles in suspension. A common measure of this effect is the attenuation length, which is the distance where the intensity of the light has dropped by a factor of  $1/e$ . In other words, the attenuation length is the distance after which about 64% of the light intensity is lost. Visibility in water ranges between one and two attenuation lengths. This means, in general, ranges from 30 to 60 m in clear waters, 6–15 m in deep waters, and 1.5–6 m in coastal waters. As will be shown throughout, using the appropriate illumination and camera can significantly increase the visibility range.

## 2.3

### Illumination Techniques

#### 2.3.1

##### Illumination Sources

Choosing the proper light sources for an efficient underwater visual system becomes an important issue because illumination conditions always determine certain imaging effects and results. Natural light sources, like daylight, can be used at low depths, but they completely attenuate before they reach significant depths. Artificial light is necessary at deeper environments, and since a single visible light source illuminates the scene producing a central bright spot surrounded by a poorly illuminated area, it is common to use different light sources strategically located, especially if they emit structured light.

From the illumination type point of view, underwater imaging systems can be classified according to different concepts. In a first approximation, illumination systems can be roughly classified as active or passive. On the one hand, passive illumination systems image scenes illuminated by some kind of natural lighting source (sunlight or bioluminescence sources) or by some artificial source non specifically placed to illuminate that environment (light coming from nearby

stations, ships or whatever that is generating and/or consuming energy). Passive imaging is especially attractive for covering operations such as fish seeking, defense, or surveillance tasks. On the other hand, active illumination and structured lighting systems take advantage of artificially generated light with one or more sources strategically placed and configured. These systems offer substantial benefits for underwater imaging because the incident light can be either continuously emitted (standard visible light sources), collimated into narrow or wide beams, monochromatic (lasers), or flashed (strobe, pulsed lasers). These more sophisticated lighting systems typically allow imaging at greater ranges and/or higher depths than passive systems. The most significant of the advanced techniques that use the effects of light at specific frequencies to overcome harmful effects such as scatter, refraction, or absorption, among others, are:

- **Synchronous scanning systems:** The illumination source emits a collimated light (rays are nearly parallel) with a minimal beam section. This causes minimum backscatter and it results in high contrast images. To compute target range, triangulation can be used (Zheng *et al.*, 2009).
- **Light stripe range scanning (LSRS):** A plane or sheet of light, typically generated by a laser diode, scans the environment or an object to be imaged to obtain its 3D reconstruction (Narasimhan and Nayar, 2005; Taylor and Kleeman, 2006). In the presence of scattering, the light sheet becomes visible and it makes the detection of the obstacle surface more complicated. This technique reduces backscatter and allows the recovery of 3D information by means of triangulation.
- **Photometric stereo (PS):** Photometric stereo techniques are a good alternative to LSRS techniques when these take too long, for example, in dynamic environments. In the absence of scattering, it is well known that three images obtained by illuminating the scene from three different but known directions are enough to reconstruct the surfaces of the different scene objects. A challenging problem arises when it is necessary to determine how many sources are needed to infer the scene features in the presence of scattering (Negahdaripour, Zhang, and Han, 2002; Narasimhan and Nayar, 2005).
- **Range gated systems:** The source emits a pulse of light and the camera shutter waits for the time the light takes to propagate from the emitter to the target, scatter in the target surface, and back again to the camera. Only the light scattered by the target is received and considered for imaging. The main difficulty with these systems is that a very precise light gating is needed in the camera receptor. Obviously, the light pulse is much shorter than the total light propagation time. The cost of these systems is high but they considerably reduce the backscatter and augment the contrast (Han, Zhang, and Ge, 2009; Tan *et al.*, 2006).

### 2.3.2

#### Selection of the Light Source Position

When using conventional illumination systems, the amount of backscatter depends on the volume of water where the light field and the camera's field of view intersect. Because of this, it is common to separate the light source as much as possible from

the camera in order to reduce the aforementioned volume of water. Figure 2.2a exemplifies the volume of water producing backscatter when the camera and the light source are close together, and Figure 2.2b shows the difference when increasing this distance. Jaffe (1990) emphasizes the importance of this aspect by stating that the basic trade-offs in underwater imaging design are between camera-light separation, contrast, and power. In fact, the rough classification of underwater imaging systems provided in Jaffe (1990) is widely referenced by the underwater vision community. According to this classification, underwater imaging systems fall into one of the following three groups:

- 1) **Conventional systems:** The light source is placed close to the camera. This configuration makes it possible to obtain images up to two attenuation lengths.
- 2) **Increased camera–light separation:** The light source is separated from the camera as much as possible in small underwater vehicles (3–5 m). This configuration allows the acquisition of images up to three attenuation lengths.
- 3) **Exotic systems:** These systems can extend the visibility by using range gated or laser based systems, but this increases their complexity and price, and also their power consumption.

Thus, increasing the separation between the light source and the camera, whenever the system frame allows it, is a very simple and cheap way to obtain images one attenuation length farther than conventional systems, neither involving major changes in the imaging architecture nor requiring more power. Although this idea has been widely used and is considered common knowledge, very few studies have quantified the effects of such an increase in separation. Jaffe models the behavior of light in water as well as the image formation process and performs several computer simulations in Jaffe (1988, 1990). These simulations assume a camera pointing to the sea floor and evaluate the image contrast for different separations between the camera and the light source, moving the light source vertically and horizontally.

Simulations show that separating the light source horizontally dramatically increases the image contrast. Separations from 10 to 20 m considerably increase

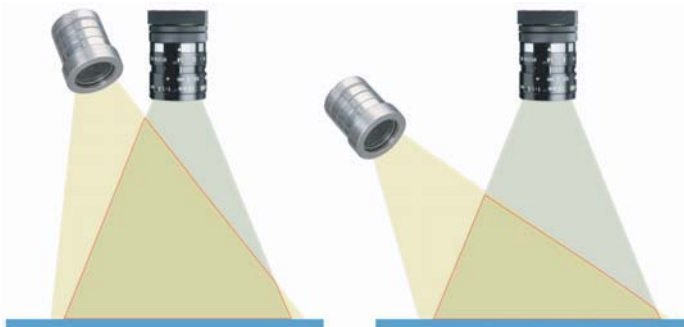


**Figure 2.2** (a) Conventional system and (b) increased camera to light source separation. The darker area depicts the volume of water where backscatter appears.

the contrast, but it tends to slightly decrease at large distances, mainly due to the light attenuation. For example, for a camera altitude of 40 m, increasing the separation from 3 to 5 m results in an approximate doubling of the image contrast. The results provided by Jaffe (1990) are summarized in Figure 2.3. The image contrast also increases when separating the light source vertically. This may seem counterintuitive, as this kind of separation does not decrease the volume of water where backscatter may appear. According to Jaffe, this improvement appears because the area directly in front of the camera is not illuminated as intensely as in the case where no separation exists.

Nevertheless, the improvements in image contrast are much smaller when moving the light source vertically than horizontally. Increasing the horizontal separation between the light source and the camera is a worthwhile improvement for some underwater imaging systems, but it can be difficult to apply in vehicles, depending on their shape and size. However, it is always possible to place the light source and the camera in different vehicles and coordinate their navigation (Jaffe, 2007). These systems increase cost and complexity in their coordination and can generate moving shadows in the image.

### 2.3.3

#### Illuminating Systems

When choosing a suitable light source for an undersea imaging installation, a balance has to be struck between the cost and the quality of the light emitted. These terms are all reflected in the parameter *efficacy* (lumens per watt). Efficacy is an important term, especially in autonomous vehicles that need to optimize the power consumption to generate the maximum light. Underwater vision systems have progressively evolved toward the use of more effective technology, and that

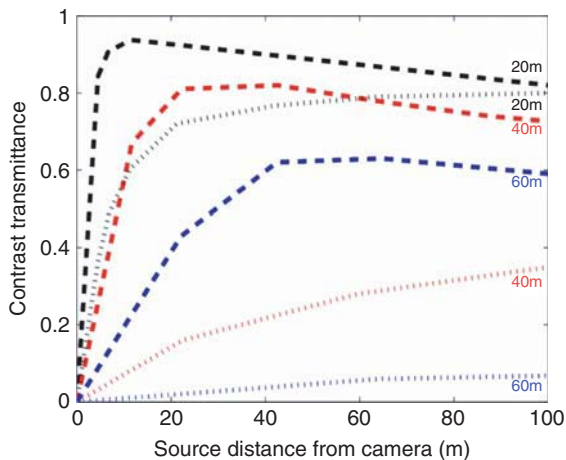


**Figure 2.3** Contrast transmittance versus separation: (| | |) Vertical separation. (— — —) horizontal separation. Source: © [1990] IEEE. Reprinted, with permission, from Jaffe (1990).

obviously includes the illuminating systems. Different types of light emitters with diverse levels of efficacy are listed below:

- **Halogens:** These use a filament to ignite halogen gas. Halogen lamps are more effective than incandescent ones since they emit a whiter and, on average, a 30% more brilliant light consuming less watts and irradiating less infrared (IR) heat. Halogens do not produce blackening of the bulb glass in usage and they are smaller than a standard incandescence emitter. Halogens have a longer lifetime than standard incandescence lamps.
- **HID (high intensity discharge) lamps (also known as xenon lamps):** These lamps use an electrical discharge between two electrodes to ignite xenon gas in a sealed bulb. They emit a blue-white light closer to natural daylight. This technology is ten-times better than halogens in terms of durability and security, and also increases efficiency, producing much more light (measured in lumens or lux) than halogens with the same power consumption and emitting much less heat. HID lamps also emit light that penetrates darkness better than halogens. HID lamps are extensively used in underwater applications such as ROVs (where the power can be supplied via its umbilical) or static underwater stations.
- **HMI (hydrargyrum medium-arc iodide lamp):** In these lamps, bulbs are filled with mercury vapor that is excited by creating an electrical arc between two electrodes. They are useful in imaging systems that need a long-time light exposure. They are typically used in the film industry, but since 1996 they have been used in underwater photography. They are usually expensive and are high power consumers (>600 W) although some manufacturers are beginning to produce low consumption HMI lights. They produce extraordinary illumination quality and are used in some ROVs for underwater filming at great depths.
- **HIF (high intensity fluorescent):** In many cases, these systems are more energy-efficient than HID solutions. They generate lower lumen depreciation rates, present better dimming options, and reduce the glare. They are able to illuminate a more extensive area than HID lamps do. Fluorescent solutions are applied underwater to attract fish but rarely for underwater vehicles.
- **LEDs (light emitting diodes):** These systems are supplied with direct and continuous current (12 or 24 V). The power consumption is four-times less, on average, than with halogens. LEDs can emit light in a wide range of wavelengths, they have a small spectral bandwidth, their lifetime is much longer than halogens, and, in general, they have a higher efficiency than HID lamps. Although they can be expensive, LEDs have become especially important and suitable for underwater autonomous vehicles equipped with batteries since they considerably reduce the power consumption.
- **Infrared:** Light is considered to be infrared for wavelengths in the 750 nm to 1 mm range. Infrared imaging is extensively used for night vision and in some underwater applications. Infrared light emission must be accompanied by the use of cameras with infrared receivers (IR cameras). Infrared light is very useful for filming marine fauna, since it can be used to remotely determine the temperature of targets and it is not visible. Infrared light penetrates less

than orange, yellow, or green light, but it has been demonstrated to be suitable for some underwater imaging applications (Lam *et al.*, 2007; Sedlazeck, Koser, and Koch, 2009). In some cases, the undesired scatter can be filtered-out in the receptor if the wavelength of the received energy is different from that the emitted one.

- **Laser:** Lasers usually operate in the 350–630 nm range. They are usually employed in underwater extended range techniques, since they permit illumination at greater distances than light with lower or higher wavelengths. Lasers, though, also allow the calculation of distances and object sizes with a high degree of precision. Lasers have two main problems: (i) emitters are considerably more expensive than HID, LEDs, or infrared and (ii) emitters generate a very narrow beam, which makes it necessary to scan the environment to take an image, thereby delaying the process and reducing the frame rate.

Although these systems are considerably more expensive than conventional incandescent lamps, they should be considered due to the wide range of benefits that they offer.

## 2.4

### Laser-Based Techniques

Techniques using laser emitters and receptors are intended to considerably extend the range of the captured scenes thanks to the laser scattering and absorption properties, improving contrast and resolution beyond that offered by other means such as infrared or systems with visible light (Funk, Bryant, and Beckman, 1972). Laser emitters concentrate intense light over a very small and narrow area, but this light propagates longer. However laser-based solutions are difficult to implement, they need important post-processing software, and can be more expensive than standard solutions. They are the best choice for long range imaging since they can be effective up to five, six, or seven attenuation lengths, while with visible light images are clear up to two–three attenuation lengths. The most outstanding techniques involving laser infrastructures are detailed below.

### 2.4.1

#### Laser Range-Gating (LRG) Methods

These systems scan the scene with laser pulses emitted at frequencies lower than 100 Hz (short pulses of approximately 6 ns). Special cameras must be provided with Intensified CCD (ICCD) sensors that can synchronously capture laser light in time gates. Knowing the speed of light in water and the distance to the target, the time that the light pulses need to travel from the emitter to the target and return to the receptor can be easily calculated. Therefore, using a gateable receiver with a sufficiently high temporal resolution, most of the undesired scatter can be filtered out leaving only the signal returned by the target. In 1994, range-gating was already a consolidated technique for extending the underwater imaging range (Swartz,



1994; Weidemann *et al.*, 2005). More recently, Han *et al.* (2009) proposed a new method for synchronization control of the laser emitter and the camera receptor in a LRG system. Improving the synchronization between the emitter and receiver helped to greatly improve the image resolution (He, Li, and Zhou, 2009).

Recently, Wu *et al.* (2009) have simulated and evaluated the performance of gated ICCD cameras to be applied in LRG-based underwater imaging applications.

#### 2.4.2

##### Laser Line Scan (LLS) Methods

Laser line scan (LLS) systems scan the environment with a narrow laser beam perpendicularly to the direction of the sensor support platform and sweeping out light rays as the vehicle moves. LLS techniques can use either continuous or pulsed laser reducing the backscatter effect by displacing the receiver from the laser source. Pulsed LLS can reduce the undesired scatter by time gating the receiver aperture to capture the light only at certain time intervals. Caimi *et al.* (2007) and Dalglish *et al.* (2008) demonstrated that pulse-gated LLS provide a much better performance than previous continuous wave (CW) LLS configurations. CW-LLS systems, under certain conditions, are limited by multiple backscattering caused by an increase of turbidity or an increase of the illumination distance (Dalglish *et al.*, 2009).

LLS systems have recently been considered as the optimal technology for extended range underwater imaging.

#### 2.4.3

##### Scattered Light Rejection Using Modulation/Demodulation Techniques

Modulation/demodulation consists of displacing the frequency spectrum of a signal, and it can be used, for example, to discriminate useful components from noise, or to transmit several digital channels in a unique physical infrastructure. Coherent demodulation uses a receiver equipped with a phase-locked-loop (PLL) that tracks the phase and the frequency of the received signal. The fact that seawater particles cause an important dispersion of the light (especially at high optical frequencies) has motivated many researchers to question if coherent/non-coherent modulation/demodulation techniques could be efficient in underwater imaging systems. Illumination with laser or infrared light (amplitude modulated at 100MHz, typically) has the advantage that the frequency, wavelength, phase, or amplitude of the emitted light are known and can be demodulated in the receptor separating the signal spectrum from the scatter frequency components. Infrared light has been scarcely considered because it is absorbed by water at shorter distances than laser light. Other systems demonstrated that it is possible to enhance contrast and image quality at large distances by coherently modulating and demodulating the illuminating laser signal in phase (B-PSK or Q-PSK; Cochenour, Mullen, and Laux, 2007; Laux, Mullen, and Cochenour, 2007).

## 2.5

### Underwater Imaging Infrastructures

The following review of previous research and practical applications will assist with the design of optimal systems for underwater imaging. Many of the existing systems seek to improve images by using several cameras for different purposes and/or various light sources:

- 1) Eye-in-the-sea: This is an unobtrusive deep-sea observatory and uses a LED that emits red light (wavelength 680 nm) in combination with a low-light-level (LLL) camera (Widder, 2007).
- 2) Rosenkranz *et al.* (2008) present an underwater imaging system designed for fisheries detection and observation. A gigabit Ethernet high-resolution camera is connected via optical fiber to the control computer. The environment is illuminated with strobe light to eliminate motion.
- 3) Lam *et al.* (2007): These authors have built an underwater camera system for monitoring marine fauna in coral reefs. The system is provided with a wide-angle IR-sensitive camera connected via optical fiber to an on-land controlling computer.
- 4) The submarine observatory NEPTUNE (Pacific Ocean) needs to integrate station nodes and static imaging systems to support ROVs in their surveillance tasks. Imaging platforms have been equipped with a high-definition camera, and three different light sources: (i) a three beam laser system to provide range information to the user, (ii) two dimmable LEDS with more than 406 lm with an equivalent power of 250 W, and a life of 50 000 h, and (iii) a 150 W HID light to extend the range of visualization (Roston, Bradley, and Cooperstock, 2007).
- 5) Sedlazeck, Koser, and Koch (2009) have presented a 3D reconstruction system based on feature tracking. Images were provided by the ROV Kiel 6000, equipped with three cameras: (i) a high-definition camera, (ii) a standard color PAL still camera and, (iii) a slave-mode controlled camera with automatic flash shot. The ROV is also equipped with a 250 W halogen lamp, another 70 W HID light and a 400 W HMI dimmable focus.
- 6) Negahdaripour and Firoozfam (2006) have presented a vision system for automatic ship hull inspection, applicable to AUV but firstly tested with images provided by a ROV. The ROV was equipped with a stereo camera.
- 7) Negahdaripour, Sekkati, and Pirsiavash (2007) have explored the possibility and results of using optical-acoustic stereo imaging for 3D shape recovery of underwater targets. DIDSON (2009) acoustic cameras provide acoustic images with such a high degree of reliability that they can be analyzed and processed in the same way as standard images.
- 8) The CSIRO Marine and Atmospheric Research Division in Australia (Shortis *et al.*, 2007) has developed a towed platform for sea bottom map construction, fisheries study, detection, and surveillance. The system was equipped with two standard PAL cameras in stereo configuration for video recording that could be accurately geo-located thanks to the vessel Differential GPS (DGPS)

equipment and to the navigation data and to ultra-short baseline (USBL) tracking beacon data on the towed body. Additionally, a high-resolution still camera for computing mosaicking and a forward-looking camera for obstacle detection and avoidance were also available. For illumination, two 250 W incandescent lamps were used for the video recording and two strobes for the still camera.

- 9) Some years ago, an underwater docking station was developed to enhance the performance of the AUV REMUS (Allen *et al.*, 2006). The vehicle incorporated several cameras for different purposes: (i) one Ethernet video camera to provide real-time information about the process of entering and leaving the docking station and (ii) a periscope camera for sea surface observation. This camera was mounted in a housing that could be deployed and retracted above and below the sea surface.
- 10) Hercules (IFE, 2009) is a ROV especially designed for working in the deep sea, manipulating, recovering, or digging in ancient shipwrecks. Hercules is equipped with one high-definition video camera for monitoring the sea bottom and two still cameras for mosaicking tasks.
- 11) ARGUS is a ROV produced by Woods Hole Marine Systems, Inc. (Woods Hole Oceanographic Institution) that can operate independently or as a partner of other ROVs and it is equipped with cameras and HMI lighting for underwater image registration (WHMS, 2009).
- 12) Phantom DHD2+2 and Phantom HD2+2 [DOE (Deep Ocean Engineering) ([www.deepocean.com](http://www.deepocean.com))] are two ROVS designed for fisheries and scientific research, military missions, gas/oil pipes inspection, or underwater filming, and are especially suitable for deep water and strong currents. Both vehicles incorporate a high-resolution PAL/NTSC color camera with a wide-angle lens, and two 250 W halogen lamps to illuminate the area of inspection.
- 13) SubSea7/Seebyte AIV (Autonomous Inspection Vehicle)([www.subsea7.com](http://www.subsea7.com)): Although this is still a prototype and it has not been yet commercialized, the cooperation of both companies has lead to the presentation of a new AUV for inspection and intervention on offshore oil and gas installations. This vehicle will carry sonars and cameras powered by the robot batteries.

## 2.6

### Image Improvement via Polarization

As explained above, a fraction of the light that passes through water is backscattered to the camera before reaching the target, significantly reducing the contrast of the resulting image. The effects of backscatter depend on the amount of water in the line of sight and, thus, on the distance to the object being observed. Moreover, the backscatter is magnified when artificial illumination is used (Treibitz and Schechner, 2009a). As artificial illumination is a common requirement for sub-sea operation, backscatter is an important problem in underwater robotics.

Different authors have pointed out that the media responsible for the backscatter and the objects in the environment behave in different ways when they are exposed to polarized light. However, there is no consensus in the research community regarding this subject. According to Treibitz and Schechner (2006) some studies assume that objects in the scene preserve polarization while backscatter does not, and some other studies state that polarization is preserved only by the backscatter. Despite these opposed points of view, polarization can be used to reduce the negative effects of backscatter because, either in one sense or another, media and scene objects have different responses to polarized light.

This section focuses on describing the potential benefits of using polarization to increase contrast in underwater images and shows some tests conducted to determine its usefulness for applications in underwater robotics. It is beyond the scope of this chapter to explain the basic concepts of polarization, so the reader is referred to the papers authored by Schechner that are cited in the references section.

Although uncommon, light with a high degree of polarization (*DOP*) can be found in nature. For example, according to Waterman (1954), sunlight becomes polarized in underwater environments when traversing the interface between air and water. Besides, unpolarized light can be polarized by means of a polarizing filter. The cost of this transformation is a very important loss of light energy. Off-the-shelf polarizing filters reduce the light intensity by more than 50%.

#### 2.6.1

##### Extended Range Using Polarization

The different interactions of objects and backscatter with polarized light can be used to improve contrast in underwater imaging. Some studies exploit this idea in underwater environments where sunlight is sufficient and no artificial illumination is required (Karpel and Schechner, 2004; Schechner and Karpel, 2004, 2005). These studies are based on the assumptions that, first, the interface between air and water partially polarizes the sunlight and, second, that backscatter preserves polarization while the observed objects do not. The authors' proposal is to attach a polarizing filter to the camera and capture two images of the same scene using orthogonal polarization angles. By properly combining the resulting two images, backscatter can be significantly removed. This idea is illustrated in Figure 2.4a. Similar approaches have been proposed (Morgan, Khong, and Somekh, 1997; Treibitz and Schechner, 2009a) to deal with those underwater environments where sunlight is not sufficient. In these cases, the artificial light source is fitted with a filter so that the scene is illuminated with polarized light (Figure 2.4b).

#### 2.6.2

##### Housing

Another important issue when designing an underwater imaging system involving polarization is related to the interface of the camera with the water, as it should have a minimum effect on the polarization (Karpel and Schechner, 2004). First,



orthogonal states for both polarizers and a second image is obtained with polarizers parallel. By combining both images, the effects of backscatter should be reduced.

The water tank used was  $1.5\text{ m} \times 0.4\text{ m} \times 0.45\text{ m}$  and contained 240 l of water. The only light source during the experiments was a 3 W LED lamp fitted with a linear polarizer. The images were taken using a 10 megapixel reflex camera. Shutter speed, aperture, focus, and any other camera parameter were manually adjusted to optimize the quality of the images gathered. Calibrated sheets, as well as some other objects, ranging from 0.5 to 1.1 m to the camera lens, were placed inside the water. To cause water turbidity, various amounts of milk were dropped into the tank. Figure 2.5 illustrates the experimental setup.

Some of the results are given in Figure 2.6, where two images taken for each scene, as well as the image resulting from the scatter reduction process, are shown. The figure shows the results for two different levels of water turbidity. As can be seen, the reconstructed image contains less backscatter than the corresponding originals. However, a detailed analysis shows that the resulting images have more noise and are saturated in some areas. This observation is consistent with Treibitz and Schechner 2009a and 2009b, who state that keeping the camera's exposure time constant, which is usual in video acquisition, never improves the signal to noise ratio (SNR) of the resulting images. Moreover, they also showed that even the use of automatic exposure and assuming optimal exposure times only improve SNR in rare cases.

Clearly, the question to answer here is whether polarization-based methods provide sufficient benefits, compared to simply using a camera with no filters and an unpolarized light source. Comparison with other more complex and expensive methods, such as laser based ones, was not the aim of these experiments.

The main problem found is that the double filtering process needed by this method strongly attenuates the light. In most cases, low illumination of the scenes increases the SNR in digital cameras. To minimize this effect, the lighting power should be increased, reducing the energy available for the complete system. This fact strongly restricts the usefulness of this method in limited energy platforms like AUVs. In addition, two images per scene, obtained from the same camera



Figure 2.5 Experimental setup.

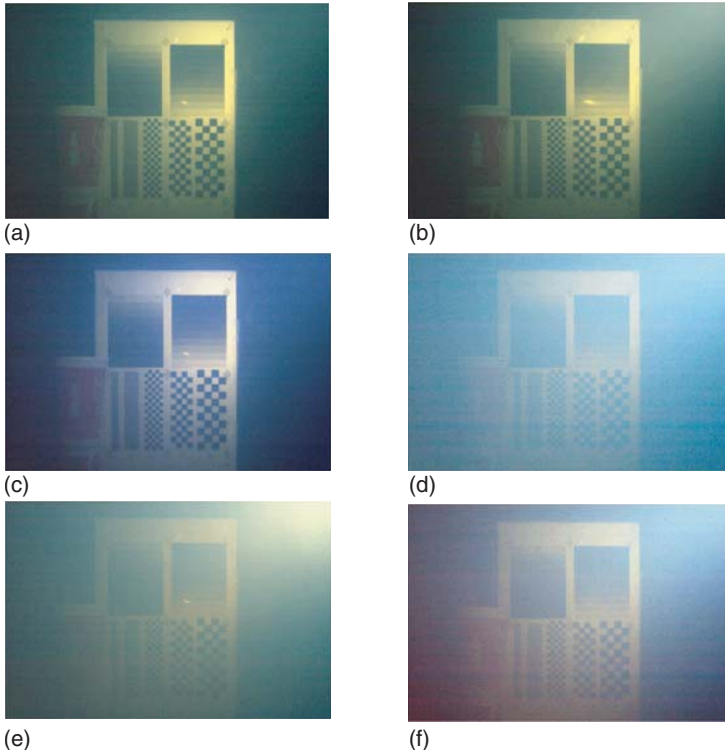


**Figure 2.6** Some results using polarization: (a) and (d) light and camera polarizers perpendicular; (b) and (e) light and camera polarizers parallel; (c) and (f) reconstructed images; (a)–(c) with 20 cc of milk and (d)–(f) with 50 cc of milk.

position, are needed. Thus, if the camera is attached to a moving platform, it is not possible to guarantee this premise. Moreover, using two images per scene reduces the available frame rate by half, which is a strong restriction if vehicle or object motions are to be tracked. Other approaches, such as polarized light stripping (Gupta, Narasimhan, and Schechner, 2008) and polarization vision (Wolff, 1997) are also useful in removing backscatter at the cost of additional, expensive hardware in the first case and the requirement of three images per scene in the second case.

## 2.7

### A Vision System for Underwater Applications

Having analyzed the fundamentals of underwater image formation and some of the most accepted imaging techniques, a new vision system being developed at the University of the Balearic Islands is now presented. First, the hardware structure and the software architecture are introduced and, then, different configurations of the system and some recent experiments carried out with it are described. The

vision system has been conceived to provide visual perception to an AUV with intervention capabilities (I-AUV). The main specifications and limitations that have conditioned the resulting design are listed below:

- **mechanical:** maximum volume 9 l, neutral buoyancy, minimum depth rating 100 m;
- **electrical:** voltage source 14.4 V and 50 W of maximum power consumption
- **perception needs:** image resolution  $640 \times 480$  or higher, minimum frame rate ten frames per second, possibility of 3D reconstruction; color images optional; two cameras could be connected if necessary;
- **communication:** wired Ethernet link to other modules of the vehicle of 100 Mbps or higher.

Another requirement that was taken into account was the configuration flexibility of the system, so it would permit different geometries and easy adaptation to different underwater platforms. In addition, during development of the system, some changes were introduced, mainly concerning mechanical aspects, to enable stand-alone operation, thus, creating a micro-vehicle that could be operated in shallow waters at a reasonable cost.

### 2.7.1

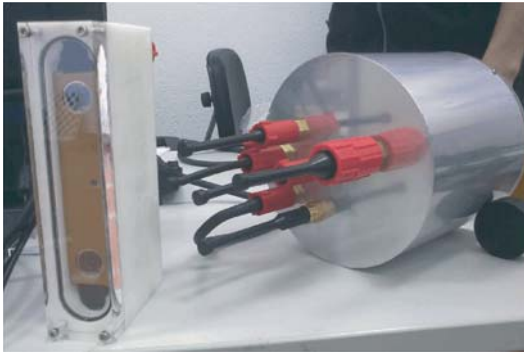
#### The Fugu Vision System

The Fugu vision solution is based on two stereo rigs and a computer system linked through a firewire bus. When the system is configured in its *flexible* option, which is called *Fugu-F*, each module is placed in an independent watertight case rated for up to 100 m depth. Each camera is connected to the computer cylinder through an independent waterproof cable and a connector's set. Other connectors, visible on the cylinder cover (Figure 2.7a) are used for power supply and communication purposes. *Fugu-F* is a modularized solution that allows different cameras to be used and a variable geometry setting, depending on the mission to be carried out and the power and payload available. Both configurations shown in Figure 2.7 are using Bumblebee2 cameras, but any other firewire compliant devices could be easily adapted.

Identical hardware used for the *Fugu-F* version has been employed for a more *compact* solution, called *Fugu-C*, by substituting the aluminum cylinder for a transparent container and adding horizontal and vertical propellers (Figure 2.7b). *Fugu-C* can carry its own batteries and, at present, it can be remotely operated through a thin data cable. An autonomous navigation module that, thanks to a MEMS (Micro-ElectroMechanical System) based inertial unit and to visual information, will allow the vehicle to follow short programmed paths is under development. This new setting provides a solution for underwater image recording and observation, up to depths of 15 m, at moderate cost.

The software control architecture of the Fugu vision system is based on the robot operating system (ROS) middleware (Quigley *et al.*, 2009). Thus, services or capabilities are managed as messages and modules compartmentalized and





(a)



(b)

**Figure 2.7** (a) Fugu-F system, the stereo cameras in its watertight case and the cylinder containing the computer system; (b) Fugu-C, a compact and auto propelled configuration with identical vision functionality.

implemented as nodes. All the vision related services are run on the Fugu computer. Other capabilities like navigation, mapping, or guidance, among others, can reside on the same computer or on other independent hardware, depending on whether the compact or the flexible setting is implemented, respectively. Most of the basic vision services like visual feature detection and tracking, motion estimation, target identification or image tagging, and storage, have already been implemented. Other functionalities, especially regarding 3D information processing, are still under development.

Fugu has already been tested on different vehicles. First, the Girona-500 (Ribas *et al.*, 2012) carried the Fugu-F with one camera during a set of autonomous search and recovery experiments made in sea conditions (García *et al.*, 2012). The Girona-500 is an AUV developed at the University of Girona as part of a Spanish research project aimed to design and test new methodologies for multipurpose autonomous intervention tasks (Prats *et al.*, 2012). During the above-mentioned trials, some important functionalities of the vision system were tested. First, when

the vehicle was traveling close to the sea floor, the visual odometer function provided a high rate of motion estimate to the navigation system thanks to the homography obtained from frame to frame. During the search step, the target detection module was in charge of determining if the object to be recovered was observed in the field of view. Finally, the target tracking function fed the station keeping and the arm controller to guide the vehicle while maneuvering during the recovery stage. Figure 2.8a shows the Girona-500, equipped with the arm and the Fugu-F. The white box placed at the bow of the lower hull is the downwards-looking camera. Next to the camera, a cylindrical case can be observed, which corresponds to the port LEDs based focus. Another identical focus is placed on the starboard side. The computer cylinder was placed in one of the upper hulls of the vehicle.

Some more experiments have been made in coastal waters using both login visual and acoustic images to analyze their correspondence and complementary information. In these experiments Nessie-VI was the vehicle used, equipped with the Fugu-F system and a multibeam imaging sonar (Figure 2.8b). Nessie-VI is a torpedo shaped AUV developed by the Ocean Systems Laboratory at Heriot-Watt University. During these experiments, the Fugu-F cylinder could not be installed in the hull, so it was placed just underneath it. The stereo camera was placed at the bow area in a downward looking and slightly forward orientation to maximize the overlapping area with the imaging sonar.

The main objective of the experiments with Girona-500 and Nessie-VI was to test for the first time the Fugu-F system under real conditions, that is, integrated as part of the equipment of an AUV and in the sea. Consequently, attention was focused on verifying technical and operative aspects like power supply stability, non-interference with other on board equipment, response of the vision system functions, communication issues, and proper integration of the whole system from the mechanical and electrical point of view. In fact, a complementary result of the experiments is the recording of a few hours of video gathered synchronously with the navigation data of the vehicles. This information is under study to determine the best configuration of the vision equipment and to develop a vision-based navigation system to improve the autonomous capabilities of the AUV when it operates at a short distance from the sea floor or to the target.

Finally, the Fugu-F can also be equipped with its own batteries and, thanks to the hard drive housed in the cylinder, operate in a stand-alone mode. Thus, the system can be installed on a submarine fixed position and remain deployed from several hours to a few days depending on the functions being executed.

## 2.8 Conclusion

Owing to the interaction between water and light, sub-sea images have special characteristics that should be taken into account when designing an underwater optical imaging system. Aspects such as the illumination type or the camera's housing shape and material, which are generally not relevant in many terrestrial



(a)



(b)

**Figure 2.8** Two different vehicles carrying Fugu-F on board: (a) the Girona-500 and (b) Nessie-VI. Photograph: David March Morla, reproduced with kind permission.

applications, become important when going under water. If the imaging system has to be mounted on a ROV or on an AUV, some constraints like limited power supply, weight or size become critical. In addition, human intervention is often undesirable or impractical in many underwater scenarios. In these cases a fully autonomous operation is required. This work presents most aspects to consider when designing an imaging system for underwater applications. First, the macroscopic water–light interaction phenomena have been described, and then the illumination techniques available and most of the known imaging systems were reviewed. Next, a polarization-based technique to improve images in turbid waters was analyzed and some experiments carried out at the authors' laboratories described. As a consequence of all the aspects previously mentioned, a new vision system, called *Fugu*, was presented. The system has been designed to satisfy the operational requirements of a new AUV with intervention capabilities under development in the context of the Trident project. In addition to the specifications imposed by the project, *Fugu* has been designed to be highly adaptable to different applications. Thus, two versions of the system have been described and some recent trials reported.

### Acknowledgements

The authors are grateful to the Underwater Robotics Laboratory, Universitat de Girona, and to the Ocean Systems Labatory at Heriot-Watt University for providing the vehicles used for the *Fugu-F* system sea trials.

This work is partially supported by the European Commission 7th FP under grant agreement 248497 (TRIDENT Project), FEDER funding, and by the Spanish Ministry of Economy DPI2011-27977-C03-03 (TRITON Project) and PTA2011-5077-I.

### References

- Allen, B., Austin, T., Forrester, N., Goldsborough, R., Kukulya, A., Packard, G., Purcell, M., and Stokey, R. (2006) Autonomous docking demonstrations with enhanced REMUS technology, in Proceedings of MTS/IEEE OCEANS 2006, Boston, MA, 18–21 September 2006, IEEE, Washington DC, pp. 1539–1544.
- Botelho, S., Drews, P., and Leivas, G. (2008) NLMAP-visual-based self localization and mapping for autonomous underwater vehicles, in Proceedings of IEEE OCEANS 2008, Quebec City, 15–18 September 2008, IEEE, Washington DC, pp. 2050–2055.
- Caimi, F.M., Dagleish, F.R., Giddings, T.E., Shirron, J.J., Mazel, C., and Chiang, K. (2007) Pulse versus CW laser line scan imaging detection methods: simulation results, in Proceedings of IEEE OCEANS 2007 – Europe, Aberdeen, 18–21 June 2007, IEEE, Washington DC, pp. 1520–1523.
- Campos, R., Garcia, R., and Nicosevici, T. (2011) Surface reconstruction methods for the recovery of 3D models from underwater interest areas, in Proceedings of IEEE OCEANS 2011 – Spain, Santander, 6–9 June 2001, IEEE, Washington DC, pp. 20–28.

- Cochenour, B., Mullen, L., and Laux, A. (2007) Phase coherent digital communications for wireless optical links in turbid underwater environments, *Proceedings of IEEE OCEANS 2007*, Vancouver, 29 September to 4 October 2007, IEEE, Washington DC, pp. 411–415.
- Dalgleish, F.R., Caimi, F.M., Britton, W.B., and Andren, C.F. (2009) Improved LLS imaging performance in scattering-dominant waters, in *Ocean Sensing and Monitoring* (ed. W. Hou), *Proceedings of SPIE*, vol. 7317, SPIE, Bellingham, WA, 73170E–73170E-12.
- Funk, C.J., Bryant, S.B., and Beckman, P.J. (1972) *Handbook of Underwater Imaging System Design*, Ocean Technology Department, Naval Undersea Center, San Diego, CA.
- García, J.C. *et al.* (2012) An integration perspective of the trident project. 5th International Conference on Cognitive Systems, Vienna, Austria, 2012.
- Gordon, H.R. (1994) Modeling and simulating radiative transfer in the ocean, in *Ocean Optics*, Oxford Monographs on Geology and Geophysics, Oxford University Press, New York, pp. 3–39.
- Gupta, M., Narasimhan, S.G., and Schechner, Y.Y. (2008) On controlling light transport in poor visibility environments, in *Proceedings of IEEE Conference on Computer Vision and Pattern Recognition (CVPR)*, Anchorage, 23–28 June 2008, IEEE, Washington DC, pp. 3276–3283.
- Han, H., Zhang, X., and Ge, W. (2009) Performance evaluation of underwater range gated viewing based on image quality metric, in *Proceedings of International Conference on Electronic Measurements and Instruments (ICEMI)* Beijing, 16–19 August 2009, vol. 4, IEEE, Washington DC, pp. 441–444.
- He, S., Li, L., and Zhou, Y. (2009) A new synchronization control circuit based on FPGA for the laser range-gated imaging system. *Optoelectron. Lett.*, 5 (4), 248–250.
- Horgan, J. and Toal, D. (2009) *Underwater Vehicles*, In-Tech, pp. 195–214.
- IFE (Institute for Exploration) (2009) Hercules ROV. <http://www.mysticaquarium.org/ife/technology/340-hercules> (accessed 23 May 2013).
- Jaffe, J.S. (1988) Underwater optical imaging: the design of optimal systems. *Oceanography*, 11 (1), 40–41.
- Jaffe, J.S. (1990) Computer modeling and the design of optimal underwater imaging systems. *IEEE J. Oceanic Eng.*, 15 (2), 101–111.
- Jaffe, J.S. (2007) Multi autonomous underwater vehicle optical imaging for extended performance, in *Proceedings of IEEE OCEANS 2007 – Europe*, Aberdeen, 18–21 June 2007, IEEE, Washington DC, pp. 182–185.
- Karpel, N. and Schechner, Y.Y. (2004) Portable polarimetric underwater imaging system with a linear response, in *Polarization: Measurement, Analysis and Remote Sensing VI* (eds D.H. Goldstein and D.B. Chenault), *Proceedings of SPIE*, vol. 5432, SPIE, Bellingham, WA, pp. 106–115.
- Kocak, D.M., Dalgleish, F.R., Caimi, F.M., and Schechner, Y.Y. (2008) A focus on recent development and trends in underwater imaging. *Mar. Technol. Soc. J.*, 42 (1), 52–67.
- Lam, K., Bradbeer, R.S., Shin, P.K.S., Kun, K.K.K., and Hodqson, P. (2007) Application of a real-time underwater surveillance camera in monitoring of fish assemblages on shallow coral communities in a marine park, *Proceedings of IEEE MTS/OCEANS 2007*, Vancouver, 29 September to 4 October 2007, IEEE, Washington DC, pp. 863–869.
- Laux, A., Mullen, L., and Cochenour, B. (2007) I/Q data processing techniques for the analysis of an amplitude modulated laser-imaging system, *Proceedings of Conference on Laser and Electro-Optics (CLEO)*, Baltimore, 6–11 May 2007, IEEE, Washington DC, pp. 2576–2577.
- Mobley, C.D. (1994) *Light and Water: Radiative Transfer in Natural Waters*, Academic Press, San Diego, CA (CD Edition, 2004).
- Morgan, S.P., Khong, M.P., and Somekh, M.G. (1997) Effects of polarization state and scatterer concentration on optical imaging through scattering media. *Appl. Opt.*, 36 (7), 1560–1565.
- Narasimhan, S.G. and Nayar, S.K. (2005) Structured light methods for underwater imaging: light stripe scanning and photometric stereo, *Proceedings of MTS/IEEE*

- OCEANS 2005, Washington, vol. 3, IEEE, Washington DC, pp. 2610–2617.
- Negahdaripour, S. (1998) Revised definition of optical flow: integration of radiometric and geometric cues for dynamic scene analysis. *IEEE Trans. Pattern Anal. Mach. Intell. (PAMI)*, **20** (9), 961–979.
- Negahdaripour, S. and Firoozfam, P. (2006) A ROV stereovision system for ship-hull inspection. *IEEE J. Oceanic Eng.*, **31** (3), 551–564.
- Negahdaripour, S., Sekkati, H., and Pirsivash, H. (2007) Opti-acoustic stereo imaging: on system calibration and 3-d target reconstruction. *Trans. Image Process.*, **18** (6), 1203–1214.
- Negahdaripour, S., Zhang, H., and Han, X. (2002) Investigation of photometric stereo method for 3D shape recovery from underwater imaging, in Proceedings of IEEE MTS/OCEANS, vol. 2, IEEE, Washington DC, pp. 1010–1017.
- Ortiz, A. (1998) Aplicación de técnicas de visión por computador a entornos submarinos. Technical Report, Universitat de les Illes Balears.
- Ortiz, A. and Oliver, G. (2010) Analysis of colour channel coupling from a physics-based viewpoint: application to colour edge detection. *Pattern Recognit.*, **43** (7), 2507–2520.
- Prats, M. *et al.* (2012) Reconfigurable AUV for intervention missions: a case study on underwater object recovery. *J. Intelligent Service Robot.*, **5**, 19–31.
- Quigley, M. *et al.* (2009), *ROS: an Open Source Robot Operating System*, ICRA Workshop on Open Source Software.
- Ribas, D., Palomeras, N., Ridao, P., Carreras, M., and Mallios, A. (2012) Girona 500 AUV: from survey to intervention. *Trans. Mechatron.*, **17** (1), 46–53.
- Rosenkranz, G.E., Gallager, S.M., Shepard, R.W., and Blakeslee, M. (2008) Development of a high-speed, megapixel benthic imaging system for coastal fisheries research in Alaska. *Fish. Res.*, **92** (1), 340–344.
- Roston, J., Bradley, C., and Cooperstock, J.R. (2007) Underwater window: high definition video on VENUS and NEPTUNE, in Proceedings of IEEE MTS/OCEANS 2007, Vancouver, 29 September to 4 October 2007, IEEE, Washington DC, pp. 1419–1426.
- Schechner, Y.Y. and Karpel, N. (2004) Clear underwater vision, in Proceedings of the IEEE Computer Vision and Pattern Recognition (CVPR), vol. 1, IEEE, Washington DC, pp. 536–543.
- Schechner, Y.Y. and Karpel, N. (2005) Recovery of underwater visibility and structure by polarization analysis. *IEEE J. Oceanic Eng.*, **30** (3), 570–587.
- Sedlazeck, A., Koser, K., and Koch, R. (2009) 3D reconstruction based on underwater video from ROV Kiel 6000 considering underwater imaging conditions, Proceedings of IEEE OCEANS Europe, Bremen, 11–14 May 2009, IEEE, Washington DC, pp. 1367–1376.
- Shortis, M.R., Seager, J.W., Williams, A., Barker, B.A., and Sherlock, M. (2007) A towed body stereo-video system for deep water benthic habitat surveys, in Proceedings of the Eight Conference on Optical 3-D Measurement Techniques (eds. A. Grun and H. Kahmen), vol. 2, ETH Zurich, Zurich, pp. 150–157.
- Singh, H., Howland, J., and Pizarro, O. (2004) Advances in large-area photomosaicking underwater. *IEEE J. Oceanic Eng.*, **29** (3), 872–886.
- Swartz, B.A. (1994) Laser range gate underwater imaging advances, in Proceedings MTS/IEEE OCEANS Brest, France, vol. 2, IEEE, Washington DC, pp. 722–727.
- Tan, C.S., Sluzek, A., Seet, G.L., and Jiang, T.Y. (2006) Range gated imaging system for underwater robotic vehicle, in Proceedings of IEEE OCEANS 2006 – Asia Pacific, Singapore, 16–19 May 2006, IEEE, Washington DC, pp. 736–741.
- Taylor, G. and Kleeman, L. (2006) Shape recovery using robust light stripe scanning. *Visual Percept. Rob. Manipulation*, **26**, 31–56.
- Treibitz, T. and Schechner, Y.Y. (2006) Instant 3descatter, in Proceedings of the IEEE Computer Vision and Pattern Recognition (CVPR), New York, vol. 2, IEEE, Washington DC, pp. 1861–1868.
- Treibitz, T. and Schechner, Y.Y. (2009a) Active polarization descattering. *IEEE*

- Trans. Pattern Anal. Mach. Intell.*, **31** (3), 385–399.
- Treibitz, T. and Schechner, Y.Y. (2009b) Polarization: beneficial for visibility enhancement? in Proceedings of the IEEE Conference on Computer Vision and Pattern Recognition (CVPR), Miami Beach (FL), IEEE, Washington DC, pp. 525–532.
- Waterman, T.H. (1954) Polarization patterns in submarine illumination. *Science*, **120**, 927–932.
- Weidemann, A., Fournier, G.R., Forand, L., and Mathieu, P. (2005) In harbor underwater threat detection/identification using active imaging, in Photonics of Port and Harbor Security (eds M.J. DeWeert and T.T. Saito), *Proceedings of SPIE*, vol. 5780, SPIE, Bellingham, WA, pp. 59–70.
- WHMS (2009) Woods Hole Marine Systems, Argus rov. <http://www.whmsi.com/> (accessed 23 May 2013).
- Widder, E. (2007) Sly eye for the shy guy. *Oceanography*, **20** (4), 46–51.
- Wolff, L.B. (1997) Polarization vision: a new sensory approach to image understanding. *Image Vision Comput.*, **15**, 81–93.
- Wu, L., Shen, Y., Li, G., Chen, C., and Yang, H. (2009) Modelling and simulation of range-gated underwater laser imaging systems, in International Symposium on Photoelectronic Detection and Imaging (eds F. Amzajerdian, C-q. Gao, and T-yu. Xie), *Proceedings of SPIE*, vol. 7382, SPIE, Bellingham, WA, pp. 73825B–73825B-7.
- Zheng, B., Liu, B., Zhang, H., and Gulliver, T.A. (2009) A laser digital scanning grid approach to three dimensional real-time detection of underwater targets, in Proceedings of IEEE Pacific Rim Conference on Communications Computers and Signal Processing, Victoria (BC), Canada, pp. 798–801.
- van der Zwaan, S., Bernardino, A., and Santos-Victor, J. (2002) Visual station keeping for floating robots in unstructured environments. *Rob. Autom. Syst.*, **39** (3–4), 145–155.







### 3

## Holographic Microscopy of Marine Organisms

Stefan K. Jericho, Manfred H. Jericho, and Hans J. Kreuzer

### 3.1

#### Introduction

Zoo- and phytoplankton consist of populations of organisms ranging in size from copepods (up to several millimeters) to bacteria (which may be sub-micron). Plankton forms the foundation of all marine communities, from the continental shelves to coral reefs. The health of the complex ecosystems in these habitats is fundamentally dependent on a well balanced population of plankton. To obtain an understanding of population growth, prey–predator interactions, and nutrient transfer along the food chain requires observations and measurements on plankton populations over extended time periods and at many levels of the water column. To capture organism movement and feeding characteristics requires the direct imaging of organisms in their marine environment. This is particularly challenging for imaging of nano- and picoplankton, which includes cyanobacteria and small algae, since their size can be close to the theoretical resolution limit of optical imaging techniques. Microorganisms in this size range may play an important role in decomposition of organic matter and in the recycling of nutrients (Ferrier-Pages and Gattuso, 1998). Coral reefs, for example, have very productive ecosystems but exist in carbon-deficient sea-water. It has been suggested that dissolved and particulate organic matter is recycled by bacteria and thus transformed into bacterial biomass and then transferred to higher trophic levels by flagellates and ciliates (Sorokin, 1973). Imaging of organisms in this size range can greatly assist studies on the mechanisms at work at the bottom of the food chain. To address the need for high-resolution imaging in a marine environment, several groups have developed submersible holographic microscopes. This chapter reviews some of these instruments that have been successfully employed to obtain *in situ* images of plankton organisms ranging in size from micro- to picoplankton.

### 3.2

#### Advantages of Holographic Microscopy

Holographic microscopy has several advantages over conventional optical microscopy. In conventional microscopy, high resolution can only be obtained with high numerical aperture objectives. This implies a very small depth of field ( $1\text{ }\mu\text{m}$  and less) and it is therefore impossible to image organisms in motion such as marine plankton. The remarkable thing about holographic imaging is that a single hologram contains information about all objects in the illuminated volume that scatter light. Images of the objects are then obtained by applying direct optical (film) or digital (CCD, charge coupled device) reconstruction methods in selected planes in the imaged volume (Xu *et al.*, 2001). With a sufficient number of planes, a complete 3D view of the object distribution can thus be obtained. When a succession of holograms is recorded at video rates, trajectories and the whole dynamics of the object distribution can also be captured (Xu *et al.*, 2003).

Object illumination can be achieved either with plane wave fronts from collimated light or with light from a point source giving spherical wave fronts. In the latter case the hologram encodes magnified images of objects. Since holography is based on interference, the more interference fringes one can capture with the recording medium the higher the obtainable resolution. Holographic films can capture fringes spaced less than a micron apart and are a recording medium with the highest potential resolution. However, digital recording technology has advanced enormously in recent years and the many advantages of CCD chips have greatly made up for their smaller dimensions and larger pixel size.

In Section 3.3 we give a brief review of recent efforts by several groups to image marine plankton from centimeter size copepods to  $<50\text{ }\mu\text{m}$  diameter microplankton using collimated beam holography. The highest resolution can be obtained with point source digital in-line holographic microscopy (DIHM), where objects are illuminated with nearly spherical waves from pin holes with diameters of  $0.5\text{ }\mu\text{m}$  and smaller. This allows imaging of nano- and picoplankton down to the size of bacteria, and will be discussed in some detail in Section 3.4. Plankton studies with holographic microscopy can be divided into three main parts: (i) recording of high-quality holograms; (ii) reconstruction of holograms either optically or computationally to retrieve from the holograms in focus images of objects distributed throughout the sampled volume; (iii) evaluation of reconstructed sample volumes. This last point includes identification of objects, determination of the number density of objects in various size categories, construction, and evaluation of particle trajectories, and the correlation of all these with other parameters of interest such as depth, temperature, and salinity of the water. The large amount of information contained in a single hologram thus generally means that automated methods for image evaluation have to be employed. In the following we will only describe instrumentation and methods that have been used to (i) record and (ii) reconstruct holograms of *in situ* imaging of marine plankton.

### 3.3

#### Past Attempts to Image Microplankton

An early attempt at holographic imaging of marine organisms was made by Knox and Brooks (1969) with an in line cine-holographic recording system. This system was converted by Heflinger, Stewart, and Booth (1978) for off-axis recording of holograms (Figure 3.1a). A collimated beam of coherent radiation illuminated plankton in an aquarium tank and a relay lens and off-axis reference beam produced a hologram on 35 mm movie camera film capable of 200 frames  $s^{-1}$ . Recordings were carried out with a pulsed argon-ion laser (514 nm) or a xenon laser (535 nm).

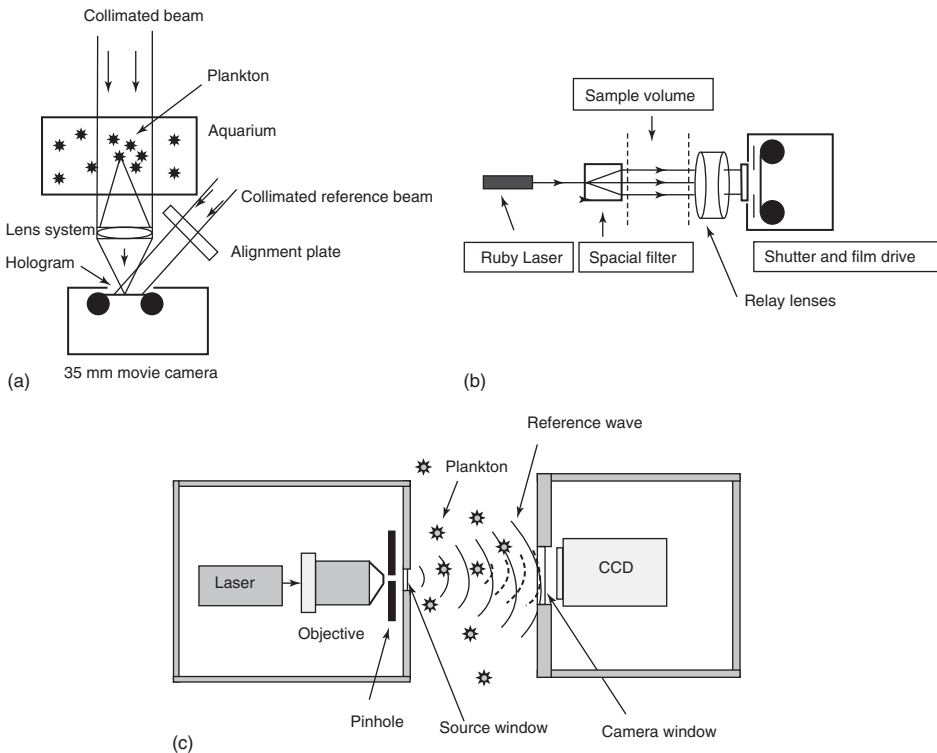


**Figure 3.1** (a) Holographic off-axis imaging system originally used by Heflinger, Stewart, and Stewart (1978). A collimated laser beam illuminates objects and produces, with the help of a collimated reference beam, a hologram on a 35 mm film. (b) Collimated beam in-line holography used by Malkiel, Alquadoomi, and Katz (1999). Holograms from a large sample volume are projected on a cine film by relay lenses. (c) Point source in-line holographic microscopy as used by

Jericho *et al.* (2006). A microscope objective illuminates a pinhole situated in a pressure chamber. The nearly spherical waves that emerge from an exit window illuminate the sample. The reference wave, together with scattered radiation, produces a *magnified* hologram on a CCD or CMOS chip situated in a second pressure chamber. The chambers are rigidly coupled together but allow fluid to pass freely between them.

Hologram reconstruction was achieved by passing a conjugate reference beam back through the lens and a column of water in a water-filled variable thickness aquarium compensation cell. This way all aberrations introduced during recording are canceled. Their system achieved sufficient resolution so that 2–3  $\mu\text{m}$  diameter spines on a marine diatom could be recognized.

*In situ* imaging of live plankton became possible when submersible holographic recording systems were deployed. The early systems developed by groups lead by Malkiel, Alquaddoomi, and Katz (1999), Craig *et al.* (2000), and Watson *et al.* (2001) all recorded holograms on high-resolution film.

The system of Malkiel, Alquaddoomi, and Katz (1999) used collimated beam in-line holography. The principle of this is shown in Figure 3.1b. A collimated ruby laser beam illuminated a volume of sea water 287 mm long and 63 mm in diameter. Mirrors and a relay lens then allowed the recording of the hologram on high-resolution 70 mm holographic film at a maximum rate of one hologram every 30 s. The HoloCamera system was mounted on a manned submersible, the Johnson Sea Link (Liberatore *et al.*, 1997). This HoloCamera could record 400 holograms on slow buoyancy driven ascents or when moving at 1 kt during powered transects.

Collimated beam in-line holography and high-resolution film recording allows imaging of liters of sampled volume. The retrieval of information that is stored in the hologram can, however, be time consuming and requires two basic steps. The film has to be developed and the hologram must be reconstructed. Hologram reconstruction for the Malkiel, Abras, and Katz (2004) holocamera was accomplished with conjugate collimated He-Ne illumination of the holograms. The same relay lenses that were used in the hologram recording were also used to bring the real image volume close to a digital camera (3.59  $\mu\text{m}$  per pixel) equipped with a Micro-Video-Zoom-Objective and a 0.75  $\times$  sub-lens. The camera was mounted on a three-axis motorized traverse. The sample volume was scanned with 2 $\times$  magnification at 14  $\times$  14 camera positions in each recording plane. Plankton information throughout the imaged volume was obtained in this way for 200 planes with successive planes separated by 1 mm. The 1 mm spacing between reconstruction planes is much larger than the dimensions of most plankton organisms in a sampled volume. Nevertheless, this coarse slicing of a single scanned reconstructed volume resulted in about 35 GB of image information. Since hologram recording and image reconstruction were performed with different wavelengths, the reconstructed volume was compressed by 18%. Despite these complications, image resolution was adequate to detect particles down to 10  $\mu\text{m}$  in diameter. For particles smaller than 50  $\mu\text{m}$  in diameter, improved resolution was obtained through band-pass filtering by insertion of a pin and iris filter at the focal point of the first relay lens. With the holocamera of Katz's research group, the first *in situ* high-resolution images of marine organisms such as calanoid copepods and ctenophores were obtained so that information about plankton distribution, such as particle density and its variation with depth, was obtained for the first time with holographic imaging (Malkiel *et al.*, 2006).

As part of a multinational project funded by the European Commission under the Mast III initiative, a holographic recording system, the HoloCam, was developed

by the group lead by Watson *et al.* (2001). The objective of the project was to develop a holographic imaging system to analyze and monitor the populations of living organisms and inanimate particles within the world's oceans. The laser in their HoloCam instrument was a frequency doubled Nd:YAG laser (532 nm) capable of 700 mJ single pulse power and a pulse duration of 10 ns. The laser beam was split, with one beam (100 mJ) performing collimated in-line holography (Figure 3.1b) while the other beam (600 mJ) was used to image the same water column in an orthogonal direction using an off axis reference beam. The water sample for off-line holography was illuminated through three specially designed light rods. All holograms were recorded on Agfa Millimask high-resolution silver halide photographic emulsions supported on glass plates (102 mm<sup>2</sup>). Holograms could be collected at 10 s intervals. The combination of in-line and off-line holography on one instrument allowed recording of very large volumes with 3.5 l for the in-line part and 50 l for the off-line system. During three dives to a depth of 100 m at Bonawe Deep in Loch Etive (a sea loch in the west of Scotland) 107 holograms were recorded.

Hologram reconstruction was performed with conjugates of the original reference beams, with beams normal to the photographic plates for in-line holograms and at 60° for off-line holograms. As with Katz's holocamera, the projected real images in front of the holograms were scanned in  $x$ - $y$ - $z$  by a video camera mounted on computer-controlled micropositioning stages. Allowances for optical aberrations and refractive index mismatch between recording and replay were also made through selection of replay wavelength and beam angles (Hobson and Watson, 2002). The HoloCam recorded high-quality images of calanoid copepods as well as of marine snow with both the in-line and off-line holographic cameras (Hobson and Watson, 2002).

The collimated beam illumination of sample volume employed by both HoloCam and Holocamera gives unmagnified holograms of all particles present in the illuminated volume. The off-line method is capable of imaging objects, including their surface features, several millimeters in diameter. The particle density can be high since the reference wave does not pass through the sample and is thus not corrupted through scattering events. The method, however, gives poorer resolution for organisms below 500  $\mu$ m and requires steps to minimize optical aberration on image reconstruction. Collimated beam in-line holography has allowed imaging of objects upward of 10  $\mu$ m in length. For opaque objects, reconstruction will only give the silhouette of the objects and, since the reference wave passes through the imaged volume, the reference beam is also affected by high particle densities.

The recorded holograms contain information about all the illuminated objects in the sample volume and images of objects are obtained through hologram reconstruction in selected image planes. To reconstruct larger objects, such as copepods, the density of reconstruction planes along the optic axis can be low and planes may be mm apart. To determine the density of plankton organisms in all size categories including picoplankton, however, requires a much higher density of reconstruction planes. To locate plankton particles 10  $\mu$ m in diameter in a 300 mm long water column (liter size sample volume) would require a reconstruction

plane at least every 20–30  $\mu\text{m}$  or a total of at least  $10^4$  reconstruction planes. The information to be processed for a *single hologram* would be in the TB range. The quantitative evaluation of a sample thus requires enormous computing power and long reconstruction and image processing times. Even if the sampled volume is restricted to only 60  $\text{mm}^3$ , for example, the image information from a single hologram would still amount to 5 GB. The volume of information that must be processed is even more problematic when sequences of holograms are recorded to determine the trajectories and swimming behavior of plankton. It is therefore essential to develop fast reconstruction algorithms as well as automated methods for the evaluation of reconstructed holograms. A number of these automated methods have been described in the literature (Malkiel, Abras, and Katz, 2004; Hobson and Watson, 2002; Sun *et al.*, 2008) and include automatic detection of in-focus objects in a reconstruction plane as well as automatic distortion corrections, false trace removal, and more.

A much simplified and physically smaller system was recently developed by J. Watson's group (Sun *et al.*, 2007). Their eHoloCam, with a design depth of 3 km, uses collimated beam illumination from a pulsed (1 mJ per pulse at 4 ns pulse duration) frequency-doubled Nd-YAG laser at 532 nm. The design principle is similar to that shown in Figure 3.1b. Instead of a film recording medium, the eHoloCam uses a  $2208 \times 3000$  pixel CMOS (complementary metal oxide semiconductor) detector with a square pixel pitch of  $3.5 \times 3.5 \mu\text{m}^2$ . The camera can record holograms from a water column of 36.5  $\text{cm}^3$  at a rate of 25 Hz. The camera was designed to be towed at speeds of up to  $2 \text{ m s}^{-1}$  and is self-contained in terms of power and data storage.

### 3.4

#### Point Source Digital In-Line Holographic Microscopy

The recording systems discussed in Section 3.3 all used collimated laser beams, illuminated liter-size sample volumes, and were able to record microplankton. Most of the systems, however, were very bulky and had to use film to record the holograms. In addition, they were less successful in obtaining high-resolution images and trajectories of particles below 20  $\mu\text{m}$  in diameter. Even for objects up to 50  $\mu\text{m}$  in diameter (Malkiel, Alquaddoomi, and Katz, 1999), resolution was at times insufficient to decide between dinoflagellates, microzooplankton, or pieces of detritus. The aim of plankton imaging is to measure and monitor the abundance of living organisms in the oceans from microplankton down to picoplankton, including bacteria. The latter two are at the bottom of the food chain and serve as prey for ciliate plankton, which in turn are eaten by larger organisms such as copepods. Identification of organisms in the nano- and picoplankton size range, the determination of their contribution to the ocean biomass, and possibly their grazing rates are therefore important objectives for plankton imaging. The size range from 0.5 to 10  $\mu\text{m}$  can include bacteria, cyanobacteria, both auto- and heterotrophic picoflagellates, nanoflagellates, and also small ciliates. The concentration of

planktonic microorganisms depends on location, temperature, and depth, and concentrations can show substantial diurnal as well as seasonal variations.

We can obtain insight into plankton density and size distribution in ecologically significant areas by, for example, considering the data of Ferrier-Pages and Gattuso (1998). The concentration of heterotrophic bacteria in the water over a coral reef at Miyako Island (Japan) was measured to be  $4\text{--}8 \times 10^5$  cells  $\text{ml}^{-1}$  and represented a biomass of  $10 \mu\text{g C l}^{-1}$ . Autotrophic picoflagellates were present at a concentration of  $10^2$  cells  $\text{ml}^{-1}$  ( $0.2 \mu\text{g C l}^{-1}$ ) while heterotrophic picoflagellates in the  $2 \mu\text{m}$  size range amounted to  $3\text{--}5 \times 10^3$  cells  $\text{ml}^{-1}$  ( $1 \mu\text{g C l}^{-1}$ ). Auto- and heterotrophic nanoflagellates in the  $5\text{--}10 \mu\text{m}$  range were present at the  $10^3$  cells  $\text{ml}^{-1}$  ( $9 \mu\text{g C l}^{-1}$ ) level while the concentration of microplankton was low. Diatoms ( $\sim 40 \mu\text{m}$  size range), for example, were present at the  $100$  cells  $\text{l}^{-1}$  level and represented the lowest biomass. The size range from  $<1 \mu\text{m}$  ( $10^{-8} \mu\text{g C cell}^{-1}$ ) to a few tens of micrometer ( $2 \times 10^{-2} \mu\text{g C cell}^{-1}$ ) was not accessible to past collimated beam holography systems. This size range is, however, important since it represents the high end of the marine plankton biomass and also determines production rates of organisms in the larger size ranges. To image plankton organisms and to identify them in their respective plankton groups requires true image resolution, and not just object visibility, at the micron level. This kind of resolution has been achieved with point source digital in-line holography (Garcia-Sucerquia *et al.*, 2006). Examples of high-resolution point source DIHM images of algae and measurements of the temperature dependence of algae movement are given in Lewis *et al.* (2006).

Figure 3.1c illustrates the principle of point source DIHM. A low-power laser in a pressure vessel is focused on a pinhole with the help of an objective. The pinhole is situated close to a thin optical window and the emerging light illuminates a conical region of the water to be examined. The detector is located in a second pressure chamber immediately behind a second optical window as shown in the figure. The pinhole emits nearly spherical waves, the reference waves, which interfere with waves scattered by objects to form a hologram at the detector. Hologram reconstruction then recovers images and coordinates of all objects in the illuminated volume. With modern CCD or CMOS cameras as detectors, this in-line digital holographic microscopy allows the construction of extremely small and robust high-resolution imaging systems. Use of a digital rather than film-based recording system was pioneered by Owen and Zozulya (2000), who used a CCD array to capture and reconstruct in-line holograms of marine organisms to a depth of 16 feet. More recently the Dalhousie University holographic imaging group lead by H.J. Kreuzer and M.H. Jericho developed submersible point source DIHM instruments that achieved sub-micron resolution with CCD as well as CMOS detectors.

#### 3.4.1

##### Instruments

Two instruments have been developed. One for ocean studies with a design depth that covers most depths encountered over continental shelves. The second instrument was designed for shallower coastal waters and for limnological studies.

The design principle of the instruments is as shown in Figure 3.1c. The instruments consist of two chambers rigidly coupled together with four bolts. The source chamber houses the laser, microscope objective (100 $\times$ ), and pinhole while the recording chamber houses the CCD or CMOS camera. For shallow water applications the holograms are transferred directly to the recording station via a FireWire while for the greater depth marine version of the instrument the camera chamber also housed the data transfer units for the USB-2 connection to the computer at the surface. Two USB-2 to ether net converters allowed data transmission up to 480 Mbits $s^{-1}$ . The optical window on the camera chamber is 25 mm in diameter and 4 mm thick and is situated about 4 mm from the CCD chip. Construction of the source window is more problematic. For high-resolution, short pinhole to object distances are required. This implies that the source window has to be very thin. Since the window is close to the point source it, fortunately, also means that the window can be very small in diameter. The source windows therefore had diameters of 2 mm and were only 150  $\mu$ m thick. The lasers used in our marine version of the microscope were solid-state lasers with wavelengths of 532 or 632 nm and powers between 3 and 15 mW, while our shallow water instrument used a 25 mW, 405 nm wavelength laser.

The CCD camera in the deep sea instrument is a Lumenera Lu160M with  $1392 \times 1040$  pixels of 6.4  $\mu$ m in size. The camera has a frame rate of seven frames per second and a minimum exposure time of 0.045 ms. This short exposure time ensured that sharp images of microplankton in motion could be obtained. In an ocean environment with the submersible DIHM suspended from a vessel, however, wave action and tidal currents generated excessive motion of the water in the imaging volume. Under these conditions and for a 15 mW laser, the typical exposure time of 0.2 ms was insufficient for sharp imaging of organisms. The imaging volume was therefore surrounded by an isolation chamber that could be opened to the ocean or closed for imaging. Further design details can be obtained from Jericho *et al.* (2006, 2010). We recently succeeded in performing high-resolution DIHM imaging with high numerical aperture optical fibers. The light intensity obtained with such fibers was sufficient to produce good holograms with 60  $\mu$ s exposure times. Exposure times of a few microseconds on standard cameras will soon be available so that isolation mechanisms, as mentioned above, may become unnecessary in future.

### 3.4.2

#### Image Reconstruction

The 3D structure of the object can be recovered from the digital two-dimensional hologram by applying a Kirchhoff–Helmholtz transform (Xu *et al.*, 2002; Kreuzer, 2002):

$$K(\vec{r}) = \int_S d^3\xi \tilde{I}(\vec{\xi}) \exp[2\pi i \vec{\xi} \cdot \vec{r} / \lambda \xi] \quad (3.1)$$

In Eq. 3.1 the integration extends over the surface of the CCD chip with coordinates  $\xi = (X, Y, L)$ , where  $L$  is the distance from the source to the center of the chip and



$\tilde{I}$  is the contrast image (hologram). The contrast image is obtained by subtracting the images with and without the object present or in the case of plankton imaging it is obtained by subtraction of successive exposures of a sample. The function  $K(r)$  is significantly structured and differs from zero only in the space region occupied by the object. By reconstructing the wave front  $K(r)$  on a number of planes at various distances from the source in the vicinity of the object, a 3D image can be built up from a single 2D hologram. The plot of  $|K(r)|$ , on a 2D plane perpendicular to the optical axis, is equivalent to a single in-focus image taken in a conventional compound microscope. In DIHM one can generate a stack of 2D holographic reconstructions from a single hologram. Combining such a stack into a 3D reconstruction will result in a 3D image of the object. For numerical implementation of the transform a fast algorithm was developed that evaluates  $K(r)$  without any approximations. It is now incorporated in a self-contained program packages, called *Swordfish* and *Octopus*, that not only perform the numerical reconstruction but also all data management and image visualization and analysis operations (Resolution Optics Inc.).

In plankton imaging it is of considerable interest to not only record an image of an organism but also obtain a detailed record of its trajectory. This is easily achieved in DIHM with the procedure illustrated in Figure 3.2: (i) a sequence of holograms ( $h_i$ ) are recorded at fixed time intervals; (ii) undesired background effects, such as spurious interferences from optical windows, for example, are removed by subtracting consecutive hologram pairs, pixel by pixel, to generate difference holograms ( $h_1 - h_2$ ), ( $h_3 - h_4$ ), and so on; and (iii) the resulting difference holograms can be summed to generate a single data file that contains all holograms (with alternate signs), but that has the same size as any single original hologram. Reconstruction of this final data set with Eq. 3.1 in different depth planes then

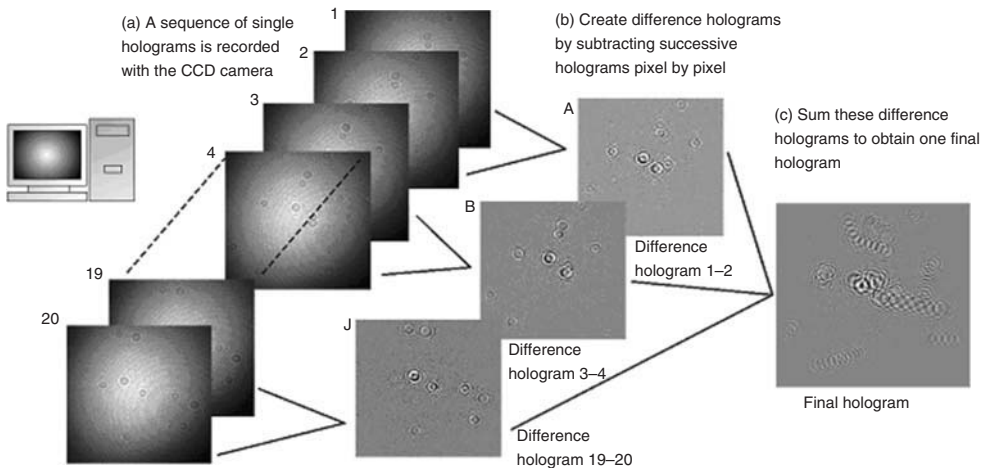


**Figure 3.2** Recording and processing of a sequence of holograms to construct a sum hologram; subsequent reconstructions of the sum hologram in different slices through the sample volume yields images of plankton trajectories.

gives a record of the trajectories of all objects in the illuminated sample volume (Xu *et al.*, 2003).

### 3.4.3

#### Image Examples

Figure 3.3 illustrates the high resolution that can be obtained with point source DIHM under laboratory conditions. Figure 3.3a is an image of a diatom obtained with a  $0.5\ \mu\text{m}$  pinhole,  $405\ \text{nm}$  illumination, and a  $2000 \times 2000$  pixel camera. The  $1.3\ \mu\text{m}$  wide ribs of the organism are well resolved. Figure 3.3b shows an image of a dividing *E. coli* bacterium that was imaged under similar conditions as the diatom. Although the septum is not clearly resolved, the partition region can be clearly identified and the image suggests sub-micron resolution. Figure 3.4 shows an image of a copepod that was obtained with our deep sea DIHM at a depth of  $10\ \text{m}$  in coastal waters off Nova Scotia. The organism, in the microplankton size range, could be easily imaged with high resolution. Figure 3.4 shows the antennae and the numerous fibers that protrude from them. Small fibers on the side of the copepod (white arrow) have a diameter of  $2\ \mu\text{m}$ . Figure 3.5 shows a trajectory of a marine rotifer taken in coastal waters of Nova Scotia. Images were recorded at  $5\ \text{f s}^{-1}$  but only every second frame was used for Figure 3.5. The rotifer undulates about the swimming direction and proceeds from right to left in Figure 3.5 at an average speed of  $175\ \mu\text{m s}^{-1}$ . The recording of such particle trajectories can clearly help to distinguish living matter from detritus. The images demonstrate that *in*

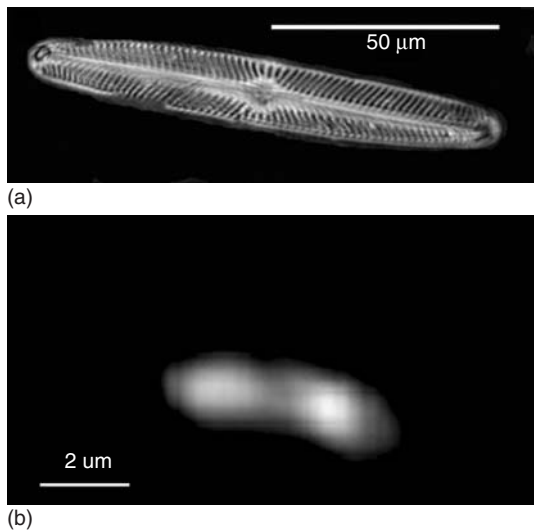


**Figure 3.3** High-resolution DIHM image of (a) a diatom – the width of a rib-like structure is  $1.3\ \mu\text{m}$  (source–camera distance =  $15\ \text{mm}$ ; source–object distance =  $500\ \mu\text{m}$ ;  $\lambda_{\text{eff}} = 405\ \text{nm}$ ;  $0.5\ \mu\text{m}$  pinhole); (b) *Escherichia coli* bacteria (source–camera distance =  $15\ \text{mm}$ ; source–object distance =  $500\ \mu\text{m}$ ;  $\lambda_{\text{eff}} = 405\ \text{nm}$ ;  $0.5\ \mu\text{m}$  pinhole).

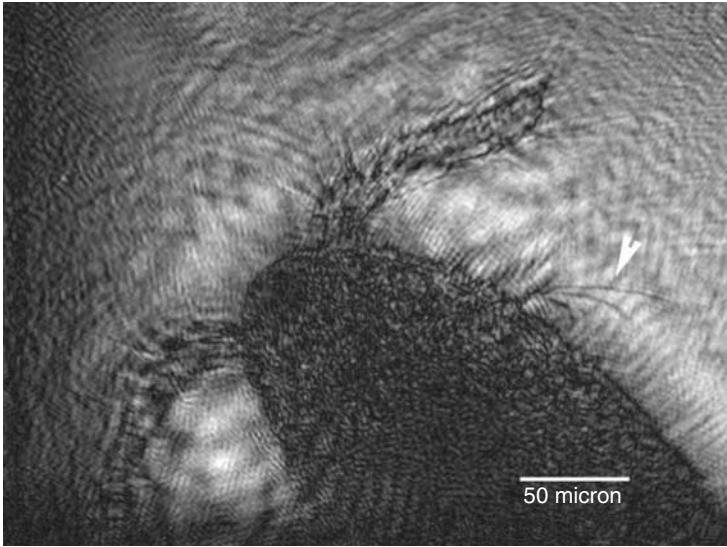


**Figure 3.4** Image of a copepod taken in coastal waters of Nova Scotia at a depth of 10 m. The hair-like protrusions on the two antennae of the copepod are visible. The small fibers on the

side of the copepod (white arrow) are  $2\text{ }\mu\text{m}$  in diameter. (Source–camera distance = 13.7 mm; source–object distance  $\sim 700\text{ }\mu\text{m}$ ;  $\lambda_{\text{eff}} = 422\text{ nm}$ ;  $1.0\text{ }\mu\text{m}$  pinhole.)



**Figure 3.5** Image sequence of a marine rotifer in motion; average swimming speed was  $175\text{ }\mu\text{m s}^{-1}$ . (Source–camera distance = 13.7 mm; source–object distance =  $600\text{ }\mu\text{m}$ ;  $\lambda_{\text{eff}} = 422\text{ nm}$ ;  $1.0\text{ }\mu\text{m}$  pinhole.)

*situ* imaging of marine plankton with resolution at the micron level is possible and that studies of nano- and even some picoplankton are possible with point source DIHM. Figure 3.6 shows a gallery of organisms that we managed to image with our submersible DIHM, while Figure 3.7 shows a 3D rendering of bacteria from an arctic lake on Axel Heiberg Island in the Canadian high arctic.

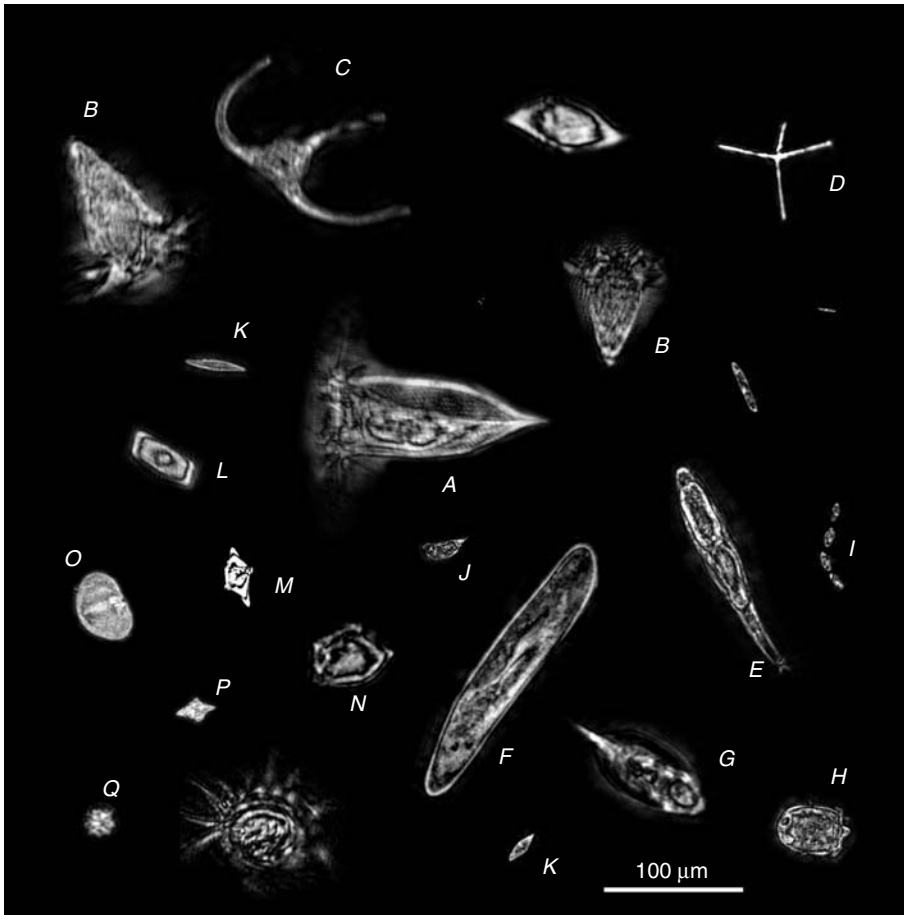


**Figure 3.6** A gallery of marine and some freshwater organisms taken with the submersible DIHM and identified from the image: A: marine ciliate *Favella*; B: marine ciliate *Strombidium conicum*; C: dinoflagellate *Ceratium* sp.; D: diatom; E: rotifer; F: *Paramecium*; G: rotifer; H: ciliate

*Didinium*; I: swimming ciliate; J: ciliate; K: marine pennate diatom; L and M: *Pleurosigma/Gyrosigma* sp.; N: marine silicoflagellate *Dictyocha*; O: centric diatom; and P: dinoflagellate (unknown Peridinales); Q: unidentified organism.

#### 3.4.4 Resolution

The resolution of a microscope is given in terms of the numerical aperture (NA) of the objective lens. The lateral resolution,  $\Delta$ , is given by Garcia-Sucerquia *et al.* (2006):

$$\Delta_t \geq \lambda/2NA$$

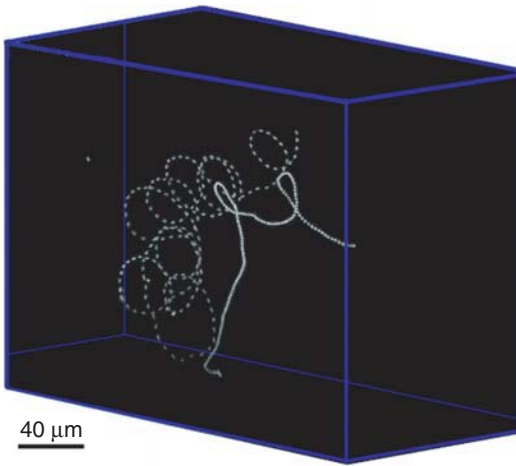


**Figure 3.7** Three-dimensional rendering of bacteria from an arctic lake on Axel Heiberg Island. (Source–camera distance = 21 mm; source–object distance = 800 μm;  $\lambda = 405$  nm; 0.5 μm pinhole; CCD chip size  $1.28 \times 1.28$  cm<sup>2</sup>; reconstruction volume  $500 \times 500 \times 300$  μm<sup>3</sup>.)

The resolution along the optic axis is generally lower than the lateral resolution and is given by:

$$\Delta_l \geq \lambda/2(\text{NA})^2$$

The numerical aperture depends on the ratio of the detector width to the object–detector distance. The resolution thus increases at shorter wavelength and with larger screen width (larger NA). When the optic path crosses several media with different refractive indexes it is possible to show (Jericho *et al.*, 2006) that hologram formation depends on an effective wavelength that is determined by the length of path through each medium. In our submersible instruments for high-resolution plankton imaging, the optic path involved air ( $n = 1$ ), water ( $n = 1.33$ ), and glass ( $n = 1.52$ ), and with a laser wavelength of 532 nm the effective wavelength was  $\lambda_{\text{eff}} = 422$  nm. The resolution of a holographic microscope can also be discussed in terms of the number of interference fringes that can be resolved by the recording medium. For digital CCD or CMOS detectors, faithful recording of interference fringes is only possible if the pixel size of the recording chip is much smaller than the smallest fringe spacing that needs to be recorded. Simulations with computer-generated holograms suggested that two scattering centers can be resolved if the number of captured fringes is large (tens of fringes) and that only fringes separated by more than three camera pixels contribute to image reconstruction and resolution. Either too few fringes or fringes that are too close together will lead to reduced resolution. In general, a shorter wavelength will produce more fringes, and usually results in higher resolution. However, the larger number of fringes is spread over a fixed number of pixels on the chip so that at shorter wavelength the average number of pixels per fringe decreases and the resolution may thus be less than expected. A more detailed discussion on

fringe number and spacing and its effect on resolution can be found in Jericho *et al.* (2006). Point source DIHM with a nearly spherical reference wave produces a magnified hologram at the recording screen. This implies that the number of fringes captured, and hence the resolution, depends on the object–screen distance. Figure 3.8 shows a calculation of the obtainable resolution for our deep-sea submersible DIHM with the source–screen distance set to 13.7 mm and an effective wavelength of 422 nm. A resolution of  $1\text{ }\mu\text{m}$  is easily obtainable with the object close to the point source and the smallest measurable separation of two scattering points increases nearly linearly with source–object distance. The imaged volume is essentially determined by the volume of a pyramid that has the CCD chip as a base and the point source as the apex. As shown in Figure 3.8a, a resolution of  $2\text{ }\mu\text{m}$  or better is obtainable up to a source–object distance of 1.5 mm in an image volume of  $1\text{ mm}^3$ . At a source–screen distance of 4 mm the expected resolution is  $6\text{ }\mu\text{m}$  or better in a volume of about  $10\text{ mm}^3$ . If the gap between the source and camera chamber is increased then the imaged volume will increase, albeit with some reduction in resolution. Figure 3.8b shows a plot of resolution and imaged volume for a 60 mm source to screen distance and for an effective wavelength of 400 nm. At a source–object distance of 40 mm in a volume of  $650\text{ mm}^3$ , the expected resolution is  $10.5\text{ }\mu\text{m}$  or better. Point source DIHM with pinhole diameters between  $0.5$  and  $1\text{ }\mu\text{m}$  have consistently imaged picoplankton with micron resolution and can identify organisms and can determine their number densities as well as their swimming characteristics.

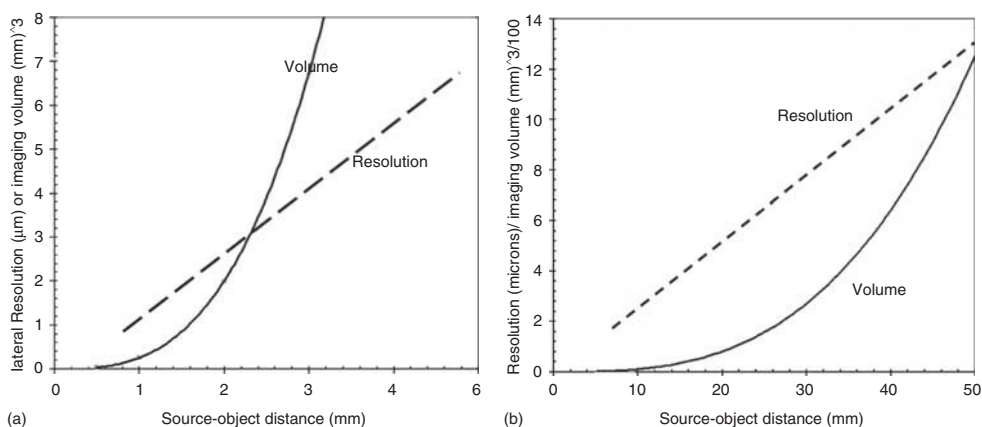


**Figure 3.8** (a) Obtainable resolution for marine submersible DIHM at 13.7 mm source–screen distance and with  $\lambda_{\text{eff}} = 422\text{ nm}$  as function of source–object distance;  $1000 \times 1000$  pixel CCD camera with  $6\text{ }\mu\text{m}$  square pixels. The resolution (-----) and image volume (—) are shown that give

the indicated or better resolution at a specified source–screen distance. (b) The same as for (a) but with the distance between point-source and camera increased to 60 mm to increase the volume of the imaged sample;  $\lambda_{\text{eff}} = 400\text{ nm}$ .

## 3.4.5

## Volume Imaging Challenges

In DIHM a single hologram contains all the information about scattering objects within the illuminated volume. Reconstruction of the imaged objects is then performed by slicing the volume into individual reconstruction planes oriented perpendicular to the optic axis. The number of slices needed will depend on the size of the imaged objects and on the desired resolution. To image a 20  $\mu\text{m}$  diameter nanoplankton organism with high resolution will require a minimum of five reconstruction planes to home in on the slice where the object displays the sharpest silhouette. To reconstruct all particles of that size that may be distributed over a  $z$ -depth of 5 mm will thus require 1250 reconstruction operations that have to be performed on that one hologram. If the reconstruction time for a  $1024 \times 1024$  pixel hologram is 240 ms ( $1/4$  of this for a  $512 \times 512$  hologram) on a PC, in-focus images of all organisms that may be present will take a minimum of 5 min. Holograms  $512 \times 512$  in size still give acceptable resolution and an imaged volume of  $10 \text{ mm}^3$  (obtained at a source–object distance of  $\sim 5 \text{ mm}$ ; see Figure 3.8a) could be reconstructed in less than 2 min. The equivalence of  $1 \text{ cm}^3$  of sea water with high resolution can be imaged through multiple sampling of  $10 \text{ mm}^3$  volume elements. The 100 required samples would take about 3.3 h of reconstruction time for  $512 \times 512$  holograms. This time can be shortened considerably if holograms in a sequence are added pixel by pixel to form sum holograms as explained in Figure 3.2. Each sum hologram would then contain information about all objects that were imaged in the sequence. For example, if ten individual holograms are added to form a sum hologram then imaging of  $1 \text{ cm}^3$  volume would generate only ten sum holograms that need to be reconstructed. For  $512 \times 512$  holograms at 60 ms per  $z$  slice, the reconstruction time would take less than 20 min.

In practice the search for organisms in the imaged volume can be accelerated considerably by first locating organisms approximately with more widely spaced  $z$  slices, which is then followed for each located organism with a higher slice density for organism identification. At low particle density, this method allows the reconstruction of organisms in a  $1 \text{ cm}^3$  volume in much less than 1 h. The example nevertheless illustrates the large amount of information that has to be processed for picoplankton imaging and the importance of high hologram reconstruction speeds. We have recently obtained very fast hologram reconstruction with the Helmholtz–Kirchhoff transform using graphics processing units (GPUs) as coprocessors. With the Tesla C-1060 card, for example, we can perform a single reconstruction of a  $2048 \times 2048$  hologram in 40 ms or reconstruction of a  $512 \times 512$  hologram in 7 ms (reconstruction time did not scale well with hologram size). Reconstruction of all pico- and nanoplankton objects in a cubic centimeter of water can now be achieved in a few minutes on a PC. The high reconstruction speed of nearly 150 reconstructions per second for a  $512 \times 512$  pixel hologram implies a near video speed reconstruction capability and real-time holographic imaging of plankton motion through several hundred  $\mu\text{m}$  thick sample volumes is now also possible. In the next few years the new generation of GPUs is expected

to allow further increases in reconstruction speeds by perhaps as much as an order of magnitude. This substantial gain in reconstruction speed could then be increased further if several graphics processing cards are operated in parallel so that high-resolution real time 3D imaging of picoplankton will soon be possible.

### 3.5

#### Future Outlook

For microorganisms above  $\sim 30\text{ }\mu\text{m}$  identification can be accomplished through optical imaging or reconstructions of DIHM holograms. Organisms smaller than  $\sim 20\text{ }\mu\text{m}$  such as algae, mammalian cells, many forms of nano- and picoplankton in marine environments, as well as organisms at the micron length scale, such as bacteria are, however, generally difficult to identify from their static images alone. However, organisms often have characteristic swimming behavior that can help in their identification. For example, consider the three bacteria *Vibrio cholerae*, *Escherichia coli*, and *Enterococcus faecalis*. All three are indicator microbes for the presence of harmful organisms in ship's ballast water. The first is a curved-rod shaped bacterium with a single flagellum. The second is a straight rod bacterium with several flagella that bundle when the bacterium swims forward but periodically unbundle to give the bacterium a characteristic tumbling motion. The third organism is a non-motile bacterium that exists as pairs or short chains of individuals. The trajectories of a curved-rod bacterium differ from the straight and occasional tumbling motion of *E. coli* while the third organism should only execute Brownian motion steps.

An important future objective therefore is to exploit the high depth of field of DIHM and to measure and characterize organism trajectories. At high organism density, trajectory analysis will have to be automated and powerful analysis software needs to be developed so that organism coordinates, speed, swimming direction, trajectory curvature, and general trajectory shape (i.e., straight, circular, helical, etc.) can be determined and cataloged.

Important progress in that direction has already been made by Heydt *et al.* (2009). In connection with a general research program on surface fouling by marine organisms by Rosenhahn *et al.* (2010) the authors used point source DIHM to study the three-dimensional settling dynamics of algal zoospores in the vicinity of surfaces. They developed algorithms and techniques for high-throughput analysis of holographic microscopy data. The large depth of field of holographic microscopy enabled them to determine, in a nearly automatic manner, distributions of swimming speeds as well as diving directions of multiple zoospores near a surface (Heydt *et al.*, 2007, 2009).

The high resolution obtainable with point source DIHM together with the extreme simplicity of DIHM construction makes these instruments excellent candidates for the exploration of microscopic life forms in harsh and challenging environments. Their potential for monitoring plankton populations of coastal waters has been well demonstrated, as discussed in this chapter. Furthermore,



DIHM technology in future can include automatic *in situ* monitoring of plankton populations by instruments powered by photovoltaics and that transmit hologram image information to laboratories via satellite links. More challenging, but also within present technological capability, is the design of instruments that can image microscopic life in deep-sea trenches or even carry out exobiological studies on other planets (Jericho *et al.*, 2010). At an ocean depth of 10 km, instruments have to be completely self-contained with no power and data transfer links to a surface vessel and all power supplies, imaging protocols, and data manipulation and storage must be controlled by on-board computers. For imaging at extreme depth, the camera and point source chambers require thick walls. This makes it impossible to position the pin hole of the point source close to the source window as required for high-resolution imaging. In collaboration with Alexander Bochsansky from the Old Dominion University, Norfolk VA we recently developed an optic fiber based point source that allowed high-resolution imaging to a depth of 6000 m (Bochsansky *et al.* 2013). Very little is known about the existence and behavioral traits of microscopic organisms at that depth and pressure and DIHM can help in providing a window on this last frontier on our planet.

## References

- Bochsansky, A.B. Jericho, M.H. and Herndl, G.J. (2013) Development and deployment of a point-source digital inline holographic microscope for the study of plankton and particles to a depth of 6000 m. *Limnol. Oceanogr. Methods*, **11**, 28–40.
- Craig, G. *et al.* (2000) HoloCam: a subsea holographic camera for recording marine organisms and particles. *Proc. SPIE*, **4076**, 111–119.
- Ferrier-Pages, C. and Gattuso, J.P. (1998) Biomass, production and grazing rates of pico- and nanoplankton in coral reef waters (Miyako Island, Japan). *Microb. Ecol.* **35**, 46–57.
- Garcia-Sucerquia, J., Xu, W., Jericho, S.K., Klages, P., Jericho, M.H., and Kreuzer, H.J. (2006) Digital in-line holographic microscopy, *Appl. Opt.*, **45**, 836–850.
- Heflinger, L.O., Stewart, G.L., and Booth, C.R. (1978) Holographic motion pictures of microscopic plankton. *Appl. Opt.*, **17**, 951–954.
- Heydt, M., Divos, P., Grunze, M., and Rosenhahn, A. (2009) Analysis of holographic microscopy data to quantitatively investigate three-dimensional settlement dynamics of algal zoospores in the vicinity of surfaces. *Eur. Phys. J. E*, **30**, 141–148.
- Heydt, M., Rosenhahn, A., Grunze, M., Pettitt, M., Callow M.E., and Callow, J.A. (2007) Digital in-line holography as a three-dimensional tool to study motile marine organisms during their exploration of surfaces. *J. Adhes.*, **83**, 417–430.
- Hobson, P.R. and Watson, J. (2002) The principles and practice of holographic recording of plankton. *J. Opt. A: Pure Appl. Opt.*, **4**, S34S49.
- Jericho, S.K., Garcia-Sucerquia, J., Xu, W., Jericho, M.H., and Kreuzer, H.J. (2006) *Rev. Sci. Instrum.*, **77**, 43706.
- Jericho, S.K., Klages, P., Nadeau, J., Dumas, E.M., Jericho, M.H., and H.J., Kreuzer (2010) In-line digital holographic microscopy for terrestrial and exobiological research. *Planet. Space Sci.*, **58**, 701–705.
- Knox, C. and Brooks, R.E. (1969) Holographic motion picture microscopy. *Proc. R. Soc. London, Ser. B*, **174**, 115–121.
- Kreuzer, H.J. (2002) Holographic microscope and method of hologram reconstruction, US Patent 6,411,406 (June 25).
- Lewis, N.I., Cambella, A.D., Xu, W., Jericho, M.H., and Kreuzer, H.J. (2006) Swimming speed of three species of the marine dinoflagellate *Alexandrium* as determined

- by digital In-line holography. *Phycologia*, **45**, 61.
- Liberatore, D., Askew, T., Tusting, R., *et al.* (1997) Harbor branch submersibles command a role in underwater scientific sampling. *Mar. Technol. Soc. J.*, **31**, 55–60.
- Malkiel, E., Abras, J.N., and Katz, J. (2004) *Meas. Sci. Technol.*, **15**, 601.
- Malkiel, E., Abras, J.N., Widder, E.A. and Katz, J. (2006) On the spatial distribution and nearest neighbor distance between particles in the water column determined from in situ holographic measurements. *J. Plankton Res.*, **28**, 149–170.
- Malkiel, E., Alquaddoomi, O., and Katz, J. (1999) Measurements of plankton distribution in the ocean using submersible holography. *Meas. Sci. Technol.*, **10**, 1142.
- Owen, R.B. and Zozulya, A.A. (2000) *Opt. Eng. (Bellingham)*, **39**, 2187.
- Resolution Optics Inc. (2012) DIHM Software Package, Swordfish and Octopus, Halifax.
- Rosenhahn, A., Schilp, S., Kreuzer, H.J., and Grunze, M. (2010) The role of inert surface chemistry in marine biofouling prevention. *Phys. Chem. Chem. Phys.*, **12**, 4275–4286.
- Sorokin, Y.I. (1973) Trophic role of bacteria in the ecosystem of the coral reef. *Nature*, **242**, 415–417.
- Sun, H., Benzie, P.W., Burns, N., Hendry, D.C., Player, M.A., and Watson, J. (2008) *Philos. Trans. R. Soc. A*, **366**, 1789–1806.
- Sun, H., Hendry, D.C., Player, M.A., and Watson, J. (2007) In situ underwater electronic holographic camera for studies of plankton. *IEEE J. Oceanic Eng.*, **32**, 373–382.
- Watson, J. *et al.* (2001) Simultaneous in-line and off-axis subsea holographic recording of plankton and other marine particles. *Meas. Sci. Technol.*, **12**, L9–L15.
- Xu, W., Jericho, M.H., Meinertzhagen, I.A., and Kreuzer, H.J. (2001) *Proc. Natl. Acad. Sci. U.S.A.*, **25**, 11301.
- Xu, W., Jericho, M.H., Meinertzhagen, I.A., and Kreuzer, H.J. (2002) Digital in-line holography of microspheres. *Appl. Opt.*, **41**, 5367–5375.
- Xu, W., Jericho, M.H., Meinertzhagen, I.A., and Kreuzer, H.J. (2003) Tracking particles in 4-D with in-line holographic microscopy. *Opt. Lett.*, **28**, 164–166.





## 4

# Confocal Laser Scanning Microscopy – Detailed Three-Dimensional Morphological Imaging of Marine Organisms

*Jan Michels*

## 4.1

### Introduction

Although the principle of confocal laser scanning microscopy (CLSM) had been invented in 1955 (Minsky, 1988), it was not until about three decades later that new scanning techniques and developments in the fields of microelectronics and laser and computer technologies enabled the construction of the first commercial confocal laser scanning microscope (e.g., Amos and White, 2003). Since then CLSM has become a powerful standard technique in the field of life sciences, and numerous very successful CLSM methods have been developed for high-resolution visualizations and analyses of a large variety of tissues, compounds, and substances in biological and medical specimens. In recent years the greatly increased power of computer and data processing systems in combination with the development of faster scan techniques and new effective CLSM and 3D software has resulted in CLSM now also having a large potential for 3D and live cell imaging. Today, CLSM is mainly used in the scientific disciplines cell biology, molecular biology, biochemistry, and medical science. In the context of some applications in materials science this technique has also gained importance within the last years. By contrast, the use of CLSM in classical disciplines of biology such as morphology and taxonomy is still rare. The present chapter describes the technical and methodological background of CLSM, highlights, based on various examples, the potential of CLSM for precise morphological imaging of marine organisms, and gives information about the most important aspects of the respective methods.

## 4.2

### Technical and Methodological Aspects of Confocal Laser Scanning Microscopy

When visualizing thick specimens with conventional light microscopy techniques, such as bright field microscopy and wide-field fluorescence microscopy, the structures, which are in focus, typically do not appear clear and sharp but look blurry instead. The reason for this is that during the visualization process light coming

from all layers of the specimen reaches the oculars of the microscope or the sensor of the camera. However, only the light signal coming from a specific layer at the focal plane provides sharp and clear information about the respective structures. The thickness of this layer, called the *focal layer* in the following, is equal to the microscope optics' depth of field, which is limited and typically rather small at high magnifications. The light signal coming from this focal layer is overlaid with light information originating from out-of-focus layers above and below the focal layer. Because of this overlay the structures of interest, which are in focus, appear blurry. By contrast, in confocal microscopy, as the name indicates, only light from the focal layer is used to create the micrographs while out-of-focus light either does not occur or its detection is avoided. Several different confocal microscopy techniques have been developed, all of them using different ways to achieve the goal of exclusively visualizing structures located in the focal layer. In CLSM, this is achieved by a specific pinhole technique. The technical details of CLSM are described below:

- 1) Laser light is used to illuminate the specimen. This light passes a first (illumination) pinhole (Figure 4.1a.a) [Modern commercial CLSM systems do no longer feature such a pinhole because it is not essential (Figure 4.1a.b).], enters the optical system via a dichroic mirror, and is focused by the optical system, resulting in a tiny illumination spot in the focal plane within the specimen (Figure 4.1a).
- 2) Light coming from the specimen passes the optical system in the opposite direction and is focused on the second side of the optical system, opposite to the specimen. On this side, a second (exit or detection) pinhole is located exactly in the second focal (micrograph) plane, which is optically conjugated to the first focal plane in the specimen. Owing to this setup, only light coming from a distinct layer at the first focal plane can pass the pinhole (Figure 4.1b), while nearly all light coming from all other layers of the specimen is blocked (or filtered out) by the pinhole (Figure 4.1c,d).
- 3) Behind the detection pinhole a specific detector collects and processes the light. By means of a photomultiplier the light signal is transformed into an electronic signal, whose intensity can be increased by applying a certain detector gain.
- 4) The light detected can be laser light reflected by the specimen, fluorescence light exhibited by the specimen, or a combination of both. For fluorescence visualizations it has to be ensured that the reflected laser light is filtered out and the fluorescence of interest is detected, which is achieved by specific detection setups. While in conventional CLSM systems classical fluorescence emission filters have been used, most of the recent commercial systems are equipped with spectral detectors, which enable the user to select any desired detection wavelength range.

In context with this setup, several aspects have to be considered. The thickness of the layer, from which light is detected, depends on the size of the pinhole. The smaller the pinhole the thinner this layer is and vice versa (Figure 4.2). Only if the thickness of this layer (called the *optical section* in the following) is equal to or smaller than the thickness of the focal layer (depth of field) of the optical system,

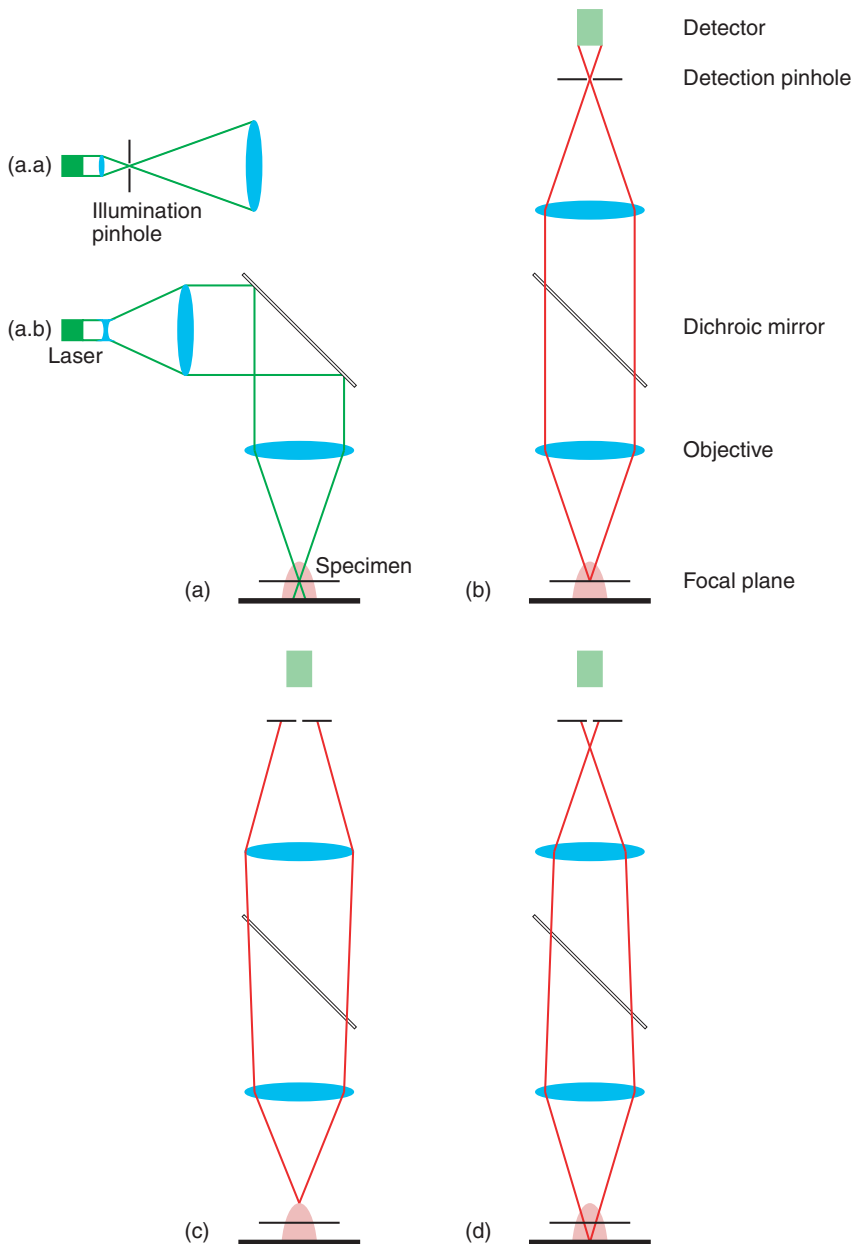


**Figure 4.1** Schematic illustration of the CLSM principle. The excitation light path is shown in green (a). Three exemplary paths of either fluorescence light originating in the specimen or laser light reflected by the specimen are shown in red and represent

light coming from the focal layer (b) and from two out-of-focus layers (c, d). While older CLSM systems feature an illumination pinhole (a.a), the illumination techniques of modern CLSM systems are normally no longer equipped with such a pinhole (a.b).

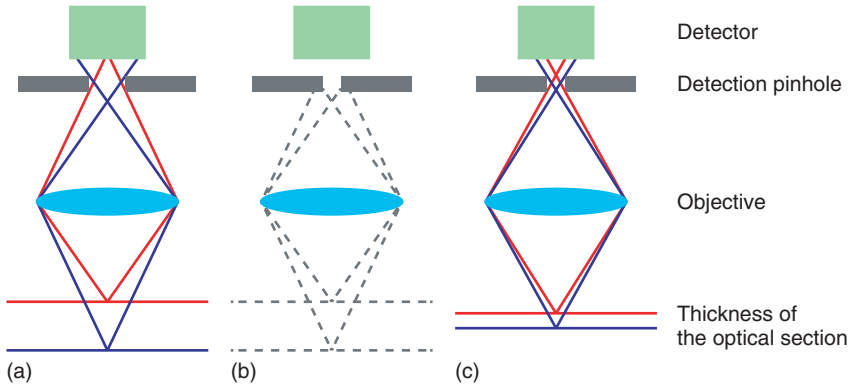


**Figure 4.2** Schematic illustration of the influence of the pinhole size on the thickness of the optical sections (for convenience only one lens is shown). A pinhole with a given size lets light pass to the detector. This light comes from an optical section

with a defined thickness (a). If the pinhole size decreases light coming from upper and lower parts of the optical section will be blocked by the pinhole (b). As a result, only light coming from a thinner optical section will reach the detector (c).

the microscope setup will be in a confocal state. The thickness of the focal layer depends on the properties of the microscope optics. Accordingly, the maximum size of the pinhole, at which the system is still in a confocal state, also depends on these properties.

If the microscope system has a tiny punctiform illumination its resolution will depend on the numerical aperture of the objective used and the wavelength of the light detected and will be limited by diffraction. In such a microscope system an infinitely small luminous object point is visualized as a circular so-called Airy diffraction pattern featuring a central bright disk, the Airy disk, and progressively weaker concentric dark and bright rings (Inoué, 2006). The radius  $r_{\text{Airy}}$  of the Airy disk is determined by:

$$r_{\text{Airy}} = 0.61 \frac{\lambda}{\text{NA}}$$

where NA is the numerical aperture of the objective used and  $\lambda$  is the wavelength of the light detected (Inoué, 2006).

The diffraction patterns of two incoherently radiating light points, which are located in the focal plane and separated by a certain distance, are visualized next to each other in the micrograph plane. According to the Rayleigh criterion these light points, if they are equally bright, will only be fully resolved by the microscope system and visible on the micrograph if the distance between them is larger or equal to the radius of the Airy disk (Inoué, 2006). In CLSM, the size of the image of the Airy disk displayed by the optical system in the pinhole plane (depending on the numerical aperture of the objective applied, the wavelength of the light detected, and the magnification of the optical system) is used to describe the opening size of the pinhole. In this context, 1 Airy unit (AU) corresponds to the size of the



Airy disk image. The maximum size of the pinhole, at which the system is still a confocal one, is about 1.2 AU.

### 4.3

#### Prerequisites for Generating High-Quality Confocal Laser Scanning Micrographs

To create micrographs of the optical sections the laser illumination spot is moved line by line over the field of view with a certain scan velocity. At the same time the light coming from the single areas illuminated is detected, and the micrograph is generated line by line. A zoom function enables the user to freely choose the size of the scanned area (field of view) within certain ranges, and the micrograph size can also be freely chosen (in modern commercial CLSM systems up to a size of  $8192 \times 8192$  pixels). In this context, specific requirements have to be fulfilled to obtain micrographs showing the visualized structures with the highest resolution possible. The Nyquist–Shannon sampling theorem says that for a precise and complete conversion of a continuous analog signal into a digital signal it is necessary to sample the analog signal with a frequency, which is at least two times the frequency of the analog signal [In practice, often higher minimum sampling frequencies are recommended (Centonze and Pawley, 2006).]. Accordingly, for the creation of optical sections, which show all structural information resolved by the objective, the pixel size, which is the real size each pixel of the micrograph represents, must not be larger than half the size of the smallest structure resolved by the objective. That means, for example, when applying an objective with a resolution of 200 nm, that the micrograph must contain at least as many pixels as result in each pixel representing a size of 100 nm.

As mentioned above, if the pinhole is closed to a size of about 1.2 AU the setup will be a confocal one. However, it is advisable to apply smaller pinhole sizes to obtain thinner optical sections resulting in clearer and crisper micrographs. Another positive effect of further decreasing the pinhole size is that the  $xy$ -resolution of the confocal system increases above the resolution described above (Centonze and Pawley, 2006). On the other hand, the amount of light being detected decreases significantly with a decreasing pinhole size. For this reason such a setting will only be advantageous if light with high intensities (either reflected laser light or intense fluorescence light) coming from the specimens is detected, while the visualization of specimens exhibiting relatively low fluorescence intensities would demand either intense excitation laser light or high gain values to increase the signal intensity. This would result in an increased risk of fluorescence bleaching or a decreased signal-to-noise ratio. Accordingly, for a large proportion of CLSM applications in practice the use of a pinhole size of 1 AU is recommended as a good compromise.

In terms of the laser light intensity applied, the selected scan velocity, and the detection of the light signal a few aspects have to be kept in mind. Both the scan velocity and the detector gain are positively correlated with the signal and micrograph noise. This means that increased scan velocity and gain will result in

an increased noise (or a decreased signal-to-noise ratio) being detected and visible on the micrographs. In general, it is recommended that slow scan velocities and low gain values are used, the latter being achieved by higher laser intensities in case of low fluorescence intensities. However, the specimens often do not allow for this. For example, unstable or moving specimens (as often present, for example, in the framework of live cell imaging) and fluorescence dyes, which are very sensitive to bleaching, preclude long scanning times and high laser intensities, respectively. Accordingly, in such situations good compromises have to be found. Modern detection techniques have greatly improved and feature relatively low noise levels, allowing for the application of relatively fast scan velocities and high gain values. Despite all of this, sometimes it is not possible to obtain high-quality micrographs because of the properties of the specimens and the fluorescence dyes used. In such situations reducing the micrograph size (and thus increasing the pixel size) below (above) the one necessary to meet the Nyquist–Shannon sampling theorem is often a good option to obtain reasonable results, which can still provide all the information desired. For many scientific questions it is not essential to approximate the resolution limit of the CLSM system, while other requirements are important and can also be matched with smaller micrograph sizes.

The optical sectioning properties of CLSM make 3D analyses of specimens possible. For this purpose, micrographs of a defined number of optical sections, which are uniformly distributed along the  $z$ -axis and cover the whole structures of interest, are created (Figure 4.3). The resulting micrograph stack can be processed with methods identical to those performed with 3D data obtained from other 3D imaging techniques such as computer tomography. A very common method for displaying 3D data is the maximum intensity projection (MIP), a volume rendering method (Figure 4.3a). To create this pseudo-3D visualization the voxels (volumetric picture elements, each representing a value on a regular grid in a three-dimensional space) with the maximum intensities along parallel axes from the viewpoint to the projection plane are projected in the visualization plane. MIPs provide a good 3D impression of the morphology of the analyzed structures, which is adequate for many applications. If it is necessary to perform precise measurements, calculations, or simulations with the 3D data, different types of 3D models can be created (e.g., Figure 4.3b–f).

As for the micrograph size (number of pixels in the  $xy$ -direction) of the optical sections, it is also important to meet the Nyquist–Shannon sampling theorem when collecting data in the  $z$ -direction. To achieve maximum resolution in the  $z$ -direction when creating a micrograph stack with CLSM, the distance between the centers (focal planes) of two consecutive optical sections must be at least half the thickness of the respective optical sections. Again, to decrease the scanning time, this distance can be increased to reduce the number of micrographs per stack. However, this should only be done if it is not necessary to create a precise 3D model afterwards. For the creation of MIPs it is often not problematic to reduce the number of micrographs below that necessary according to the Nyquist–Shannon sampling theorem. In any case this has to be done carefully as such a reduced micrograph number can sometimes cause artifacts also in MIPs.



**Figure 4.3** Part of a CLSM z-stack and examples of pseudo-3D and 3D visualizations created from this z-stack. The 15 small micrographs in the upper section of the figure are a part of a z-stack consisting of 179 optical sections covering a

complete mandibular gnathobase of the marine cyclopoid copepod *Acanthocyclops mirnyi*. (a) Maximum intensity projection, (b) isosurface model, and (c–f) smoothed isosurface model shown from different angles. Scale bar = 20  $\mu\text{m}$ .

With respect to the signal intensities and micrograph qualities, it is also important to take care of the embedding and immersion media. Usually, several components (e.g., tissue of the specimen, embedding medium, cover slip, immersion medium, glass of the objective) form the complete optical system. In general, if light passes

the border between different materials or substances with different refractive indices reflection and refraction will take place. The larger the differences between the refractive indices the more pronounced these effects are. Accordingly, to achieve good signal intensities and micrograph qualities it is important to choose embedding and immersion media and cover slips whose refractive indices are as close as possible to the refractive index of the glass of the objective lenses. Often, immersion oil with a refractive index identical to that of the glass is used as immersion medium, and several potential embedding media with the same refractive index have been developed so far. However, in many situations the properties of the preparations demand specific embedding media (e.g., water or certain buffers for the visualization of live specimens) with other refractive indices resulting in decreased signal and micrograph qualities. When precise and reliable 3D analyses are desired it is very important to avoid mismatches between the refractive indices of the embedding and the immersion media (Egner and Hell, 2006). If such a mismatch exists the movement of the objective with constant intervals along the z-axis will result in increasing or decreasing (depending on the ratio of the refractive indices) z-axis intervals between the respective focal planes, causing axial distortion in the 3D data set. For exactly known refractive indices this effect can be mathematically determined and removed from the data set after the micrograph acquisition. However, it is generally recommended that this effect is avoided by using embedding and immersion media having identical refractive indices. As a negative result of this, in situations in which the application of embedding media with relatively low refractive indices (e.g., water) is essential, losses in the signal and micrograph qualities have to be accepted. But in most cases the latter effect is negligible and compensated for by the clearly improved quality of the 3D information.

In the framework of analyses of internal structures the thickness and the transparency of the preparations have a considerable impact on the CLSM results. If the preparations are too thick or not transparent enough (or a combination of both) refraction and absorption effects will result in poor quality signals coming from the deeper layers in the preparation part located opposite the lasers. In practice, good signal qualities and good signal yield are often limited to the upper 100–200  $\mu\text{m}$  of the preparations.

As mentioned above, both laser light reflected by the specimen and fluorescence light originating in the specimen can be used for CLSM visualizations. In the following sections respective visualizations of the morphology of marine organisms will be demonstrated using selected examples.

#### 4.4

#### Using Autofluorescences for Detailed Three-Dimensional Morphological Imaging

A considerable variety of substances and materials present in a large number of organisms exhibits autofluorescences. In the context of many fluorescence microscopy applications such autofluorescences can interfere with the results

and are, therefore, unwanted. However, at the same time, if they are sufficiently intensive they can be successfully applied for effective microscopic analyses.

In general it is advisable to test all species of interest for autofluorescences at the start of the analyses. To increase the chance of finding such autofluorescences all laser lines available should be applied successively, and it should be ensured that each of the excited autofluorescences is completely visualized by using either appropriate long-pass filters or, in case of a spectral detection system, a broad detection range. Such settings are often very appropriate for visualizations of complete specimens. However, if specimens exhibit different intensive autofluorescences it might be of interest to visualize a combination of these or a combination of autofluorescences and the fluorescences of dyes (see below). For such situations it is necessary to gain information about the spectral properties of the autofluorescences, and then the detection can be refined by adjusting the selection of the emission filters or the settings of the spectral detection system to the autofluorescence properties. Spectral detection systems enable the user to perform so-called lambda scans, which provide detailed information about the spectral properties of fluorescences. With the results it is possible to specifically detect the autofluorescences and the fluorescences of dyes.

Only a few autofluorescences have been investigated in detail so far. Among those present in marine organisms, the chlorophyll autofluorescences are well known and widely applied to visualize the chloroplasts of algae cells. Typically, the excitation and emission maxima of the combined autofluorescences of different algae chlorophylls are located in the blue and red parts of the light spectrum, respectively. They can easily be detected in both live and dead cells (Figures 4.4a,c,d,f and 4.6b,d,e below). Besides the chlorophylls, algae contain additional pigments, some of them being specific for single algae taxa and having autofluorescence properties different from those of the chlorophylls. Because the excitation and emission spectra of the chlorophylls and of many other important pigments are known in detail (e.g., French and Young, 1952; French *et al.*, 1956) different algae taxa can be visualized separately by choosing appropriate excitation wavelengths and emission detection ranges.

Among the arthropods, the exoskeletons of many taxa also exhibit intensive autofluorescences. In recent years several studies have demonstrated that these autofluorescences allow for precise CLSM visualizations (e.g., Zill *et al.*, 2000; Klaus, Kulasekera, and Schawaroch, 2003; Schawaroch, Grimaldi, and Klaus, 2005; Klaus and Schawaroch, 2006; Michels, 2007; Michels and Gorb, 2012). In the field of marine biology, the application of the respective methods can contribute significantly to morphological analyses of crustaceans, which play important roles in many marine ecosystems and food webs and are, therefore, the subject of a large variety of studies. Even relatively thin exoskeletons such as those often found in, for example, calanoid and cyclopoid copepods can be efficiently visualized based on autofluorescences, resulting in precise 3D models of the structures of interest (Figure 4.3). However, an occasional problem is the occurrence of pronounced differences in the autofluorescence intensities between different parts of the exoskeletons caused by differences in the thickness and the density of the

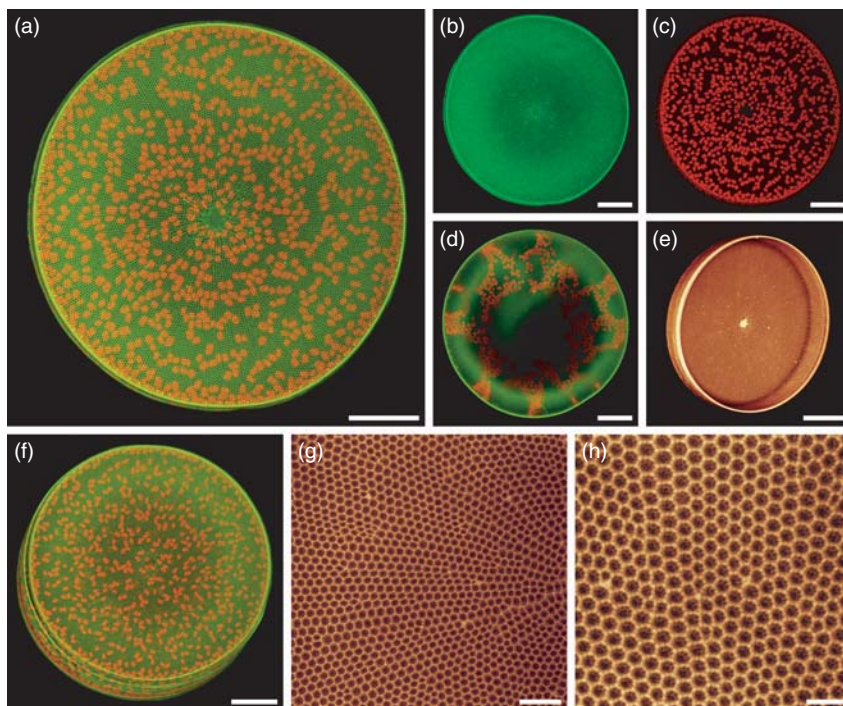


**Figure 4.4** Confocal laser scanning micrographs showing frustules and chloroplasts of the marine diatom *Coscinodiscus wailesii*. (a–c, e–h) MIPs, (d) optical section. (a, d, f) Overlays of the autofluorescence of the chloroplasts (red) and the PDMPO fluorescence (excited with 405 nm) of the stained frustules (green) of living diatoms. (b) Frustule from (a) illustrated separately. (c) Chloroplasts from (a) illustrated separately.

(d) Exposure to laser light with too high intensities stressed the diatom cell, which is indicated by the abnormal distribution of the chloroplasts. (e, g, h) Isolated and cleaned frustules stained in living diatoms with the fluorescence dye rhodamine 19. The fluorescence of rhodamine 19 is shown in the glow mode of the software Leica LAS AF. Scale bars = (a–f) 50, (g) 10, and (h) 5  $\mu\text{m}$ .

respective exoskeleton material. In such situations, sometimes oversaturation of signals coming from single parts of the specimens has to be accepted to successfully visualize the whole specimens (see, for example, Figure 4.5a,b).

The maximum resolution of CLSM is much lower than that of scanning electron microscopy (SEM), but at relatively low magnifications the results obtained with both techniques are comparable in terms of structure detail information (see below). Compared to SEM, CLSM visualizations using autofluorescences have two significant advantages: (i) Most of the preparation methods are much easier and much faster. For example, in case of CLSM analyses of whole specimens the only working step is to transfer these specimens to the embedding medium and place a cover slip on top of them. (ii) The specimens can be visualized in a non-invasive and non-damaging way. For a large variety of applications glycerin or a mixture of glycerin and water have proved to be very appropriate (e.g., Michels, 2007;



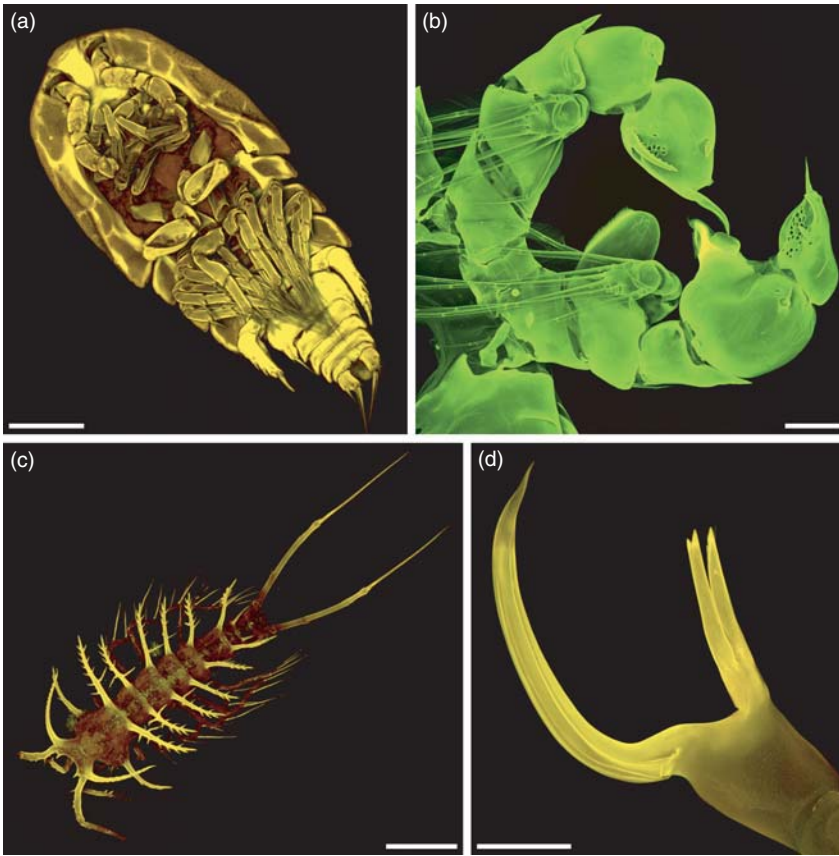


**Figure 4.5** CLSM MIPs showing overlays of different autofluorescences present in the exoskeleton of marine copepods. (a) Ventral view of the harpacticoid copepod *Alteutha potter*. (b) Pair of fifth swimming

legs of a male calanoid copepod *Heterorhabdus* sp. (c) Dorsal view of the harpacticoid copepod *Ceratonotus steiningeri*. (d) Mandibular gnathobase of *Heterorhabdus* sp. Scale bars = (a) 200 and (b–d) 100  $\mu\text{m}$ .

Michels and Gorb, 2012). The application of such embedding media does not harm the specimens and allows for removing and cleaning them from the medium after CLSM visualization. This enables the user to include the same specimens in other analyses afterwards. Furthermore, rare or unique museum specimens can be analyzed and returned without any alteration.

In addition to morphological imaging, the autofluorescences also permit analyses of material compositions (Michels, 2007; Michels and Gorb, 2012). However, such analyses have to be performed with great care because the sources and the properties of many autofluorescences are not yet known. For example, the autofluorescences observed in arthropod exoskeletons have, with one exception, not yet been analyzed in an absolutely certain way. Only the autofluorescence properties of resilin, a very elastic and flexible protein found in many arthropod exoskeleton structures

(e.g., Weis-Fogh, 1960; Andersen and Weis-Fogh, 1964), are known in detail (e.g., Andersen, 1963). Accordingly, the presence of resilin can be reliably determined by specifically visualizing its typical autofluorescence (shown below in Figures 4.7a and 4.8a). In contrast, for the sources of other autofluorescences found in arthropod exoskeletons only a few indications are known. It seems that the autofluorescences of strongly sclerotized chitinous materials are mainly excited by green to red light, with the emission being mainly in the red part of the light spectrum, while less sclerotized or non-sclerotized chitinous materials exhibit mainly green autofluorescences with excitation maxima located in the blue to green part of the light spectrum (Michels and Gorb, 2012). If different autofluorescences are detected separately and the resulting fluorescence micrographs are overlaid differences in the autofluorescence composition will indicate differences in the material composition (e.g., Figure 4.5c,d). In the case of such analyses it is essential that for each of the autofluorescences the signal is detected with maximum intensity while simultaneously any oversaturation is avoided. Otherwise, the visualization of proportions of the different materials would bear the risk of not being in accordance with the real material composition (e.g., Figure 4.5a,b). In addition, to obtain reliable results, for such analyses only fresh specimens should be used because to date the influence of fixation chemicals on the properties of the autofluorescences has not been investigated.

#### 4.5

#### Application of Fluorescence Dyes

In the framework of many studies and analyses the autofluorescences present in organisms are not intensive enough for successful visualizations. In such situations, fluorescence dyes, which today exist in a great diversity (Tsien, Ernst, and Waggoner, 2006; Johnson, 2006), can be used instead. This allows for selective fluorescence labeling of structures, tissues, cell compartments, substances, and physiological processes of interest. In the following, some examples are described of the application of fluorescence dyes in combination with CLSM for morphological analyses of marine organisms.

Diatoms dominate the phytoplankton in many ocean areas and contribute significantly to biogeochemical processes in marine ecosystems. For this reason it is of great interest to intensively study a wide variety of different aspects of diatom biology and physiology. For numerous geological, biological, and biomechanical investigations detailed knowledge of diatom frustule formation, morphology, and architecture is of importance. In recent years several studies have demonstrated the great potential of the fluorescent dye 2-(4-pyridyl)-5-((4-(2-dimethylaminoethylaminocarbonyl)methoxy)-phenyl)oxazole (PDMPO) for a very efficient and quick incorporation into the newly synthesized frustules of live diatoms (Shimizu *et al.*, 2001; Hazelaar *et al.*, 2005; Leblanc and Hutchins, 2005). In the forming frustules PDMPO is deposited together with freshly deposited silica, resulting in the frustules exhibiting a typical intense green fluorescence (Shimizu *et al.*, 2001). This allows for both live cell imaging of diatoms including their



frustules (Figure 4.4a,b,d,f) and visualizing diatom frustules separated and cleaned from the organic material after the staining procedure. In general, PDMPO can be successfully applied to stain all newly formed structures containing biogenic silica such as siliceous skeletons of radiolarians (Ogane *et al.*, 2010). However, one disadvantage of this dye is that its excitation maximum is located in the UV range of the light spectrum. Today, not many commercial CLSM systems present in institutes and laboratories are equipped with UV lasers. In addition, lasers with a wavelength of 405 nm, which also excites the PDMPO fluorescence (Figure 4.4a,b,d,f), are still infrequent. Accordingly, not all CLSM users have the opportunity to use PDMPO. However, several other dyes, including different rhodamine derivatives, have been proven to efficiently label the silica of newly forming frustules of live diatoms, and the fluorescences of all of these dyes are excited with laser light wavelengths typically available in most CLSM systems (Figure 4.4e,g,h; Li, Chu, and Lee, 1989; Kucki *et al.*, 2006; Descl  s *et al.*, 2008; Annenkov *et al.*, 2010; Kucki and Fuhrmann-Lieker, 2012).

In all the studies mentioned above, live diatoms have been used and the dyes' potential to stain newly forming frustules has been evaluated. However, in many situations it might be of interest to stain the frustules of dead diatom cells or isolated diatom frustules (e.g., from sediment samples). The potential of two rhodamine derivatives to stain readily polymerized silica of diatom frustules was reported some years ago, but no details were described (Hildebrand and Palenik, 2003). Recent studies showed that conjugates of silane coupling agents such as (3-aminopropyl)trimethoxysilane and fluorescence dyes (e.g., fluorescein isothiocyanate) efficiently label the silica of isolated diatom frustules and allow for precise CLSM visualizations and 3D modeling (Friedrichs, Maier, and Hamm, 2012; Friedrichs, 2013). Furthermore, in an analysis of the material composition of copepod gnathobases a respective staining method was successfully applied to stain silica (Michels, Vogt, and Gorb, 2012), indicating that such conjugates label all structures containing biogenic silica.

Besides diatoms, dinoflagellates represent another important group of marine unicellular algae. Among them, armored forms feature a so-called theca consisting of cellulose plates, which can be labeled with the fluorescence dye Fluorescent Brightener 28 (synonym: Calcofluor White M2R) (Fritz and Triemer, 1985), a dye known to stain, among other compounds, cellulose and chitin in cell walls (e.g., Maeda and Ishida, 1967; Hughes and McCully, 1975; Herth and Schnepf, 1980). The staining of the dinoflagellate cellulose plates is very efficient (Figure 4.6a–c). In general, Fluorescent Brightener 28 seems to allow for live cell imaging, because concentrations of  $10\text{--}20\text{ }\mu\text{g mL}^{-1}$  within the growth media are reported to be non-toxic for the cells (Fritz and Triemer, 1985). However, the thecae of living motile cells are not stained, which is probably due to the intact outermost membrane preventing contact between the dye and the cellulose plates (Fritz and Triemer, 1985). On the other hand, Fluorescent Brightener 28 stains the cellulose structures of living cysts and those of motile cells with damaged or removed outer membranes enabling the dye to bind to the cellulose (Fritz and Triemer, 1985). Unfortunately, to damage the membranes the cells must be treated harshly, which often causes the

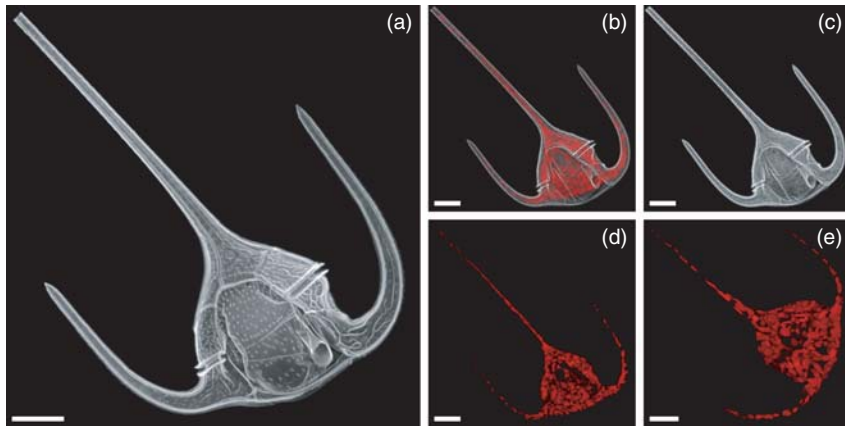


**Figure 4.6** CLSM MIPs showing thecae and chloroplasts of living dinoflagellates of the marine genus *Ceratium*. The thecae were stained with Fluorescent Brightener 28 whose fluorescence was excited with 405 nm and is shown in gray. (a) Detailed view of a theca. (b) Overlay of the Fluorescent Brightener 28 fluorescence of a stained theca and the autofluorescence of the chloroplasts

(red). (c) Theca from (b) illustrated separately. (d) Chloroplasts from (b) illustrated separately. After the staining, the cell was still alive. However, compared to the chloroplasts of an unstained *Ceratium* sp. (e), the chloroplasts of the stained *Ceratium* sp. (d) looked slightly degenerated, indicating that the cell had been harmed by the staining procedure. Scale bars = 25  $\mu\text{m}$ .

cells' death and leads to alteration of intracellular structures such as chloroplasts (Figure 4.6b,d). Accordingly, live cell imaging of motile dinoflagellates is very difficult. By contrast, the analyses of fixed cells (e.g., with glutardialdehyde) yield good results (Fritz and Triemer, 1985). Like PDMPO, Fluorescent Brightener 28 has the disadvantage that its excitation maximum is located in the UV range of the light spectrum. The fluorescence of Fluorescent Brightener 28 can also be excited with 405 nm laser light (Figure 4.6a–c), but this is not as effective as excitation with UV light. For this reason it might be of interest to use other dyes. In this context, a potential dye might be Congo red, because it has been reported to efficiently stain cellulose fibers in plant cell walls (Frey-Wyssling, 1976). Unfortunately, up to now its potential to stain the thecae of dinoflagellates has not been analyzed.

As mentioned above, marine crustaceans are extensively studied because they play important roles in marine ecosystems. The exoskeleton autofluorescences of many species are relatively weak and, therefore, do not allow for successful CLSM visualizations of the external morphologies. In such situations, there are different options to solve this problem. In some studies complete specimens have been stained with non-specific or not completely specific fluorescence dyes, for example with DiI, a lipophilic membrane dye, which stains cell membranes and enables the user to visualize whole organisms (e.g., Carotenuto, 1999; Zupo and Buttino, 2001; Buttino *et al.*, 2003). However, in the case of arthropods this is not efficient, because dyes such as the latter one do not completely stain the exoskeletons. As a result the external shape of the specimens is badly resolved, especially when the exoskeletons

are relatively thick, and the fluorescence of many of the stained internal structures (e.g., muscles) can be dominant in the resulting MIPs. To avoid this, the soft tissues can be digested using, for example, KOH, and the remaining exoskeleton can be precisely visualized with a non-specific fluorescence dye (e.g., Maruzzo, Minelli, and Fusco, 2009). A fluorescence dye, which was found to have a good potential for staining copepods, enabling taxonomic analyses of the exoskeleton using CLSM, is acid fuchsin (Kottmann *et al.*, 2012). However, the staining properties involved have not been evaluated yet. Because acid fuchsin stains several different compounds and tissues, a respective study is necessary to understand in detail which parts of the copepods are stained.

The exoskeleton material of arthropods contains, with only a few exceptions, high proportions of chitin. Therefore, when analyzing the morphology of crustacean exoskeletons it is recommended to use a fluorescence dye, which specifically labels chitin. For this, the chitin-binding probe (available from New England Biolabs, Ipswich, USA), a recombinant fusion protein that binds specifically to chitin, can be used. However, little experience in staining arthropod exoskeletons with this probe exists. Furthermore, the production and application of the chitin-binding probe are relatively time-consuming. For these reasons, it is generally preferable to use the fluorescent dye Congo red, which has been shown to successfully stain chitin in the exoskeleton of crustaceans and in the cuticle of polychaetes (Figures 4.7 and 4.8a;

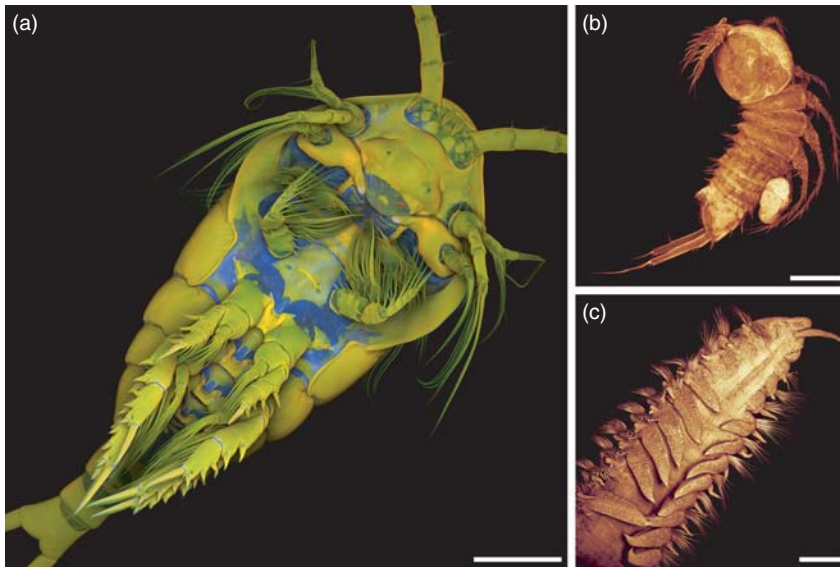


**Figure 4.7** CLSM MIPs showing marine copepods and a marine polychaete stained with Congo red. (a) Ventral view of the calanoid copepod *Temora longicornis*. The Congo red fluorescence is shown in yellow, and the autofluorescence of resilin is shown in blue. (b) Lateral view of a harpacticoid

copepod of the genus *Mesocletodes*. (c) Ventral view of a polychaete of the genus *Aricidea*. In (b) and (c) the fluorescence of Congo red is shown in the glow mode of the software Leica LAS AF. Scale bars = (a) 200, (b) 100, and (c) 250  $\mu\text{m}$ .

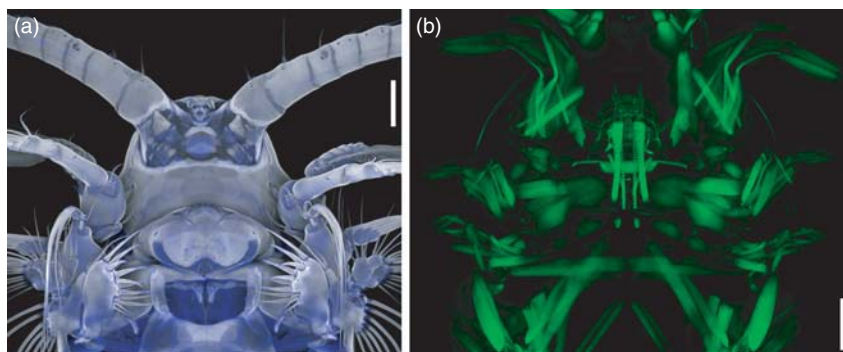


**Figure 4.8** CLSM MIPs illustrating the staining of different components of the marine calanoid copepod *Centropages hamatus*. (a) Ventral view of the anterior part of a specimen stained with Congo red. The fluorescence of the dye is shown in gray, and the autofluorescence of resilin is shown in blue.

(b) Ventral view of the anterior part of the muscle system of a specimen stained with a conjugate of phalloidin and the fluorescence dye tetramethylrhodamine-5-(and-6)-isothiocyanate. The fluorescence of the dye is shown in green. Scale bars = 75  $\mu\text{m}$ .

Michels and Büntzow, 2010). Congo red is very easily and rapidly applied (Michels and Büntzow, 2010), and the fluorescence of the stained structures is rather stable and allows for long scanning times. These properties make Congo red a very suitable dye for detailed CLSM analyses of the exoskeleton morphology within taxonomic studies. Furthermore, the fluorescence of Congo red can efficiently be visualized in combination with that of other dyes and with autofluorescences to obtain information about the material composition of arthropod exoskeleton structures (Figures 4.7a and 4.8a; Michels and Gorb, 2012; Michels, Vogt, and Gorb, 2012). Bacterial chitinases labeled with fluorescence dyes were shown to efficiently stain chitin in aquatic fungi due to a chitin-binding domain (Wurzbacher and Grossart, 2012). In this study chitin present in other organisms, including zooplankton, was also stained. However, the staining of crustacean exoskeletons has not been assessed in detail so far.

In the following, a few additional examples are described of applications of fluorescence dyes for CLSM imaging of the morphology of marine organisms. However, owing to space constraints only a small overview is given. One common and important application is the staining of F-actin using phalloidin conjugates. Phalloidin is a toxic peptide isolated from the mushroom *Amanita phalloides*. It selectively binds to F-actin in fixed cells, and by using phalloidin conjugated to dyes cell cytoskeletons can be fluorescently labeled. In addition, such conjugates are often applied to visualize muscle systems of organisms (Figure 4.8b; e.g., Müller and Worsaae, 2006; Bergter, Brubacher, and Paululat, 2008; Winchell, Valencia, and Jacobs, 2010; Worsaae and Rouse, 2010). Nervous systems of organisms can be visualized using, for example, monoclonal anti-acetylated  $\alpha$ -tubulin as antibody, which can be labeled with a second fluorescing antibody (e.g., Winchell, Valencia, and Jacobs, 2010; Worsaae and Rouse, 2010). 4',6-diamidino-2-phenylindole

(DAPI) is commonly used to stain DNA and visualize bacteria cells (e.g., Davidson *et al.*, 2004; Garneau *et al.*, 2009; Romanova and Sazhin, 2011) and cell nuclei (e.g., Worsaae and Rouse, 2010). This enables the user to show the overall morphology of organisms. DAPI simply has to be put into the embedding medium together with the specimens, making it very easy to apply this dye. A disadvantage of DAPI is that its excitation maximum is also located in the UV range of the light spectrum so that not all CLSM users can apply it (see above). As alternatives other nucleic acid staining dyes are available. Among them are TOTO<sup>®</sup>-3 iodide (e.g., Winchell, Valencia, and Jacobs, 2010) and SYTO<sup>®</sup> dyes. The latter are available in several versions with several different excitation and emission properties so that the selection of the dye can be adjusted to the imaging needs. SYTO<sup>®</sup> dyes are known to efficiently stain bacteria (e.g., Davidson *et al.*, 2004; Romanova and Sazhin, 2011). Among the different SYTO<sup>®</sup> versions, SYTO<sup>®</sup> 9 is often used in combination with propidium iodide (e.g., Davidson *et al.*, 2004; Romanova and Sazhin, 2011). While SYTO<sup>®</sup> 9 penetrates and stains both live and dead bacteria cells with intact and damaged membranes, propidium iodide penetrates only dead bacteria cells with damaged membranes. This enables the user to distinguish between live and dead bacteria.

Today, studies on the influence of ocean warming and acidification on marine organisms have become very important. In this context, the visualization of calcium carbonate structures is often of interest. The fluorescence dye calcein, which binds to calcium and is incorporated into newly forming calcium carbonate structures, can be used to visualize the morphology and development of such structures in living organisms (e.g., Moran, 2000; Tambutte *et al.*, 2012).

#### 4.6

#### Surface Topography Analyses

In recent years CLSM has also become a frequently used technique in materials science. In this scientific discipline CLSM has the potential for several different applications (Hovis and Heuer, 2010), the most common being analyses of surface topographies. By contrast, in biological science disciplines such analyses are not yet prevalent although many potential applications are conceivable. In the following, the methodological prerequisites of CLSM topography analyses of biological surfaces are described.

Fluorescence light can generally be used for surface topography analyses. However, in many situations this is not suitable because either the fluorescence intensity is not high enough or the bleaching of the fluorescence is too intense to yield good results (or even both effects are present in combination). Furthermore, compared to deeper tissue layers, the outermost tissue layers of specimens often exhibit lower fluorescence intensities, making precise analyses of the surface topography very difficult or sometimes even impossible. As already mentioned, besides fluorescence light the laser light reflected from the specimens can be used for CLSM visualizations. In general, all structures with good reflective properties can be successfully visualized in this way, and for surface topography analyses the use of reflected

laser light commonly is the method of choice. In transparent specimens, internal surfaces with suitable reflective properties can be analyzed, but most investigations typically focus on outer surfaces.

The investigated surfaces must exhibit a pronounced reflectivity. Although surfaces of transparent samples can be successfully analyzed, transparency often causes problems. For example, when analyzing the surface topography of diatom frustules a considerable proportion of the laser light is transmitted into the transparent frustules. Owing to the frustules' complex geometries, this light is reflected at the frustule boundaries in various different directions, often resulting in interferences, which affect the detected signal. In such a situation it is necessary to increase the reflectivity of the outer surfaces. In general, the larger the proportion of the light reflected at the surface and the smaller the proportion of the light transmitted into the specimen the higher are the efficiency and the quality of the surface topography analyses. The reflectivity can be enhanced by sputter-coating the specimens with metal layers. For example, the snail shell and the diatom frustules shown in Figure 4.9 were sputter-coated with a gold palladium (80/20) layer. While for the snail shell a 20 nm thick layer proved to be very suitable, the diatom frustules had to be coated with a 50 nm thick layer to yield good results. In this context it is very important to ensure that the thickness of the coating is not too large compared to the surface structures. Otherwise, the results of the surface topography analyses would be affected and would no longer be correct.

When trying to improve the reflectivity of outer specimen surfaces the embedding medium is also important. Surface topography analyses of specimens embedded in media such as water, glycerin, and immersion oil are generally possible and can yield good results. Sometimes, however, the application of air embedding is necessary. If light hits an interface between two media with different refractive indices a certain proportion of this light will be reflected at the interface, and the rest of the light will be transmitted into the second medium. The larger the difference between the refractive indices of the two media involved the larger is the proportion of the light reflected at the interface (e.g., Pedrotti, Pedrotti, and Pedrotti, 2006). As the refractive index of air shows a greater difference from those of most biological materials than those of, for example, water or glycerin, it can be of advantage to dry the specimens and analyze them in air. For this, specific objectives designed for air immersion and preparations without a cover slip are available. However, this will of course only be reasonable if the specimens do not tend to exhibit drying artifacts. If the specimens possess low transparency and their outer surfaces are very reflective it will be advantageous to embed them in media with higher refractive indices. This allows for the application of objectives with higher numerical apertures and provides the opportunity to perform surface topography analyses with higher resolutions.

In an optimal situation, the reflectivity properties of the specimen are so good that just one single surface, which is the surface of interest, reflects the light. The CLSM analysis system can then provide a resolution in the *z*-direction, which is much higher than according to the Rayleigh criterion in situations when two light points have to be separated from each other by the optical system (Hovis and



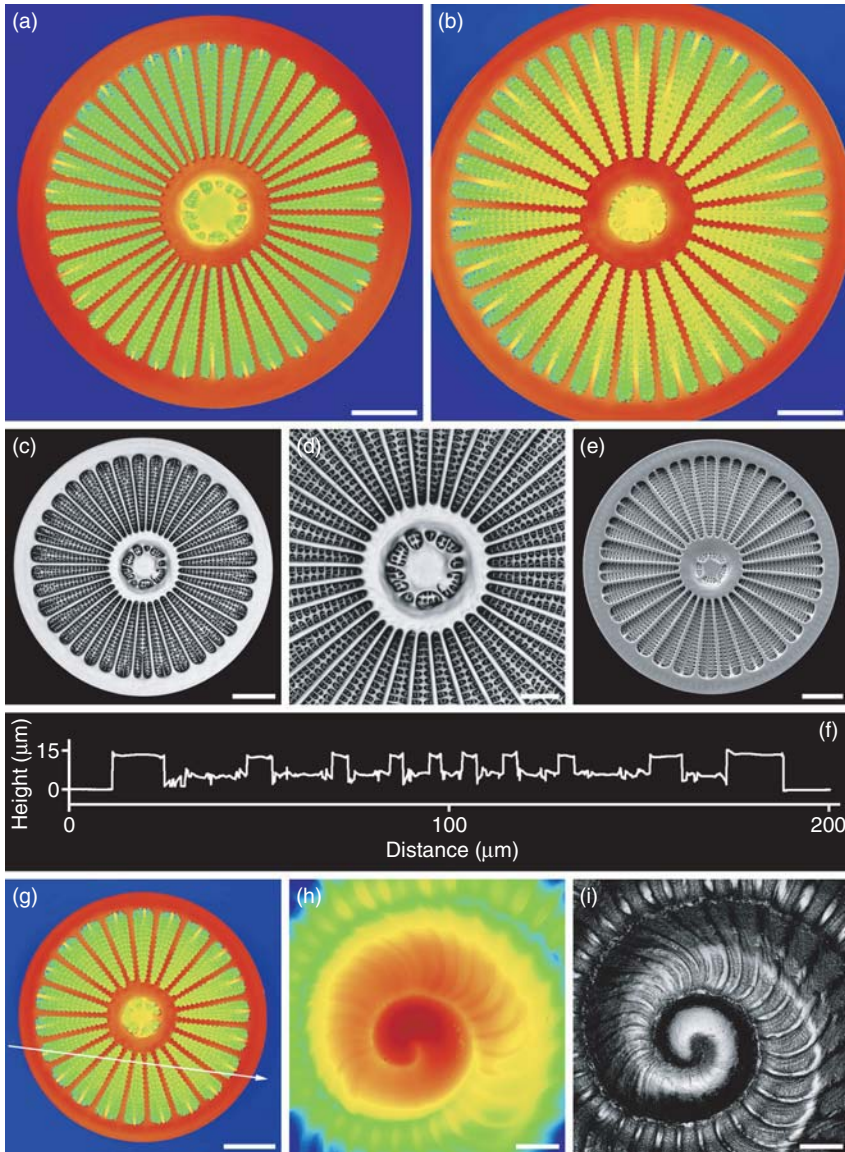


**Figure 4.9** CLSM analyses of the surface topography of diatom frustules and a snail shell. (a–e, g) Frustules of marine diatoms of the genus *Arachnoidiscus*. (h, i) Protoconch of the shell of the marine snail *Tornus subcarinatus*. (a, b, g, h) Color-coded height maps, (c, d, i) MIPs, (e) scanning electron micrograph (Courtesy of Lars Friedrichs/Alfred-Wegener-Institut), and (f)

height profile along the arrow shown in (g). The height maps illustrate the different heights of the surface structures with a color code ranging from blue via green, yellow, and orange to red representing heights between  $0\mu\text{m}$  (dark blue) and maximum values (dark red) of  $14.87\mu\text{m}$  (a),  $15.81\mu\text{m}$  (b),  $15.85\mu\text{m}$  (g), and  $215.23\mu\text{m}$  (h). Scale bars = (a–c, e, g)  $40$ , (d)  $20$ , and (h, i)  $100\mu\text{m}$ .

Heuer, 2010). To determine the exact  $z$ -position of the surface the system just has to detect the  $z$ -position with the highest signal intensity. The latter can be achieved with a precision similar to that of the microscope's focus system. For example, in upright microscopes focusing is performed by moving the stage. Accordingly, the precision of measuring the  $z$ -dimensions of a specimen depends on the precision of the stage control system, which can be in the range of a few tens of nanometers. To allow for the application of this precision it is necessary to adapt the properties of both the optical sectioning and the  $z$ -stack collection of the CLSM system by making the optical sections thin enough and decreasing the distance between the centers of consecutive optical sections within the micrograph stack. For this, the use of a pinhole size of 0.3 AU and a  $z$ -distance, which is a quarter of the thickness of the respective optical sections, is recommended. As a result, the optical sections are very thin and the amounts of light detected from each optical section are rather small. However, despite this, the signal qualities are still high because of the relatively high intensity of the laser light.

Another aspect, which requires attention, is the adjustment of the detected signal. In the context of surface topography analyses it is absolutely necessary to avoid any oversaturation. This is because oversaturated signals would result in the loss of information about the respective surface structures. Accordingly, the surface areas concerned would not be visualized correctly, and the results would not be consistent with the real conditions.

If all the aspects described above are considered and the imaging setup is well-adjusted the analyses will provide detailed information about the surface topography and enable precise measurements of the surface structures in 3D (Figure 4.9). Furthermore, based on the results, standard parameters (e.g., surface roughness parameters), which are well established to describe and compare the properties of surfaces, can be calculated. Besides color-coded height maps, which are typically used to display the results of surface topography analyses (Figure 4.9a,b,g,h), MIPs can be created from the results (Figure 4.9c,d,i). The structural information obtained from such MIPs is similar to that obtained from comparable scanning electron micrographs created at relatively low magnifications (Figure 4.9c–e).

#### 4.7

#### Future Perspectives

Although CLSM has, as demonstrated, great potential for efficient and precise morphological imaging of marine organisms and can be used in a large variety of scientific contexts, the number of projects with respective CLSM applications is still relatively small. However, in recent years, knowledge of CLSM and its potential applications has increased and spread considerably in the scientific community, and many of the scientific institutions in the field of marine biology have become equipped with confocal laser scanning microscopes. Accordingly, today, many marine biologists have access to CLSM systems. In addition, the CLSM producing companies have greatly improved the operating software of the modern commercial



CLSM systems to make it more user-friendly and to enable inexperienced users to also successfully apply CLSM and yield good scientific results. Consequently, it is very likely that CLSM will be applied more often and gain more importance for morphological studies in marine biology in the near future. This chapter will hopefully contribute to such a development.

## Acknowledgements

I am very grateful to Lars Friedrichs, Verónica Fuentes, Kai Horst George, Christian Hamm, Gritta Veit-Köhler, Melanie Kucki, Ira Richling, and Sigrid Schiel for providing samples. Olga Lévai and Winfried Goltz enabled me to test a then-new CLSM system from Leica Microsystems GmbH. Lars Friedrichs provided the scanning electron micrograph of the *Arachnoidiscus* sp. frustule.

## References

- Amos, W.B., White, J.G. (2003) How the confocal laser scanning microscope entered biological research. *Biol. Cell* **95**, 335–342.
- Andersen, S.O. (1963) Characterization of a new type of cross-linkage in resilin, a rubber-like protein. *Biochim. Biophys. Acta* **69**, 249–262.
- Andersen, S.O., Weis-Fogh, T. (1964) Resilin. A rubberlike protein in arthropod cuticle. *Adv. Insect Physiol.* **2**, 1–65.
- Annenkov, V.V., Danilovtseva, E.N., Zelinskiy, S.N., Basharina, T.N., Safonova, T.A., Korneva, E.S., Likhoshway, Y.V., Grachev, M.A. (2010) Novel fluorescent dyes based on oligopropylamines for the in vivo staining of eukaryotic unicellular algae. *Anal. Biochem.* **407**, 44–51.
- Bergter, A., Brubacher, J.L., Paululat, A. (2008) Muscle formation during embryogenesis of the polychaete *Ophryotrocha diadema* (Dorvilleidae) – new insights into annelid muscle patterns. *Front. Zool.* **5**, 1.
- Buttino, I., Ianora, A., Carotenuto, Y., Zupo, V., Miralto, A. (2003) Use of the confocal laser scanning microscope in studies on the developmental biology of marine crustaceans. *Microsc. Res. Tech.* **60**, 458–464.
- Carotenuto, Y. (1999) Morphological analysis of larval stages of *Temora stylifera* (Copepoda, Calanoida) from the Mediterranean Sea. *J. Plankton Res.* **21**, 1613–1632.
- Centonze, V., Pawley, J.B. (2006) in: *Handbook of Biological Confocal Microscopy*, (ed. J.B. Pawley), 3rd edn, Springer, New York, pp. 627–649.
- Davidson, A.T., Thomson, P.G., Westwood, K., van den Enden, R. (2004) Estimation of bacterioplankton activity in Tasmanian coastal waters and between Tasmania and Antarctica using stains. *Aquat. Microb. Ecol.* **37**, 33–45.
- Desclès, J., Vartanian, M., El Harrak, A., Quinet, M., Bremond, N., Sapriel, G., Bibette, J., Lopez, P.J. (2008) New tools for labeling silica in living diatoms. *New Phytol.* **177**, 822–829.
- Egner, A., Hell, S.W. (2006) in: *Handbook of Biological Confocal Microscopy*, (ed. J.B. Pawley) 3rd edn, Springer, New York, pp. 404–413.
- French, C.S., Smith, J.H.C., Virgin, H.I., Airth, R.L. (1956) Fluorescence-spectrum curves of chlorophylls, pheophytins, phycoerythrins, phycocyanins and hypericin. *Plant Physiol.* **31** (5), 369–374.
- French, C.S., Young, K.V. (1952) The fluorescence spectra of red algae and the transfer of energy from phycoerythrin and chlorophyll. *J. Gen. Physiol.* **35** (6), 873–890.
- Frey-Wyssling, A. (1976) *The Plant Cell Wall. Encyclopedia of Plant Anatomy III*, Gebrüder Borntraeger, Berlin, Stuttgart, pp. 1–294.

- Friedrichs, L. (2013) A simple cleaning and fluorescent staining procedure for recent and fossil diatom frustules. *Diatom Res.* **28** (3), 317–327.
- Friedrichs, L., Maier, M., Hamm, C. (2012) A new method for exact three-dimensional reconstructions of diatom frustules. *J. Microsc.* **248** (2), 208–217.
- Fritz, L., Triemer, R.E. (1985) A rapid simple technique utilizing Calcofluor White M2R for the visualization of dinoflagellate thecal plates. *J. Phycol.* **21** (4), 662–664.
- Garneau, M.-E., Vincent, W.F., Terrado, R., Lovejoy, C. (2009) Importance of particle-associated bacterial heterotrophy in a coastal Arctic ecosystem. *J. Mar. Syst.* **75**, 185–197.
- Hazelaar, S., van der Strate, H.J., Gieskes, W.W.C., Vrieling, E.G. (2005) Monitoring rapid valve formation in the pennate diatom *Navicula salinarum* (Bacillariophyceae). *J. Phycol.* **41**, 354–358.
- Herth, W., Schnepf, E. (1980) The fluorochrome, Calcofluor White, binds oriented to structural polysaccharide fibrils. *Protoplasma* **105**, 129–133.
- Hildebrand, M., Palenik, B. (2003) Investigation into the Optical Properties of Nanostructured Silica from Diatoms. Storming Media, Pentagon Report A266314, pp. 1–7.
- Hovis, D.B., Heuer, A.H. (2010) The use of laser scanning confocal microscopy (LSCM) in materials science. *J. Microsc.* **240** (3), 173–180.
- Hughes, J., McCully, M.E. (1975) The use of an optical brightener in the study of plant structure. *Stain Technol.* **50**, 319–329.
- Inoué, S. (2006) in: *Handbook of Biological Confocal Microscopy*, (ed. J.B. Pawley) 3rd edn, Springer, New York, pp. 1–19.
- Johnson, I.D. (2006) in: *Handbook of Biological Confocal Microscopy*, (ed. J.B. Pawley) 3rd edn, Springer, New York, pp. 353–367.
- Klaus, A.V., Kulasekera, V.L., Schawaroch, V. (2003) Three-dimensional visualization of insect morphology using confocal laser scanning microscopy. *J. Microsc.* **212** (2), 107–121.
- Klaus, A.V., Schawaroch, V. (2006) Novel methodology utilizing confocal laser scanning microscopy for systematic analysis in arthropods (Insecta). *Integr. Comp. Biol.* **46**, 207–214.
- Kottmann, J., Kihara, T.C., Glatzel, T., Veit-Köhler, G. (2013) A new species of *Wellsopsyllus* (Copepoda, Harpacticoida, Paramesochridae) from the deep Southern Ocean and remarks on its biogeography. *Helgol. Mar. Res.*, **67** (1), 33–48.
- Kucki, M., Fuhrmann-Lieker, T. (2012) Staining diatoms with rhodamine dyes: control of emission colour in photonic biocomposites. *J. R. Soc. Interface* **9**, 727–733.
- Kucki, M., Landwehr, S., Rühling, H., Maniak, M., Fuhrmann-Lieker, T. (2006) Light-emitting biological photonic crystals: the bioengineering of metamaterials. *Proc. SPIE* **6182**, 61821S.
- Leblanc, K., Hutchins, D.A. (2005) New applications of a biogenic silica deposition fluorophore in the study of oceanic diatoms. *Limnol. Oceanogr. Methods* **3**, 462–476.
- Li, C.-W., Chu, S., Lee, M. (1989) Characterizing the silica deposition vesicle of diatoms. *Protoplasma* **151**, 158–163.
- Maeda, H., Ishida, N. (1967) Specificity of binding of hexapyranosyl polysaccharides with fluorescent brightener. *J. Biochem.* **62** (2), 276–278.
- Maruzzo, D., Minelli, A., Fusco, G. (2009) Segmental mismatch in crustacean appendages: the naupliar antennal exopod of *Artemia* (Crustacea, Branchiopoda, Anostraca). *Arthropod Struct. Dev.* **38**, 163–172.
- Michels, J. (2007) Confocal laser scanning microscopy: using cuticular autofluorescence for high resolution morphological imaging in small crustaceans. *J. Microsc.* **227** (1), 1–7.
- Michels, J., Büntzow, M. (2010) Assessment of Congo red as a fluorescence marker for the exoskeleton of small crustaceans and the cuticle of polychaetes. *J. Microsc.* **238** (2), 95–101.
- Michels, J., Gorb, S.N. (2012) Detailed three-dimensional visualization of resilin in the exoskeleton of arthropods using confocal laser scanning microscopy. *J. Microsc.* **245** (1), 1–16.
- Michels, J., Vogt, J., Gorb, S.N. (2012) Tools for crushing diatoms – opal teeth in copepods feature a rubber-like bearing composed of resilin. *Sci. Rep.* **2**, 465.

- Minsky, M. (1988) Memoir on inventing the confocal scanning microscope. *Scanning* **10** (4), 128–138.
- Moran, A.L. (2000) Calcein as a marker in experimental studies newly-hatched gastropods. *Mar. Biol.* **137**, 893–898.
- Müller, M.C.M., Worsaae, K. (2006) CLSM analysis of the phalloidin-stained muscle system in *Nerilla antennata*, *Nerillidium* sp. and *Trochonerilla mobilis* (Polychaeta; Nerillidae). *J. Morphol.* **267**, 885–896.
- Ogane, K., Tuji, A., Suzuki, N., Matsuoka, A., Kurihara, T., Hori, R.S. (2010) Direct observation of the skeletal growth patterns of polycystine radiolarians using a fluorescent marker. *Mar. Micropaleontol.* **77**, 137–144.
- Pedrotti, F.L., Pedrotti, L.S., Pedrotti, L.M. (2006) *Introduction to Optics*. 3rd edn, Prentice Hall, Upper Saddle River, NJ, pp. 1–656.
- Romanova, N.D., Sazhin, A.F. (2011) Methodological aspects of the determination of the bacterioplankton number, biomass, and production. *Oceanology* **51** (3), 518–527.
- Schawaroch, V., Grimaldi, D., Klaus, A.V. (2005) Focusing on morphology: applications and implications of confocal laser scanning microscopy (Diptera: Campichoetidae, Camillidae, Drosophilidae). *Proc. Entomol. Soc. Wash.* **107**, 323–335.
- Shimizu, K., Del Amo, Y., Brzezinski, M.A., Stucky, G.D., Morse, D.E. (2001) A novel fluorescent silica tracer for biological silicification studies. *Chem. Biol.* **8**, 1051–1060.
- Tambutte, E., Tambutte, S., Segonds, N., Zoccola, D., Venn, A., Erez, J., Allemand, D. (2012) Calcein labelling and electrophysiology: insights on coral tissue permeability and calcification. *Proc. R. Soc. London, B, Biol. Sci.* **279**, 19–27.
- Tsien, R.Y., Ernst, L., Waggoner, A. (2006) in: *Handbook of Biological Confocal Microscopy*, (ed. J.B. Pawley), 3rd edn, Springer, New York, pp. 338–352.
- Weis-Fogh, T. (1960) A rubber-like protein in insect cuticle. *J. Exp. Biol.* **37**, 889–907.
- Winchell, C.J., Valencia, J.E., Jacobs, D.K. (2010) Confocal analysis of nervous system architecture in direct-developing juveniles of *Neanthes arenaceodentata* (Annelida, Nereididae). *Front. Zool.* **7**, 17.
- Worsaae, K., Rouse, G.W. (2010) The simplicity of males: dwarf males of four species of *Osedax* (Siboglinidae; Annelida) investigated by confocal laser scanning microscopy. *J. Morphol.* **271**, 127–142.
- Wurzbacher, C., Grossart, H.-P. (2012) Improved detection and identification of aquatic fungi and chitin in aquatic environments. *Mycologia* **104** (6), 1267–1271.
- Zill, S., Faith Frazier, S., Neff, D., Quimby, L., Carney, M., DiCaprio, R., Thuma, J., Norton, M. (2000) Three-dimensional graphic reconstruction of the insect exoskeleton through confocal imaging of endogenous fluorescence. *Microsc. Res. Tech.* **48**, 367–384.
- Zupo, V., Buttino, I. (2001) Larval development of decapod crustaceans investigated by confocal microscopy: an application to *Hippolyte inermis* (Natantia). *Mar. Biol.* **138**, 965–973.



## 5

### Optical Projection Tomography

Karl Gaff, Luke McCormac Parker, Dee Lawlor, and Emmanuel G. Reynaud

#### 5.1

##### Introduction

In the Greek language, the word “tomos” can be translated as “section” or “slice.” The definition of the term “*tomography*” from *Merriam-Webster’s Dictionary* is:

“a method of producing a three-dimensional image of the internal structures of a solid object (as the human body or the earth) by the observation and recording of the differences in the effects on the passage of waves of energy impinging on those structures.”

Optical projection tomography (OPT) is an emerging technology that provides a novel approach to recreating three-dimensional (3D) images of small biological specimens. The technique was developed to fill an imaging gap that existed between  $\mu$ MRI ( $\mu$  magnetic resonance imaging) and confocal microscopy. Being most suited to specimens ranging in size from 1 to 10 mm across, the technique is similar to X-ray computed tomography (CT). In this chapter, OPT is explained, its most important applications in biomedical research explored, and comparisons drawn of its pros and cons with respect to various alternative imaging technologies.

#### A Brief History of Optical Projection Tomography

In 2001, Dr James Sharpe of the MRC Human Genetics Unit (HGU) in Edinburgh developed OPT as a new tool to generate a 3D atlas of the genes and proteins in mouse embryos. Since the confocal technique is typically restricted to samples thinner than 200  $\mu$ m, there was no alternative technology to suit his requirements. His only option was the laborious and time-consuming technique of physically sectioning the sample into very fine slices; however, due to the scale of the sample this was, of course, also ruled out. The principle behind OPT technology is not a new idea as this approach had been used for the previous two decades in X-ray CT. The technology, however, had never been employed for optical imaging of

biological samples. Consequently, Sharpe began to build such a system using spare parts lying around the laboratory. He recorded multiple projections of the specimen through different orientations using a low numerical aperture (NA) (large depth of field) lens to gather as much information as possible in a single image. He concluded that his setup could reconstruct 3D images of whole specimens in size range 1–15 mm (Sharpe *et al.*, 2002).

The technique could also be combined with staining methods to label internal structures and, most importantly, the complex genetic activities in different tissues, simultaneously. OPT can image specimens that are too large for conventional confocal microscopy and too small for  $\mu$ MRI. The OPT technique proves to be cost-effective because it is able to image biological structures *in vivo* without damaging the specimen in the process.

## 5.2

### What Is Optical Projection Tomography?

OPT can operate as either emission optical projection tomography (EOPT) or transmission optical projection tomography (TOPT). The two modes can be employed respectively to image fluorescent light emission from excited fluorophores or the magnitude of absorption of transmission light through biological samples (Wang and Wang, 2007).

For EOPT, the specimen is illuminated with a specific frequency of light whose energy provides the threshold energy required to excite the fluorophores of interest in the sample. For example, green fluorescent protein (GFP) possesses a major excitation peak at 395 nm and a minor excitation peak at 475 nm. This means that GFP emits green light with frequencies of 600 THz, corresponding to energies of 3.9 eV, when excited by photons with energies of 5 and 4.18 eV respectively. Therefore, the excitation light source must generate light whose emission spectrum correlates with that of the excitation spectrum of GFP. The resulting detected signal intensity depends on the fluorescence emission intensity arising from the fluorophores, which itself depends on the intensity of the excitation light probing the fluorophores within the tissue structures (Lee *et al.*, 2006).

For TOPT, a broadband lamp situated behind a frosted screen provides a diffuse source of uniform illumination. Projected onto the specimen, this bright field illumination is detected on the opposite side of the specimen, where the intensity depends on the amount of absorbed light. In other words, the resultant image is essentially a projection that is dependent on the attenuation coefficients through the specimen: a “shadow.” Detected by a wide-field objective lens, and ultimately by a camera, the light rays propagate through the specimen in approximately straight lines called *projections*. Analysis software on a computer performs a calculation to measure the degree to which each of the individual rays incident on each pixel has undergone attenuation. This is carried out by measuring the number of photons detected along each projection and then reconstructing either the absorbance or

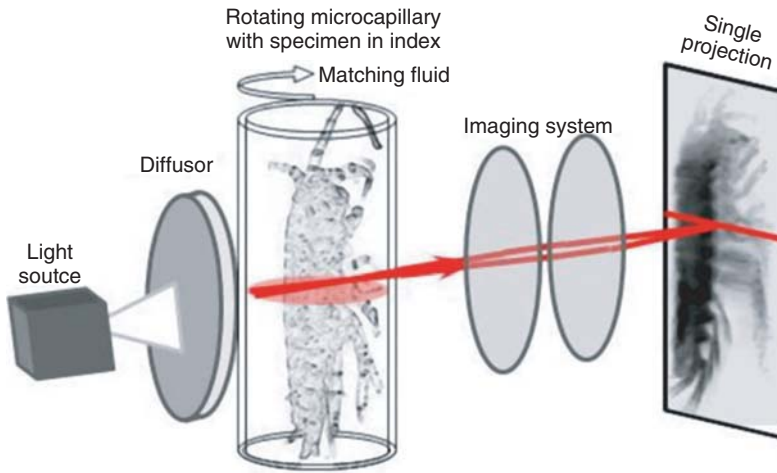


**Figure 5.1** Principle of the application of light to a sample and its detection in optical projection tomography. The light from a light source is transmitted through a diffuser in order to apply a homogeneous illumination to the object of the complete field of view

of the detector sided imaging system. A single projection contributes the data from the whole depth of the sample and, thereby, it already contains full volumetric information. (Reproduced with permission from Heiko Meyer).

emission distribution by performing a back-projection algorithm called the *inverse Radon transform function* (Sharpe, 2004).

The specimen to be visualized is typically embedded in a cylinder of agarose, or in a capillary, as in Figure 5.1, and is strategically positioned at the focal point of the objective lens along the optical axis. The longest axis of the sample is aligned with the axis of rotation and is perpendicular to the optical axis. This orientation provides the shortest optical path through the specimen and is therefore the optimal way of measuring the transmission through the specimen. The depth of field is optimized to cover the region from the center of the object to the edge of the object closest to the objective. The cylinder is precisely fixed in the center of a rotary stage.

A series of 2D optical projections through the specimen are acquired at several different azimuths, from which the 3D structure of the sample can be computationally reconstructed (Swoger and Sharpe). For each successive image that is recorded, TOPT requires that the projection data acquired from specific planes are collected by a linear row of pixels and that the points located along a line parallel to the optical axis should be projected onto the same pixel of the CCD (charge-coupled device) array (Wang and Wang, 2007).

To acquire 2D optical projection images, the sample, is rotated not through  $180^\circ$  as one might expect but through  $360^\circ$ . This is because images that are recorded  $180^\circ$  apart are not mirror images since the depth of focus lies halfway from the center of the specimen to its front edge closest to the objective. This focal region was chosen as a compromise due to the limited depth of field held by all optical



imaging systems. However, this method yields excellent results, not only in terms of image quality but also in maximizing the amount of information obtained in as few images as possible, thereby keeping imaging time to a minimum (Quintana and Sharpe, 2011).

Usually, 400 images are recorded throughout the  $360^\circ$  revolution (one image every  $0.9^\circ$ ). It is apparent, however, that a higher angular resolution would result in a higher image resolution. As with most imaging techniques, a compromise must therefore be met between image resolution, acquisition speed, and processing, and for most practical purposes this is likely to be an angular resolution of approximately  $0.5^\circ$  (Sharpe, 2004).

An infinity-corrected objective lens allows the implementation of auxiliary components, such as a filter wheel or a variable aperture (iris) into the parallel optical path between the objective and the tube lens (Figure 5.2). The infinity-corrected objective lens shapes the diverging light rays into a collimated wave train. For EOPT, an emission filter ensures that only the light within a narrow frequency

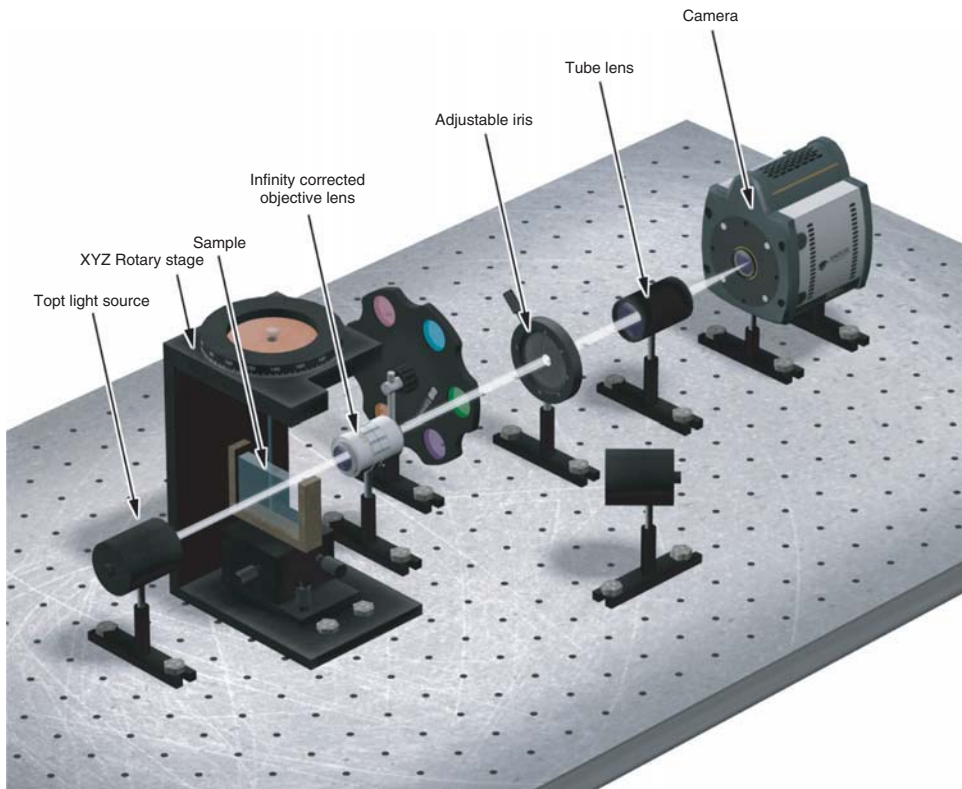


**Figure 5.2** Illustration of the setup for TOPT showing all the components of the OPT configuration.



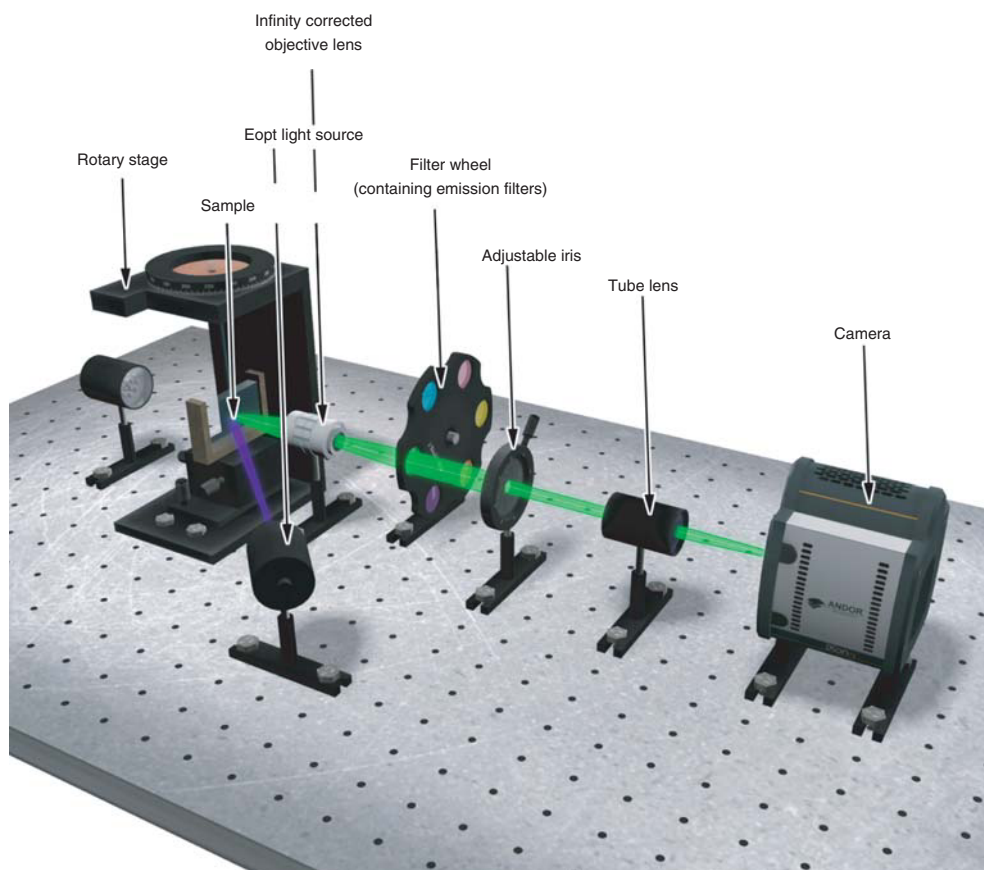


**Figure 5.3** Illustration of the setup for EOPT showing all the components of the OPT configuration.

band corresponding to the fluorophore emission spectrum reaches the detector. The optical configuration for EOPT can be seen in Figure 5.3. An iris positioned between the filter wheel and the tube lens provides control of the effective NA or f-number of the optical system (Wang and Wang, 2007). The tube lens focuses the propagating electromagnetic field onto the photosensitive surface of the camera, which lies in the focal plane of the tube lens.

The sensitive surface of the camera, typically a CCD array, consists of a large number of light sensing elements called *pixels*. These pixels operate as individual photodetectors and respond to incident light via the photoelectric effect. This process results in the liberation of electrons leading to the build up of a charge in the pixel element. In an ideal situation, the generation of photoelectrons is linearly proportional to the number of incident photons. Initially, each pixel in the

sensor array functions as a potential well, storing the electronic charge during the exposure to incident light.

### 5.2.1

#### Assembly of an OPT System

An OPT consists of five basic units. The wide-field objective lens, together with the camera, makes up the detection unit and is essentially a wide-field microscope. There are two illumination units, each consisting of a light source. One source provides transmission illumination, while the other provides the energy to induce fluorescence in the specimen. Both sources contain optical components for shaping the beam as necessary prior to illumination. The sample manipulation unit holds the sample and embedding media and moves it relative to the stationary optical setup. The fourth unit is the control unit that operates the hardware such as the motorized rotary stage, the motorized filter wheel, the camera, and controls the data acquisition process. The opto-mechanical parts are mounted on an optical table, and the whole system can be controlled by a program written in LabVIEW (National Instruments).

##### 5.2.1.1 Detection Unit

The detection unit is similar to that of a conventional wide-field fluorescent microscope. It consists of an objective lens, a filter wheel, an iris, a tube lens, and a camera. To increase the depth of field, the effective NA of the objective can be reduced by means of an iris positioned behind the objective (Sharpe *et al.*, 2002).

An infinity-corrected air objective lens is used (Greger *et al.*, 2007), because the light rays exiting from the rear of the objective are parallel rather than converging, as in finite objectives. To form an image, the light rays need to converge. This is carried out with an additional lens called a *tube lens*. The tube lens focuses the light onto the image plane.

##### 5.2.1.2 Illumination Units

The illumination unit for EOPT uses a beam of light from a lamp assembly. The collimated beam is expanded to the required diameter for the sample under study, by a zoom beam expander.

The illumination unit for TOPT uses a white light source. A piece of frosted glass is inserted at the exit pupil of the lamp assembly so that the geometry of the wave front becomes diffuse, to provide uniform illumination to the sample.

##### 5.2.1.3 Sample Manipulation Unit

Since the optical arrangement is fixed, the sample is centered with its longest axis perpendicular to its axis of rotation prior to scanning. A computer-controlled rotary stage rotates the sample in the plane transverse to the longitudinal axis of the sample.

### 5.2.2

#### Illumination Sources

OPT is often compared to CT as an imaging technology and the main difference between them is that OPT creates an image using visible instead of the X-ray wavelengths of light employed in CT.

The most common source of illumination for OPT is the xenon/mercury bulb. The benefits of xenon light are that they give off a high level of luminance and the light produced is uniform over the lifetime of the bulb. This is a vital characteristic in imaging to ensure continuity. The light generated by xenon bulbs is similar to that of sunlight and can be used to excite a wide variety of fluorophores.

Laser light is the second most commonly used after xenon/mercury. The monochromatic light of a laser is beneficial for the excitation of specific fluorophores. However, for some applications, a regular white incandescent bulb can be used. LEDs (light-emitting diodes) are becoming increasingly popular for lighting and although many microscopy techniques use lasers for illumination, the LED has several advantages – firstly, they are inexpensive and have a low power consumption compared to conventional light sources such as xenon lamps, they have a long life time, and they are readily available and easily replaced (Albeanu *et al.*, 2008). LEDs also come in a wide variety of colors, covering the visible spectrum of wavelengths.

### 5.2.3

#### System Capabilities and Limitations

In previous years, the traditional method for imaging the inner structures of a tissue was to physically section the sample. By imaging successive layers of the sample, a 3D reconstruction could then be compiled. However, this technique is very laborious and time consuming. Novel technologies such as OPT remove the need for physical sectioning of a specimen by using the tomography technique to acquire optical projections from a range of different azimuths to create a 3D virtual reconstruction of the sample. The capabilities of OPT imaging have been invaluable to many fields of biology, particularly developmental biology, gene expression research, and investigating the inner structures of tissues and biological specimens.

The capabilities of OPT for creating a 3D reconstruction are competitive with those of other technologies and it is a relatively easy and affordable technique to use. Imaging can be carried out at up to 10–15 frames per second (Wang and Wang, 2007), which enables the operator to explore the sample and gain good quality, detailed images without having to wait for long periods of time. A limitation of imaging in 3D is that some features can be obscured by others, but the real-time capabilities of the hardware and software can compensate for this. When the sample is imaged with the additional dimension of time, 4D information can be obtained, which makes this technology invaluable in studying embryology and

developmental biology (Boot *et al.*, 2008). Quantitative information such as volume and length can also be obtained using software (Fauver *et al.*, 2005).

In addition to time-lapse 3D reconstructions, gene expression imaging illustrates an extra advantage of OPT. Prior to OPT the location of gene expression could not be investigated without dissecting or mechanically sectioning the sample. But, with the dawn of this novel technology, gene expression in whole embryos can now be imaged using fluorescent or traditional dyes, allowing localization of the distribution of gene activity through 4D imaging (Fisher *et al.*, 2008).

The limitations of OPT are mainly in regard to sample size and penetration. OPT has been optimized to image samples ranging from as small as  $2.82\text{ }\mu\text{m}$  (Fauver *et al.*, 2005) up to 15 mm; anything larger can be imaged with CT. Samples at the larger end of the scale may need to be chemically cleared with an organic solvent. This involves replacing the natural fluids contained within the cells of the tissues with a fluid that matches the optical refractive index with that of the cellular membranes (Fumene Feruglio *et al.*, 2010). This significantly reduces the amount of scattering, aiding clear, crisp image quality.

OPT can operate in either transmission or fluorescent emission mode, while thin samples may only require traditional staining (Sharpe, 2004). Samples can be stained with fluorescent dyes (for gene expression) or with commonly used stains such as methyl blue (for histological imaging). Sample preparation for OPT is relatively simple and not as time consuming as sample preparation for technologies such as SEM (scanning electron microscopy) or TEM (transmission electron microscopy).

### 5.3

#### Comparison with Other 3D Microscopy Techniques

Single-plane illumination microscopy (SPIM), an implementation of light-sheet microscopy (LSFM, light-sheet fluorescence microscopy), is a technique with applications similar to OPT. SPIM, however, in contrast with OPT, projects a thin sheet of light in a direction perpendicular to the detection axis, whose illumination is confined to the region around the detection focal plane and thereby suppresses out-of-focus light (Ntziachristos, 2010). The illumination of only the focal plane reduces the amount of background because no out-of-focus regions of the sample are excited.

The optical selection of “slices” removes the need for a reconstruction method, whereas OPT requires back-projection reconstruction to form a readable image (individual images must be correlated to remove scattering effects; they are not utilized separately as SPIM images can be). SPIM image quality can be improved by illuminating the sample from both sides. As with OPT, chemical clearing can be used with SPIM. SPIM, like OPT, can be used for extended imaging of samples *in vivo* under their natural environmental conditions and the specimen can be removed afterwards from the gelling agent unharmed.

SPIM, however, is limited to the detection of fluorescence and is not capable, as OPT is, of imaging intrinsic or extrinsic absorption (Rieckher *et al.*, 2011). Inexpensive colored dyes can be employed with OPT for staining tissues or for imaging gene expression.

Ultramicroscopy is the forerunner to SPIM – its modern version is almost the same as SPIM – and so most of the above comparison also applies between ultramicroscopy and OPT. The primary difference between ultramicroscopy and SPIM is the orientation of the system. In ultramicroscopy, the objective is situated above the specimen (Dodt, 2007), which is held horizontally along its longest axis. The light sheet remains perpendicular to the objective. While the positions are relatively the same, the orientation does have a key difference. As it is imaged from above, the sample can be subject to deformation, as the gel is not rigid enough to resist the effects of gravity. The gel can be deformed, sinking downwards, bending or flattening the gel and, in severe cases, deforming the image, which is further complicated as the downward bend remains as the sample is rotated. This can lead to inconsistencies that can hamper the image processing. In OPT the gel is held vertically, which minimizes deforming gravitational effects.

### 5.3.1

#### Confocal Microscopy

Confocal microscopy is an implementation of epi-microscopy in that both the excitation and emission beam are directed through the same objective lens. This optical configuration results in an elongated point spread function (*PSF* – the response of an imaging system to a point source, causing a blurred image of unresolved objects) in the longitudinal axis and is said to be anisotropic. The confocal technique is presently the commonest form of microscopy for obtaining 3D images. At the same time it is a rather inefficient way of imaging fluorophores, as a great amount of energy is expended while very little of the fluorescent light is acquired by the detector. Most confocal imaging techniques, such as laser scanning confocal microscopy (*LSCM*), employ sequential, point-by-point illumination of the sample with a laser (or several lasers), along the same axis as the detector, and reject the out-of-focus light by means of an iris or pinhole in front of the detector. This subjects the specimen to high levels of electromagnetic radiation along the path of the laser, which can lead to photodamage and fluorophore bleaching after a short imaging period (Kurtz, 2007). Added to this is the fact that not all of the excess light is excluded from the image, as the confocal technique cannot entirely remove out-of-focus light from outside the focal plane. This “flooding” of light does not assist in the imaging and is a limiting factor that must be taken into account for live cell imaging. The excess light also results in additional background noise, which reduces image quality. Complicating matters is the fact that reducing the pinhole diameter to improve the optical sectioning also decreases the intensity of light reaching the detector (Semwogerere and Weeks, 2005), requiring even more excitation light (with corresponding photodamage) to image the sample. In contrast, OPT illuminates the whole sample, but exposes the sample to much lower

intensity, thus resulting in lower phototoxic, photodamaging, and photobleaching effects on the sample.

Confocal microscopy can offer a lateral resolution of about 250 nm, compared with that of about 800 nm for the axial resolution (Gustafsson and Agard, 1999). This is due to the oval shaped PSF produced by the optical system. With such a PSF, the depth of field is a thin sliver of distance along the optical axis (z-axis). Upon scanning a plane of the sample with the excitation energy, the entire 3D sample is bathed in the excitation radiation, exposing every fluorophore to this energy. This not only induces toxicity and photobleaching in the sample but also limits the resolving power of the instrument. OPT utilizes software to combine the data from images taken from all around the sample to ascertain the location of various elements. Thus, the lack of axial resolution of one view is supported by the lateral resolution of other projections taken from different angles, which are combined to form the 3D model.

### 5.3.2

#### Two-Photon Microscopy

Two-photon microscopy utilizes the near-simultaneous absorption of two long-wavelength (low energy–high penetration) photons to excite the fluorophores at a particular point in a sample. Only where the two photons superimpose is there enough energy to generate fluorescence, as the two photons together can provide enough energy to excite a molecule that either alone could not excite. This provides very fine control over which point of a specimen is excited for imaging. The long-wavelength photons used can also penetrate further into a sample than is possible with most other optical imaging techniques, allowing larger specimens to be used, because the long wavelength light is scattered less by the constituents of the sample. Compared to single-photon confocal imaging, two-photon microscopy has an inherently high signal-to-noise ratio (Potter, 2005), as no light-rejecting pinhole is required to achieve optical sectioning. Through a different mechanism, the same can be said of OPT: very little out-of-focus light is produced (in the case of OPT this is because of the large depth of field used rather than nonlinear absorption effects).

### 5.4

#### Sample Preparation

As with all microscopy techniques, various protocols have been developed for OPT, to suit the preparation of different specimens and to image different investigative targets (neuronal tissue, expressed genes, etc.). Standard procedures for fixation and staining of a specimen are generally suitable and are applied where appropriate to the experiment. Some procedures are, however, characteristic of OPT in general.

Samples are most often mounted in a transparent gel prior to imaging. This is done to allow for the gel to be manipulated and imaged at any point in rotation

without the apparatus used to suspend the sample interfering with the imaging process (such as a clamp that may block the view at some angles or a slide that will interact with the light differently at each angle). It also provides a more natural three-dimensional suspension, as opposed to laying the specimen out flat on a surface (such as a slide or plate), so there is less effect on the morphology of the specimen (the gel supports the sample, gravity is not pulling it down onto a surface). The gel also interferes much less with the light than most flat glass or plastic surfaces. The standard gel used is 1% low melting point agarose (Sharpe *et al.*, 2002). Agarose provides sufficient support, has sufficient optical qualities (dependent upon purity), and has little effect upon the biological specimen. Low melting point agarose is specifically used as it has less risk of heat shock – the sample must be placed in the gel while it is still liquid, so a higher melting point equates to a greater risk of damage to the sample. The sample is placed in the liquid gel and carefully maintained (e.g., using forceps) at a position close to the center of the gel as it sets.

An alternative method involves forming the gel within a syringe. To do this, the head of the syringe must first be removed. A suitable amount of molten gel is then drawn into the syringe, the syringe is then pressed onto the sample, and then more gel is drawn up (if the sample consists of individual cells or is sufficiently small it can be mixed into the molten gel and everything can be drawn into the syringe at once). This places the sample in the middle of the gel, which is then allowed to set in the syringe. When the gel is set, it is gently pushed out of the syringe to form a ready-made gel cylinder. This method, however, depends on the ability to acquire a syringe of suitable size for the specimen (particularly in terms of the width – see below).

The sample should not be touching the sides or bottom of the container and should be adequately covered by gel on all sides. When the gel sets, excess gel is cut away. The gel is cut to form a roughly cylindrical shape so that the longest axis of the gel is the same as the longest axis of the specimen. The gel should be approximately three times greater in diameter than the axial depth of the sample.

For specimens that are not naturally transparent, a clearing agent must be used to allow the light to penetrate for imaging. The sample must first be dehydrated, such as with a gradient of alcohol. The most common clearing agent used is BABB (benzyl alcohol to benzyl benzoate), also known as *Murray's Clear* (Sharpe *et al.*). BABB is a 1 : 2 ratio mixture of benzyl alcohol to benzyl benzoate. BABB is toxic and so cannot be used to clear organisms or tissues for *in vivo* imaging. Some samples, such as *Drosophila*, may require bleaching (such as with hydrogen peroxide) prior to clearing to properly remove pigmentation (McGurk, 2007).

A magnetic holder is then attached to the top of the gel (along the shorter axes). This allows the gel to be held in the chamber for imaging by a magnetic stage that can rotate the sample without interfering with the light. Holding the gel in this orientation also helps limit deformation of the gel due to gravity. The OPT chamber is filled with an index matching liquid (a liquid with a refractive index similar to the gel) to minimize the scattering of light from refraction or diffraction, creating a more accurate image at the detector. BABB is often used as an index matching liquid (Sharpe *et al.*).

If the sample is going to be imaged *in vivo* then conditions suitable for the specimen must be maintained (e.g., the gel must be submerged in water for an aquatic specimen) both during and between imaging sessions. Anesthetic is generally added to the gel to minimize stress on the specimen. If the sample is aquatic, some agarose can be added to the water to increase viscosity, thereby minimizing movements of the specimen that may disrupt the imaging process (McGinty, 2011).

## 5.5

### Image Processing and Analysis

Digital image processing software offers an enormous collection of computational algorithms, which contribute in many different ways to the processing and analysis of digital images. The role played by software, in the framework of digital imaging, is a crucial aspect in the pipeline of digital image processing and analysis. Such is the case with the visual programming environment LabVIEW, developed by National Instruments, which has played, and will continue to do so, a major role in data acquisition and 3D reconstruction.

One method of image processing is taken from a PhD thesis entitled “*In vivo* optical projection tomography in biological model organisms” (McGinty, 2011) and is briefly described as follows.

With a custom-made LabVIEW program developed, the raw projections are imported as a tif-stack. The first step of the reconstruction process is to set the upper and lower threshold limits of the dynamic range. Background data is subtracted from the image stack, to minimize artifacts such as noise and hot pixels. In addition to the image stack, the acquired data is assigned with a header file that includes all of the parameters used in the experiment such as acquisition time, gain setting, chip size, binning factor, excitation power, excitation wavelength, aperture size, sample information, employed excitation, and fluorescence filters.

The subsequent stage in the reconstruction process is to define the region of interest, along with a defined center of rotation and the frequency of the Radon filter required for the back-projection algorithm (Meyer, 2010). Once filtered, the processed files are saved in 32-bit raw format files. Three-dimensional reconstruction can be rendered and visualized using commercial off-the-shelf volumetric rendering software.

## 5.6

### Marine Biology Applications

OPT is used primarily to attain 3D models of mesoscopic specimens, such as embryos, with microscopic resolution (Figures 5.4 and 5.5) (Sharpe, 2004). This allows for much larger samples than most other techniques will allow to be imaged in great detail. In this way, OPT serves much of the role of X-ray CT or MRI for specimens that are too small for those modalities, and forms a bridge between



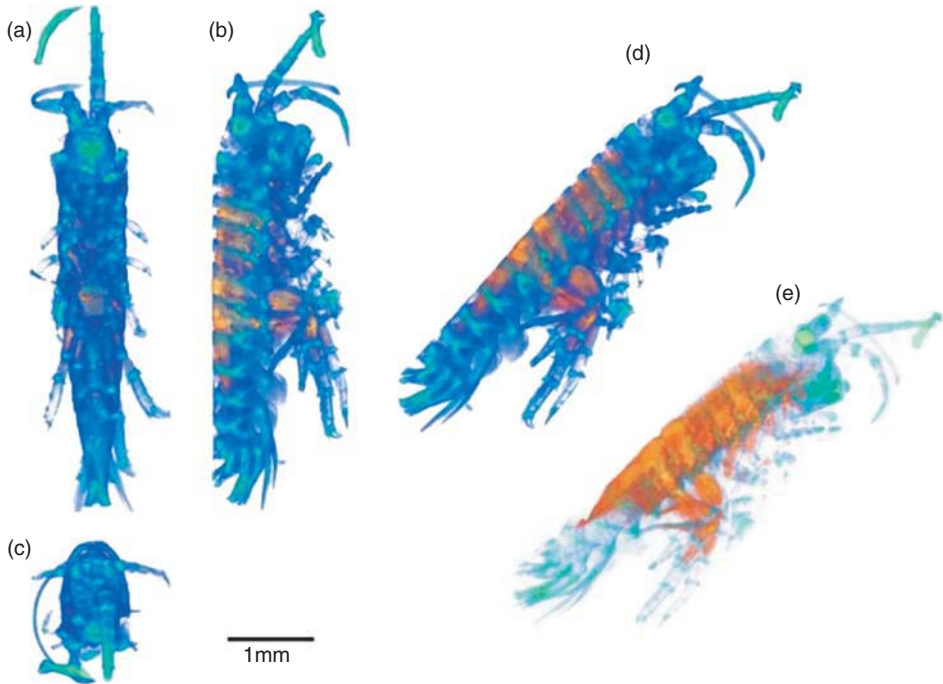


**Figure 5.4** (a–c) Frontal, sagittal, and transversal view of the superimposed reconstruction of the exoskeleton (bluish-green) and dsRed expression from the 3XP3 promoter in the muscular system of a *Parhyale hawaiiensis*; (d) 3D spatial view, and (e)

same as (d) but with reduced opacity in the exoskeleton. The sample was kept in halo carbon oil to match the refractive index of the capillary. Reproduced with permission from Heiko Meyer.

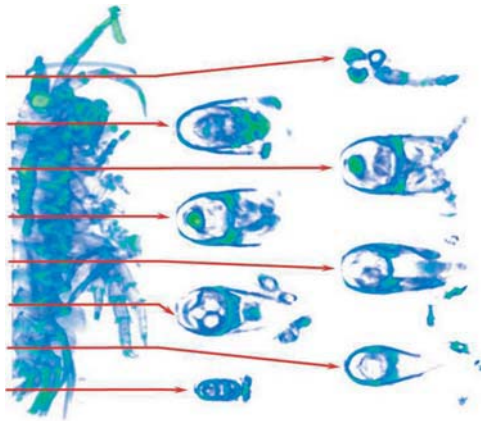


**Figure 5.5** 3D reconstruction of the exoskeleton of *P. hawaiiensis* shown in Figure 5.4. Red lines mark the transverse optical sections depicted on the right. Data acquired by white light illumination. Reproduced with permission from Heiko Meyer.

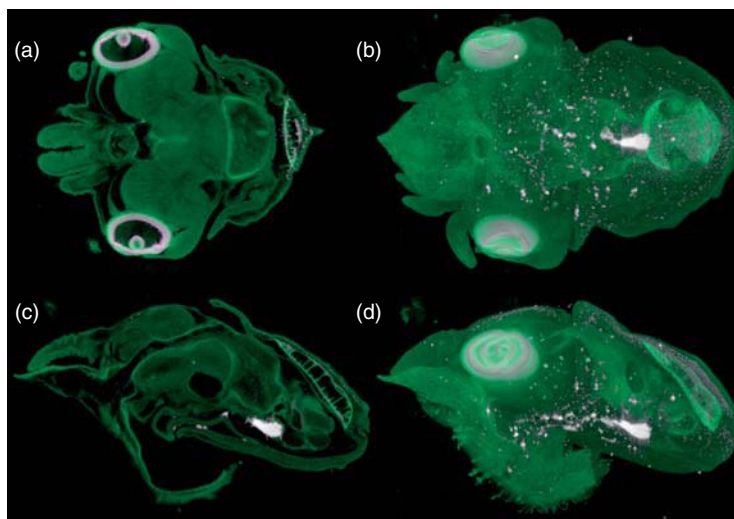


**Figure 5.6** OPT imaging of *Sepia officinalis* larval stages. (a, b) Max-value projections through the entire reconstruction; (c, d) single slice taken from the mid plane. Green = autofluorescence; white = absorption. Sample courtesy of Laure Bonnaud; OPT scanning and reconstruction courtesy of Laura Quintana.

macro- and micro-imaging. OPT can, therefore, be used to study complex tissue, such as brain tissue (Kerwin *et al.*, 2004), in greater detail, as the tissue is not as affected by cutting artifacts and the cells are *in situ* relative to one another. OPT can also be used to study the development of tissues in some whole organisms, such as squid larvae (Figure 5.6), embryos (Boot *et al.*, 2008), or plants (Rieckher *et al.*, 2011).

The variety of dyes and fluorophores that can be used with OPT has the advantage of not only allowing the specimen structure to be observed (such as with autofluorescence) but also the expression of a gene (or multiple genes) of interest within the specimen (Sharpe *et al.*, 2002). The ability of OPT to utilize simple colored dyes allows for the application of assays on the sample for which no corresponding fluorescent dyes have been found, such as the whole-mount detection of the expression of mRNAs (Sharpe, 2003). It also presents the opportunity to image both fluorescence and absorbance in the same specimen (with the same instrument) in three dimensions.

The ability to image some samples *in vivo* even allows for 4D imaging (Boot, 2009). These methods can be combined to allow for the expression of genes in a living organism to be observed in 3D models over time (Riecker *et al.*, 2011).

OPT can be used for the phenotyping of mutants (Albeanu *et al.*, 2008), as many mutations have an unclear effect upon the phenotype of an organism when viewed in a two-dimensional manner. The capabilities of OPT allow for the differences caused by a mutation to be identified quickly and much more easily.

More recently, OPT has been applied towards other avenues, such as the study of cancer tissue cultures, to allow culturing without subtype bias (Leeper *et al.*, 2011).

This may allow researchers to quantify drug sensitivity in such cultures instead of using a predictive method.

Three-dimensional imaging techniques such as OPT have opened new doors into studying the growth and gene expression of plant tissues – providing both visual and quantitative information. Traditionally, plant tissues are sectioned and stained for imaging but this has limitations for investigation of living cell function and retaining cell and tissue structures. An advantage of OPT is that it can detect non-fluorescent signaling, gene expression, and obtain histological information.

Algae are single-celled or multicellular plants that can be found in most fresh or salt water habitats. Optical sectioning can be performed on samples up to 15 mm thick (Truernit *et al.*, 2008). Fluorescent imaging can be conducted by transfecting with fluorescent stains or by natural autofluorescence from endogenous fluorophores.

Zebrafish are a model organism of vertebrate biology, and are widely studied (Bassi *et al.*, 2011), although due to their size (in the centimeter range) there are relatively few imaging modalities suited to studying them or organisms of a similar scale. Juvenile zebrafish are naturally transparent, thus providing the perfect opportunity to develop three-dimensional models of vertebrate biology *in vivo* and with high resolution through OPT. A specific development in OPT, called *flow optical projection tomography* (Bassi *et al.*, 2011), was designed to take advantage of the opportunities presented by organisms such as zebrafish. The purpose of flow-OPT is to image the vasculature of the organism by detecting the movement of the blood cells (the use of anesthetic removes most other sources of motion from the specimen). An algorithm for motion analysis is applied to the images, allowing a map of the vascular system to be built up.

Casper zebrafish that were 30 days post-fertilization and transgenic for tg(fli1:GFP)y1 were originally used as they do not have skin pigmentation and only weakly scatter visible light (Bassi *et al.*, 2011). Although flow-OPT does not require the use of a label, fluorescent tags can be used with previously untested organisms to verify results gained and to detect artifacts (such as absorbance from the skeleton or intestines) (Bassi *et al.*, 2011), although many artifacts are compensated for by images taken from different angles. The flow-OPT system consists of a light source positioned behind a diffuser that in turn is adjacent to an iris. A telecentric illumination lens collimates the light beam prior to illumination of the sample. A telecentric objective lens collects the transmission light and focuses it on the photosensitive surface of a camera. To ensure the samples remain stationary, they are mounted in a tube, 2 mm in diameter, made from fluorinated ethylene propylene (FEP) filled with agarose, permitting rotation of the sample. FEP has the same refractive index as the surrounding water in the chamber and thereby minimizes optical aberrations and artifacts.

In a given stack of successive images, the flow contrast is calculated at each pixel by means of a mathematical equation (Bassi *et al.*, 2011), providing a data set that can be rendered into a 3D reconstruction of the specimen's vasculature. The specimen's vasculature can then be sectioned virtually along any plane and viewed in two, three, or four dimensions.

Flow-OPT offers the capability to image living organisms from the millimeter scale of drosophila embryos, for example, up to the centimeter scale of zebrafish. The technology is capable of imaging large volumes in a non-invasive manner for long periods of time, without the need for fluorophores. With acquisition times of approximately 3 min, the technology is a relatively low cost method that can be combined with laser speckle imaging (Briers, 2006), which it is hoped will permit imaging of larger and highly scattering specimens.

### Acknowledgments

The authors thank Jim Swoger and James Sharpe for proofreading the manuscript. E.G.R. is supported by EMBL and the Science Foundation Ireland.

### References

- Albeanu, D.F., Soucy, E., Sato, T.F., Meister, M., and Murthy, V.N. (2008) LED arrays as cost effective and efficient light sources for widefield microscopy. *PLoS ONE*, **3** (5), e2146.
- Bassi, A., Fieramonti, L., D'Andrea, C., Mione, M., and Valentini, G. (2011) In vivo label-free three-dimensional imaging of zebrafish vasculature with optical projection tomography. *J. Biomed. Opt.*, **16** (10), 100502.
- Boot, M.J., Westerberg, C.H., Sanz-Ezquerro, J., Cotterell, J., Schweitzer, R., Torres, M., and Sharpe, J. (2008) In vitro whole-organ imaging: 4D quantification of growing mouse limb buds. *Nat. Methods*, **5**, 609–612.
- Briers, J.D. (2006) *Proceedings of the Symposium on Photonics Technologies for 7th Framework Program*, October 12–14, Oficyna Wydawnicza Politechniki Wrocławskiej, Wrocław, pp. 328–332.
- Dodt, U.H. *et al.* (2007) Ultramicroscopy: three-dimensional visualization of neuronal networks in the whole mouse brain. *Nat. Methods*, **4**, 331–336.
- Fauver, M., Seibel, E., Rahn, J.R., Meyer, M., Patten, F., Neumann, T., and Nelson, A. (2005) Three-dimensional imaging of single isolated cell nuclei using optical projection tomography. *Opt. Exp.*, **13** (11), 4210–4223.
- Fisher, M., Clelland, A., Bain, A., Baldock, R., Murphy, P., Downie, H., Tickle, C., Davidson, D., and Buckland, R. (2008) Integrating technologies for comparing 3D gene expression domains in the developing chick limb. *Dev. Biol.*, **317**, 13–23.
- Fumene Feruglio, P., Vinegoni, C., Gros, J., Sbarbati, A., and Weissleder, R. (2010) Block matching 3D random noise filtering for absorption optical projection tomography. *Phys. Med. Biol.*, **55** (18), 5401–5415.
- Greger, K., Swoger, J., and Stelzer, E.H. (2007) Basic building units and properties of a fluorescence single plane illumination microscope. *Rev. Sci. Instrum.*, **78** (2), 023705.
- Gustafsson, M.G.L., Agard, D.A., and Sedat, J.W. (1999) I<sup>5</sup>M: 3D widefield light microscopy with better than 100 nm axial resolution. *J. Microsc.*, **195** (1), 10–16.
- Kerwin, J. *et al.* (2004) 3 dimensional modelling of early human brain development using optical projection tomography. *BMC Neurosci.*, **5** (1), 27.
- Kurtz, R. (2007) Bright solutions to get sharp images: confocal and two-photon fluorescence microscopy and the pros and cons of new multifocal approaches, in *Modern Research and Educational Topics in Microscopy* (eds A. Mendez-Vilas and J. Diaz), Formatex.
- Lee, K., Avondo, J., Morrison, H., Blot, L., Stark, M., Sharpe, J., Bangham, A., and Coen, E. (2006) Visualizing plant

- development and gene expression in three dimensions using optical projection tomography. *Plant Cell*, **18** (9), 2145–2156.
- Leeper, A.D., Joanne Farrell, J., Dixon, M., Wedden, S.E., Harrison, D.J., and Katz, E. (2011) Long-term culture of human breast cancer specimens and their analysis using optical projection tomography. *J. Visualised Exp.*, **53**, 3085. doi: 10.3791/3085.
- McGinty, J. *et al* (2011) *In vivo* fluorescence lifetime optical projection tomography. *Biomed. Opt. Exp.*, **2** (5), 1340–1350.
- McGurk, L., Morrison, H., Keegan, L.P., Sharpe, J., and O'Connell, M.A. (2007) Three-dimensional imaging of *Drosophila melanogaster*. *PLoS ONE*, **2** (9). doi: 10.1371/journal.pone.0000834
- Meyer, H. (2010) *In vivo* optical projection tomography in biological model organisms. PhD thesis, Erasmus University of Rotterdam.
- Ntziachristos, V. (2010) Going deeper than microscopy: the optical imaging frontier in biology. *Nat. Methods*, **7**, 603–614.
- Potter, S.M. (2005) in *Imaging in Neuroscience and Development: A Laboratory Manual* (eds R. Yuste and A. Konnerth), Cold Spring Harbor Laboratory Press, pp. 59–70.
- Quintana, L. and Sharpe, J. (2011) Optical projection tomography of vertebrate embryo development. *Cold Spring Harbour Protoc.*, doi: 10.1101/pdb.top116
- Rieckher, M., Birk, U.J., Meyer, H., Ripoll, J., and Tavernarakis, N. (2011) Microscopic optical projection tomography *in vivo*. *PLoS ONE*, **6** (4), e18963. doi: 10.1371/journal.pone.0018963
- Semwogerere, D. and Weeks, E.R. (2005) Confocal microscopy, in *Encyclopedia of Biomaterials and Biomedical Engineering*, 2nd edn, Informa Healthcare, New York.
- Sharpe, J. (2003) Optical projection tomography as a new tool for studying embryo anatomy. *J. Anat.*, **202** (2), 175–181.
- Sharpe, J. (2004) Optical projection tomography. *Annu. Rev. Biomed. Eng.*, **6**, 209–228.
- Sharpe, J., Ahlgren, U., Perry, P., Hill, B., Ross, A., Hecksher-Sørensen, J., Baldock, R., and Davidson, D. (2002) Optical projection tomography as a tool for 3D microscopy and gene expression studies. *Science*, **296** (5567), 541–545.
- Truernit, E. *et al.* (2008) High-resolution whole-mount imaging of three-dimensional tissue organization and gene expression enables the study of phloem development and structure in *Arabidopsis*. *Plant Cell*, **20**, 1494–1503.
- Wang, Y. and Wang, R.K. (2007) Optimization of image-forming optics for transmission optical projection tomography. *Appl. Opt.*, **46** (27), 6815–6820.





## 6

# Electron Microscopy Techniques for Imaging Marine Phytoplankton

Gustaaf Hallegraeff

### Abstract

It is only since the 1950s, when the electron microscope was commercialized, that we have been able to fully appreciate the ultrastructural detail of marine phytoplankton. While there is no single, generic protocol for preparing phytoplankton for electron microscopy, this chapter provides a guide to the general approaches used for high-resolution imaging of species such as coccolithophorids with their calcareous scales, diatoms with silica frustules, and dinoflagellates with and without cellulose armor. Advances in sample collection, algal culturing, and molecular genetics have paved the way toward redefining many new taxa of prokaryotic and eukaryotic micro-, nano-, and picoplankton.

## 6.1

### Introduction

In 1673 the Dutch pioneer microscopist Anton Van Leeuwenhoek, using crude glass lenses, was the first human to see minute creatures, which he called “*animalcules*,” in pond water. From the 1890s to the 1930s, expeditions by vessels such as *HMS Beagle*, *Challenger*, and *Meteor* charted this newly recognized microscopic plant and animal world, describing thousands of new plankton species from the world’s oceans. Both the methods of collection (improved plankton nets, sampling bottles, fixatives, culturing skills) and techniques of observation have dramatically improved in the past century. The best optical microscopes, limited by the wavelengths of visible light, magnify no more than 1000 $\times$  and cannot discriminate between objects closer than about 0.2  $\mu\text{m}$ . Different forms of illumination such as dark-field, bright-field, phase-contrast, polarized, interference, or fluorescence microscopy can be used to improve the resolution of particular structural details. It has been only since the 1950s when scientists developed the much more powerful electron microscope that we have been able to fully appreciate the unique shapes and structures of these microorganisms. Ernest Ruska (awarded the Nobel Prize in Physics

1986) first developed the application of a beam of electrons in a microscope. With a wavelength about 100 000 times less than the average wavelength of visible light, this offers an increase in resolving power to about  $0.001\ \mu\text{m}$ . In the scanning electron microscope (SEM), a beam of electrons scans the outer surface of objects previously coated with a thin layer of gold or platinum to make them conductive. This instrument can produce a wide range of magnifications, from 20 to 30 000 $\times$ , and creates a great depth of focus or three-dimensionality 400–500-times that achievable by light microscopy. The first micrographs showing this striking three-dimensional imaging capability were obtained in Cambridge in 1952 with a resolution of only 50 nm. The next important development was to improve the secondary electron detector by adding a scintillator to convert electrons into photons, and pave the way for enhancing the signal-to-noise ratio. Nowadays, the field emission scanning electron microscope (FESEM) produces much clearer, less electrostatically distorted images with spatial resolution down to 1.5 nm, that is, three to six times better than a conventional SEM. In another type of instrument, the transmission electron microscope (TEM), electrons pass through thin biological specimens, such as thinly silicified diatom cell walls or thin slices of cells embedded in epoxy resin and sectioned by means of a diamond knife in an ultramicrotome. In this way, magnifications up to 100 000 $\times$  can be achieved. Starting in the 1960s Manton and Parke (1960) and coworkers (Leedale, Leadbeater, Dodge, and Moestrup) made important contributions to elucidate the fine structure of microalgal groups (Dodge, 1973), but TEM skills have become increasingly rare today. TEM sections are critical, however, in defining new taxa of prokaryotic and eukaryotic picoplankton (e.g., *Synechococcus*, *Prochlorococcus*, *Ostreococcus*; Chrétiennot-Dinet *et al.*, 1995).

## 6.2

### Collecting and Processing Specimens

Qualitative sampling in oceanic plankton surveys can be achieved using  $37\ \mu\text{m}$  plankton nets, either towed horizontally or used in a free-fall mode (Heron, 1982). For inshore collections a small conical net (23 cm mouth diameter, 40 cm length, 4.5 cm cod end diameter) of  $20\ \mu\text{m}$  monofilament nylon is often used. Another sampling device is the continuous plankton recorder (CPR). This collects plankton continuously by seawater entering the instrument through a square aperture onto a  $270\ \mu\text{m}$  filtering silk mesh, which is then wound onto a storage spool in a tank containing 4% formaldehyde (Richardson *et al.*, 2006). In contrast, quantitative sampling, which is needed, for example, when assessing changes in the abundance of potentially harmful phytoplankton, requires the collection of “water bottle” samples from various depths using 1, 5, or 8 l Niskin bottles. Water samples of at least 1 l are preserved and concentrated by settling or centrifugation. For some purposes a continuous plankton centrifuge (15 000g; flow rate  $100\ \text{ml min}^{-1}$ ) can be used to concentrate 2 l to about 10 ml (Davis, 1957). To obtain sufficient material of some rare species, the establishment of enrichment cultures



is invaluable. One milliliter of concentrated sample, obtained after continuous centrifuging, is inoculated into enrichment media, including dilutions of modified media (Andersen, 2005).

### 6.3

#### Light Microscopy

It is always best to examine living phytoplankton microscopically as soon as possible after collection, either using bright-field or differential interference contrast, paying attention to swimming behavior and chloroplast colors. Alternatively, samples can be preserved for later examination, a commonly used preservative being Lugol's iodine fixative (potassium iodide plus iodine; Sournia, 1978). However, this can overstain many algal cells, thus obscuring details that are important for their identification. For some species 1–2% formaldehyde (buffered with hexamine) or, for more delicate taxa, 2% glutaraldehyde (buffered with phosphate buffer and stored in a refrigerator at 4 °C) are preferred. Both fixatives should only be used in well-ventilated rooms. Diatom net samples can be preserved in 2% formalin neutralized with hexamine, then rinsed with distilled water to remove salt and preservatives, and cleaned of organic material by overnight oxidation with potassium peroxodisulfate at 60 °C (Ma and Jeffrey, 1978). For mucilaginous or oil-rich diatoms more rigorous oxidants such as hydrogen peroxide and potassium permanganate, or potassium permanganate and hydrochloric acid, may be needed to remove organic contents. Cleaned diatom cells can be mounted in coumarone or Norland optical adhesive (refraction index 1.6–1.7) and inspected by phase-contrast light microscopy. For armored dinoflagellates the use of the fluorescent cellulose stain Calcofluor White M2R has become a valuable aid in the elucidation of plate tabulation (Fritz and Triemer, 1985). A major recent advance is the widespread availability of high-quality digital cameras (e.g., Zeiss AxioCam HR). This allows for on the spot verification of the successful capture of images, which then can be digitally shared with international colleagues for taxonomic verification.

### 6.4

#### Sediment Cyst Surveys

For species such as dinoflagellates that produce resting spores (cysts; Figure 6.1), the examination of sediment samples is also recommended. The choice of sampling site should be based on an inspection of local bathymetric maps (depth contours) and knowledge of local currents. Black undisturbed sediments from deep basins offer better opportunities for cyst surveys than coarse sandy sediments characteristic of strong current regimes. Perspex coring tubes (20–40 cm long, 4.5 cm diameter) can be pushed into the sediment by SCUBA divers and then withdrawn and capped. Bottom samplers such as dredges or grab buckets often lose the lighter material at the sediment surface and are less suitable. A modified Craib corer (Craib, 1965) has

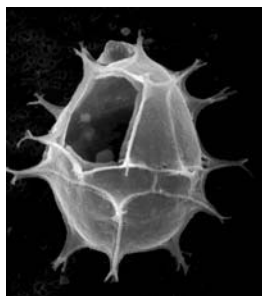


**Figure 6.1** JEOL-35C SEM; air-dried; sediment sample from Tasmanian waters; cyst of the dinoflagellate *Gonyaulax digitata*, showing diagnostic germination opening (archeopyle); cell 45  $\mu\text{m}$  long.

also been used to collect undisturbed sediment cores. The uppermost 6–10 cm of sediment was carefully extruded from the coring tube and mixed with filtered seawater to obtain a watery slurry. Subsamples (5–10 ml) were sonicated for 2 min to dislodge detritus particles. The sample can then be screened through a 90  $\mu\text{m}$  sieve and collected onto a 20  $\mu\text{m}$  sieve, and the remaining fraction panned to remove denser sand grains and larger detritus particles. Sediment samples with comparatively few cysts are best concentrated using sodium polytungstate density gradient centrifugation (Bolch, 1997). Individual cysts can be germinated in tissue wells with 2 ml filtered seawater with nutrients added to confirm taxonomic identification. For some purposes destructive palynological sediment treatment techniques, involving the addition of 10% hydrochloric acid (to remove calcareous fossils) and heating with concentrated hydrofluoric acid, should be used (Sargeant, 1974).

## 6.5

### Transmission Electron Microscopy

Cleaned diatom samples prepared as above can be pipetted onto coated copper grids (400 mesh per in.), dried, and then immediately examined in TEM at 100 kV (Figures 6.2 and 6.3). For the study of small flagellates, 2 l water samples should

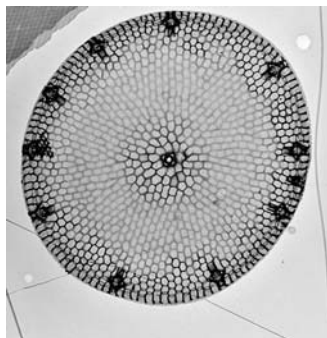


**Figure 6.2** Philips-515 TEM; potassium peroxodisulfate cleaned; field sample from Gulf of Carpentaria, Australia; diatom *Thalassiosira partheneia*, with a single small marginal labiate process located in between two larger marginal strutted processes; 10  $\mu\text{m}$  diameter.

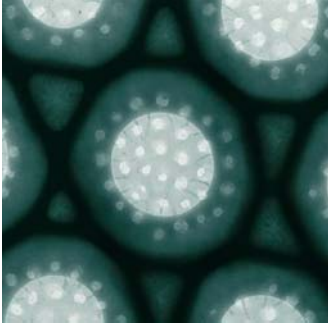


**Figure 6.3** Philips-515 TEM; potassium peroxodisulfate cleaned; field sample from East Australian Current; detail of areola chamber of large diatom *Coscinodiscus* with internal sieve membrane (cribrum) and external foramen.

be first screened through a 20  $\mu\text{m}$  mesh to remove larger particles and then concentrated to 8–10 ml using filtration or a continuous plankton centrifuge. A drop of this concentrate can then be pipetted onto formvar- or parlodion-coated TEM grids. Samples can be fixed with 2% osmium tetroxide vapor for 15–25 s and allowed to settle for 10–15 min before removing excess liquid using dental absorbent points. **Caution:** osmium tetroxide fumes are highly toxic and impact on the eyes in particular! Grids should be washed in distilled water and allowed to air dry. Grids can then be shadow cast (Moestrup and Thomsen, 1980) with Au:Pd (60:40) at an approximate angle of  $30^\circ$  in a Dynavac coating unit before viewing using the a TEM at 60 kV (Figures 6.4 and 6.5). Until recently, the resolution of SEM

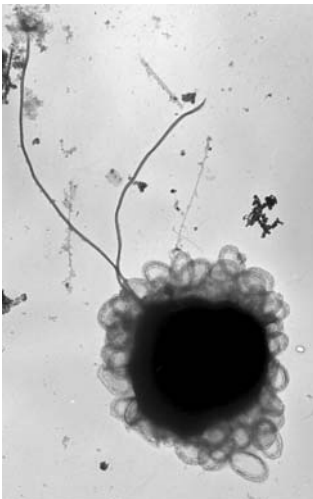


**Figure 6.4** Philips-515 TEM; Lugol fixed; air dried; field sample from Southern Australian coastal waters; haptophyte *Pleurochrysis carterae* with thinly calcified oval coccolith scales (cricoliths); cells 12–17  $\mu\text{m}$  diameter.

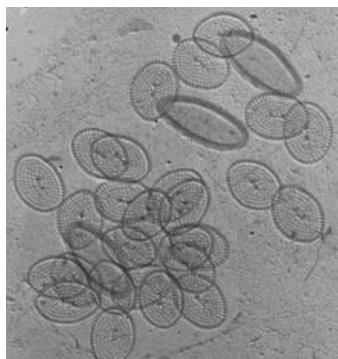


**Figure 6.5** Philips-515 TEM; osmium tetroxide fixed; shadow cast using Pt; field sample from Tasmanian waters; body scales of haptophyte *Chrysochromulina polylepis* including small oval ( $0.6\text{--}0.7 \times 0.4\text{--}0.5 \mu\text{m}$ ) and larger elliptical scales ( $1.0\text{--}1.1 \times 0.4\text{--}0.5 \mu\text{m}$ ). Image courtesy of Jeannie-Marie LeRoi, University of Tasmania.

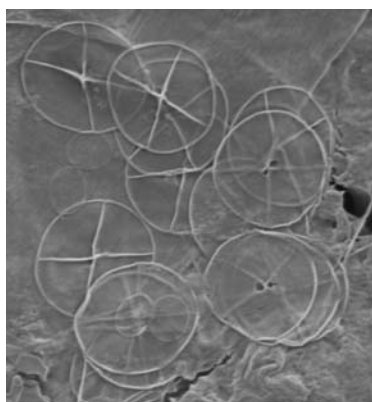


**Figure 6.6** Hitachi SU-70 FESEM FEI; buffered formalin preserved; field sample from North Atlantic using continuous plankton recorder; body scales of haptophyte *Chrysochromulina cf. vexillifera* ( $0.9\text{--}1.0 \times 0.6\text{--}0.7 \mu\text{m}$ ).

did not approach that of the TEM, but this has changed with the advent of FESEM. Scale-bearing flagellates can now also be readily studied by FESEM (Figure 6.6).

## 6.6

### Scanning Electron Microscopy

Seawater samples (100 ml to 3 l) can be filtered gently onto Nuclepore™ filters (pore diameter  $1 \mu\text{m}$ ) immediately after collection. Other filter types produce less satisfactory backgrounds for SEM imaging. The filters should be rinsed with 100 ml distilled water to remove salt crystals and then air-dried. Small pieces of filter can be mounted on aluminium SEM stubs, coated with gold or gold-palladium (20 nm

layer thickness), and examined with a SEM at 20–25 kV. Instruments that we have worked with include JEOL JSM-35C, or JSM 840, Philips 515, FEI Quanta 600 MLA environmental SEM, and Hitachi SU-70 FESEM (Hallegraeff *et al.*, 2010). Filtration immediately after collection, and the omission of dehydration and critical-point drying, minimizes the aggregation of detritus. For most species of armored dinoflagellates (Figures 6.7–6.10), diatoms (Figure 6.11), and coccolithophorids (Figure 6.12) structural deformation during air drying does not pose serious



**Figure 6.7** JEOL-35C SEM; air-dried; field sample from Papua New Guinea waters; recently divided pair of toxic dinoflagellate *Pyrodinium bahamense*, showing ornate cellulose plate tabulation; cells in 60  $\mu\text{m}$  diameter.

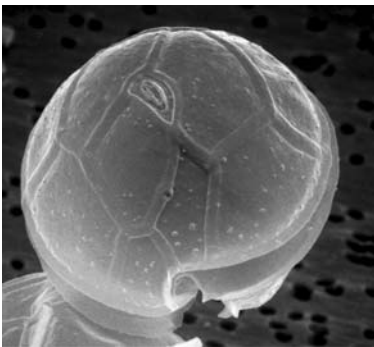


**Figure 6.8** JEOL-35C SEM; osmium tetroxide fixed; critical-point dried; field sample from Adelaide coastal waters; toxic dinoflagellate *Alexandrium minutum*, showing diagnostic cellulose plate tabulation with triangular apical pore plate, connected to a polygonal first apical plate containing a ventral notch; cell 15  $\mu\text{m}$  in diameter.

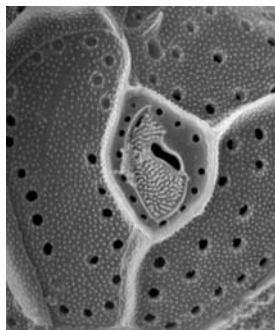


**Figure 6.9** JEOL-35C SEM; air-dried; field sample from Papua New Guinea waters; diagnostic triangular apical pore of the toxic dinoflagellate *Pyrodinium bahamense*.



**Figure 6.10** JEOL-35C SEM; air-dried; field sample from Great Barrier Reef; diagnostic triangular apical pore of the toxic dinoflagellate *Gambierdiscus toxicus*.

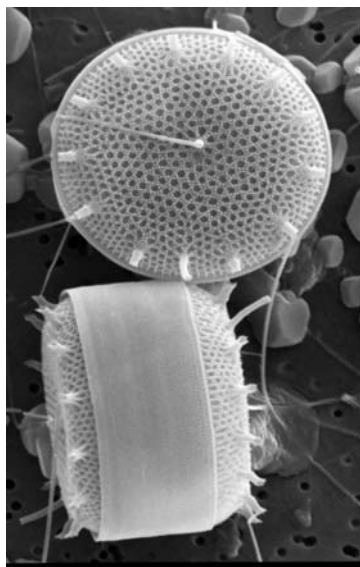


**Figure 6.11** JEOL-35C SEM; air-dried; field sample from Sydney coastal waters; diatom *Thalassiosira allenii*; 15  $\mu$ m in diameter.

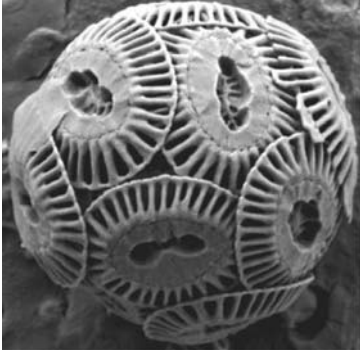


**Figure 6.12** Hitachi SU-70 FESEM; air-dried field sample from Southern Ocean; coccolithophorid *Emilia huxleyi* covered by disc-like coccoliths (placoliths) composed of T-shaped elements radially arranged as in a spoked wheel; highly calcified morphotype; cell diameter 5–10  $\mu\text{m}$ .

problems. For selected diatoms, cleaned net samples can be prepared for SEM. Delicate unarmored dinoflagellates can be fixed for 1 h at room temperature by the addition of equal volumes of 4% osmium tetroxide solution prepared in culture medium. The fixed culture then needs to be rinsed once in seawater, once in half-concentration seawater in deionized water, and once in deionized water, using centrifugation (600g) to separate the cells from the medium. The material should then be dehydrated using a methanol, ethanol, or acetone concentration gradient (e.g., 10, 30, 50, 70, 80, 90, 95, and 100% MeOH in distilled water, followed by 100% dry methanol and two changes of 100% dry acetone), soaking for 15 min at each concentration. Samples can then be critical-point-dried (Figures 6.13–6.15). In this process the solvent is replaced with liquid  $\text{CO}_2$  and the temperature then raised to above the critical temperature (approximately 35 °C at a pressure of around 1200 psi) at which the liquid  $\text{CO}_2$  changes to vapor without a change of density and, therefore,

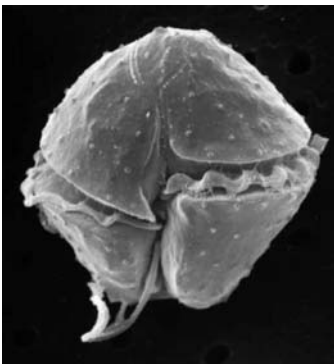


**Figure 6.13** FEI Quanta 600 SEM; osmium tetroxide fixed; critical-point dried; culture from Tasmanian waters; unarmored dinoflagellate *Gymnodinium aureolum* with horse-shoe shaped apical groove. Image courtesy Dr Chris Bolch, University of Tasmania.



**Figure 6.14** FEI Quanta 600 SEM; osmium tetroxide fixed; critical-point dried; culture from Tasmanian waters; unarmored dinoflagellate *Takayama tasmanica* with sigmoid apical groove. Image courtesy Dr Miguel de Salas, University of Tasmania.

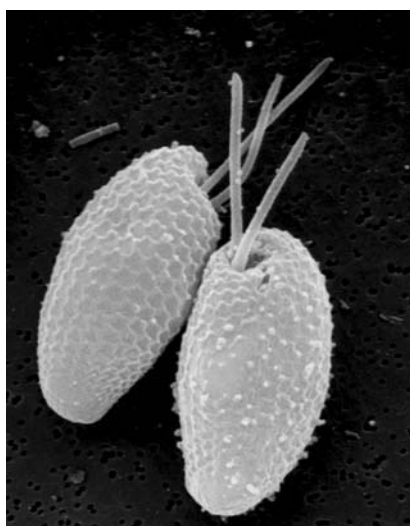


**Figure 6.15** JEOL-35C SEM; osmium tetroxide fixed; critical-point dried; cryptomonad *Rhodomonas* sp. with hexagonally arranged periplast plates and two emerging flagella. Image courtesy Tony Rees, CSIRO Marine & Atmospheric Research.

without surface tension effects that distort morphology and ultrastructure. After sputter coating, specimens for SEM can be stored under vacuum in a desiccator for long periods of time. As with light microscopy, the electronic capture of SEM images allows for on the spot verification of successful images, which then can be digitally shared with colleagues for taxonomic verification. As a general rule, electron microscopy is as much an art as a science, and phycologists must be prepared to experiment with new ways of handling cells if standard procedures appear inadequate.



## Acknowledgements

I thank the numerous scientists and technicians who have helped me over the past 30 years, operating a range of different electron microscopes: Dr Maret Vesk (University of Sydney), Dr Tony Rees (CSIRO Marine Laboratories), Rick van den Enden and Gerry Nash (Australian Antarctic Division), and Karsten Goemann (University of Tasmania). Some of the images used here were taken in collaboration with my students and collaborators Chris Bolch, Tom Coad, David MacLeod, Jeannie-Marie LeRoi, Tony Rees, and Miguel de Salas.

## References

- Andersen, R.A. (ed.) (2005) *Algal Culturing Techniques*, Elsevier, New York, p. 596.
- Bolch, C.J.S. (1997) The use of sodium polytungstate for the separation and concentration of living dinoflagellate cysts from marine sediments. *Phycologia*, **36**, 472–478.
- Chrétiennot-Dinet, M.J., Courties, C., Vaquer, A., Neveux, J., and Claustre, H., *et al.* (1995) A new marine picoeucaryote: *Ostreococcus tauri* gen et sp nov (Chlorophyta, Prasinophyceae). *Phycologia*, **34**, 285–292.
- Craib, J.S. (1965) A sampler for taking short undisturbed marine cores. *J. Cons. Perm. Int. Explor. Mer.*, **30**, 34–39.
- Davis, P.S. (1957) A method for the determination of chlorophyll in sea water. *Techn. Rep. Div. Fish. Oceanogr. CSIRO*, **7**, 1–8.
- Dodge, J.D. (1973) *Fine Structure of Algal Cells*, Academic Press, New York, p. 261.
- Fritz, L. and Triemer R.E. (1985) A rapid simple technique utilizing Calcofluor white m2r for the visualization of dinoflagellate thecal plates. *J. Phycol.* **21**, 662–664.
- Hallegraeff, G.M., Bolch, C.J.S., Hill, D.R.A., Jameson, I., Leroi, J.M., McMinn, A., Murray, S., De Salas, M.F., and Saunders, K. (eds) (2010) *Algae of Australia: Phytoplankton of Temperate Coastal Waters*, ABRS, Canberra; CSIRO Publishing, Melbourne, p. 421.
- Heron, A.C. (1982) A vertical free fall plankton net with no mouth obstructions. *Limnol. Oceanogr.*, **27**, 380–383.
- Ma, J.C.W. and Jeffrey, L.M. (1978) Description and comparison of a new cleaning method of diatom frustules for light and electron microscope studies. *Trans. Am. Microscop. Soc.*, **105**, 152–157.
- Manton, I. and Parke, M. (1960) Further observations on small green flagellates with special reference to possible relatives of *Chromulina pusilla* Butcher. *J. Mar. Biol. Assoc. U.K.*, **39**, 275–298.
- Moestrup, Ø. and Thomsen, H.A. (1980) in *Handbook of Phycological Methods. Developmental and Cytological Methods* (ed. E. Gantt), Cambridge University Press, Cambridge, pp. 385–390.
- Richardson, A.J., Walne, A.W., John, A.W.G., Jonas, T.D., Lindley, J.A., Sims, D.W., Stevens, D., and Witt, M. (2006) Using continuous plankton recorder data. *Prog. Oceanogr.*, **68**, 27–74.
- Sargeant, W.A.S. (1974) *Fossil and Living Dinoflagellates*, Academic Press, New York, p. 182.
- Sournia, A. (ed.) (1978) *Phytoplankton Manual*, Monographs on Oceanographic Methodology, vol. 6, UNESCO, Paris, p. 337.



## 7

## Looking Inside Marine Organisms with Magnetic Resonance and X-ray Imaging

*Irene Zanette, Gheyleen Daghfous, Timm Weitkamp, Brigitte Gillet, Dominique Adriaens, Max Langer, Peter Cloetens, Lukas Helfen, Alberto Bravin, Françoise Peyrin, Tilo Baumbach, Jean-Michel Dischler, Denis Van Loo, Tomas Praet, Marie Poirier-Quinot, and Renaud Boistel*

### Abstract

In this chapter we describe computer-based tomographic methods using magnetic resonance imaging (MRI) and X-ray absorption as well as X-ray phase-contrast imaging techniques. The latter are based on refraction and near-field diffraction of X-rays and are gaining increased attention due to the increase in sensitivity they offer over conventional, attenuation-based X-ray techniques. The increased sensitivity is of particular interest in marine biology imaging, especially for soft tissue visualization and analysis. The basic principles of the imaging techniques are described, starting with an analysis of the image formation process, followed by a review of several tomography methods, such as MRI or X-ray imaging, and practical guidelines for parameter selection. Finally, two relevant examples of imaging are presented: imaging in marine biology (segmentation and visualization) and small animal (sea horse) imaging. These examples illustrate imaging under different conditions and using different reconstruction options.

## 7.1

### Introduction

Knowledge of marine life and its modifications through historical time or as a consequence of ongoing climate change requires the accurate description of plankton and marine organisms from microorganisms to fishes. However, our biological knowledge in terms of, for example, physiology, biomechanics, evolution, ecology, and taxonomy of 70% of the Earth is extremely limited. The ultimate way to perform large-scale biological analysis is to achieve full three-dimensional (3D) imaging of every specimen collected.

Recent developments have allowed tomographic methods to be used for scientific study in a wide range of fields. In this chapter we will focus on recent applications

of different types of tomography in marine biological imaging. We will review the fundamentals (essential base) of tomography and show the contrast formation models. We will illustrate the different experimental approaches used to study a marine organism and give some practical advice for image acquisition, parameter selection, and reconstruction.

Computer-based tomography is emerging as a qualitative and/or quantitative, 3D imaging technique used in a wide range of applications. The term “*tomography*” actually represents a large panel of methods. Magnetic resonance imaging (*MRI*) is devoted to the examination of soft tissues. On the other hand, X-ray computed tomography (*CT*) allows very high spatial resolution. X-Ray phase-contrast imaging (*PCI*) techniques offer a substantially higher sensitivity than standard, attenuation-based X-ray microtomography ( $\mu$ *CT*). This offers new possibilities, especially in marine biological imaging, where  $\mu$ CT often lacks the sensitivity needed to image soft tissues in the presence of strongly calcified tissues – *PCI* overcomes this issue. As there are several ways to obtain phase contrast with X-rays, we present the most important ones. We will review the first applications in marine biological imaging and discuss the prospects for further development and application of the technique.

## 7.2

### Magnetic Resonance Imaging

Microscopic magnetic resonance imaging (micro-MRI, MRM, or  $\mu$ MRI) (Glover and Mansfield, 2002) is one of the best imaging methods available for assessing soft tissues structures and monitoring biological processes as they occur *in vivo* (Van der Linden *et al.*, 2004). This technology does not rely upon ionizing radiation, yet it offers a spatial resolution of tens of microns (Glover and Mansfield, 2002; Tyszka, Fraser, and Jacob, 2005), thus exhibiting clear advantages over other imaging methodologies, such as positron emission tomography (*PET*). *MRI* is a non-invasive *in vivo* (Hart *et al.*, 2003; Pohlmann *et al.*, 2007), as well as post-mortem, imaging technique that allows the study of “soft” tissue (e.g., brain, bone marrow, muscle, etc.) (Tyszka, Fraser, and Jacob, 2005; Pohlmann *et al.*, 2007). It can be used to map anatomical structure (anatomical magnetic resonance imaging, *aMRI*) (Narasimhan and Jacobs, 2002), or as a monitor of organ function (functional magnetic resonance imaging, *fMRI*) (Lorenzetti *et al.*, 2010). Moreover, magnetic resonance spectroscopy allows one to track various metabolic processes. The advent of high-magnetic-field *MRI* systems for small animals, that is, with an average magnet bore size that fits an adult rat body, has made this technique accessible for the study of smallest animal models (Hart *et al.*, 2003; Tyszka, Fraser, and Jacob, 2005; Null *et al.*, 2008).

#### 7.2.1

##### Experimental Setup

*MRI* is based upon the nuclear magnetic resonance principle. Certain nuclei, such as hydrogen nuclei (proton), for example, have a weak magnetic moment or

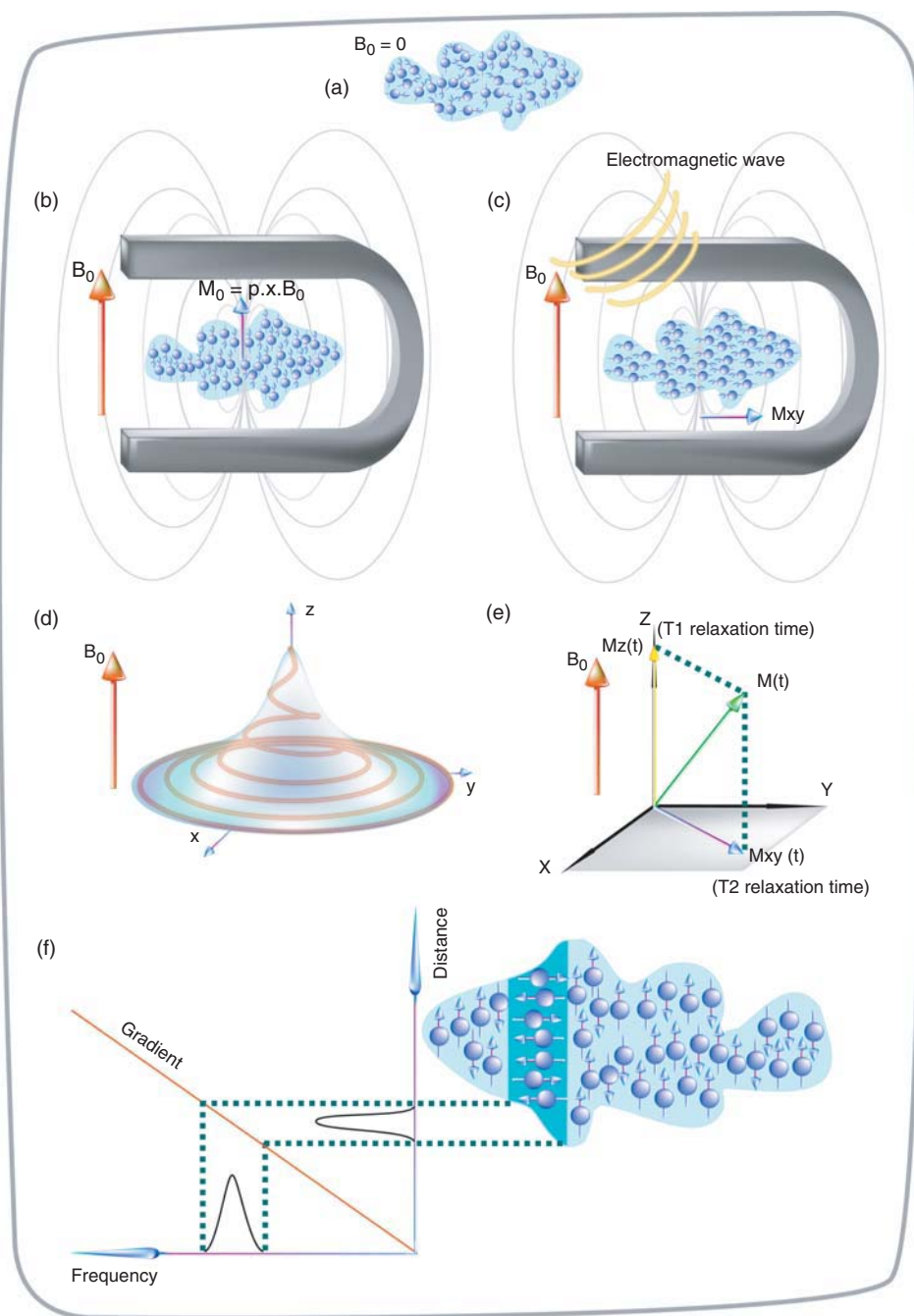
spin (Figure 7.1a). This magnetic moment allows the observation of a magnetic resonance signal caused by transitions between nuclear spin levels. Two hydrogen atoms are present in a water molecule, which is the principal constituent of living organisms. Their protons have the same resonance frequency and give one MR signal characteristic of the corresponding water molecule. Such MR signals are used to carry out anatomical and functional studies by MRI.

The sample is placed in a static magnetic field,  $B_0$  (Figure 7.1b), which polarizes the populations of hydrogen nuclei (Glover and Mansfield, 2002) so that a bulk magnetization  $M_0$  appears, which is proportional to the number of hydrogen nuclei ( $N$ ) and to  $B_0$  ( $M_0 \approx N\gamma^2\hbar^2 B_0 / 4k_B T$ , where  $\gamma$  is the gyromagnetic coefficient,  $\hbar$  is Planck's constant divided by  $2\pi$ ,  $k_B$  the Boltzmann's constant, and  $T$  is the temperature). This magnetization, which is flipped using a radiofrequency pulse created by a radiofrequency probe (Figure 7.1c), returns along the direction of  $B_0$ , inducing in a detection probe a signal of which pulsation  $\omega_0$  is proportional to the magnetic field intensity, following the Larmor frequency law:  $\omega_0 = \gamma B_0$  (Figure 7.1d,e).

The time constant, which describes how the magnetization returns to its equilibrium value, is called the *spin-lattice (or longitudinal) relaxation time*,  $T_1$ . This process involves an exchange of energy between the spins and the environment. However, it must be pointed out that additional relaxation processes occur, which involve interactions between the spins without any change in the relative population of the energy levels. They induce dephasing of their magnetizations in the plane perpendicular to  $B_0$ . This phenomenon is described by the time constant  $T_2$ , which is called the *spin-spin (or transverse) relaxation time*. Notably,  $T_2$  is  $\leq T_1$  in biological tissues. Moreover, the heterogeneity of  $B_0$  in the sample also contributes to the decay of the transverse magnetization. This contribution is made by the time constant  $T_2^*$ , whose value is given by  $1/T_2^* = 1/T_2 + 1/T_2^{\text{inh}}$ . As a consequence of these two phenomena the  $T_1$ ,  $T_2$ , and  $T_2^*$  of water protons in a biological tissue can be measured. Notably, these relaxation parameters depend on the tissue and on  $B_0$ , and are used to obtain contrast in the MR images. For example, anatomical images are obtained using  $T_1$  or  $T_2$  weighted images, using MRI pulse sequences, which minimize  $T_2^*$  effects and avoid susceptibility artifacts. The  $T_2^*$  value is also very sensitive to susceptibility variations;  $T_2^*$  weighted experiments are used, for example, in fMRI, based on the blood oxygen (paramagnetic) level in vessels and its effects on surrounding tissues.

As shown above, when a sample is placed in a homogeneous static field  $B_0$ , all the nuclei have the same resonance frequency, and only one signal is recorded without spatial information. To form an image of the sample, magnetic fields gradients have to be used. They establish a linear relation between the spatial positions of the nuclei and their frequency resonances, so the spatial information is contained in the MR signal (Figure 7.1f).

The quality of an image is also related to the spatial resolution, the signal-to-noise ratio (SNR), and the contrast between the different tissues or organs. These three parameters are not completely independent.



The spatial resolution achievable depends on the product of the strength of each gradient and its application duration. Consequently, there should be no limit in spatial resolution.

Actually, the spatial resolution is limited by the SNR, and the diffusion of the water molecules; in fact, the spatial resolution achieved is about 10  $\mu\text{m}$ . However, for *in vivo* experiments the total experimental time has to be taken in account, and the question is “How to increase the sensitivity and resolution power of MRI?” Diffusion is a physical parameter that depends on the biological tissue studied, and cannot be changed. Even if the SNR depends on the biological sample, it also depends on the hardware. In fact, the SNR depends on the initial magnetization ( $M_0$ ) linked to  $B_0$ , on the coils, and on transmitter/receiver circuits. It also depends on the local  $B_0$  homogeneity, linked to gradient and shim coil systems. Most improvements made to increase the sensitivity and resolution power of MRI concern magnets, gradient coils systems, and radio-frequency probes used for emission and reception.

The contrast between two different tissues can be characterized by the contrast-to-noise ratio  $[C = (S_1 - S_2)/(\sigma_1^2 + \sigma_2^2)^{1/2}]$  where  $S_i$  and  $\sigma_i$  are the mean of the signal and standard deviation of the noise  $i = 1, 2$ , respectively]. It is linked to the difference between signal intensities (contrast) in the different tissues, which can

**Figure 7.1** Summary illustrating the basic principles underlying nuclear magnetic resonance. (a) A fish submitted to a natural magnetic field; hydrogen nuclei are randomly aligned, resulting in a null resultant magnetic field. (b) A fish submitted to a strong magnetic field,  $B_0$ . Each hydrogen nucleus (proton) gives rise to a magnetic moment ( $\mu = \gamma I$  where  $I$  is the spin moment of the proton and  $\gamma$  is the gyromagnetic ratio characteristic of proton), which precesses around  $B_0$  at the Larmor frequency  $\nu_0 = \gamma B_0 / 2\pi$ . Considering Cartesian coordinates with the z-direction along  $B_0$ ,  $\mu$  has a stationary component along z and a component rotates at the Larmor frequency in the x-y plane. In the fish, all the magnetic moments of protons have the same Larmor frequency. The  $\mu_{xy}$  are spread over the x-y plane, and there is no net magnetization  $d$ . The  $\mu_z$  components can be parallel or antiparallel to  $B_0$ . The difference in population in the two states follows the Boltzmann distribution with a surplus in the lower energy state (parallel), and gives rise to a macroscopic magnetization  $M_0$  parallel to  $B_0$ . (c) A fish submitted to  $B_0$ , and to an oscillating field  $B_1$  (at Larmor frequency) perpendicular to  $B_0$ . A pulse, which consists of turning on  $B_1$  during a given time then turning it off, flips

the macroscopic magnetization in the x-y plane ( $M$ ), and a MR signal can be detected. (d) After turning off  $B_1$ , the magnetization precesses around  $B_0$  and returns to the equilibrium state. (e) Two time constants  $T_1$  and  $T_2$  characterize the exponential return to equilibrium of the longitudinal  $M_z(t)$  and the transverse  $M_{xy}(t)$  components, respectively.  $T_1$  is the longitudinal or spin-lattice relaxation time. The spin-lattice relaxation involves an energy exchange between the spin and the lattice, with these two systems being coupled via molecular motion.  $T_2$  is the transverse or spin-spin relaxation time. Spin-lattice relaxation contributes to  $T_2$ , but additional processes occur, which dephase the spins without energy exchange with the lattice. The value of these two relaxation times depends on the considered tissue. In a fish,  $T_1$  and  $T_2$  depend on the different organs. This property is used to produce contrast between biological structures in MR images. (f) The application of a linear magnetic field gradient, along a defined direction, associated with a selective pulse allows us to excite selectively protons contained in a given virtual slice perpendicular to the gradient direction, and to obtain a MR image of this slice.

arise from the difference of concentration, relaxation times, or diffusion properties of water molecules. These different contrasts can be used to readily discriminate the different tissues in order to obtain anatomical or functional data. Noticeably, the contrast-to-noise ratio between two tissues also depends on their own SNRs. Increasing the resolution power decreases these SNRs, but it also decreases the partial volume effects occurring in the border pixels, and allows us to readily discriminate these tissues. Below, we will look at the influence of these different hardware systems on the sensitivity and resolution power of MRI.

### 7.2.2

#### Hardware Improvements

As the signal intensity is proportional to  $B_0$ , increasing  $B_0$  leads to higher sensitivity of the measurement. Specialized high-field MRI systems ( $4.7 \leq B_0 \leq 17.6$  T) are well suited for high-resolution studies on small animals. Moreover, they are equipped with small bore gradient systems able to reach large amplitudes, which readily give fast access to high spatial frequency information. However, the signal intensity also depends on the radio-frequency probe (also known as the coil or resonator) used, which has to match the sample. A coil can receive or transmit or do both. The most common types of probes are surface coils (high sensitivity but produce a non-homogeneous magnetic field) and birdcage type coils (lower sensitivity but produce a homogeneous magnetic field). For experimental studies at high field, they can be combined to optimize homogeneity of the emission and sensitivity of the reception. Another way to optimize the MRI measurement is to develop “phase-array” coils, which are commonly used for clinical studies (Mispelter, Lupu, and Briguët, 2006).

Even dedicated high-field systems, usually employed for experimental studies, can also be performed at low field using standard clinical whole-body MR scanners and may be of interest for some studies, particularly those using clinical contrast agents. The low SNR available at the typical field strength of 1.5 T may be overcome thanks to, for example, the use of specially designed radio-frequency probes in a superconducting material (Poirier-Quinot *et al.*, 2008).

### 7.2.3

#### Contrast

To assess the morphology of marine organisms, Optimized SNR and resolution are often not good enough to assess morphology. If signal differences do not exist between different structures inside the image, the image will be flat and featureless. Thus an adequate contrast, or signal-to-background ratio, is required to distinguish structures of interest. For a given tissue the signal intensity depends on the proton density (water content), the relaxation parameters ( $T_1$ ,  $T_2$ , or  $T_2^*$ ), and the diffusion properties of protons. These quantities vary from one tissue to another and are responsible for contrast between tissues. Different MR imaging protocols may be used to control the degree of contrast that can be achieved (referred to as the *image*



“weighting”). In 1980 Hansen *et al.* published the first anatomically interpretable MR images of a normal living rat body (Hansen *et al.*, 1980) and thus laid the groundwork for the many MR applications in small animals that soon followed.

#### 7.2.4

#### Applications

##### 7.2.4.1 Anatomical MRI

Owing to the variation of  $T_1$ ,  $T_2$ , or proton density between the tissues, MRI makes it possible to visualize most body organs (Figures 7.2 and 7.3). It allows us to generate cross-sectional images detailing brain structure (gray matter, white matter) (Narasimhan and Jacobs, 2002), or other aspects of body morphology (Kabli *et al.*, 2006; Null *et al.*, 2008; Ziegler *et al.*, 2008). Such images are recorded with spin-echo type sequences, which are rather insensitive to  $B_0$  heterogeneities and susceptibility effects. Noticeably, at high field ( $B_0 > 4.7$  T), anatomical images are based on  $T_2$  weighting techniques, whereas below this value anatomical images are obtained with  $T_1$  weighting protocols. The typical pixel size obtained is between  $100 \times 100$  and  $10 \times 10 \mu\text{m}^2$ . For example, anatomical images have been obtained, *in vivo*, on a whole mouse brain with a voxel size of  $78 \times 78 \times 500 \mu\text{m}^3$  at 7 T in 15 min, and *in vitro* on a fixed specimen of about the same size with voxels of  $43 \times 43 \times 43 \mu\text{m}^3$  at 9.4 T in less than 7 h.

##### 7.2.4.2 Functional MRI

Neural activity in the brain is accompanied by local changes in blood flow and thus oxygen levels. As oxygen is paramagnetic, the  $T_2^*$  of the tissues are locally affected. The difference in  $T_2^*$  relative to surrounding tissues causes a contrast between the tissues, referred to as the blood oxygen level dependent (BOLD) response (Ogawa *et al.*, 1990). fMRI is now recognized as the most prominent research tool in cognitive neuroscience (Poldrack, 2008; Dolan, 2008). It can also be used on animal models (Silva *et al.*, 2011). The fMRI images are often obtained with gradient echo type sequences ( $T_2^*$  weighting) and using an echo planar imaging (EPI) acquisition scheme to obtain images with a very good temporal resolution.

##### 7.2.4.3 Diffusion Tensor Imaging or Diffusion MRI (DTI)

Water diffusion in tissue is an intrinsic physical three-dimensional process. For most anatomical studies its effect has to be minimized. However, for specific purposes, water diffusion in biological tissues at a microstructural level can be used deliberately to generate contrast (Basser and Pierpaoli, 1996) by a method named diffusion tensor imaging (DTI). DTI is a powerful tool, providing access to the mean diffusivity, diffusion anisotropy, and fiber orientation in tissues (e.g., neuronal and muscular tissues). It offers a more direct and non-invasive method of measurement of the local orientations in tissues compared with other conventional 3D imaging techniques (Beaulieu and Allen, 1994; De Groof *et al.*, 2006; Aggarwal *et al.*, 2009). The most advanced application of DTI is fiber tracking in the central nervous system (Le Bihan, 2003).

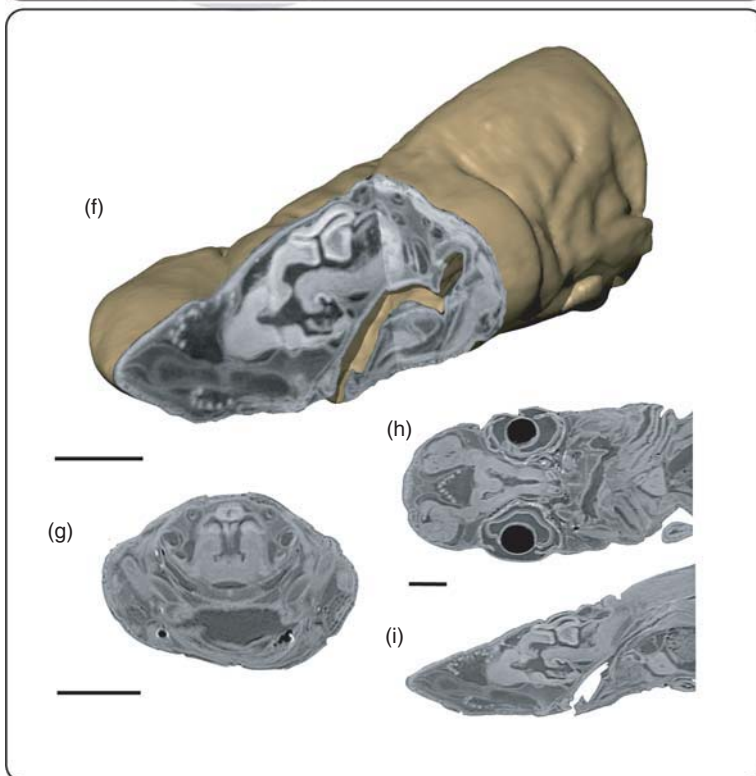
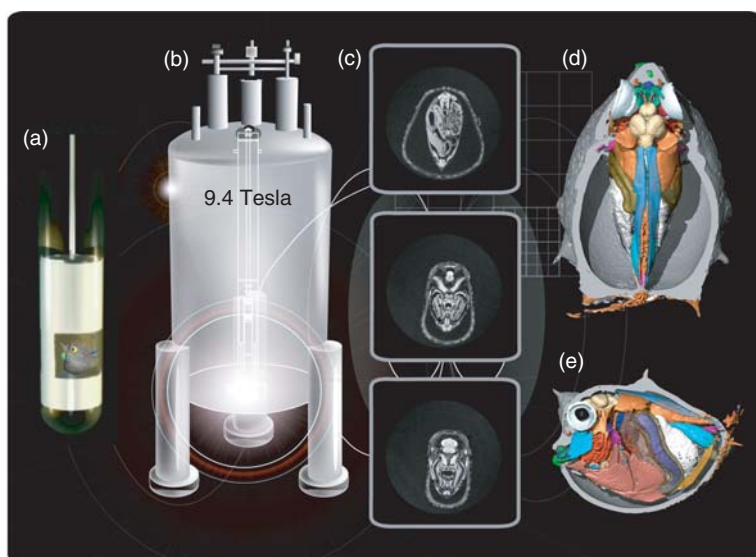


**Figure 7.2** High-field MRI experimental setup. (a) MRI volumic probe enclosing the scrawled cowfish species *Acanthostracion quadricornis*. (b) Vertical high-field magnet 9.4 T with integrated gradient and shim systems. (c) Top, middle, and bottom virtual coronal slices of the body start at the middle trunk and finish at the level of the head (you can see the brain). Volume rendering of a scrawled cowfish in (d) dorsal and (e) lateral views. Note that

the dorsal part of the cowfish has been virtually removed. Visually classification of features of the organs (muscles, brain, live, eyes, etc.) allow a virtual dissection of the specimen. (f) Iso-surface three-quarter view of the head with cutting planes of the velvet belly lantern shark *Etmopterus spinax*, and virtual slice; (g) coronal, (h) frontal, and (i) sagittal planes. Scale bar = 5 mm.

The DTI sequence is obtained by inserting diffusion gradients in a spin-echo sequence, to link the proton signal intensity of a water molecule to its diffusion properties, more particularly diffusion rate and direction. At least six different gradient directions (30 are usual in experimental studies) must be used during acquisitions to allow calculation of the diffusion tensor. The diffusion tensor is a symmetric  $3 \times 3$  matrix, the eigenvalues of which are related to the diffusivities along three directions given by the eigenvectors. The first eigenvalue represents diffusion along the preferred or primary direction, while the second and third relate to perpendicular directions. Noticeably, the different gradient directions are obtained from combinations of gradients applied in the three spatial directions. To minimize the acquisition time and avoid movement artifacts rapid schemes for acquisition are used (EPI or spiral).

#### 7.2.4.4 MEMRI or Manganese-Enhanced Magnetic Resonance Imaging

Manganese(II) ( $\text{Mn}^{2+}$ ), a well-known  $\text{Ca}^{2+}$  analog, has been used in the field of light microscopy in conjunction with fluorescent dyes such as fura-2 to indirectly monitor the influx of  $\text{Ca}^{2+}$  ions, which is an indicator of neuronal spiking activity. In addition,  $\text{Mn}^{2+}$  is also paramagnetic, causing positive contrast enhancement in  $T_1$ -weighted MRI images in tissues where it accumulates. These properties have led to the development of manganese-enhanced magnetic resonance imaging (MEMRI) for cerebral (Massaad and Pautler, 2011) and cardiac (Edelman, 2004) studies. However, as  $\text{Mn}^{2+}$  is neurotoxic it can only be used in experimental studies with well-defined protocols (Canals *et al.*, 2008). MEMRI is principally used for three types of brain studies (Silva *et al.*, 2004). First, as  $\text{Mn}^{2+}$  accumulates in cells in an activity-dependent manner, it can be used to monitor activity in the brain.  $\text{MnCl}_2$  is infused while the brain is stimulated. In this technique, referred to as activity-induced manganese-enhanced magnetic resonance imaging (AIM-MRI),  $\text{MnCl}_2$  is bath-applied while the brain is stimulated. Second, the use of  $\text{Mn}^{2+}$  as an *in vivo*, trans-synaptic, MRI-detectable neuronal tract tracer has also been demonstrated (Tucciarone *et al.*, 2009). In this case  $\text{MnCl}_2$  is locally injected to the target organ. The third use of MEMRI is to enhance the contrast in animal brain cytoarchitecture using systemic injections. Taken together, results in the literature indicate that MEMRI provides an efficient and powerful *in vivo* method for following brain development in physiological and physiopathological studies (Gillet *et al.*, 2010).

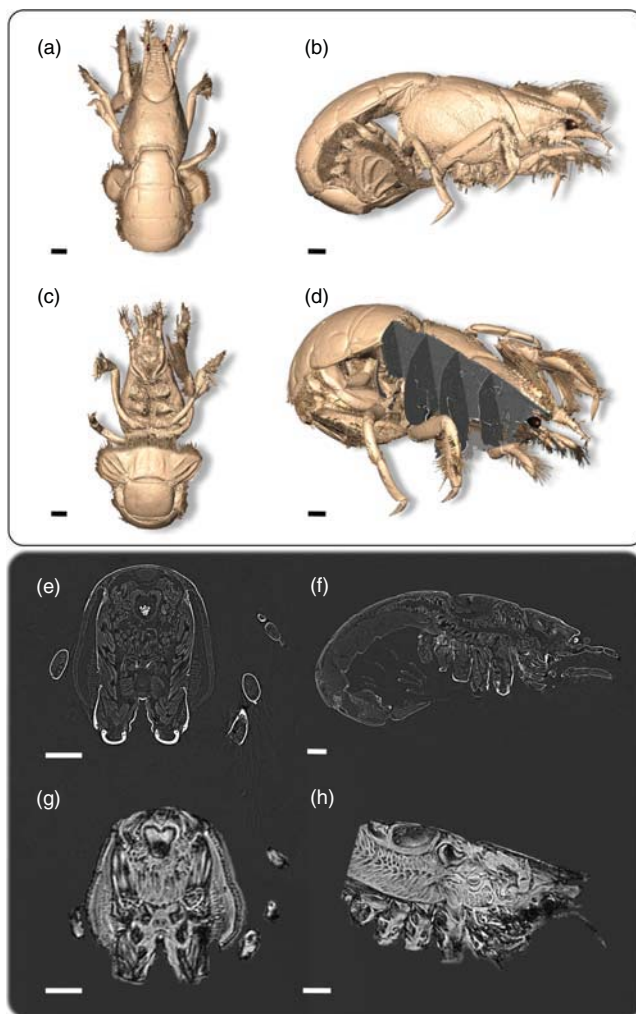


**Figure 7.3** Comparison between synchrotron phase-contrast X-ray microtomography and microscopy MRI of the Thalassinidea shrimp *Upogebia pusilla*. Views of the iso-surface of the shrimp: (a) dorsal, (b) lateral, (c) ventral, and (d) three-quarters,

with cutting planes and coronals slices. Virtual slice obtain by X-ray phase-contrast microtomography: (e) coronal and (f) sagittal plane. Virtual slice obtain by a high-field MRI (g) coronal and (h) sagittal plane. Scale bar = 1 mm.

### 7.3

#### X-Ray Microtomography

X-Rays were discovered as early as 1895, and their immediate first practical application was in biological and medical imaging. Computed tomography (CT) was developed in the late 1960s and extends X-ray radiography from two to

three dimensions. This is achieved by acquiring projections (i.e., radiographs) of an object along different directions and computing a cross-sectional slices (Cormack, 1963; Hounsfield, 1972, 1973) through the object or a complete 3D volume reconstruction (corresponding to virtual slice stacks). Since the 1980s, this technique has been primarily used for medical applications [i.e., large-scale biological samples with a resolution of about 1 mm (Kalender, 2006)]. However, with the arrival of synchrotron radiation (SR) and high-resolution CT equipment, tomography has been considerably improved and samples can now be imaged at submicrometric resolution (Baruchel *et al.*, 2008), with effective pixel sizes down to about 50 nm (Langer *et al.*, 2012).

### 7.3.1

#### Sources

##### 7.3.1.1 Laboratory-Based Setups

In contrast to synchrotron sources, laboratory sources can be installed in relatively confined spaces with small high-voltage generators (typically 50–450 kV). The electrons are produced by the thermionic emission of a heated filament at the cathode side, and are then accelerated and focused in a vacuum environment before hitting the anode. The collision of electrons on the anode material is responsible for the X-ray photon generation. Part of the radiation is produced by the deceleration of the electrons (bremsstrahlung or braking radiation) while another part of the radiation is released when electrons from a higher electron shell of the anode material atoms fill up vacancies in the lower electron shells where electrons were knocked out during the collision (characteristic radiation). The X-ray photons of the bremsstrahlung spectrum have an energy ranging from a few kilo-electronvolts up to the energy corresponding to the acceleration voltage (this is why laboratory sources are polychromatic). In contrast, the energy of characteristic radiation photons corresponds to the difference in energy of the initial and final orbital jump of the electron that filled the vacancy. The combination of both radiation types is the spectrum of an X-ray tube and is thus dependent on the acceleration voltage (setting in kilovolts of a tube) and the anode material. Typically, the anode is made of a metallic material with a high melting point, such as tungsten, because most of the energy of the colliding electrons is transformed into heat and only 1% into X-ray photons. This spectrum can be altered by placing filters between the source and the detector.

X-Ray CT with laboratory sources is also often called *cone-beam tomography* (Figure 7.4b,d) since the photons that are produced in a small location in the anode material, the focal spot, are dispersed in all directions. The photons that are directed toward the 2D imaging detector placed in front of the source make up the field of view. For every object placed inside the field of view, a transmission image, or radiograph, can be recorded. As the beam is conic, the radiograph of an object that is placed close to the source will be projected as a magnified transmission image on the detector, this magnification  $M$  equals the relative difference between the source–object distance (SOD) and the source–detector distance (SDD). For this

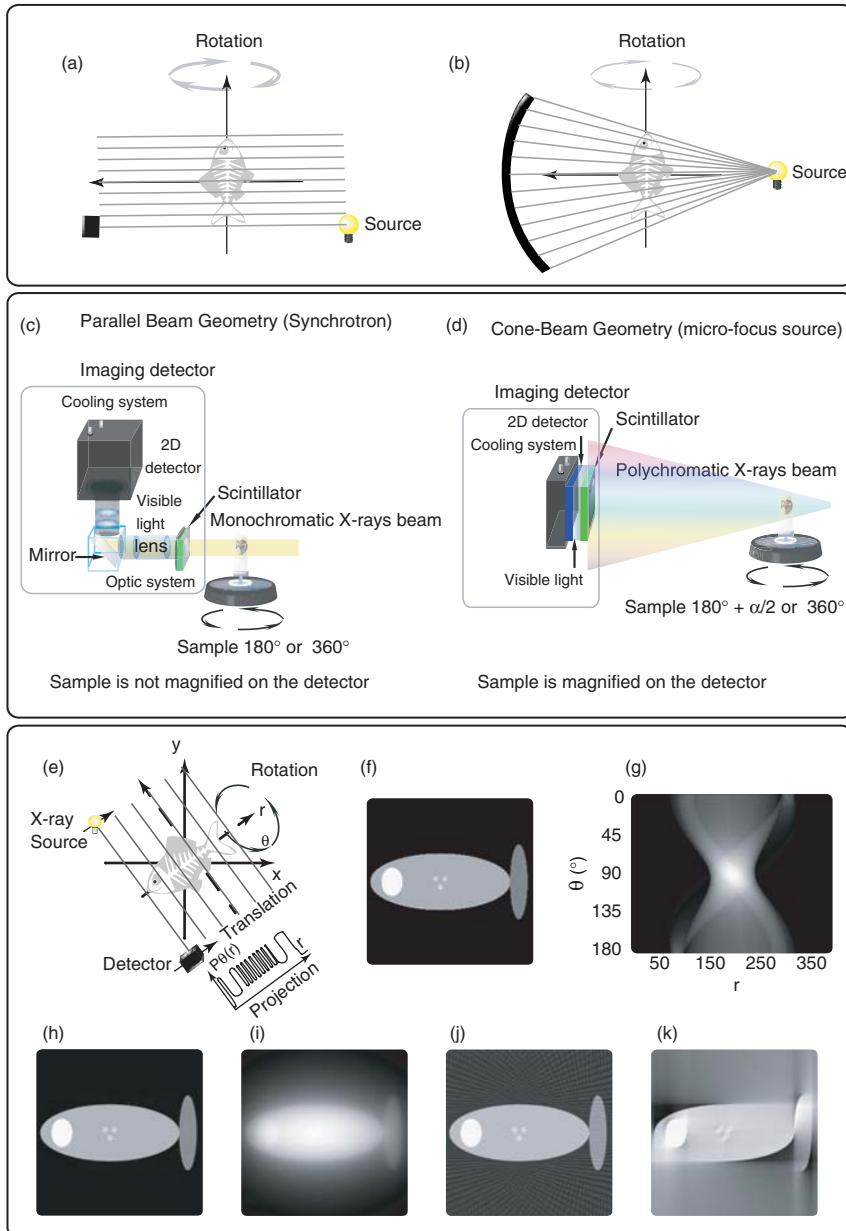


**Figure 7.4** Principle of 2D and 3D CT. (a, b) Geometry of acquisition system in 2D CT: (a) translation–rotation acquisition (first generation); the attenuation of a thin X-ray pencil beam is measured on a single detector. The X-ray source and detector are then sequentially translated and rotated. (b) Fan-beam acquisition (third generation). The attenuation of a fan beam X-ray source is recorded on a linear detector. (c) Optical paths of X-rays in 3D parallel beam synchrotron radiation microtomography (SR- $\mu$ CT). (d) Optical paths of X-rays in 3D cone-beam desktop microtomography ( $\mu$ CT). In both cases, when the sample is sequentially rotated, a set of radiographs is acquired. They are processed through a tomographic reconstruction algorithm to obtain the 3D digital image of the sample. (e)–(k) Illustration of

data acquisition and tomographic reconstruction in 2D parallel CT. (e) For a given angle of projection, one projection is measured on parallel X-ray paths. A complete data set (sinogram) includes all projections when the angle varies between 0 and 180°. (f) Original synthetic 256 × 256 “fish” image and (g) corresponding sinogram (or Radon transform) of the “fish” image. (h) Tomographic reconstruction of the “fish” image from the FBP algorithm: each projection is filtered and then back-projected. (i) Reconstruction without filtering the projections: a blurred image is obtained, (j) FBP reconstruction after using a limited number of projections: streak artifacts appear, and (k) FBP reconstruction from projections in the 0–90° range: distortions appear due to missing information.

reason, the resolution ( $R$ ) of a CT-scan is a combination of the pixel size ( $d$ ) of the detector, the magnification ( $M$ ) of the object, and the size of the X-ray focal spot ( $s$ ):

$$R = \frac{d}{M} + s \left( 1 - \frac{1}{M} \right)$$

In this way, using a small focal spot and large magnification, small objects can be scanned with good image resolution. With present laboratory sources a spot size of <1  $\mu$ m can be achieved.

### 7.3.1.2 Synchrotron-Based Setups

A synchrotron is a particle accelerator that can be used to generate electromagnetic radiation and, in particular, X-rays. Synchrotrons used for microtomographic applications in biological imaging are distributed worldwide and include the following: Canadian Light Source (Canada), the Advanced Photon Source APS, the Advanced Light Source ALS, and the National Synchrotron Light Source NSLS (USA); Shanghai Synchrotron Radiation Facility (SSRF); Pohang Light Source PLS (Korea), SPring-8, and the KEK Photon Factory (Japan); European Synchrotron Radiation Facility ESRF and Synchrotron Soleil (France), Angströmquelle Karlsruhe ANKA, Helmholtz-Zentrum Berlin HZB/BESSY, and Deutsches Elektronen-Synchrotron DESY (Germany), Elettra Sincrotrone Trieste (Italy), the Swiss Light Source SLS (Switzerland), and Diamond Light Source (UK); and the Australian Synchrotron (Australia). Compared to conventional X-ray sources, synchrotrons have the advantages of a wide energy range (4–200 keV), high photon flux, and a monochromatic ( $\Delta E/E \approx 10^{-2}$ – $10^{-4}$ ), parallel, and partially coherent beam (Figure 7.4a,c; Betz *et al.*, 2007; Baruchel *et al.*, 2008). In terms of performance for  $\mu$ CT, the main advantages of using SR over X-rays from laboratory generators are, first, the higher spatial resolution that can be obtained and, second, the higher density resolution (or better contrast) (Betz *et al.*, 2007). In terms of sample preparation, X-ray imaging techniques can be non-destructive (Boistel *et al.*, 2009) and selective to a wide range



of properties (density, chemical elements, chemical bonds, strains), and provide 3D morphometric information with resolution down to nanoscales.

Synchrotron facilities are very large installations, with circumferences ranging from about 100 m (ANKA) to about 1500 m (SPring-8). A synchrotron is a closed-orbit particle accelerator that, when built for the generation of X-rays, uses charged particles, such as electrons, to produce very intense light beams. The operating principle of a SR facility is schematically represented in Figure 7.5. As in a conventional X-ray generator, the electrons are produced by the thermionic emission of an electron gun. However, they are accelerated through the sequence of a linear accelerator (LINAC; Figure 7.5a) and, usually, a first circular accelerator (booster ring; Figure 7.5a) where they reach their final energy level (respectively

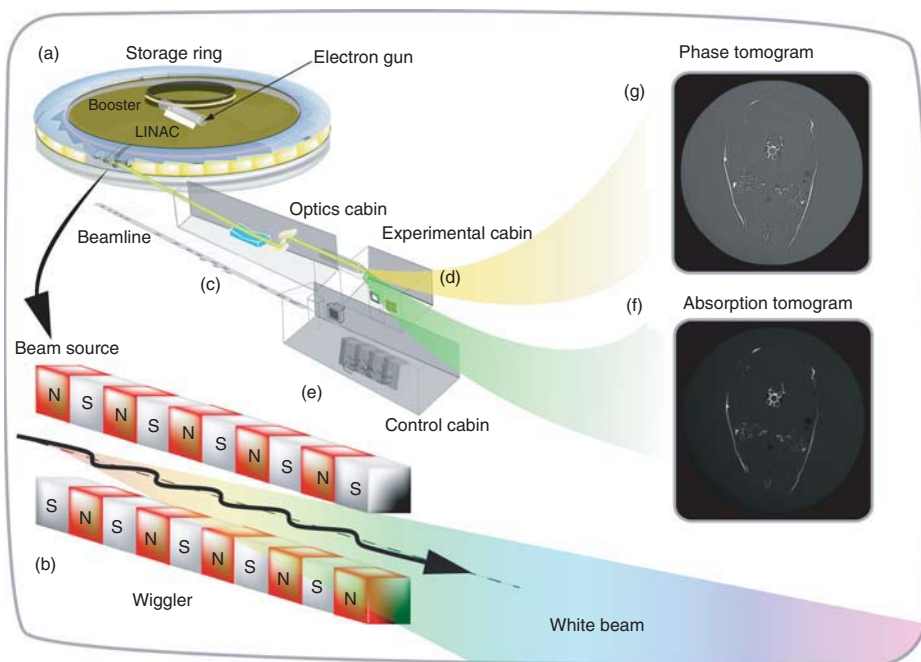


**Figure 7.5** Schematic summary of a third generation synchrotron facility. Third generation synchrotron (a): electrons are emitted by an electron gun and first accelerated in a linear accelerator (LINAC) before being transmitted to a circular accelerator (booster ring) where they are accelerated to reach an energy level of several billion electron-volts. These high-energy electrons are then injected into the large storage ring where they circulate in a vacuum environment at a constant energy level. Beamline are constituted of a beam source (b) and three cabins:

(c) optics, (d) experimental, and (e) control cabin. Radiographs exhibiting absorption and interference patterns attributable to Fresnel diffraction are recorded at two distances: (f) close to the sample in absorption and (g) far from the sample to obtain phase contrast; (f) and (g) are, respectively, absorption and phase-contrast images of a virtual transverse slice of *Osmerus eperlanus* at trunk level. Bone tissues only are visible on the absorption image, whereas bone and soft tissues can be visualized on the phase-contrast image.



8, 6, and 2.75 GeV at the SPring-8, ESRF, and Soleil facilities) before entering a final accelerator, the storage ring, in which they are kept at constant operating energy. Electrons in the booster and storage ring travel close to the speed of light (Figure 7.5a). The storage ring is a polygon made of straight sections angled together with bending magnets (dipole magnets). SR is produced whenever the electrons in the storage ring deviate from a straight travel path. In practice, this is the case in the bending magnets, but also in special arrays of magnets called *insertion devices* (undulators and wiggler), which are placed in the straight sections of the ring. A bending magnet provides a uniform magnetic field, whereas an insertion device provides a spatially periodic magnetic field. As bending magnets, wigglers, and undulators are considerably different, it is important to know their characteristic radiation spectra and choose the one best suited for a given experiment. Indeed, the electrons follow a bending path with bending magnets and a wiggling path with inserted devices (which produces more intense and tunable light) (Figure 7.5b). Bending magnets and wigglers produce a continuous spectrum of X-ray wavelengths, whereas undulators produce a line spectrum. In any case, the X-ray beam produced by a synchrotron is many orders of magnitude brighter than that produced by a laboratory X-ray machine. Synchrotron X-rays are exploited in experimental stations (or “beamline”) located outside the radiation shielding of the storage ring. Each beamline includes an optical cabin, an experimental cabin, and a control cabin (Figure 7.5c–e, respectively). The optical cabin contains diaphragms, slits, filters, and a shutter that allows for control of the bandwidth, photon flux, and beam dimensions of the X-rays. Synchrotron X-ray sources deliver X-rays with a large energy spectrum range (white beam). A wavelength adapted to the specimen under investigation is selected by a suitable combination of absorption filters and mirror reflections (“pink” beam) and/or by a monochromator (e.g., a set of Bragg crystals or a multilayer system). In the experimental cabin one or several detectors record the signal produced as a result of the interactions between the X-ray beam and the sample. The researchers conducting experiments at a beamline control the experimental equipment and the data collection process remotely from a control cabin located near the experiment. In several synchrotrons, long beamline are available that deliver a relatively large beam that is several centimeters wide. This is particularly useful for imaging techniques such as  $\mu$ CT. For example, the experimental station of beamline ID19 at the ESRF is located 150 m from the source point in the storage ring, and the beamline of the Biomedical Imaging Center (RI Laboratory) at the SPring-8 synchrotron in Japan reaches a record length of 1 km. SR can be used for many imaging methods, including (i) absorption  $\mu$ CT [using the intrinsic sample contrast (Figure 7.5f) or with a contrast agent]; (ii) X-ray PCI (Figure 7.5g), which can be classified into (1) free-space propagation methods, (2) crystal interferometer methods, (3) analyzer-based techniques, and (4) grating-based methods; and (iii) X-ray microspectroscopy, or chemical imaging. The latest developments can give access to these methods down to nanoscale resolution.

### 7.3.2

#### Sample Stage

To position the sample in the field of view and to adjust magnification, most CT-systems are equipped with several motorized stages. On the top of these positioning stages a rotational stage, upon which the sample is fixed, is mounted. By rotating the sample, radiographs in different angular orientations can be recorded. These radiographs are then further used to compute tomographic cross-sections of the objects. Precise and repeatable positioning are crucial to enable good reconstructions, especially at higher resolutions.

### 7.3.3

#### Detector

Most X-ray detectors currently used are composed of a scintillator (Figure 7.4c,d) and a light sensitive camera. The scintillator is a thin layer of material that emits light when interacting with X-ray photons. In this way, a portion of the X-ray photons are transformed into visible light that can be detected and recorded using a light-sensitive sensor (very similar to that of a digital photography camera). Scintillators can be made out of different polycrystalline or monocrystalline materials [cesium iodide (CsI), gadolinium oxysulfide (Gadox), yttrium aluminum garnet (YAG), lutetium aluminum garnet (LAG)], which have different sensitivities for X-ray photons with different energies.

The scintillator can either be placed in direct contact with the sensor (this is the case, for example, in the flat-panel detectors often used in laboratory-based  $\mu$ CT) or it can be coupled to the sensor via an optical system, for example, a fiber-optic system or a lens system. Lens systems consisting of visible-light microscope optics are used in high-resolution synchrotron-based microimaging, where the physical pixel size of the available digital sensors is too large to reach the desired spatial resolution with direct coupling, and magnification of the image created by the scintillator is therefore needed before it is recorded by the sensor.

Another important aspect is the sharpness of the image obtained. The visible light produced by the scintillator will propagate and scatter inside the scintillator layer; and so will secondary particles generated upon impact of the X-ray photons in the scintillator. These effects lead to blurring of the image. The thicker the scintillator, is the higher the probability of internal scattering and, therefore, the stronger the blurring. Moreover, in a microscope configuration the scintillator thickness should not exceed the depth of focus of the objective lens. For these reasons, the best resolving scintillators are usually rather thin.

The light-sensitive sensor (Figure 7.4c,d) itself is typically a solid-state device, such as a charge-coupled device (CCD) or a complementary metal–oxide–semiconductor (CMOS) system, similar to the sensors used in digital photography. It is actually a 2D array of very small sensor elements that translate the incident light photons into a digital signal (Figure 7.6c,f). Each of these small sensor elements will represent one picture element (pixel) in the resulting radiography image. These sensors

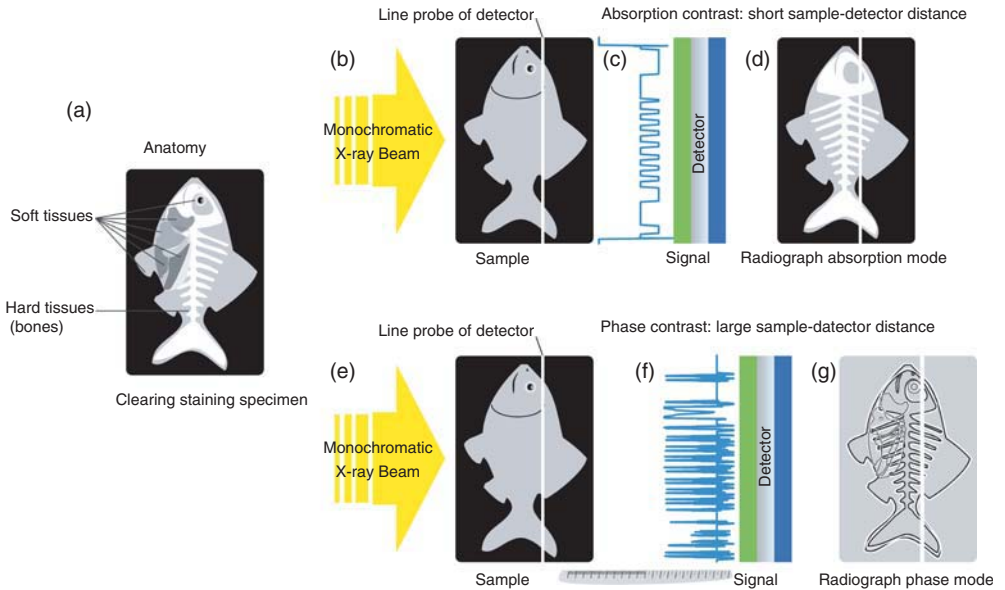


**Figure 7.6** The two types of contrast mechanism exploited in X-ray imaging of the anatomy of a sample (a), that is, absorption contrast (b–d) versus phase-contrast (e–g). (b, e) X-ray beam; (c, f) signals detected by the detector; (d, g) radiography. Comparison of the contrast obtained by absorption

(d) and phase contrast (g): in absorption (d) only the mineral part of skeleton (white) and uniform contrast for soft tissues (gray) is obtained, while in phase contrast (g) fringes in white and black are seen at the interface of different soft and hard tissues.

have an array size ranging from  $500 \times 500$  pixels (0.25 megapixel) to  $8000 \times 8000$  pixels (64 megapixel). If a  $1 \text{ cm} \times 1 \text{ cm}$  area of the scintillator is mapped on a sensor of  $1000 \times 1000$  pixels matrix, each pixel will have a maximum size ( $d$ ) of  $10 \mu\text{m} \times 10 \mu\text{m}$  and the center-to-center distance between adjacent pixels (pixel pitch) is  $10 \mu\text{m}$ .

In synchrotron facilities, owing to the large source–object distance, no significant magnification can be realized with restricted object–detector distances and, therefore, the resolution of a CT scan will be determined by the pixel size and the blurring introduced by the scintillator. Consequently, very thin scintillators are used. When the thickness is reduced, the probability of interaction with an X-ray photon is also diminished, resulting in a lower signal-to-noise. But as the flux of a synchrotron beam is extremely high, this does not constitute a real concern, at least in applications where the specimens are not radiation sensitive. In practice, the spatial resolution of a high-resolution X-ray imaging detector at a synchrotron is limited to approximately  $0.5 \mu\text{m}$ , both by scattering of secondary particles in the scintillator and by the diffraction limit of resolution in the visible-light microscopy optics that project the image created in the scintillator onto the surface of the digital sensor. Higher spatial resolution – going down to a few dozen nanometers – can be reached, but this requires the use of X-ray optical elements to magnify the image

even before it impinges on the scintillator. Such methods are usually referred to as “X-ray microscopy” methods.

With laboratory sources, on the other hand, the flux is more limited and it is thus crucial to detect as many photons as possible by using a thicker scintillator. To obtain sharp images with such a thicker scintillator the pixels will have to be larger, but since the resolution is determined by the magnification, the pixel size is not important and so relatively large pixels are recommended.

#### 7.3.4

##### Forward Problem (Contrast Formation)

A radiograph of an object is an image containing information on the intensity of the X-ray beam after being transmitted through the object ( $I$ ) that can be compared with the beam intensity without the object ( $I_0$ ). Using digital detector systems, an image without the object in the field of view is recorded first (flat-field image) and each pixel of the X-ray detector will return a digital signal (counts) that is related to the number of X-ray photons that interact with the pixel. Since every pixel has a slightly different efficiency, and due to other fluctuating parameters, it is important to record such a flat-field, which represents the intensity  $I_0$  of the beam and detector response in every pixel. Once an object is placed inside the field of view, the X-ray photons will have to travel through the object before hitting the detector. During travel through the object, an interaction between the photon and the object’s material may occur. If such an interaction does occur, the photon will not reach the detector, or reach it at a different position, and thus the intensity of the beam ( $I$ ) will be different. The ratio of the beam intensity with and without an object in the beam is usually referred to as transmission.

Two types of interaction with matter are commonly used as contrast modes in standard (attenuation-contrast) X-ray (Figure 7.7) tomography of marine life: photoelectric absorption and Compton scattering (Figure 7.5). In the case of photoelectric absorption, the entire energy of the interacting X-ray photon is used to knock an electron out of the shell of an atom of the object and the photon is totally absorbed (Figure 7.7a). With Compton scattering, the energy of the photon is considerably higher than the binding energy of the electron and an interaction will result in a loss of energy of the photon and cause a change in direction. Both effects cause the beam intensity to diminish in the forward direction when the photons are travelling through the object. Whether a photon will interact is a statistical process; therefore, a relatively large number of photons have to be sent through the object to measure a correct transmission value.

The probability of such an interaction depends on the energy of the photon, the thickness of the object ( $L$ ), and the composition of the object and its density. In the following we assume a monochromatic X-ray beam of energy  $E$  with incident intensity  $I_0$ , and an attenuated intensity  $I$  after passing through the object. For a homogeneous material, the Beer–Lambert law expresses the exponential decay of the intensity  $I$  as a function of the material thickness  $L$  multiplied by its linear attenuation coefficient  $\mu$ . For an inhomogeneous object, the Beer–Lambert law

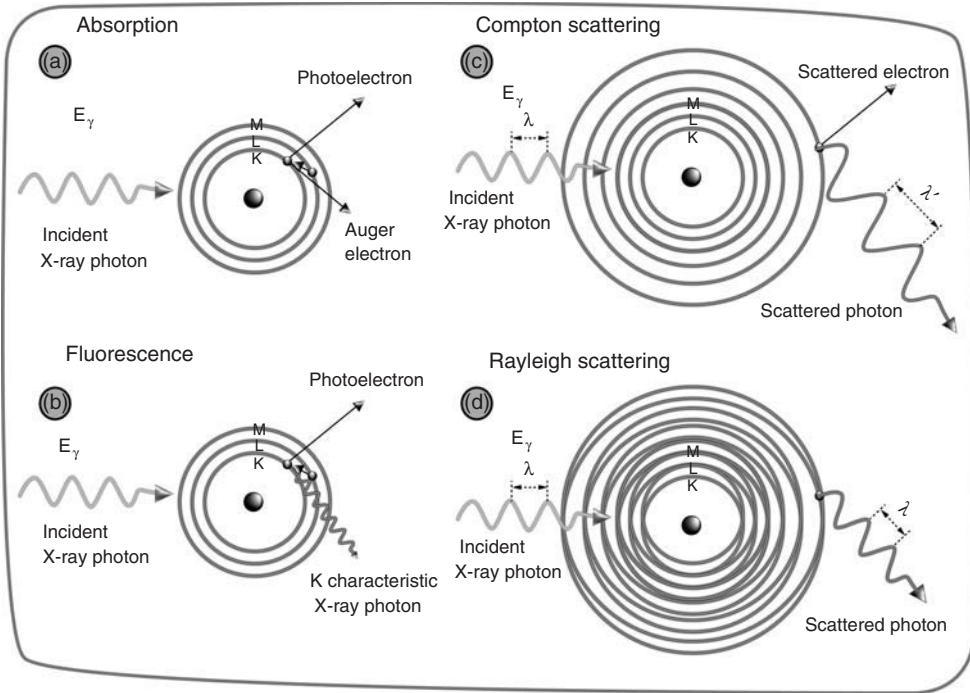


**Figure 7.7** Summary illustrating the different types of X-ray interactions. (a) Photoelectric absorption results in total removal of the incident X-ray photon with energy greater than binding energy of electron in its shell, with the excess energy distributed to kinetic energy of photoelectron. (b) X-ray fluorescence: excitation of an atom by an X-ray photon results in decay of the excited state by either X-ray fluorescence or the Auger

effect. K, L, and M are the core electron levels. (c) Compton scattering interactions occur with essentially unbound electrons, with the transfer of energy shared between recoil electron and scattered photon. (d) Rayleigh scattering is an interaction with an electron (or a whole atom) in which no energy is exchanged and the incident X-ray energy equals the scattered X-ray energy with a change in direction.

can be generalized to:

$$I = I_0 \exp \left[ - \int_D \mu(x, y) ds \right] \quad (7.1)$$

where  $\mu(x, y)$  denotes the map of linear attenuation coefficients for energy  $E$  at each point  $(x, y)$ , and  $D$  is the straight line joining the X-ray source to the detector pixel under consideration.

The mass attenuation coefficient, defined by the ratio  $\mu/\rho$ , where  $\rho$  is the density of the material, is related to the atomic number of the different elements in a material. The higher the atomic number of the elements of the material, the higher the mass attenuation coefficient and therefore the more probable that an X-ray photon will interact with the material. This mass attenuation coefficient varies for

different materials and also varies with the photon energy. Generally, the higher the photon energy the higher, the chance it will travel through the object without interacting.

### 7.3.5

#### Tomographic Reconstruction

At a given detector point, the measured transmitted intensity  $I$  gives access to the integral over the line  $D$  of the unknown image function  $\mu$ , known as a *projection value* for this detector point:

$$\int_D \mu(x, y) ds = \ln \left( \frac{I_0}{I} \right) \quad (7.2)$$

The organization of the projections values depends upon the acquisition system, which has evolved from the 2D parallel or fan-beam geometries to the 3D parallel or cone beam geometry (Figure 7.4) (Kalender, 2005).

Tomographic reconstruction consists of processing all measurements to reconstruct the digital image of the object. Owing to the nature of these data, this inverse problem is known as *image reconstruction from projections* (Herman, 1980).

Image reconstruction methods were first developed for 2D translation–rotation CT scanners, historically proposed by Hounsfield (1973, Figure 4a). This geometry is known as a *2D parallel beam geometry* since for a given rotation angle all projection rays are parallel. In this case, the problem is equivalent to inverting the Radon transform of the image; it was solved in a purely theoretical context by the Austrian mathematician Johann Radon long before the emergence of CT scanners (Radon, 1917). In practice today, there are basically two broad classes of reconstruction methods: Fourier (and series expansion) methods and algebraic methods (Herman, 1980; Kak and Slaney, 1988). Fourier methods are based on a continuous formulation of the problem where the image is expressed as a function of its projections by an analytic inversion formula. In algebraic methods, the image is obtained through the solution of a large linear system, which, given the size of the problem, is solved iteratively. While the historical method proposed by Hounsfield was an algebraic method called *ART* (algebraic reconstruction technique), analytic methods based on filtered back-projection (*FBP*) are currently more popular and effectively used in all commercial systems. The analytic reconstruction algorithms are strongly dependent on the acquisition geometry. Below, we detail FBP in the simple 2D parallel geometry and discuss its extension to 3D parallel and cone beam geometries.

#### 7.3.5.1 2D Filtered Back-Projection

**Expression of 2D Parallel Projection** Let  $f(x, y)$  be the image to be reconstructed [e.g., the function  $\mu(x, y)$  introduced for the linear attenuation coefficient above]. The parallel projection  $p_\theta(r)$  at angle  $\theta$  and at detector position  $r$  (Figure 7.4) is the line integral of  $f(x, y)$  over the straight line of direction  $(-\sin\theta, \cos\theta)$  passing

through the point  $(r\cos\theta, r\sin\theta)$ . Thus it can be expressed as:

$$p_{\theta}(r) = \int_{-\infty}^{+\infty} f(r\cos\theta - s\sin\theta, r\sin\theta + s\cos\theta) ds$$

The set of projections when  $\theta$  and  $r$  varies can be represented as a 2D image (the Radon transform), which is also called a *sinogram* in CT. Owing to symmetries in the Radon domain, it is sufficient to acquire projections for  $\theta$  between 0 and  $\pi$ . Figure 7.4f,g illustrates a synthetic digital image and its sinogram. The vertical axis corresponds to the rotation angle between 0 and  $\pi$  and the horizontal axis to the detector position.

**Fourier Slice Theorem** Image reconstruction consists in recovering  $f(x,y)$  from its sinogram. A fundamental theorem in CT reconstruction is the Fourier slice theorem. It states that the 1D Fourier transform of  $p_{\theta}(r)$  is a section profile of the 2D Fourier transform of the image along the straight line in direction  $\theta$ . Thus, when  $\theta$  spans the interval  $[0, \pi]$ , the entire 2D Fourier transform of the image is filled, showing that measured data are necessary and sufficient to reconstruct the image. Although the Fourier slice theorem can be used directly for reconstruction, methods based on back-projection are often preferred.

**Filtered Back-Projection (FBP)** The back-projection  $B_p(x, y)$  of all projections  $p_{\theta}(r)$  is the 2D image defined by:

$$B_p(x, y) = \int_0^{\pi} p_{\theta}(x\cos\theta + y\sin\theta) d\theta$$

Mathematically, the back-projection operator is the dual of the projection operator. From a geometrical point of view, the back-projection of a given projection “spreads” the values of the projection back onto the reconstruction image plane along the projection direction. The total back-projection is the sum of the back-projections of each projection. If the projections are filtered with a suitable filter before back-projection, the image is exactly recovered. This is the filtered back-projection method, which can be written as (Ramachandran and Lakshminarayanan, 1971; Shepp and Logan, 1974):

$$f(x, y) = \frac{1}{2} \int_0^{\pi} \tilde{p}_{\theta}(x\cos\theta + y\sin\theta) d\theta$$

$$\tilde{p}_{\theta}(r) = (p_{\theta} * h)(r)$$

where  $*$  denotes the convolution operator and  $h$  is called the *reconstruction filter*. If the bandwidth of the projection is within the interval  $[-W, W]$ , then the Fourier transform of the reconstruction filter  $h$  should satisfy the following property:

$$F_1 h(R) = |R| \quad \text{for } R \in [-W, W] \quad (7.3)$$

where  $F_1$  denotes the 1D Fourier Transform operator. This corresponds to the so-called ramp filter.

Figure 7.4h illustrates the result of FBP for the synthetic  $256 \times 256$  “fish” image when 400 projections between 0 and  $180^\circ$  are used. These reconstructions provide a good estimate of the original image. Figure 7.4i shows the result of back-projection directly applied to projections without filtering. In this case, a blurred version of the image is obtained, a result that can be demonstrated mathematically. Thus, filtering is mandatory for reconstruction of the original image. Filtering introduces negative values in the projections, which are compensated once all FBPs are combined. Filtering can be implemented as a convolution in object space or a multiplication in frequency space. In this latter case, the projection is first zero padded to avoid aliasing. FBP has been presented here for the 2D parallel geometry, but it can be generalized to the 2D fan beam geometry (Herman, 1980).

### 7.3.5.2 Image Quality and Artifacts

Achieving good results with FBP assumes that the sinogram is well sampled in terms of angles and spatial resolution. The detector sampling  $\Delta r$  limits the bandwidth of the reconstructed image to a disk of radius  $1/(2\Delta r)$  in the Fourier domain. The angular sampling must be sufficient in the  $[0, \pi]$  interval. The rule of thumb is to take  $(\pi/2)P$  projection angles if  $P$  is the number of samples in the detector. When the number of projections is insufficient, streak artifacts appear in the image (cf. Figure 7.4j). If the total angle of view is smaller than  $[0, \pi]$ , the image cannot be recovered exactly (cf. Figure 7.4k).

The reconstruction filter is another important parameter in FBP. The ideal ramp filter defined above is also known as the *Ram–Lak filter*, an abbreviation of the authors who introduced it (Ramachandran and Lakshminarayanan, 1971). In the presence of noisy projection data, the ramp filter will amplify the noise in the filtered projections and therefore in the reconstructed image. To improve the SNR in the reconstructed image, other filters obtained by multiplication with a smoothing window in the frequency domain are often used. The Shepp–Logan filter uses a sinc window but other filters such as Hamming or Hann windows have been used as well (Shepp and Logan, 1974). Note that the improvement in the SNR is obtained at the cost of a loss in spatial resolution in the reconstructed image.

Whatever the method, image reconstruction requires precise knowledge of the position of the axis of rotation axis and of the angular step. Thus, the acquisition geometry has to be accurately calibrated with a subpixel precision. Moreover, the object must not move during the scan, otherwise motion artifacts appear, leading to inconsistent data.

Exact CT reconstruction also requires the object to be completely included in the field of view of the detector. If this is not the case, the projections are truncated, which compromises the accuracy of the reconstructed image. In the case of truncated projections, also known as *local tomography* or region-of-interest (ROI) tomography, it is possible to use additional information about the object to



improve the reconstruction, or to reconstruct a high frequency version of the image (Natterer, 1986).

Other typical CT artifacts are ring artifacts, which appear as rings in the reconstructed image, due to imperfect flat-field correction, and beam hardening artifacts related to the polychromaticity of the beam, which generates nonlinearities in the direct problem that are not modeled by the Radon transform.

### 7.3.5.3 3D Image Reconstruction

**3D Parallel Beam CT** In the 3D parallel beam geometry, the reconstruction problem is straightforward since it can be implemented by the 2D FBP algorithm, which can be sequentially applied to the different parallel transverse sections of the 3D image. This task is particularly straightforward and can be dramatically speeded up by parallel computations (Chilingaryan, 2011) if the axis of rotation, beam direction, and detector rows are aligned mutually perpendicular. Thus, the great advantage of this geometry is that it is associated to fast and exact reconstruction algorithms.

**3D Cone Beam Geometry** Cone beam CT reconstruction algorithms are more complex because the information relative to a single slice is distributed along different detector lines. Thus, it is not possible to perform a sequence of 2D tomographic reconstructions; specific reconstruction methods adapted cone-beam projections have to be developed (Herman, 1980; Tuy, 1983; Peyrin, 1985; Grangeat, 1991). Tuy defined a sufficiency condition for exact cone-beam reconstruction (Tuy, 1983): it states that a 3D image is completely determined by its cone-beam projections if any plane that intersects the image also intersects the source trajectory. This condition is satisfied by a spiral but not by a circular source trajectory. Thus a cone-beam acquisition using a circular trajectory does not uniquely determine the 3D image. This non-uniqueness can be interpreted in terms of missing data in the 3D Radon space (defined as integrals of the 3D image on 2D planes). As in the 2D case, there is an inversion formula expressing the 3D image as a function of its 3D Radon transform. But the 3D Radon transform cannot be completely sampled from the cone-beam projections when the source describes a circular path. Hence, reconstructed images from circular cone-beam data are always approximate whatever method is used. Despite this limitation, several cone-beam reconstruction methods have been proposed.

The most popular approach is the Feldkamp algorithm (FDK), which is a generalization of the FBP algorithm for cone-beam geometry (Feldkamp, Davis, and Kress, 1984). It consists in three steps: weighting of the cone-beam projections, filtering of each row of the 2D projections with the usual ramp filter, and cone-beam back-projection of the 2D filtered projection. Unlike the 2D FBP, this formula is not exact, except for the central plane ( $z = 0$ ) where the rotation axis is perpendicular to the beam direction. The reconstruction errors increase with the distance to the central plane. Cone-beam artifacts are more visible on high-contrast objects and manifest themselves in the form of geometric distortions and intensity attenuations in the vertical direction. Note that cone beam artifacts increase with the cone-beam

angle. For this reason, the useful part of the data is sometimes limited to the central area of the detector. Many heuristic methods have been proposed to correct cone-beam artifacts in circular cone beam geometry (Valton, Peyrin, and Sappey-Marini r, 2006).

Exact cone-beam reconstruction algorithms can be derived if the source describes a spiral trajectory. In particular, Katsevich proposed various inversion formulas, which can be expressed in terms of FBP (Katsevich, 2004). However, in practice these algorithms are rarely used.

FBP and its variant are the methods currently used in micro-CT scanners due to their simplicity and speed. They provide good image quality given the limitations and preconditions discussed above. While iterative algebraic methods are more demanding in terms of memory and computing time, they are currently regaining interest with the advance in high-performance computations. They are more flexible in terms of tackling incomplete data sets and they allow the inclusion of prior knowledge of the object. They thus offer new perspectives in some applications, such as low dose CT with a small number of projections.

## 7.4

### Synchrotron laminography

#### 7.4.1

##### Introduction

Synchrotron-radiation computed laminography (SR-CL) is a non-destructive technique for 3D imaging of flat, laterally extended specimens (Helfen *et al.*, 2005). It was first developed for inspection of microsystem devices or electronic circuit boards (Helfen *et al.*, 2006b) but has now spread to other applications, like materials science (Moffat *et al.*, 2010; Morgeneyer *et al.*, 2011), cultural heritage studies (Krug *et al.*, 2008), and paleontology (Houssaye *et al.*, 2011), where flat, plate-like objects are prevalent. The technique is conceptually similar to SR-CT in the sense that 3D images are reconstructed from 2D projection data of the specimen. In comparison to SR-CT, which is particularly adapted to 3D imaging of specimens that are elongated in one direction (e.g., match stick or rod-like samples), SR-CL allows the specimens to be extended in two dimensions (e.g., plate-like objects).

Some basic principles of laminography were already proposed in the 1920s to 1930s by Bocage and Ziedses des Plantes, who independently worked on early concepts (Bocage, 1922; Ziedses des Plantes, 1932) in which 2D cross-sectional slices (from one to a few) could be imaged by a single scan. It involved employing a synchronized motion of a movable X-ray source and 2D detector (film) during exposure. The geometry of this synchronous motion defines one so-called focal plane, which appears sharply imaged. The greater the distance towards this focal plane, the more blurred the object planes away from this focal plane are rendered. Up until the 1960s this concept was steadily refined toward a technique called *tomosynthesis* (Grant, 1972). By acquisition of several radiographs during the scanning motion any given

plane could be optically reconstructed from a single scan. With the development of CT (Cormack, 1963; Hounsfield, 1972) during the 1960s/1970s, medical imaging researchers gradually abandoned this technique, which, however, remained in use for industrial applications (e.g., for device inspection). In industry it was retained as it enabled flat, and laterally extended, components (like printed circuit boards) to be investigated non-destructively (Zhou *et al.*, 1996; Kalukin and Sankaran, 1997; Gondrom *et al.*, 1999). Owing to the widespread use of digital imaging detectors (such as flat panel detectors or CCD-based X-ray detectors) and to increasing computing power, these methods (nowadays called *digital tomosynthesis* and *computed laminography*) have regained strong interest (Dobbins and Godfrey, 2003).

The benefits of using synchrotron-generated X-rays instead of desktop-generated X-rays in laminographic imaging techniques are similar to the case of CT. As an example, monochromatic radiation increases the image contrast due to avoidance of beam hardening artifacts. Element-specific imaging can be performed by working in the vicinity of absorption edges of specific chemical elements, as described in the following sections. Moreover, fast acquisition times at high spatial resolutions can be realized due to the high photon flux density. Finally, the method can be sensitive towards the electron density via various phase-contrast methods (Nugent, 2010; see also the following sections).

Presently, in most synchrotron imaging set-ups the usable beam cross-section is rather small, which is well suited for high-resolution imaging but offers a limited field of view compared to a conventional laboratory X-ray tube. In synchrotron laminography, the source cannot be moved and thus has to be kept stationary compared to its laboratory counterparts. Moreover, high-resolution X-ray detectors need to be positioned with a precision of a fraction of the effective pixel size during the scanning motion. Consequently, SR-CL uses a scanning scheme where both X-ray source and detector are stationary and only the specimen is rotated around an axis inclined with respect to the beam direction.

SR-CL can be considered as a generalization of SR-CT (Helfen *et al.*, 2011), with a variable inclination angle  $\theta$  between the rotation axis and the direction of the transmitted beam (Figure 7.8a,b). For CT, this corresponds to  $\theta = 90^\circ$ . The specimen itself can be laterally (i.e., in the two directions perpendicular to the rotation axis) larger than the width of the detector's field of view but should be thinner in the third dimension (i.e., along the rotation axis). If the specimen is oriented approximately perpendicular to the rotation axis, the average X-ray transmission to the 2D detector does not change significantly during specimen rotation. If the inclination angle of the rotation axis is well chosen, reliable projection data (i.e., projections with sufficient X-ray transmission and SNR) can be acquired for the entire scanning range of  $360^\circ$  around the rotation axis.

Similarly to all limited-angle scanning schemes, the main drawback of this scanning geometry lies in unsampled spatial frequencies in the specimen's Fourier domain, which prohibits accurate reconstruction. These missing frequencies oriented in a double-cone around the rotation axis (Figure 7.8a,b) give rise to artifacts in the reconstructed images that depend on the specimen's structure (Helfen *et al.*, 2005). In the case of CT ( $\theta = 90^\circ$ ) the coverage of the Fourier domain is complete

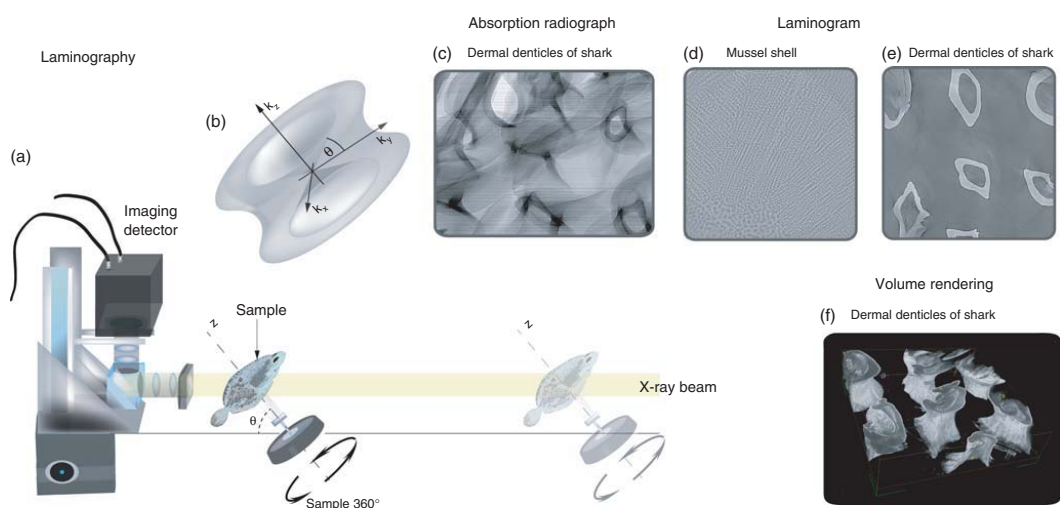


**Figure 7.8** Synchrotron laminography (SRCL) with parallel-beam geometry: (a) experimental setup illustrating the acquisition geometry and (b) Fourier-domain coverage of SRCL; (c) absorption radiograph, (d,e) laminogram (reconstructed slice) of a mussel shell, *Mytilus edulis*, and dermal denticles of shark, *Centroscyrnus coelepis*, and (f) volume rendering of dermal denticles of a shark.

(up to a given resolution limit) and the specimen can be reconstructed faithfully. If insufficient transmission is the reason for the inaccessible angles, then these missing frequencies have to be accepted for any scanning scheme, however, and the given X-ray energy determines the maximum angle at which the specimen can be inclined to provide useful projection data. The SR-CL scanning geometry maximizes coverage of the specimen's Fourier domain in these cases.

#### 7.4.2

##### Image Reconstruction

In analogy to Section 7.3.5, Fourier methods can be derived for analytical 3D image reconstruction. A projection is now considered as a 2D image with the additional parameter  $t$  expressing the height coordinate (defined along the projected rotation axis) in the image. The image acquisition geometry has a further parameter  $\vartheta$ , which is the inclination angle between the rotation axis and the direction of the transmitted beam:

$$p_{\theta,\vartheta}(r,t) = \int_{-\infty}^{\infty} f[\mathbf{R}_{x,z}^T(\theta,\vartheta) \cdot (r,s,t)^T] ds \quad (7.4)$$

where the superscript T denotes the transpose operation, and the coordinate transform matrix:

$$\mathbf{R}_{x,z}(\theta,\vartheta) = \begin{pmatrix} \cos \theta & \sin \theta & 0 \\ -\sin \vartheta \sin \theta & \sin \vartheta \cos \theta & \cos \vartheta \\ \cos \vartheta \sin \theta & -\cos \vartheta \cos \theta & \sin \vartheta \end{pmatrix} \quad (7.5)$$

describes a rotation around the axes  $x$  and  $z$  by the angles  $90^\circ - \vartheta$  and  $\theta$ , respectively. The angle  $\theta$  is varied for 2D data acquisition around the scanning axis  $z$ . In the case of 3D parallel-beam CT, the axis inclination angle  $\vartheta$  corresponds to  $90^\circ$ .

To calculate the back-projection image  $B_p(x,y,z)$ , all radiographic projections  $p_{\theta,\vartheta}(r,t)$  are smeared back in the reconstruction space along the same trajectory as the projections were measured initially. More formally, it is defined by:

$$B_p(x,y,z) = \int_0^{2\pi} p_{\theta,\vartheta}[\mathbf{R}_{x,z}^{[1,3]}(\theta,\vartheta) \cdot (x,y,z)^T] d\theta \quad (7.6)$$

where  $\mathbf{R}_{x,z}^{[1,3]}$  denotes a  $3 \times 2$  matrix where only the first and the third rows of the matrix  $\mathbf{R}_{x,z}$  are retained.

Again, the Fourier slice theorem can be used to express correspondence between the 2D Fourier transform of the projection image and the central slice (i.e., through  $\mathbf{k} = 0$ ) through the 3D Fourier domain, whose normal vector has the same direction as the projection direction. The principle of back-projection from Section 7.3.5 can now be extended to three dimensions, incorporating this additional parameter  $\vartheta$  corresponding to the axis inclination. The point-spread function of the 3D back-projection for the laminography geometry has been derived by Matsui *et al.* 1993

and can be written in cylindrical coordinates as:

$$H(k_p, k_\theta, k_z) = \begin{cases} \frac{\sin \vartheta}{2} \sqrt{k_p^2 - k_z^2 \cdot \cot^2 \vartheta} : k_p \geq |k_z| \cdot \cot \vartheta \\ 0 : \text{elsewhere} \end{cases} \quad (7.7)$$

where  $k_p = \sqrt{k_x^2 + k_y^2}$ ,  $k_\theta = \arctan(k_y/k_x)$ , and  $\mathbf{k} = (k_x, k_y, k_z)^T$  is the Fourier conjugate to the real-space vector  $(x, y, z)^T$  of a coordinate system fixed to the specimen.

As mentioned before, we see that there are vacancies with the shape of two cones along the positive and negative  $k_z$  directions in the 3D Fourier domain. In these regions, information about the specimen is missing completely, and therefore image reconstruction can only be approximated. This also explains why in laminography the reconstructions are more prone to artifacts than in tomography reconstructions.

Defining the (approximate) 3D inverse filter function (Lauritsch and Härer 1999; Helfen *et al.* 2006a):

$$\bar{H}(k_p, k_\theta, k_z) = \begin{cases} \left( \frac{\sin \vartheta}{2} \sqrt{k_p^2 - k_z^2 \cdot \cot^2 \vartheta} \right)^{-1} : k_p \geq |k_z| \cdot \cot \vartheta \\ 0 : \text{elsewhere} \end{cases} \quad (7.8)$$

the unknown image function can be estimated using the reconstruction equation:

$$f(x, y, z) = \{\bar{h} * B_p\}(x, y, z) \quad (7.9)$$

where  $\bar{h} = \mathbf{F}_3^{-1}\{\bar{H}\}$  and  $*$  again denotes convolution.

As for 2D tomography, a filter function can be derived which can be employed with the back-projection operation introduced above and serves to dampen the overrepresented low spatial frequencies in the back-projected 3D image while retaining as much information as possible from the specimen.

Using the filter function (Helfen *et al.*, 2011):

$$F_2\{\bar{h}_{\theta, \vartheta}(r, t)\} = \bar{H}_{\theta, \vartheta}(k_r, k_t) = \frac{\sin \vartheta}{2} \cdot |k_r| \quad (7.10)$$

filtering is then performed for all 2D projections by the relationship:

$$\bar{p}_{\theta, \vartheta}(r, t) = (p_{\theta, \vartheta} * \bar{h}_{\theta, \vartheta})(r, t) \quad (7.11)$$

prior to back-projection.

We see that projection filtering is the same for all projections acquired, that is, there is no dependency on the scanning angle  $\theta$ . Furthermore, it does not depend on the direction  $t$  parallel to the rotation axis (projected to the detector plane) and it can be performed by a procedure similar – apart from the (constant) factor  $(\sin \vartheta)/2$  – to the 1D filtering known from CT.

SR-CL allows imaging of relatively small regions from laterally large objects with high spatial resolution, that is, only a small ROI defined by the detector's field of view is reconstructed around the crossing point of beam axis, rotation axis, and specimen. The field of view of the detector along the rotation axis then determines the maximum specimen thickness.

In the following, we outline the interest of SR-CL for high-resolution cross-sectional or 3D imaging of specimens typical in marine biology. As in other application fields, employing phase-contrast methods to improve contrast conditions is a substantial benefit to laminographic imaging (Helfen *et al.*, 2009; Xu *et al.*, 2010; Altapova *et al.*, 2012). In comparison to SR-CT, the interest in laminography lies in its abilities to achieve high spatial resolutions for laterally extended specimens that are too precious to be cut down to the size required to perform a CT scan, for example, museum objects, fossils, or extinct species.

As for SR-CT, the specimens should be stable enough to withstand the irradiation by X-rays without deformation on the micrometer scale during the scanning. Otherwise, motion artifacts would occur. This is especially important for soft tissues (e.g., skins), which may need to be embedded into a resin of another supporting matrix to be stabilized.

#### 7.4.3

#### Example Applications

To illustrate the potential of our approach, we applied SR-CL to image the skin structure of a shark and the microstructure of shells. Figure 7.8d shows a reconstructed slice through the microstructure of a mussel shell (*Mytilus edulis*). A mussel shell is the product of biomineralization processes. Biominerals are composite materials made up of inorganic and organic components, and show unique morphologies. However, climate change is predicted to affect biomineralization processes in many marine organisms and thus scientists seek to understand how these processes may be affected by biotic and abiotic factors. Figure 7.8c,e,f shows a radiograph, a reconstructed slice, and a 3D rendering of shark skin. Both scientists and engineers have long suspected that the denticles on the skin of sharks reduce hydrodynamic drag during locomotion. In a recent study Oeffner and Lauder 2012 demonstrated the hydrodynamic nature of the denticles on the skin of sharks and developed two biomimetic applications.

### 7.5

#### Absorption Imaging

##### 7.5.1

##### Natural Contrast

X-Ray  $\mu$ CT (Baruchel *et al.*, 2008; Peyrin, 2009) is based on absorption, that is, the contrast in attenuation between different tissues. In conventional X-ray imaging, the observed contrast results from the variation in photon absorption arising from density and composition differences between different tissues. The technique yields excellent results when a highly absorbing structure is embedded in a matrix of relatively weak absorbance (e.g., bone inside a body or shells) (Stock *et al.*, 2003; Prymak *et al.*, 2005; Pérez-Huerta *et al.*, 2009; Pasco-Viel *et al.*, 2010). Bones and

shells have both a higher density and a chemical composition with a higher mass attenuation coefficient than soft tissue, such as muscles or fat, and are therefore very easy to discern. As the soft tissues of marine organism are predominantly composed of water, it is very hard to distinguish soft tissue structures from one another. In some cases, it is possible to distinguish water-filled volumes from muscle and fatty tissues, but these differences are rarely sufficient to study the morphology of these organisms. As illustrated in Figures 7.9 and 7.10, a standard CT-scan of a fish reveals bones but soft tissue information is absent.

### 7.5.2

#### Staining Contrast

When the contrast is insufficient to study soft tissue morphology, it is possible to use staining agents. These agents are very similar to those used for staining histological samples in optical, fluorescence, and electron microscopy (Betz *et al.*, 2007; Metscher, 2009).

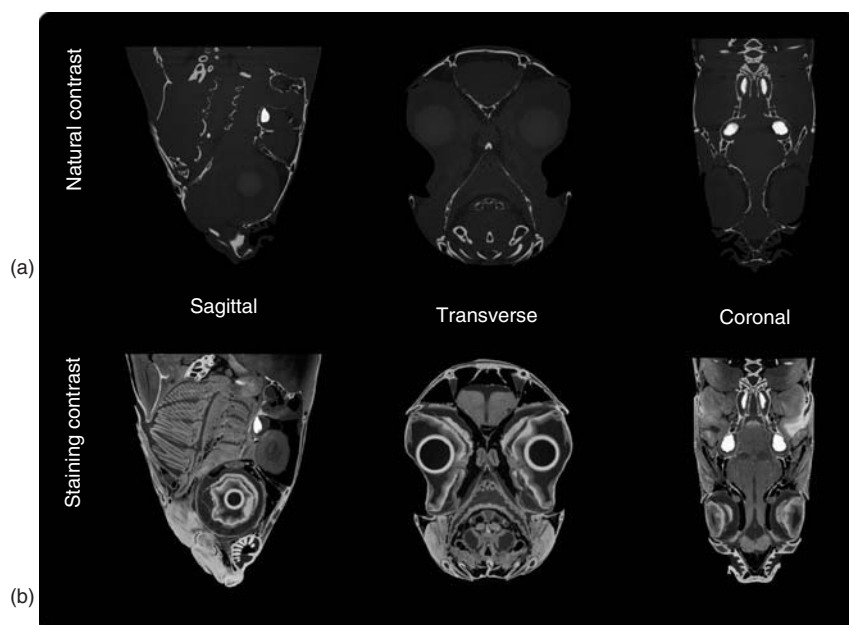


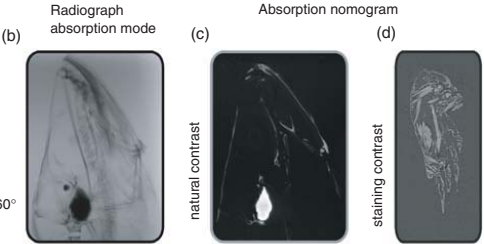
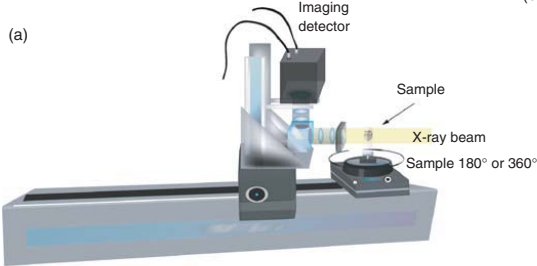
**Figure 7.9** Two types of contrast formation available in absorption X-ray microtomography, that is, natural contrast (a) versus staining contrast (b). This plate illustrates three cross-sectional slices (sagittal, transverse, and coronal) of a golden ide (*Leuciscus idus*) scanned with a desktop  $\mu$ CT for consistency. (a) The set of slices of a fish with no

staining. Bones can be distinguished from the apparently homogeneous soft tissues. (b) The second set of slices shows another specimen of the same species of fish but stained with phosphor-molybdenic acid. The morphological features of soft tissue are now accessible.



Absorption contrast

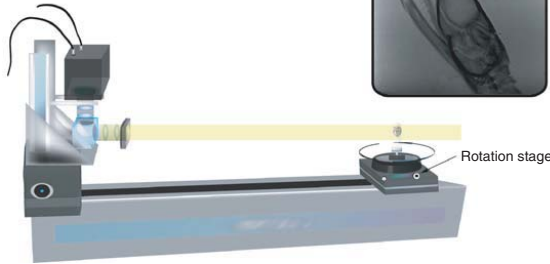
(a)



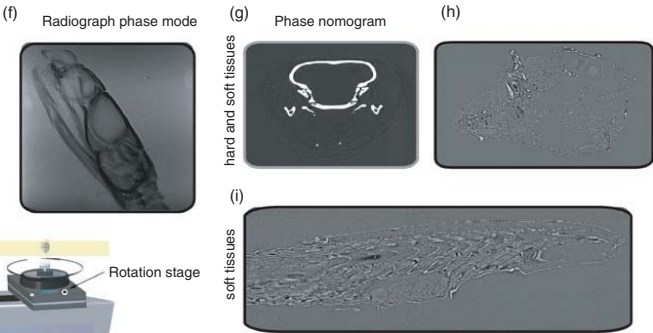
Camera close to sample

Phase contrast

(e)



Large distance between sample to camera



These agents typically have a much higher mass attenuation coefficient due to the presence of elements with a high atomic number, such as zinc, bromine, molybdenum, silver, iodine, barium, gadolinium, tungsten, osmium, gold, mercury, and lead. This results in a higher absorption of the structures that contain the agent and therefore a better contrast between the different structures (Figure 7.9), which, in turn, allows. This allows the visualization of soft tissues, such as nerves (Johnson *et al.*, 2006), muscles (Johnson *et al.*, 2006; Betz *et al.*, 2007), or vascular system (Plouraboué *et al.*, 2004; Heinzer *et al.*, 2006; Wirkner and Prendini, 2007; see also Figure 7.10d).

In addition to the enhanced contrast, special imaging methods, such as K-edge digital subtraction imaging (KES) can be applied to improve image quality and structure discrimination, as the contrast agents contain one specific chemical element not normally present in the organisms (Figure 7.11). The K-edge of a chemical element describes a sudden increase in the attenuation coefficient of photons occurring at a photon energy just above the binding energy of the K shell electrons of the atoms interacting with the photons (Adam *et al.*, 2005).

To perform K-edge imaging, two images are recorded, ideally simultaneously (to avoid motion artifacts on images), using monochromatic beams with energies that are below and above the K-edge of the chemical element used as contrast agent (Figure 7.11).

A simple algorithm allows retrieval of the distribution map of the contrast agent (Esteve *et al.*, 2002; Sarnelli *et al.*, 2005). Using SR, the technique has been applied in several biological fields, including bronchography (Bayat *et al.*, 2001), coronary angiography (Esteve *et al.*, 2002; Sarnelli *et al.*, 2005), brain vessel imaging (Schultke *et al.*, 2010), and high atomic number (Z) based nanoparticles metabolization (Alric *et al.*, 2008).

The development and application of the KES technique are closely related to the scarce availability of suitable SR sources and the engineering of compact dual-energy sources coupled with adapted detectors. Compact sources tailored for pre-clinical and clinical application of the dual-energy technique are described in the literature (Baldelli *et al.* 2005). In these sources, the beam generated by a conventional X-ray tube is monochromatized (down to a few keV energy bandwidth) by highly oriented pyrolytic graphite mosaic crystals. Two thin adjacent parallel beams of energies bracketing the K-edge of iodine, 31.2 and 35.6 keV, respectively (energy resolution <10%), are obtained by means of a proper collimation system. Unfortunately, these promising prototypes have not yet reached widespread use.

**Figure 7.10** X-Ray microtomography with a parallel-beam geometry; experimental setups of (a) absorption tomography and (e) phase-contrast tomography. (b) Radiography and (c) virtual slice of *Osmerus eperlanus* in sagittal view at head level. (d) *Thermocyclops consimilis* sagittal radiography. (f) Lateral radiography and (g) coronal virtual slice of *Laticauda saintgironsi*,

a sea snake from New Caledonia (îlot Brosse, November 2003; MNHN 2009.0168 Coll. Ivan Ineich), at head level. Sagittal slice of (h) *Argyropelecus aculeatus* and of (i) *Branchiostoma platæ* – view of anterior part of animal. Note that in phase contrast the black and white fringes represent interfaces between tissues.

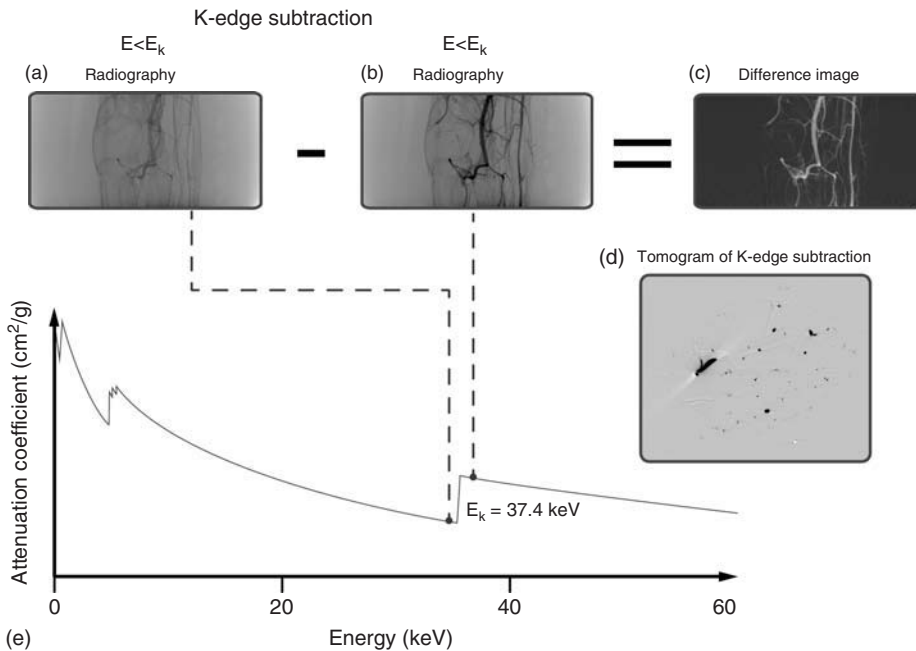


**Figure 7.11** K-edge subtraction (KES) imaging. In KES imaging, two CT images are acquired using X-ray beams at two different energies, above and below the K-edge of a given chemical element (in this case Ba in

the compound barium sulfate). The absolute quantity of the contrast agent at any given point of the CT image (a vessel in this example) is determined by subtracting the two images on a logarithmic scale.

Alternative K-edge imaging and dual energy techniques are being developed for polychromatic sources typically found in laboratory setups and medical scanners. These methods consist of comparing the reconstructed attenuation coefficient of a voxel for scans performed with a different X-ray spectrum. The variation of this coefficient is related to its energy-dependency, which can be calculated with a system of equations. This approach has proven to be very successful and is currently being implemented in the latest medical CT scanners and laboratory setups.

## 7.6

### Phase-Contrast Imaging

#### 7.6.1

##### Introduction

X-Ray PCI enables mapping of the variations in the X-ray refractive index of the object under study and, thereby, of its electron density. Unlike absorption contrast, phase contrast is generated by the interference of the diffracted or refracted components of the beam with each other. At the detection plane, these

interferences form intensity variations, that is, an X-ray image that can be recorded, usually with the same type of detector as an absorption-contrast image. Phase contrast takes its name from the fact that it is not only created by differences in the amplitude of the X-ray wave after it has passed through the object but also by variations of its phase (Figure 7.6).

The great advantage of PCI is that it can be up to 1000 times stronger than absorption contrast for hard X-rays, especially when the object investigated consists largely of elements with low atomic number  $Z$  (as is the case, for example, for biological soft tissue), or when the absorption differences within the sample are weak (as in many fossilized organisms).

In addition, most phase-contrast techniques are *differential*, that is, the images obtained with these techniques represent a spatial derivative of the object function's projections, rather than the projection itself. For example, in propagation-based phase contrast (Section 7.6.2, below), edges and interfaces in the object are particularly enhanced in the images, through a pair of bright/dark fringes (Figures 7.3, 7.5, 7.6, and 7.10). This improves the visibility of small structures.

On the other hand, one additional challenge posed by the use of differential contrast techniques is that the usual tools for the quantitative analysis of structures are adapted to absorption-based CT datasets and that their application to phase-contrast datasets is not always possible.

This problem can be solved by the application of *phase retrieval* techniques. In differential PCI, phase retrieval (also named phase reconstruction) essentially consists of obtaining the original object function from the derived images, measured by the detector in a differential phase-contrast (DPC) measurement, and in separating the information on the refractive index from that on the absorption coefficient. These two contributions are usually superimposed on each other in the raw detector images. Such techniques are also called *quantitative phase-contrast techniques* or simply *phase imaging* (as opposed to PCI). In general, quantitative phase imaging either requires more data than a simple absorption-contrast data set (Cloetens *et al.*, 1999; Weitkamp *et al.*, 2005a) or it requires *ad hoc* assumptions on the sample composition (Nugent *et al.*, 1996; Paganin *et al.*, 2002; Groso *et al.*, 2006), otherwise it will result in an image with inferior spatial resolution than the detector would allow for absorption-contrast images. This latter phenomenon occurs, for example, when moiré techniques are used (Weitkamp *et al.*, 2005b; Momose *et al.*, 2011).

Among the different X-ray phase-contrast techniques used today, some require additional X-ray optical elements in the beam, while others do not. In addition, depending on the method, the quantitative phase recovery process may be very simple and highly-automated, or more complicated and require careful manual intervention.

A requirement common to all phase-contrast techniques is that of a sufficient degree of lateral coherence, and sometimes also longitudinal coherence, of the X-ray beam. Lateral coherence can simply be expressed in terms of the size at which the X-ray source appears when seen from the position of the sample: if the source has a lateral size  $s$  and is located at a distance  $L$  from the sample its

angular size is approximately  $s/L$  (if there are no focusing or scattering optical elements in the beam between source and sample). The lateral coherence of the beam becomes stronger as the angular source size decreases, and it is often expressed in terms of the lateral coherence length  $\lambda L/s$  (where  $\lambda$  is the X-ray wavelength). Since the source size can be different in the two transverse directions  $x$  and  $y$  (i.e., orthogonal to the beam propagation direction  $z$ ), so can the lateral coherence length. Longitudinal coherence, on the other hand, is simply related to the monochromaticity of the X-rays used: the narrower the X-ray spectrum, the higher the longitudinal coherence.

Although we present here phase-contrast data taken at a third-generation synchrotron (ESRF), which delivers X-rays with a high degree of lateral (and, when needed, longitudinal) coherence, it is important to point out that monochromaticity and spatial coherence requirements for qualitative PCI are minimal if the required sensitivity is only moderate (Margaritondo and Tromba, 1999).

In fact, X-ray PCI has been used at second-generation synchrotrons, especially for medical and materials science applications (Momose *et al.*, 1996; Beckmann *et al.*, 1997; Castelli *et al.*, 2011; Tsai *et al.*, 2002; Muehleman *et al.*, 2004), and even with conventional X-ray sources (Wilkins *et al.*, 1996; Zhang *et al.*, 2008). In the following, we describe in more detail three different classes of X-ray PCI: free-space propagation, analyzer-based imaging (ABI), and grating interferometry.

### 7.6.2

#### Free-Space Propagation Methods (Holotomography)

If a sufficiently coherent X-ray beam is used, a particularly simple mode of PCI becomes available. By simply letting the X-ray beam propagate in free space after interaction with the object, phase contrast is achieved (Snigirev *et al.*, 1995). The contrast formation process can be understood in the framework of Fresnel diffraction. When an X-ray beam passes through an object, it may be affected in two ways: it might be absorbed in the object, which changes its amplitude, and it might be slowed down in the object, which changes its phase (Figures 7.10 and 7.12).

Amplitude and phase modulation are, respectively, related to the imaginary and the real part of the complex-valued X-ray refractive index:

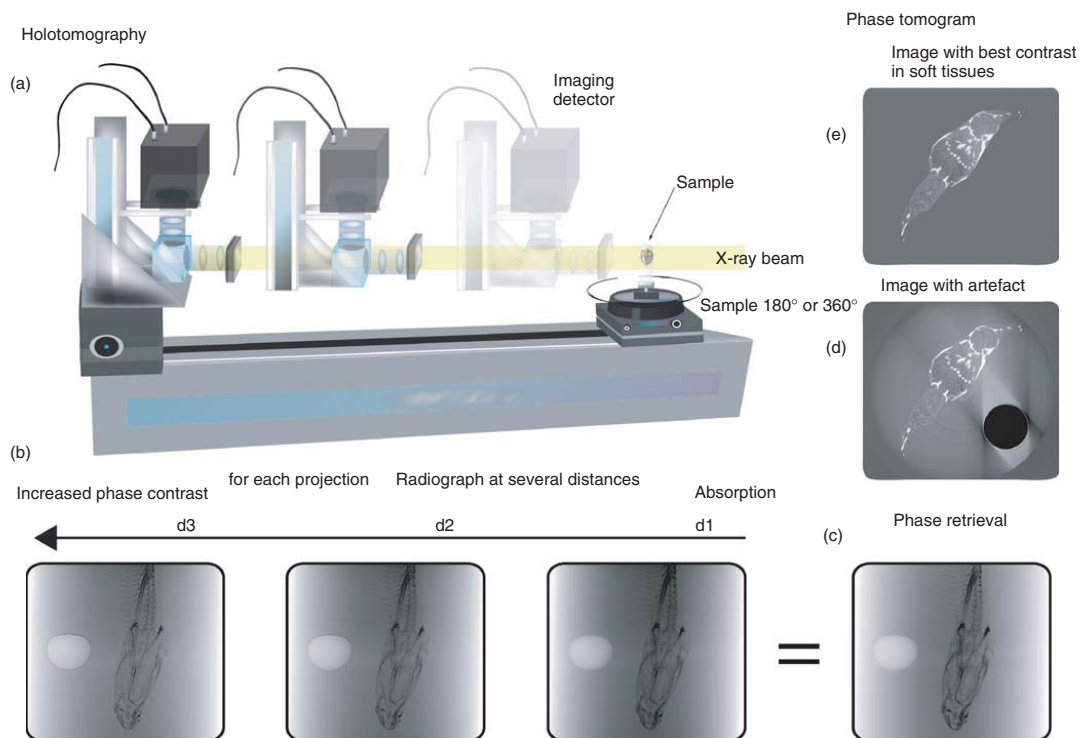
$$n(x, y, z) = 1 - \delta_n(x, y, z) + i\beta(x, y, z) \quad (7.12)$$

where  $\delta_n$  is the refractive index decrement,  $\beta$  is the attenuation index,  $i$  is the imaginary unit number, and  $(x, y, z)$  are the spatial coordinates. Both the attenuation and the phase shift induced by the object can be described as projections through the absorption and refractive index distributions, respectively, with the amplitude:

$$B(\mathbf{x}) = \left( \frac{2\pi}{\lambda} \right) \int \beta(x, y, z) dz \quad (7.13)$$

and phase:

$$\varphi(\mathbf{x}) = - \left( \frac{2\pi}{\lambda} \right) \int \delta_n(x, y, z) dz \quad (7.14)$$



This means that both parts of the complex refractive index can be reconstructed by tomographic reconstruction if amplitude and phase can be measured for different angular settings of the sample. The wave field at the exit plane of the object, assuming a flat incident beam, is then:

$$T(\mathbf{x}) = \exp[-B(\mathbf{x}) + i\varphi(\mathbf{x})] \quad (7.15)$$

For the relatively short propagation distances we are interested in here, usually up to 1 m, the effect of propagation on the exit wave-field can be described in the framework of Fresnel diffraction (Goodman, 2005). The intensity  $I_D(\mathbf{x})$  at propagation distance  $D$  downstream of the object is then written as:

$$I_D(\mathbf{x}) = |\text{Fr}_D[T](\mathbf{x})|^2 = |T(\mathbf{x}) * P_D(\mathbf{x})|^2 \quad (7.16)$$

where  $\text{Fr}_D$  denotes the Fresnel transform,  $T(\mathbf{x})$  is the wave field at the exit of the sample, and  $P_D(\mathbf{x})$  is known as the *Fresnel propagator*. We can see that the relationship between phase shift and wave field at distance  $D$  is linear, while the relationship between phase and contrast is nonlinear.  $I_D(\mathbf{x})$  is the quantity that can be detected and is called a *phase-contrast image* or a *Fresnel diffraction pattern*. These images can be used directly as input for tomographic reconstruction algorithms. The reconstructed image then shows an edge enhancement effect that is related to the Laplacian of the 3D refractive index (Cloetens *et al.*, 1997), which can be a useful modality in its own right. More interestingly, the phase shift can be reconstructed from a series of phase-contrast images at different distances through a process known as *phase retrieval*. This is not straightforward due to the nonlinearity in Eq. 7.15. Usually, this problem is addressed by linearization of Eq. 7.16 (Nugent *et al.*, 1996; Cloetens *et al.*, 1999). Several approaches have been developed. A frequently-used method is based on linearization with respect to the object and yields the linear contrast model (Guigay *et al.*, 2007):

$$\tilde{I}_D^{\text{MOD}}(\mathbf{f}) = \tilde{I}_D^{(\varphi=0)}(\mathbf{f}) + 2 \sin(\pi\lambda D|\mathbf{f}|^2) \mathbf{F}\{I_0\varphi\}(\mathbf{f}) + \cos(\pi\lambda D|\mathbf{f}|^2) \frac{\lambda D}{2\pi} \mathbf{F}\{\nabla \cdot (\varphi \nabla I_0)\}(\mathbf{f}) \quad (7.17)$$

where  $\tilde{f}(\mathbf{f}) = \mathbf{F}\{f\}(\mathbf{f})$  denotes the 2D Fourier transform of  $f(\mathbf{x})$ , which is valid under slow variation conditions on the attenuation and phase. The phase is retrieved by

**Figure 7.12** Holotomography. (a) Acquisition geometry: The imaging setup of a synchrotron radiation propagation-based phase-contrast imaging system. X-rays are taken from an insertion device, and then monochromatized. The long source-to-sample distance yields a high degree of spatial coherence. The sample is mounted on a translation–rotation stage (standard SR-μCT setup). The detector, consisting of a scintillator, light microscope optics, and a CCD, is mounted on a translation stage to allow

for free space propagation of the beam after the sample. (b) Radiographies of *Osmorus eperlanus* head, from d1 to d3, show the increase in phase contrast (see at interface of bubble). (c) Phase retrieval map. (d) Virtual slice obtain by holotomography showing an artifact induced by free bubble. The contrast is affected by the presence of bubble. (e) Virtual slice obtain by holotomography without free bubble. Note that the slices are windowed to obtain the best contrast in soft tissues.

solving the linear least squares minimization problem:

$$\arg \min_{\tilde{\varphi}(\mathbf{f})} \sum_D \|\tilde{I}_D^{\text{MOD}}(\mathbf{f}) - \tilde{I}_D^{\text{REC}}(\mathbf{f})\|^2 + \alpha \|\tilde{\varphi}(\mathbf{f})\|^2$$

where  $I_D^{\text{REC}}(\mathbf{x})$  are the images recorded at different distances, typically 2–4. The second term is a regularization term and is usually classic quadratic Tikhonov regularization with  $\varphi_0 = 0$ . Owing to the low sensitivity of the contrast formation mechanism to low frequencies in the phase (which can produce low frequency noise in the retrieved phases), it is sometimes desirable to introduce other a priori knowledge in the regularization term; for example, homogeneity of the object (Langer, Cloetens, and Peyrin, 2009, 2010). In the particular case of an object made of a single material with known X-ray optical properties, in which only the density of the material shows spatial variations but its chemical composition does not, the phase profile of the wave front at the exit plane of the wave front can be retrieved with a particularly simple, non-iterative equation known as *Paganin's formula*, namely, (Paganin *et al.*, 2002; Weitkamp *et al.*, 2011):

$$\varphi(x) = -\frac{\delta_n}{2\beta} \ln \left( \mathbf{F}^{-1} \left\{ \frac{\mathbf{F}[I_D(x)]}{1 + \pi \lambda D \frac{\delta_n}{\beta} \|\mathbf{f}\|^2} \right\} \right)$$

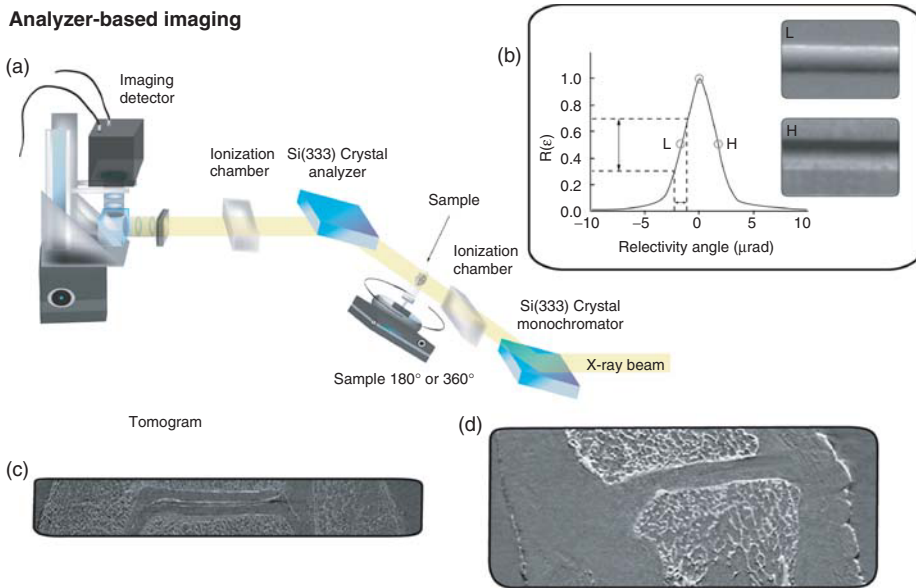
While the condition of uniform chemical composition is rarely fully met, Paganin's method is, in practice, quite tolerant to deviations from ideal conditions (Weitkamp *et al.*, 2011). This robustness, combined with the fact that the formula is easy to implement and allows reconstruction from a data set taken at a single sample-to-detector distance (just as in absorption-contrast tomography), makes Paganin's method a very versatile reconstruction method for parallel-beam, phase-contrast data in free-space propagation phase contrast.

### 7.6.3

#### Analyzer-Based Imaging

Analyzer-based imaging (ABI) is a phase-contrast technique based on the registration of a monochromatic and parallel radiation transmitted through an object, after having been analyzed by a perfect crystal. When the beam transmitted through the object falls on a perfect silicon crystal, the latter acts as a very narrow angular slit, reflecting only the rays that make the correct angle with the crystal surface. By tuning the crystal, the non-deviated, refracted, and scattered rays can be separated on images. In a typical case, the full-width at half-maximum of the reflectivity curve of the analyzer is a few microradians, and its shape is approximately triangular with linear slopes. Figure 7.13 shows a typical ABI setup. The analyzer is tuned to reflect at the angle that corresponds to the peak of the intrinsic (without an object) reflectivity curve (top), or at the mid-slope on either side of the reflectivity curve (low or high). At the top, all scattered and refracted rays are rejected, leading to the so-called apparent absorption contrast (extinction), while at low and high positions, the changes in the propagation direction of X-rays are converted into intensity changes giving rise to the (so-called) *refraction contrast*. ABI (also called *diffraction*



**Analyzer-based imaging**

**Figure 7.13** Analyzer-based imaging (ABI). (a) Schematic diagram of the ABI set-up: a narrowband monochromator using Si(333) reflections, analyzer Si(333), and the detector. The sample can be scanned vertically through the sample [radiography, e.g., L, H in part (b)] or rotated (tomography). The ionization chambers are used to tune the system. (b) Inset: reflectivity curve and the principle of the ABI method. The reflectivity curve,  $R(\epsilon)$ , demonstrates the conversion between the angular X-ray deviations (horizontal axis) and the intensity changes (vertical axis). ABI, analyzer-based X-ray

imaging; P, peak or top position; L, low-angle position; H, high-angle position. Radiography L and H shows different phase contrast. (c) Computed tomography of a human ankle images using the ABI technique; X-ray energy 51.5 keV; pixel size 45  $\mu\text{m}$ . (d) Lateral slices of a human big toe constructed by ABI tomography acquisitions (experimental parameters: X-ray energy 30 keV, pixel size 45  $\mu\text{m}$ ). The arrows indicate the edges of the cartilage tissue covering the two joint bones. (c and d: Reused from Coan *et al.* (2008) with kind permission from Elsevier.)

*enhanced imaging*) has been the principal method in PCI of human breast tissue specimens.

### 7.6.3.1 Applications

Most developments in ABI have been carried out at SR facilities, because presently these are the only sources capable of delivering intense monochromatic and collimated X-ray beams.

In mammography, after the exceptional pioneering results obtained, respectively, at the Brookhaven National Laboratories (BNL) and at ELETTRA (Trieste, Italy), on imaging thin pathological (Pisano *et al.*, 2000) or full healthy breasts (Arfelli *et al.*, 2000), research has focused at the ESRF on developing low dose tomography imaging (Keyriläinen *et al.*, 2008; Keyriläinen *et al.*, 2010). With the aim of overcoming the severe limitations imposed by present clinical X-ray tools, a very

promising application of ABI is in osteoarthritis (OA) diagnosis, with the ancillary objectives of understanding the evolution of the illness and of non-invasively studying the effectiveness of drug treatments. Examples of images of human joints acquired with the ABI technique are reported in Figure 7.13c (ankle) and in Figure 7.13d (big toe). Milestones of this development are the first radiographic detection of the structural orientation in human cartilage (Muehleman *et al.*, 2004) and the first correlation of the pathological status of a sample with the spatial distribution of the chondrons, which are clusters of cartilage cells (Coan *et al.*, 2010).

Analyzer-based images also allow the identification of the quality of ingrowth of bone into the hydroxyapatite layer of an implant; in fact, it has been shown that incomplete integration of the implant with a remaining microscopic gap caused the presence of a highly refractive edge at the implant/bone. Therefore, ABI could be utilized to diagnose implant healing and/or loosening (Wagner *et al.*, 2006).

#### 7.6.4

#### X-Ray Grating Interferometry

##### 7.6.4.1 Introduction

Propagation-based X-ray phase contrast (Section 7.6.2) yields excellent results for studies at high spatial resolution (i.e., with pixel sizes in the micron and sub-micron range) and using moderate X-ray photon energies. However, for larger pixel sizes and higher energies, carrying out a propagation-based measurement under optimum conditions becomes more and more difficult. This is because the propagation distance for optimum contrast in propagation-based setups,  $D_{\text{opt}}$ , scales with the square of the pixel size  $d_{\text{pix}}$  and with the inverse of the X-ray wavelength  $\lambda$ , that is,  $D_{\text{opt}} \approx (2d_{\text{pix}})^2/\lambda$  (Weitkamp *et al.*, 2011). Imaging full objects from centimeter size upward will usually require pixel sizes in the range of 10  $\mu\text{m}$  or more. Propagation-based phase-contrast images of such objects can still be obtained, but the experimental propagation distances often have to remain far below their theoretical optimum values, which quickly attain impractical values of dozens of meters. As the real distances used during imaging remain much smaller, the phase-contrast signal obtained is not as strong as it could be under optimum conditions.

Therefore, when the required field of view exceeds a centimeter, other phase-contrast methods can become advantageous. ABI (Section 7.6.3) is one of these techniques.

Another, more recently developed approach, is X-ray grating interferometry (XGI), sometimes also called *Talbot interferometry*. As well as providing high sensitivity in phase-contrast radiography and tomography, XGI has the important advantage of being compatible with low-brilliance X-ray sources such as standard laboratory X-ray tube generators. Moreover, XGI gives access to an additional contrast modality called “*dark-field imaging*”, in which scattering regions in the sample can be visualized.

**Principles** In XGI (Momose, 2003; Weitkamp *et al.*, 2005a), a line grating G1 is placed in the X-ray beam, usually between the sample and the detector

(Figure 7.14a). The period  $p_1$  of the grating lines is much larger than the X-ray wavelength  $\lambda$ , but often smaller than the detector pixel size. The modulation that grating G1 introduces in the X-ray wave front will produce a set of interference fringes at positions downstream of G1. If the incident wave is planar or mildly spherical, these fringes will be regular and periodic, with the same or half the period of G1 (depending on the thickness of the grating lines), and will have uniform contrast over the field of view. However, if an object under study is introduced in the beam path, the fringe pattern downstream will be displaced or distorted due to refraction of the X-rays by the specimen, and the contrast of the fringes may be locally reduced because of scattering in the object. Moreover, as in conventional X-ray absorption-contrast imaging, the overall intensity averaged over one or more fringe periods will be decreased as a function of X-ray attenuation in the sample.

The principle of XGI is to detect the distortions and/or contrast variations of the fringes created by G1 and modified by the presence of the specimen. Using this principle, three complementary images can be retrieved: a DPC image, a visibility image (also called a “dark-field image,” *DFI*), and the attenuation image. However, as mentioned above, the period  $p_1$  of the grating G1, and therefore also the period of the fringe pattern, is usually too small to be resolved by the detector. This is why a second line grating G2 is placed directly in front of the detector. Grating G2 acts as a transmission mask for the detector. Its lines should therefore strongly absorb the incident X-rays, and the period  $p_2$  of these absorbing lines should be identical to the period of the interference fringes generated by G1. In areas where the intensity maxima of the fringe pattern incident on G2 coincide with the positions of the absorbing lines, the detector will record low intensity. In areas where the fringe maxima lie in the clear spaces between the grating lines, the detector will record high intensity. G2 thus encodes fringe position into intensity values on the detector. However, in a single interferogram thus recorded the information on fringe position and fringe visibility will still be superimposed on one another and on the attenuation signal.

Several approaches exist to separate and access all three types of information. The two most common ones are moiré imaging and phase stepping (also called “*fringe scanning*”). In moiré imaging, gratings G1 and G2 are slightly rotated with respect to each other, around the beam axis (Weitkamp *et al.*, 2005b; Wang *et al.*, 2011). This results in a pattern of moiré lines recorded on the detector. Their analysis gives access to the three contrast modalities based on a single image. The spatial resolution of this technique is, however, limited to the period of one moiré fringe, that is, it is inferior to the resolution of the detector itself. In the phase-stepping technique, the full spatial resolution of the imaging system is retained. Here, the gratings are aligned with their lines parallel to each other, and several images (their number  $N$  typically ranging between 3 and 5) are recorded for different transverse positions of one of the two gratings. The scanned grating is moved transversally in steps that are a fraction of the grating period  $p$ . The full range of the scan is usually one fringe period. The intensity  $I$  in each pixel with coordinates  $\mathbf{x} = (x, y)$  will oscillate during the scan, as a function of the grating position  $x_g = (m/N) \times p$ . This oscillation can usually be well approximated by a sine function:

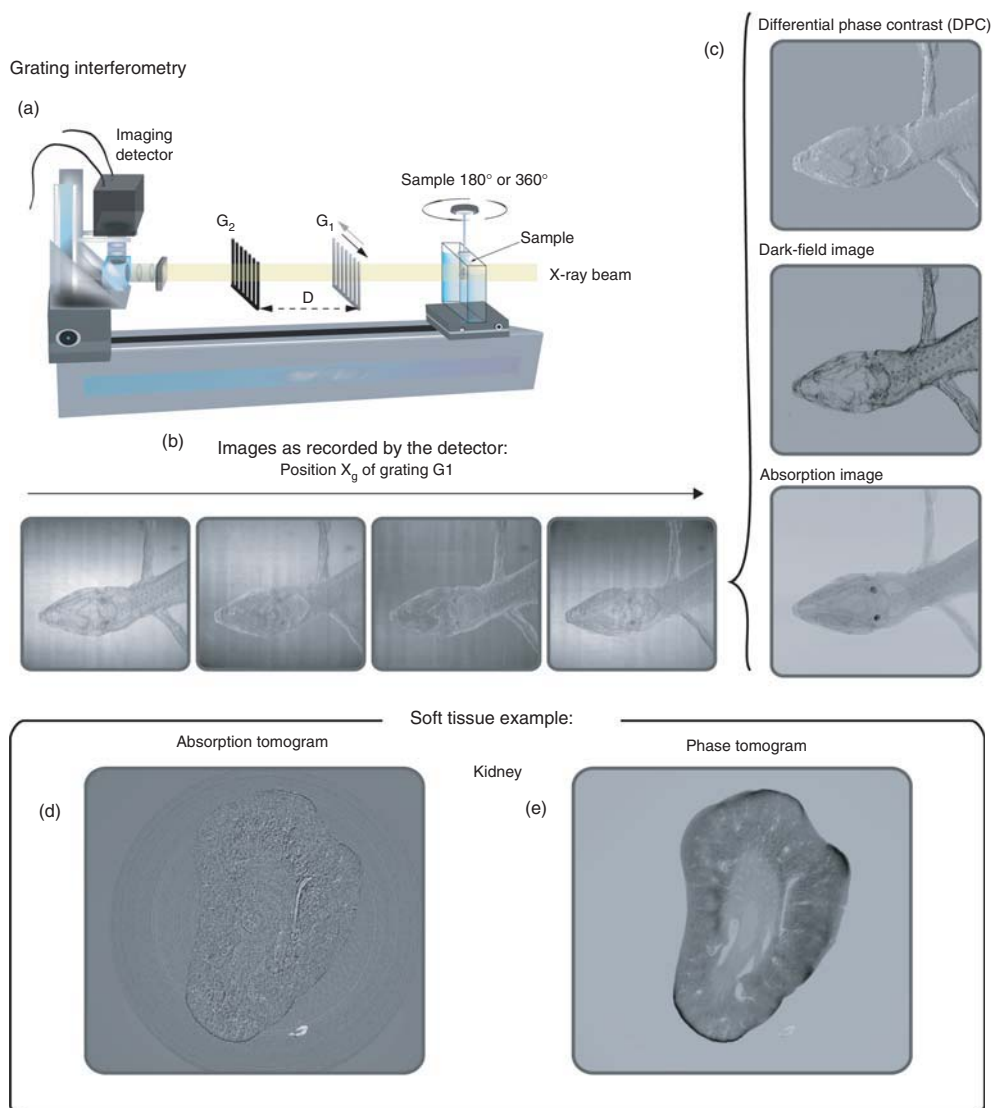


**Figure 7.14** Grating interferometry with a parallel beam geometry. Principle of tomography using X-ray grating interferometry: The setup (a) is similar to other microtomography methods but two gratings  $G_1$  and  $G_2$  are introduced between the specimen and detector. The sample and (if applicable) its container are often immersed in water (or another phase-matching liquid) to avoid artifacts from strong contrast at the outer edges. At each projection angle of

the tomography scan, one of the gratings is laterally scanned over one period in a few steps. The images recorded from the detector (b) are processed to yield three contrast modalities (c): a differential phase-contrast (DPC) radiograph, a dark-field image, and an attenuation image. The specimen is a lizard, immersed in water. The two images (d) and (e) show an absorption tomogram (d) and a phase tomogram (e) of a soft-tissue sample (the kidney of a rat).

$$I_m(\mathbf{x}) = a(\mathbf{x}) + b(\mathbf{x}) \times \sin \left[ \frac{2\pi m}{N} + \psi(\mathbf{x}) \right]; \quad m = 0, \dots, N-1$$

Here,  $I_m(\mathbf{x})$  is the detector signal recorded in the  $m$ -th phase step in the pixel coordinate  $\mathbf{x}$ . A pixel-wise analysis of the  $N$  images obtained in a phase stepping scan, for example, by Fourier methods, easily yields the parameters  $a$ ,  $b$ , and  $\psi$ . This procedure is fully automated. The attenuation image  $A(\mathbf{x})$ , DPC image  $\alpha(\mathbf{x})$ , and DFI  $v(\mathbf{x})$  are obtained from these parameters by:

$$\text{Attenuation : } A(\mathbf{x}) = a(\mathbf{x})/a_{\text{ref}}(\mathbf{x})$$

$$\text{DPC : } \alpha(\mathbf{x}) = [p_2/(2\pi D)] \times [\psi(\mathbf{x}) - \psi_{\text{ref}}(\mathbf{x})]$$

$$\text{DFI : } v(\mathbf{x}) = b(\mathbf{x})a_{\text{ref}}(\mathbf{x})/[b_{\text{ref}}(\mathbf{x})a(\mathbf{x})]$$

In the formulas above, the subscript “ref” indicates reference images taken in the beam without a sample. Note that the attenuation image  $A(\mathbf{x})$  corresponds to the intensity transmission through the sample. The DPC image  $\alpha(\mathbf{x})$  is the angle of refraction in the direction perpendicular to the grating lines. It is related to the wave-front phase shift profile  $\varphi(\mathbf{x})$  by:

$$\alpha(\mathbf{x}) = \frac{\lambda}{2\pi} \frac{\partial \varphi(\mathbf{x})}{\partial \mathbf{x}}$$

Note that the inter-grating distance  $D$  in the denominator of the DPC formula implies that the sensitivity of the instrument will increase if the distance between the gratings is increased. In this way, the phase sensitivity of a grating interferometer can be tuned by choosing the distance  $D$  between the gratings.

All three signals – attenuation, DPC, and dark-field – are amenable to tomographic reconstruction. As in conventional X-ray tomography, the tomographic reconstruction of the logarithm of  $A(x,y)$  yields the spatial distribution of linear attenuation coefficient  $\mu$  in the sample. Tomographic reconstruction of the DPC image [preceded by integration along  $x$ , or using an imaginary sign filter in the tomography routine (Pfeiffer *et al.*, 2007a)] yields the distribution of X-ray refractive index  $\delta_n$ . The DFI can be reconstructed in analogy to the attenuation image, and will yield the distribution of an effective scattering coefficient (Wang *et al.*, 2009).

#### 7.6.4.2 Performance Characteristics and Applications

XGI excels in terms of the high sensitivity and precision of the phase contrast it creates. In radiographic DPC projections obtained with XGI, a precision of down to 10 nrad (in terms of refraction angle  $\alpha$ ) can be reached. XGI phase tomography data have a precision that can reach  $0.5 \text{ mg cm}^{-3}$  (mass density), corresponding to  $2 \times 10^{-10}$  in terms of X-ray refractive index, or  $0.2 \text{ electrons nm}^{-3}$  in electron density (Pfeiffer *et al.*, 2007b; Herzen *et al.*, 2009; Schulz *et al.*, 2010; Zanette *et al.*, 2011a). The spatial resolution is limited by the diffraction on G1 and by the detector resolution. The limit imposed by diffraction on G1 scales with  $\lambda D/p_1$ . This means that an increase in sensitivity, by choosing a longer inter-grating distance  $D$ , will come at the cost of a degradation of spatial resolution.

As with other phase-sensitive radiography methods, XGI performs best with highly-brilliant sources, such as those at SR facilities. However, compared to other

X-ray phase-contrast methods, the requirements of XGI on beam monochromaticity, beam parallelism, and detector resolution are relatively relaxed (Weitkamp *et al.*, 2005a). In addition, if the transverse coherence of the beam delivered by the available X-ray source is not sufficient, an additional grating G0 can be inserted between the source and G1 to solve the problem (Pfeiffer *et al.*, 2006). In this way, XGI can be implemented with low-brilliance sources such as standard X-ray tubes.

Quantitative interpretation of the dark-field contrast modality is the subject of intensive research (Yashiro *et al.*, 2010; Bech *et al.*, 2010; Lynch *et al.*, 2011). Moreover, dark-field imaging can be extended, by rotating the sample around the optical axis, to yield not only the scattering strength in different regions of the specimen but also the degree of anisotropy and the preferential direction of the scattering structures (“directional dark-field imaging”; Jensen *et al.*, 2010). Similar information can be retrieved if gratings structured in two dimensions are used instead of line gratings (Zanette *et al.*, 2010). In moiré mode (Momose *et al.*, 2009) or using other advanced acquisition schemes (Zhu *et al.*, 2010; Zanette *et al.*, 2011b, 2012), XGI can be made compatible with fast, real-time tomographic imaging (Momose *et al.*, 2011).

Grating interferometers are currently available to the user community at several facilities in Europe (McDonald *et al.*, 2009; Weitkamp *et al.*, 2010; Herzen *et al.*, 2010) and Japan; the first tests were reported from North America (Richter *et al.*, 2009). Test setups using standard X-ray sources have been described from various research laboratories (Donath *et al.*, 2010; Jerjen *et al.*, 2010), and a first implementation in a commercial laboratory X-ray  $\mu$ CT scanner has recently been reported (Tapfer *et al.*, 2011). Developments have been published from numerous research groups around the globe, and the availability of this method is rapidly increasing. Other grating-based techniques that, unlike XGI, do not use the interference effect should also be mentioned. They include coded-aperture phase contrast (Olivo *et al.*, 2011) and Fourier X-ray scattering radiography (Wen *et al.*, 2009).

Among applications in the life sciences of this emerging method, we mention phase tomography of the rat brain (Pfeiffer *et al.*, 2007b), human brain (Schulz *et al.*, 2010), and the human inner ear (Richter *et al.*, 2009), and also in mammography (Stampanoni *et al.*, 2011) and applications in food science (Jensen *et al.*, 2011). In all these domains, the ultrahigh sensitivity of XGI makes it possible to visualize the 3D microstructure of soft tissue at unprecedented contrast. Dark-field imaging has been applied to dental structures in mammals (Jensen *et al.*, 2010), where it reveals the presence and orientation of sub-resolution structures, such as tubuli in the dentin.

## 7.7

### Applications (Post-treatment)

#### 7.7.1

##### Segmentation – Visualization Methods

The data provided by the previously described imaging technologies, such as MRI or CT scanning, generally consists of arrays of *voxels*, the 3D equivalent of pixels in

2D. We will focus on the case where each voxel holds a single scalar value, called *intensity*. In what follows, we describe methods that aim to help scientists explore these data by using a graphical computational technique, called *scientific volume visualization*.

Scientific visualization is a computational technique at the crossroads between data analysis and processing, computer graphics, and human–computer interaction. It has two goals for scientists:

- to provide insights into complex datasets to help understand and analyze data from a qualitative and quantitative point of view;
- to create expressive and aesthetically pleasant illustrations to improve scientific communication.

Several free and/or open-source software tools exist for processing and visualizing 3D voxel arrays, most of them being based on a library called the Visualization Toolkit (VTK) for visualization and on a library called Insight Toolkit (ITK) for image segmentation and registration. All-purpose visualization tools are not limited to MRI and CT scan data, such as, for example, ParaView and VisIt. Other tools are specialized, like MeVisLab, MedINRIA, MRI Studio, or Fiji (based on ImageJ). Commercial products providing image segmentation and 3D surface reconstruction tools also exist, such as Amira, Avizo, Mimics, and VGstudioMAX. In general, VTKs are based on the application of successive *filters* to the data. A survey concerning the computer science discipline “scientific visualization” as well as a description of various filters can be found in Hansen and Johnson (2004).

Scientific volume visualization uses classification to assign labels to individual voxels. Classification attempts to compute sets of voxels, called *classes*, which correspond to distinct ROIs, such as anatomical structures. Most classification techniques are based on a prior *segmentation* of the voxel array (see below). *Labeling* is the final step of assigning a color and transparency to each class to compute visual illustrations. In what follows, we first describe the main visualization techniques and then some of the main classification techniques.

#### 7.7.1.1 Main Visualization Methods

A voxel array of intensities, resulting for instance from  $\mu$ CT, can be considered to be a stack of 2D images along one of the three coordinate axes, so that these 2D images/slices can be displayed individually. Figure 7.15a depicts an example of slice visualization. Since displaying only 2D slices loses the third dimension, several elaborated visualization techniques have been developed. The objective is to restore a good perception of 3D structures. Among the most common techniques there are, on one hand, the direct volume rendering (DVR) techniques and, on the other hand, the simpler iso-surface display techniques. Both reconstruct a 3D object, which is then projected on the screen almost like a camera would take a photograph of a real-life 3D object.

The iso-surface extraction technique consists of building a smooth 3D surface from a sub-set of selected voxels, that is, a sort of hull that bounds these voxels. The sub-set of voxels is either chosen using an iso-intensity value (i.e., a set of voxels



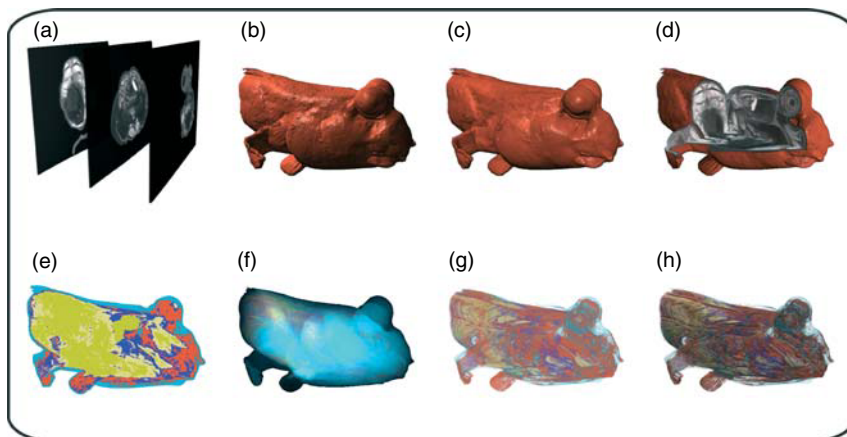


**Figure 7.15** Different techniques for rendering a voxel array of intensities of Atlantic mudskipper, *Periophthalmus barbarus*. (a) Displaying individual slices, (b,c) iso-surface reconstruction for two different light source positions, (d) iso-surface with cutting planes, (e) maximum intensity projection, (f) additive volume rendering, (g) direct volume rendering with semi-transparency, and (h) direct volume rendering with shading.

matching a certain intensity value or a certain intensity interval) or as the result of more advanced classification (see below). The *resulting surface* is defined as a set of triangles and displayed using the graphics boards available in computers. To compute the illustration, scientists essentially have to define a projection (e.g., an observer position, as for a real camera) and some lighting conditions along with the surface reflectance properties. *Shading* is the procedure that computes a color according to the local surface properties (essentially the normal vector), the lighting condition, and the reflectance properties. Advanced shading techniques might further integrate shadows, light diffusion, or specific graphical styles (such as illustrative border enhancement). Color patterns that are pasted onto the surface may also be used to highlight local surface properties, such as mean or Gaussian curvatures.

The result of the computation is a sort of “photograph” of the 3D surface, depending on the aforementioned shading technique. The chosen shading technique influences the computation time, which can range from instantaneous to several minutes. When computation of the illustration is perceived as instantaneous by the user (i.e., it is below about 300 ms), the visualization is said to be *interactive*. Interactivity is often a desired goal for both classification and illustration computation, as it offers users the possibility to browse various parameters in “real-time,” thus generally facilitating data exploration. The more complex the classification technique is, and the higher the number of visual effects integrated, the longer the computation of the illustration will take. Frequently, lighting and reflectance parameters are predefined or, at least, default values are proposed, so that the user first and foremost selects only a graphical “style” and the viewing direction, plus the zoom. It is also possible to define one or more cutting planes to



align the original X-ray  $\mu$ CT data with the reconstructed surface. Figure 7.15b–d shows an example of interactive iso-surface visualization.

The DVR technique is technically more complex. It computes an image without reconstructing an explicit 3D surface. It consists of sampling points along rays that pass through the 3D array of voxels. The samples are used to gather collections of ordered intensity values along each ray. These intensities are used to compute a corresponding color by applying a so-called compositing formula. Color and transparency values are assigned to intensities by using the transfer function. In its simplest form, the transfer function is a 1D lookup table that links each intensity value to a color and transparency. The compositing formula, that is, the way the ordered colors and transparencies are combined, determines the resulting image. Some compositing schemes are order independent. It can be reduced to applying a maximum intensity operator, which keeps only the color of the sample with highest intensity value. This kind of DVR technique is called a maximum intensity projection (MIP). An example is shown in Figure 7.15e. Order independent compositing may also be based on the weighted sum of colors, with the weight being provided by the transparency. In this case, the technique is called *additive volume rendering*. An example is shown in Figure 7.15f. Another common compositing formula, which exploits ordering, is inspired by the physics of light traversing the participating media: a semi-transparent corpus composed of small scale particles that emit, absorb, and scatter light, such as haze, fog, or clouds. Using this kind of compositing formula, interleaved structures appear more or less transparent. The further away, the less visible a structure will be due to light absorption. An example is shown in Figure 7.15g. For all of these compositing techniques, no lighting condition needs to be defined. Unfortunately, the human visual perception system is not used to easily identifying objects composed of semi-transparent materials. A solution to improve perception therefore consists of adding, as for surfaces, a shading procedure based on light sources and reflectance properties. Since no explicit surface is reconstructed and yet surface parameters are needed (such as the normal vector), the gradient of intensity is generally used as local surface descriptor. Figure 7.15h shows an example of DVR with shading.

Many more compositing techniques have been proposed. Most of them attempt to guarantee that “important” internal structures remain “best” visible. Two recent examples are the studies by Chuang, Weiskopf, and Möller (2011) and Marchesin, Dischler, and Mongenet (2010). Other techniques attempt to improve transfer functions. In particular, some transfer functions do not only use intensity values but also local operators such as the gradient and/or the Laplacian. Instead of a 1D lookup table, the transfer function becomes a 2D, 3D, or higher dimensioned table [see for instance Kniss, Kindlmann, and Hansen (2001) and Caban and Rheingans (2008)]. Some DVR methods further attempt to improve shading and shadowing without penalizing rendering performance (Šoltészová *et al.*, 2010) or propose to unify iso-surface visualization with DVR (Ament, Weiskopf, and Carr, 2010), the former being expressed as a particular case of the latter.

One particularity of the DVR approach is that it allows one to take into account the entire set of voxels. All data are used to create the illustration. The counterpart

is that all data must be stored in the graphics processing unit, thus limiting the size of voxel arrays (arrays that are too large must be down sampled). Another difficulty with this technique is to define an appropriate transfer function. Most direct volume visualization tools propose some default functions, often predefined according to the scientific context (medical, geological, etc.), but there is no universal solution to automatically define a good transfer function. Scientists often have to experiment with their own functions, which can take a considerable amount of time.

### 7.7.1.2 Classification and Segmentation

Defining transfer functions for DVR, as well as defining intensity intervals for iso-surface reconstruction, are both related to the notion of classification. Classification consists of associating to each voxel a given index called the *class*. By defining colors and transparencies using a transfer function, voxels become implicitly classified. Likewise, defining an intensity interval for iso-surface reconstruction consists of classifying the voxels. In fact, defining sets of intensity intervals is the simplest way of performing voxel classification. This classification technique is called *thresholding*. However, in most cases, threshold-based classifiers are not enough to discriminate and dissociate meaningful structures within datasets. The problem is that different anatomical components might have similar intensity responses. In addition, neighboring structures might cause blurred intensity values at boundaries, which is called the *partial volume effect*, that is, multiple tissues contribute to a single voxel. All of this makes it difficult to differentiate structures using only voxel intensity.

Some classifiers therefore use more information than just intensity, like the gradient, the Laplacian, or more generally, vectors representing responses to local filter banks, like the Gabor filter bank. These classifiers then apply a feature function to the computed information to perform the classification. A simple feature function is, for instance, the histogram. Often, local extremes, hills and valleys, in the histogram are used to define thresholds for partitioning intensities into intervals.

Computational 3D segmentation is a technique aimed at automating or at least facilitating the delineation of connected components of interest in voxel datasets – purely manual voxel-by-voxel segmentation being an excessively tedious task. Formally, computational segmentation is defined by a procedure that results in the partitioning of an image  $I$  into  $n$  sets of distinct connected components  $C_i$ . Segmentation should not be confused with the previously defined terminology of voxel classification. The distinction relates to the fact that classification produces sets of voxels that might be disconnected, such as for instance a collection of individual bones. Segmentation, on the other hand, provides sets of voxels that match connected components (each individual bone is separated). To some extent, segmentation can be considered as a particular case of classification. Most research concerning automatic segmentation is related to the field of medical imaging [see for instance the survey by Dzung *et al.*, 2000].

Classification and segmentation are generally unified, which also explains why both are frequently confused. For instance, once individual components have

been segmented, classification might simply consist in grouping or connecting components that have been separated by the segmentation. This can be carried out either manually or automatically by analyzing, for example, shapes and locations of components. Classification based on segmentation might even be performed implicitly during the labeling step by assigning an identical color/identifier to separated components. It might also be completely skipped when the amount of classes matches the number of segmented components (i.e., each component represents exactly one class). Conversely, some segmentation techniques use classifiers, for instance based on feature functions.

Different algorithmic methods for automatic segmentation can be listed (without being exhaustive): thresholding, region growing, classifiers, random field models, and atlas-based techniques. Since some of these techniques require manual intervention, they are called *semi-automatic*. For example, in its simplest form, the “region growing” algorithm requires manual selection of a seed position. Classifiers referred to as “*supervised*” use training data and perform a  $k$ -nearest neighbor classification. Classifiers referred to as “*unsupervised*” avoid the use of training data. The so-called  $k$ -means clustering algorithm is such an example. Atlas-guided approaches are based on a template, used as a reference/example to process new, yet similar, datasets. The core problem is then to register the dataset with the template. Because of the need for a template that is generally built by hand by expert scientists and because of the use of some knowledge related to the given scientific domain for performing the registration of the dataset with the template, atlas-based methods that are developed for one specific scientific domain cannot be easily transferred to another scientific domain. Despite decades of research, segmentation techniques are still not fully automated or precise. Some manual intervention (correction) is nearly always required.

Once the voxels of the array have been classified, a color, which is a strong visual feature identifier, can be assigned to the class and displayed using either one of the two previously described visualization techniques. Figure 7.16 illustrates visualization using iso-surface rendering including shadowing effects. The classification is based on semi-automatic segmentation using region growing. Segmentation is followed by manual reconnection of separated components and grouping into

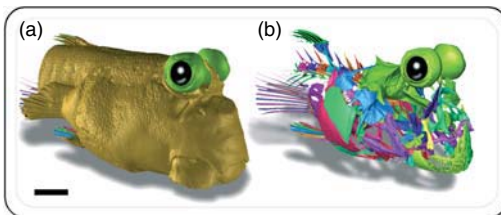


**Figure 7.16** Segmentation facilitates the delineation of regions of interest in voxel datasets, and allows visual classification of features by assigning them some individual color value. Volume rendering of (a) skin surface and (b) head and pectoral part of skeleton of the Atlantic mudskipper, *Periophthalmus barbarus*. Lens is black; scale bar = 1 mm.

classes belonging to the same anatomical structure (for instance, the eyes class, labeled with the color black, is composed of two separate components).

### 7.7.2

#### Numeric Simulation – Testing Hypotheses on Adaptive Evolution in Marine Vertebrates Using 3D Imaging Tools

Three-dimensional volumetric models allow the testing of hypotheses related to the adaptive nature of phenotypic divergence in evolutionary biology. To do so, different modeling approaches, including both forward and inverse dynamic modeling, can be used [e.g., Aerts *et al.* (2003) and Van Wassenbergh *et al.* (2003)]. More specifically, multibody dynamics analysis and finite element analysis (FEA) provide excellent quantitative tools in this context [e.g., Curtis *et al.* (2008) and Moazen *et al.* (2009)]. For the past few decades engineers have successfully been using multibody dynamics and FEA to predict the behavior of engineering structures. As these simulations are driven by a demand for efficiency, their application to biological problems in general and marine biology more specifically makes sense. However, applying these native engineering techniques to questions related to the biomechanics of marine vertebrates is accompanied by specific challenges, as accurate geometry and the forces acting on the structure of interest are often difficult to obtain. Obtaining accurate material properties can be even more troublesome: in contrast to most engineering materials, like steel or concrete, bone and soft tissues typically show a nonlinear, anisotropic elastic behavior that greatly differs not only between tissue samples but also within one sample [e.g., the Young's modulus and Poisson's ratio of biological tissues may vary locally as the result of an epigenetic, mechanical control of bone remodeling; see, for example, Biewener, Swartz, and Bertram (1986), Carter, Van Der Meulen and Beaupré (1996), Currey (2003), and Chen *et al.* (2008)]. Even in the rare case that material properties are available, variation can be considerable ([www.biomech.org](http://www.biomech.org)). This renders the interpretation of simulations with even the most advanced material modeling challenging. Luckily, obtaining quantitative values is rarely the primary goal of simulations in biomechanics. Usually, biologists are more interested in, for example, regions of high stress concentrations, although estimates of exact stresses may become crucial for studying skeletal failure under certain conditions (Soons *et al.*, 2010). In addition, combining parts of a 3D model with different material properties is a challenge, but does confer relevance in terms of a proper understanding of how biological systems behave under natural loading conditions (Porro *et al.*, 2011). Changes in the applied material model will typically only have a limited effect on the location of high stress concentrations. As such, simulations can, for example, predict where bone fracture is likely to occur under certain loading conditions, but will usually fail in accurately predicting under which loading conditions.

Few studies so far have focused on marine organisms, with studies exploring structural adaptation in the skull in burrowing eels (Herrel *et al.*, 2011) or suction feeding in seahorses (Leysen *et al.*, 2011) being an exception. Another study has focused on the caudal system in seahorses, where the tail has evolved into an

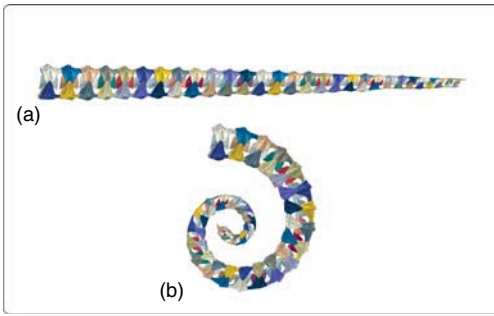


**Figure 7.17** (a, b) Bending of the seahorse caudal skeletal structure simulated using multi-body dynamics.

articulated, prehensile structure within the family of Syngnathidae (Hale, 1996; Van Cauter *et al.*, 2010, Figure 7.17). Despite its high level of flexibility, the seahorse tail still shows a relatively high resistance against radial forces (which likely makes it an effective protective armor against predators). This combination of radial stiffness and ventral flexibility can only be achieved by the articulation of a chain of uniformly shaped skeletal segments. Each segment consists of a central vertebra, surrounded by four dermal plates. In on-going research, all of these skeletal elements are being modeled as rigid bodies, connected by spring elements that represent the joints. The effect of muscle contraction (hypaxial muscles and median ventral muscles) can be simulated and several parameters can quickly be adapted so that their effect on the kinematics can be quantified. In this way, it can be determined whether these parameters are optimized by evolution for tail prehensibility of a rigid system.

Multibody simulations of the seahorse caudal structure can uncover the secrets of how radial strength and stiffness can effectively be combined with extreme bending flexibility – knowledge that could be a source of inspiration for breakthroughs in engineering fields that focus on high radial stiffness (like stent design). Further applications of 3D models of biological systems can be found in translating the quantitative data within the virtual environment into physical elements using different techniques of stereolithography and rapid prototyping [e.g., Chapman, Andersen, and Wilcox (2003) and Nielson, Kaehr, and Shear (2009)]. This not only provides a means to generate models that can be used for display, but also allows hypothesis testing on adaptive evolution as well as designing innovative models inspired from nature, with possible applications in industry or even the medical world [e.g., Simaan, Taylor, and Flint (2004), Blevins and Lauder (2011), and Fish (2011)].

## 7.8

### Conclusion

The oceans cover more than 70% of the Earth's surface and almost 99% of the planet's living space. However, despite 250 years of taxonomic classification, 91%

of the estimated 2.2 million of marine eukaryotic species still await to be described and classified (Mora *et al.*, 2011). Moreover, the rate of data accumulation on marine organisms and the increase in the phylogenetic resolution of marine taxa are both slower than for terrestrial taxa (Thomson and Shaffer, 2010). Knowing this, and considering that the world's oceans are undergoing profound changes due to anthropogenic climate changes (Jackson, 2008; Hoegh-Guldberg and Bruno, 2010), there is an urgent need to conduct large-scale taxonomic analyses of marine environments. The best way to reach this objective is to develop data collection strategies adapted to the study of marine organisms. We believe that the large panel of tomographic methods presented here may be a valuable tool for this purpose.

MRI constitutes a very convenient non-invasive and non-destructive *in vivo* method to access soft tissues information. In addition to conventional aMRI, fMRI, diffusion magnetic resonance imaging (*dmMRI*), and MEMRI provide powerful tools to gain insight into biological processes *in vivo* (particularly in the nervous system). However, the necessity to use hydrated specimens prevents the use of alcohol-preserved specimens (most collection specimens) without prior rehydration. This and the long acquisition times required for high-resolution scans (up to tens of hours) compared to X-ray  $\mu$ CT could constitute the main drawbacks of this method.

Conventional X-ray  $\mu$ CT is based on absorption and thus is not so well adapted to the imaging of animal soft-tissue at high spatial resolution, although it produces excellent results with bony or shell-bearing organisms because of the absorption difference between the bone (or shell) and the soft tissues. Staining agents can enhance the contrast between different tissues. X-ray PCI methods (free space propagation, ABI, and grating interferometry) offer contrast levels up to 1000-times higher than those obtained by absorption methods. This, combined with the high spatial resolution that can be reached by these methods, makes X-ray PCI a very appropriate technique for the study of the countless, small, soft-bodied, marine organisms. The disadvantage of these methods is that most of them have X-ray beam requirements that are only met at synchrotron-based setups. However, laboratory-based setups providing X-ray phase contrast at slightly inferior spatial resolution and sensitivity than synchrotron setups have been demonstrated and are under active further development.

Regardless of the acquisition method, the data provided by imaging techniques (MRI, X-ray tomography) are, most of the time, first exploited by scientific volume visualization methods (DVR or iso-surface display, for example). Such visualization techniques allow the reconstruction of 3D objects that can be projected into 2D images on a screen and easily manipulated to obtain visual insight into complex datasets or to create scientific illustrations. These 3D volumetric models can then be used for numerical simulation methods like FEA or multibody dynamics analyses to test biomechanical hypotheses.

Taken together, these methods offer the new ways needed to gather morphologic, anatomic, and physiologic data on marine organisms, from microscopic planktonic organisms to large marine mammals.

## Acknowledgements

We thank Dr Anthony Herrel for a critical reading of a previous version of the manuscript and are grateful to the CEMIM team. Material from MNHN, Paris, was kindly loaned by Ivan Ineich. The ESRF for the Postdoctoral Project of R. Renaud, and for the allocation of beamtime through this project is also acknowledged. We thank Pascal Deynat for material kindly given on loan from his personal collection. Elodie Boller, Paul Tafforeau, and Vincent Fernandez, ESRF, Grenoble, are acknowledged for their help during my post-doctoral work at ESRF.

## References

- Adam, J.F., Nemoz, C., Bravin, A., Fiedler, S., Bayat, S., Monfraix, S., Berruyer, G., Charvet, A.M., Le Bas, J.F., Elleaume, H., and Esteve, F. (2005) High-resolution blood-brain barrier permeability and blood volume imaging using quantitative synchrotron radiation computed tomography: study on an F98 rat brain glioma. *J. Cereb. Blood Flow Metab.*, **25** (2), 145–153.
- Aerts, P., Van Damme, R., D'Août, K., and Van Hooydonck, B. (2003) Bipedalism in lizards: whole-body modelling reveals a possible spandrel. *Philos. Trans. R. Soc. London, Ser. B*, **358** (1437), 1525–1533.
- Aggarwal, M., Zhang, J., Miller, M.I., Sidman, R.L., and Mori, S. (2009) Magnetic resonance imaging and micro-computed tomography combined atlas of developing and adult mouse brains for stereotaxic surgery. *Neuroscience*, **162** (4), 1339–1350.
- Alric, C., Taleb, J., Le Duc, G., Mandon, C., Billotey, C., Le Meur-Herland, A., Brochard, T., Vocanson, F., Janier, M., Perriat, P., Roux, S., and Tillement, O. (2008) Gadolinium chelate coated gold nanoparticles as contrast agents for both X-ray computed tomography and magnetic resonance imaging. *J. Am. Chem. Soc.*, **130**, 5908–5915.
- Altapova, V., Helfen, L., Myagotin, A., Hänschke, D., Moosmann, J., Gunneweg, J., and Baumbach, T. (2012) Phase contrast laminography based on Talbot interferometry. *Opt. Express*, **20**, 6496–6508.
- Ament, M., Weiskopf, D., and Carr, H. (2010) Direct interval volume visualization. *IEEE Trans. Vis. Comput. Graph.*, **16** (6), 1505–1514.
- Arfelli, F., Bonvicini, V., Bravin, A., Cantatore, G., Castelli, E., Palma, L.D., Michiel, M.D., Fabrizioli, M., Longo, R., Menk, R.H., Olivo, A., Pani, S., Pontoni, D., Poropat, P., Prest, M., Rashevsky, A., Ratti, M., Rigon, L., Tromba, G., Vacchi, A., Vallazza, E., and Zanconati, F. (2000) Mammography with synchrotron radiation: phase-detection techniques. *Radiology*, **215** (1), 286–293.
- Baldelli, P., Taibi, A., Tuffanelli, A., Gilardoni, M.C., and Gambaccini, M. (2005) A prototype of a quasi-monochromatic system for mammography applications. *Phys. Med. Biol.*, **50** (10), 2225–2240.
- Baruchel, J., Bleuët, B., Bravin, A., Coan, P., Lima, E., Madsen, A., Ludwig, W., Pernot, P., and Susini, J. (2008) Advances in synchrotron hard X-ray based imaging. *C.R. Phys.*, **9** (5-6), 624–641.
- Basser, P. and Pierpaoli, C. (1996) Microstructural and physiological features of tissues elucidated by quantitative-diffusion-tensor MRI. *J. Magn. Reson. B*, **11** (3), 209–219.
- Bayat, S., Le Duc, G., Porra, L., Berruyer, G., Nemoz, C., Monfraix, S., Fiedler, S., Thomlinson, W., Suortti, P., Standertskjöld-Nordenstam, C.G., and Sovijärvi, A.R.A. (2001) Quantitative functional lung imaging with synchrotron radiation using inhaled xenon as contrast agent. *Phys. Med. Biol.*, **46** (12), 3287–3299.
- Beaulieu, C. and Allen, P.S. (1994) Water diffusion in the giant axon of the squid:



- implications for diffusion-weighted MRI of the nervous system. *Magn. Reson. Med.*, **32** (5), 579–583.
- Bech, M., Bunk, O., Donath, T., Feidenhans'l, R., David, C., and Pfeiffer, F. (2010) Quantitative x-ray dark-field computed tomography. *Phys. Med. Biol.*, **55** (18), 5529–5539.
- Beckmann, F., Bonse, U., Busch, F., and Günnewig, O. (1997) X-ray microtomography ( $\mu$ CT) using phase contrast for the investigation of organic matter. *J. Comput. Assist. Tomogr.*, **21**, 539–553.
- Betz, O., Wegst, U., Weide, D., Heethoff, M., Helfen, L., Lee, W.K., and Cloetens, P. (2007) Imaging applications of synchrotron X-ray phase-contrast microtomography in biological morphology and biomaterials science. I. General aspects of the technique and its advantages in the analysis of millimetre-sized arthropod structure. *J. Microsc.*, **227** (1), 51–71.
- Biewener, A.A., Swartz, S.M., and Bertram, J.E.A. (1986) Bone modeling during growth: dynamic strain equilibrium in the chick tibiotarsus. *Calcif. Tissue Int.*, **39** (6), 390–395.
- Blevins, E.L. and Lauder, G.V. (2011) Ground effects on undulating fins: robotic modeling of stingray locomotion. *Integr. Comp. Biol.*, **51**, E12.
- Bocage, A.E.M. (1922) Procédé et dispositif de radiographie sur plaque en mouvement, French Patent no 536464.
- Boistel, R., Pollet, N., Tinevez, J.T., Cloetens, P., and Schlenker, M. (2009) Irradiation damage to frog inner ear during synchrotron radiation tomographic investigation. *J. Electron. Spectrosc. Relat. Phenom.*, **170** (1-3), 37–41.
- Caban, J.J. and Rheingans, P. (2008) Texture-based transfer functions for direct volume rendering. *IEEE Trans. Vis. Comput. Graph.*, **14** (6), 1364–1371.
- Canals, S., Beyerlein, M., Keller, A.L., Murayama, Y., and Logothetis, N.K. (2008) Magnetic resonance imaging of cortical connectivity in vivo. *Neuroimage*, **40**, 458–472.
- Carter, D.R., Van Der Meulen, M.C.H., and Beaupré, G.S. (1996) Mechanical factors in bone growth and development. *Bone*, **18** (1), 5–10.
- Castelli, E., Tonutti, M., Arfelli, F., Longo, R., Quaia, E., Rigon, L., Sanabor, D., Zanconati, F., Dreossi, D., Abrami, A., Quai, E., Bregant, P., Casarin, K., Chenda, V., Menk, R.H., Rokvic, T., Vascotto, A., Tromba, G., and Cova, M.A. (2011) Mam-mography with synchrotron radiation: first clinical experience with phase-detection technique. *Radiology*, **259** (3), 684–694.
- Chapman, R.E., Andersen, A., and Wilcox, B. (2003) Studying extinct animals using three-dimensional visualization, scanning, animation, and prototyping. *Proc. SPIE*, **5006**, 469.
- Chen, P.Y., Lin, A.Y.M., Lin, Y.S., Seki, Y., Stokes, A.G., Peyras, J., Olevsky, E.A., Meyers, M.A., and McKittrick, J. (2008) Structure and mechanical properties of selected biological materials. *J. Mech. Behav. Biomed. Mater.*, **1** (3), 208–226.
- Chilingaryan, S., Mirone, A., Hammersley, A., Ferrero, C., Helfen, L., Kopmann, A., dos Santos Rolo, Y., and Vagovic, P. (2011) A GPU-based architecture for real-time data assessment at synchrotron experiments. *IEEE Trans. Nucl. Sci.*, **58**, 1447–1455.
- Chuang, J., Weiskopf, D., and Möller, T. (2009) Hue-preserving color blending. *IEEE Trans. Vis. Comput. Graph.*, **15** (6), 1275–1282.
- Chilingaryan, S., Mirone, A., Hammersley, A., Ferrero, C., Helfen, L., Kopmann, A., dos Santos Rolo, T., and Vagovic, P. (2011) A GPU-based architecture for real-time data assessment at synchrotron experiments. *IEEE Transactions on Nuclear Science*, **58** (4), 1447–1455.
- Cloetens, P., Ludwig, W., Baruchel, J., Van Dyck, D., Van Landuyt, J., Guigay, J., and Schlenker, M. (1999) Holotomography: quantitative phase tomography with micrometer resolution using hard synchrotron radiation X-rays. *Appl. Phys. Lett.*, **75**, 2912–2914.
- Cloetens, P., Pateyron-Salomé, M., Buffière, J., Peix, G., Baruchel, J., Peyrin, F., and Schlenker, M. (1997) Observation of microstructure and damage in materials by phase sensitive radiography and tomography. *J. Appl. Phys.*, **81**, 5878–5886.
- Coan, P., Bamberg, F., Diemoz, P.C., Bravin, A., Timpert, K., Mützel, E., Raya, J., Reiser, M., and Glaser, C. (2010) Characterization of osteoarthritic and normal



- human patella cartilage by computed tomography X-ray phase-contrast imaging: a feasibility study. *Invest. Radiol.*, **45** (7), 437–444.
- Coan, P., Mollenhauer, J., Wagner, A., Muehleman, C., and Bravin, A. (2008) Analyzer-based imaging technique in tomography of cartilage and metal implants: a study at the ESRF. *Eur. J. Radiol.*, **68** (Suppl. 3), S41–S48.
- Cormack, A.M. (1963) Representation of a function by its line integrals, with some radiological applications. *J. Appl. Phys.*, **34**, 2722.
- Currey, J.D. (2003) Role of collagen and other organics in the mechanical properties of bone. *Osteoporos. Int.*, **14**, S29–S36.
- Curtis, N., Kupczik, K., O'Higgins, P., Moazen, M., and Fagan, M.I. (2008) Predicting skull loading: applying multibody dynamics analysis to a macaque skull. *Anat. Rec.: Adv. Integr. Anat. Evol. Biol.*, **291** (5), 491–501.
- De Groof, G., Verhoye, M., Van Meir, V., Tindemans, I., Leemans, A., and Van der Linden, A. (2006) In vivo diffusion tensor imaging (DTI) of brain subdivisions and vocal pathways in songbirds. *Neuroimage*, **29** (3), 754–763.
- Dobbins, J.T. III, and Godfrey, D.J. (2003) Digital X-ray tomosynthesis: current state of the art and clinical potential. *Phys. Med. Biol.*, **48**, R65–R106.
- Dolan, R.J. (2008) Neuroimaging of cognition: past, present, future. *Neuron*, **60**, 496–502.
- Donath, T., Pfeiffer, F., Bunk, O., Grünzweig, C., Hempel, E., Popescu, S., Vock, P., and David, C. (2010) Towards clinical X-ray phase-contrast CT. *Invest. Radiol.*, **45** (7), 445–452.
- Dzung, L., Pham, D.L., Xu, C., and Prince, J.L. (2000) Current methods in medical image segmentation. *Annu. Rev. Biomed. Eng.*, **2**, 315–337.
- Edelman, R.R. (2004) Contrast-enhanced MR imaging of the heart: overview of the literature. *Radiology*, **232**, 653–668.
- Esteve, F., Elleaume, H., Bertrand, B., Charvet, A.M., Fiedler, S., Le Duc, G., Corde, S., Nemoz, C., Renier, M., Lefaix, J.L., Leplat, J.J., Suortti, P., Thomlinson, W., and Le Bas, J.F. (2002) Coronary angiography with synchrotron X-ray source on pigs after iodine or gadolinium intravenous injection. *Acad. Radiol.*, **9** (Suppl. 1), S92–S97.
- Feldkamp, L.A., Davis, L.C., and Kress, J.W. (1984) Practical cone-beam algorithm. *J. Opt. Soc. Am.*, **1** (6), 612–619.
- Fish, F.E. (2011) The humpback whale flipper for application of bio-inspired tubercle technology. *Integr. Comp. Biol.*, **51**, E42.
- Gillet, B., Po, C., Dupont, D., Sébrié, C., and Méric, P. (2010) Manganèse et imagerie de résonance magnétique du développement cérébrale. *C.R. Chim.*, **13** (4), 459–465.
- Glover, P. and Mansfield, P. (2002) Limits to magnetic resonance microscopy. *Rep. Prog. Phys.*, **65** (10), 1489–1511.
- Gondrom, S., Zhou, J., Maisl, M., Reiter, H., Kröning, M., and Arnold, W. (1999) X-ray computed laminography: an approach of computed tomography for applications with limited access. *Nucl. Eng. Des.*, **190** (1-2), 141–147.
- Goodman, J.W. (2005) *Introduction to Fourier Optics*, 3rd edn, Roberts & Company, Greenwood Village, CO.
- Grangeat, P. (1991) Mathematical framework of cone beam 3D reconstruction via the first derivative of the Radon transform. *Lect. Notes Math.*, **1497**, 66–97.
- Grant, D.G. (1972) Tomosynthesis: a three-dimensional radiographic imaging technique. *IEEE Trans. Biomed. Eng.*, **19**, 20–28.
- Grosso, A., Stampanoni, M., Abela, R., Schneider, P., Linga, S., and Müller, R. (2006) Phase contrast tomography: an alternative approach. *Appl. Phys. Lett.*, **88** (21), 214104.
- Guigay, J., Langer, M., Boistel, R., and Cloetens, P. (2007) A mixed contrast transfer and transport of intensity approach for phase retrieval in the Fresnel region. *Opt. Lett.*, **32**, 1617–1619.
- Hale, M.E. (1996) Functional morphology of ventral tail bending and prehensile abilities of the seahorse, *Hippocampus kuda*. *J. Morphol.*, **227** (1), 51–65.
- Hansen, G., Crooks, L.E., Davis, P., De Groot, J., Herfkens, R., Margulis, A.R., Gooding, C., Kaufman, L., Hoenninger, J., Arakawa, M., McRee, R., and Watts, J. (1980) In vivo imaging of the rat anatomy with nuclear magnetic resonance. *Radiology*, **136** (3), 695–700.

- Hansen, C. and Johnson, C.R. (2004) *Visualization Handbook*, Elsevier Butterworth-Heinemann, Burlington, MA, 984.
- Hart, A.G., Bowtell, R.W., Köckenberger, W., Wenseleers, T., and Ratnieks, F.L.W. (2003) Magnetic resonance imaging in entomology: a critical review. *J. Insect Sci.*, **3** (5), 9.
- Heinzer, S., Krucker, T., Stampanoni, M., Abela, R., Meyer, E.P., Schuler, A., Schneider, P., and Müller, R. (2006) Hierarchical microimaging for multi-scale analysis of large vascular networks. *Neuroimage*, **32** (2), 626–636.
- Helfen L., Baumbach T., Cloetens P., Baruchel J. (2009). Phase-contrast and holographic computed laminography. *Appl. Phys. Lett.*, **94**, 104103.
- Helfen L., Baumbach T., Mikulík P., Kiel D., Pernot P., Cloetens P. & Baruchel J. (2005). High-resolution three-dimensional imaging of flat objects by synchrotron-radiation computed laminography. *Appl. Phys. Lett.*, **86**, 071915.
- Helfen, L., Baumbach, T., Pernot, P., Mikulík, P., DiMichiel, M., and Baruchel, J. (2006a) High-resolution three-dimensional imaging by synchrotron-radiation computed laminography, in *Developments in X-Ray Tomography V* (ed. U. Bonse) *Proceeding of the SPIE*, vol. 6318, p. 63180N.
- Helfen, L., Myagotin, A., Pernot, P., Di Michiel, M., Mikulík, P., Berthold, A., and Baumbach, T. (2006b) Investigation of hybrid pixel detector arrays by synchrotron-radiation imaging. *Nucl. Instrum. Methods Phys. Res., Sect. A*, **563**, 163–166.
- Helfen L., Myagotin A., Mikulík P., Pernot P., Voropaev A., Elyyan M., Di Michiel M., Baruchel J., Baumbach T. (2011). On the implementation of computed laminography using synchrotron radiation. *Rev. Sci. Instrum.*, **82**, 063702.
- Herman, G.T. (1980) *Image Reconstruction from Projections: The Fundamentals of Computerized Tomography*, Academic Press, New York.
- Herrel, A., Choi, H.F., Dumont, E., De Schepper, N., Vanhooydonck, B., Aerts, P., and Adriaens, D. (2011) Burrowing and subsurface locomotion in anguilliform fish: behavioral specializations and mechanical constraints. *J. Exp. Biol.*, **214** (8), 1379–1385.
- Herzen J., Beckmann F., Ogureck M., Riekehr S., Haibel A., Schreyer A., Donath T., David C., Pfeiffer F., Mohr J., Reznikova E., Schulz G., and Müller B. (2010), X-ray grating interferometer for imaging at a second-generation synchrotron radiation source, *Proc. SPIE* **7804**, 780407.
- Herzen, J., Donath, T., Pfeiffer, F., Bunk, O., Padeste, C., Beckmann, F., Schreyer, A., and David, C. (2009) Quantitative phase-contrast tomography of a liquid phantom using a conventional x-ray tube source. *Opt. Express*, **17** (12), 10010–10018.
- Hoegh-Guldberg, O. and Bruno, J.F. (2010) The impact of climate change on the world's marine ecosystems. *Science*, **328** (5985), 1523–1528.
- Hounsfield, G.N. (1972) A method of and apparatus for examination of a body by radiation such as X-ray or gamma radiation. British Patent office. 34, no 12839153.
- Hounsfield, G.N. (1973) Computerized transverse axial scanning (tomography). 1. Description of system. *Br. J. Radiol.*, **46** (552), 1016–1022.
- Houssaye, A., Xu, F., Helfen, L., de Buffrénil, V., Baumbach, T., and Tafforeau, P. (2011) *J. Vertebr. Paleontol.*, **31**, 2–7.
- Jackson, J.B. (2008) Ecological extinction and evolution in the brave new ocean. *Proc. Natl. Acad. Sci. U.S.A.*, **105** (Suppl. 1), 11458–11465.
- Jensen, T.H., Bech, M., Zanette, I., Weitkamp, T., David, C., Deyhle, H., Rutishauser, S., Reznikova, E., Mohr, J., Feidenhans'l. R. & Pfeiffer, F. (2010). Directional x-ray dark-field imaging of strongly ordered systems, *Phys. Rev. B*, **82**, 214103.
- Jensen, T.H., Böttiger, A., Bech, M., Zanette, I., Weitkamp, T., Rutishauser, S., David, C., Reznikova, E., Mohr, J., Bager Christensen, L., Olsen, E.V., Feidenhans'l, R., and Pfeiffer, F. (2011) X-ray phase-contrast tomography of porcine fat and rind. *Meat Sci.*, **88**, 379–383.
- Jerjen I., Revol V., Kottler C., Luethi Th., Sennhauser U., Kaufmann R., & Urban C. (2010). Phase contrast cone beam

- tomography with an X-ray grating interferometer. *AIP Conf. Proc.* **1236**, 227–231.
- Johnson, J.T., Hansen, M.S., Wu, I., Healy, L.J., Johnson, C.R., Jones, G.M., Capecchi, M.R., and Keller, C. (2006) Virtual histology of transgenic mouse embryos for high-throughput phenotyping. *PLoS Genet.*, **2** (4), e61.
- Kabli, S., Alia, A., Spaink, H.P., Verbeek, F.J., and De Groot, H.J.M. (2006) Magnetic resonance microscopy of the adult zebrafish. *Zebrafish*, **3** (4), 431–439.
- Kak, A.C. and Slaney, M. (1988) *Principles of Computerized Tomographic Imaging*, IEEE Press, New York.
- Kalender, W.A. (2005) *Computed Tomography: Fundamentals, System Technology, Image Quality, Applications*, 2nd edn, Publicis Corporate Publishing, Erlangen.
- Kalender, W.A. (2006) *Computertomographie*, Publicis Corporate Publishing, Erlangen.
- Kalukin, A. and Sankaran, V. (1997) *IEEE Trans. Compon. Packag. Manuf. Technol. Part A*, **20**, 361–366.
- Katsevich, A. (2004) An improved exact filtered back-projection algorithm for spiral computed tomography. *Adv. Appl. Math.*, **32** (4), 681–697.
- Keyriläinen, J., Bravin, A., Fernandez, M., Tenhunen, M., Virkkunen, P., and Suortti, P. (2010) Phase-contrast X-ray imaging of breast. *Acta Radiol.*, **51** (8), 866–884.
- Keyriläinen, J., Fernández, M., Karjalainen-Lindsberg, M.L., Virkkunen, P., Leidenius, M., von Smitten, K., Sipilä, P., Fiedler, S., Suhonen, H., Suortti, P., and Bravin, A. (2008) Towards high-contrast breast CT at low radiation dose. *Radiology*, **249** (1), 321–327.
- Kniss, J., Kindlmann, G., and Hansen, C. (2001) Interactive volume rendering using multi-dimensional transfer functions and direct manipulation widgets in *Proceedings IEEE Visualization, VIS '01, October 21–26, 2001*, I.E.E.E. Press, New York, pp. 255–562.
- Krug, K., Porra, L., Coan, P., Tauber, G., Wallert, A., Dik, J., Coerdts, A., Bravin, A., Elyyan, M., Helfen, L., and Baumbach, T. (2008) Relics in medieval altarpieces? Combining X-ray tomographic, lamino-graphic and phase-contrast imaging to visualize thin organic objects in paintings. *J. Synchrotron Radiat.*, **15**, 55–61.
- Langer, M., Cloetens, P., and Peyrin, F. (2009) Fourier-wavelet regularization of phase retrieval in x-ray in-line phase tomography. *J. Opt. Soc. Am. A*, **26**, 1876–1881.
- Langer, M., Cloetens, P., and Peyrin, F. (2010) Regularization of phase retrieval with phase-attenuation duality prior for 3D holotomography. *IEEE Trans. Image Process.*, **19**, 2428–2436.
- Langer, M., Pacureanu, A., Suhonen, H., Grimal, Q., Cloetens, P. and Peyrin, F. (2012) X-Ray Phase Nanotomography Resolves the 3D Human Bone Ultrastructure. *PLoS ONE* **7**(8): e35691.
- Lauritsch, G. and Härer, W.H. (1999) Medical imaging: image processing. *Proc. SPIE*, **3338**, 1127–1137.
- Le Bihan, D. (2003) Looking into the functional architecture of the brain with diffusion MRI. *Nat. Rev. Neurosci.*, **4** (6), 469–480.
- Leysen, H., Dumont, E.R., Brabant, L., Van Hoorebeke, L., and Adriaens, D. (2011) Modelling stress in the feeding apparatus of seahorses and pipefishes (Teleostei: Syngnathidae). *Biol. J. Linn. Soc.*, **104** (3), 680–691.
- Lorenzetti, V., Lubman, D.I., Whittle, S., Solowij, N., and Yücel, M. (2010) Structural MRI findings in long-term cannabis users: what do we know? *Subst. Use Misuse*, **45** (11), 1787–1808.
- Lynch S.K., Pai V., Auxier J., Stein A.F., Bennett E.E., Kemble C.K., Xiao X., Lee W.K., Morgan N.Y. & Wen H.H. (2011). Interpretation of dark-field contrast and particle-size selectivity in grating interferometers. *Appl. Opt.*, **50** (22): 4310–4319.
- Marchesin, S., Dischler, J.M., and Mongenet, C. (2010) Per-pixel opacity modulation for feature enhancement in volume rendering. *IEEE Trans. Vis. Comput. Graph.*, **16** (4), 560–570.
- Margaritondo G., Tromba G. (1999). Coherence-based edge diffraction sharpening of x-ray images: a simple model. *J. Appl. Phys.*, **85** (7): 3406–3408.
- Massaad C., Pautler R.G. (2011).in *Magnetic Resonance Neuroimaging Methods and Protocols* (eds Modo M. & Bulte J.W.M., series ed. J.M. Walker), Methods in Molecular Biology, vol. 711, pp. 145–174, Humana

- Press Springer Science+Business Media, LLC.
- Matsui, H., Iwata, A., Horiba, I., and Suzumura, N. (1993) *IEEE Trans. Med. Imag.*, **12**, 307.
- McDonald, S.A., Marone, F., Hintermüller, C., Mikuljan, G., David, C., Pfeiffer, F., and Stampanoni, M. (2009) Advanced phase-contrast imaging using a grating interferometer. *J. Synchrotron Radiat.*, **16** (4), 562–572.
- Metscher, B.D. (2009) Micro CT for comparative morphology: simple staining methods allow high-contrast 3D imaging of diverse non-mineralized animal tissues. *BMC Physiol.*, **2009**, 9–11.
- Mispelter, J., Lupu, M., and Briguët, A. (2006) NMR Probeheads for Biophysical and Biomedical Experiments, in *Theoretical Principles and Practical Guidelines*, Imperial College Press, London.
- Moazen, M., Curtis, N. *et al.* (2009) Biomechanical assessment of evolutionary changes in the lepidosaurian skull. *Proc. Natl. Acad. Sci. U.S.A.*, **106** (20), 8273–8277.
- Moffat, A.J., Wright, P., Helfen, L., Baumbach, T., Johnson, G., Spearing, S.M., and Sinclair, I. (2010) In situ synchrotron computed laminography of damage in carbon fibre-epoxy [90/0](s) laminates. *Scr. Mater.*, **62** (2), 97–100.
- Momose, A. (2003) Demonstration of X-ray Talbot interferometry. *Jpn. J. Appl. Phys.*, **42**, L866–L868.
- Momose, A., Takeda, T., Itai, Y., and Hirano, K. (1996) Phase-contrast X-ray computed tomography for observing biological soft tissues. *Nat. Med.*, **2**, 473–475.
- Momose, A., Yashiro, W., Harasse, S., and Kuwabara, H. (2011) Four-dimensional X-ray phase tomography with Talbot interferometry and white synchrotron radiation: dynamic observation of a living worm. *Opt. Express*, **19** (9), 8423–8432.
- Momose, A., Yashiro, W., Maikusa, H., and Takeda, Y. (2009) High-speed X-ray phase imaging and X-ray phase tomography with Talbot interferometer and white synchrotron radiation. *Opt. Express*, **17** (15), 12540.
- Mora, C., Tittensor, D.P., Adl, S., Simpson, A.G., and Worm, B. (2011) How many species are there on earth and in the ocean? *PLoS Biol.*, **9** (8), e1001127.
- Morgeneyer, T.F., Helfen, L., Sinclair, I., Proudhon, H., Xu, F., and Baumbach, T. (2011) Ductile crack initiation and propagation assessed via in situ synchrotron radiation computed laminography. *Scr. Mater.*, **65** (2011), 1010–1013.
- Muehleman, C., Majumdar, S., Issever, A.S., Arfelli, F., Menk, R.H., Rigon, L., Heitner, G., Reime, B., Metge, J., Wagner, A., Kuettner, K.E., and Mollenhauer, J. (2004) X-ray detection of structural orientation in human articular cartilage. *Osteoarthritis Cartilage*, **12** (2), 97–105.
- Narasimhan, P.T. and Jacobs, R.E. (2002) *Brain Mapping: The Methods*, 2nd edn, Academic Press, New York, pp. 399–426.
- Natterer, F. (1986) *The Mathematics of Computerized Tomography*, John Wiley Sons, Inc., New York.
- Nielson, R., Kaehr, B., and Shear, J.B. (2009) Microreplication and design of biological architectures using dynamic-mask multiphoton lithography. *Small*, **5** (1), 120–125.
- Nugent, K. (2010) Coherent methods in the X-ray sciences. *Adv. Phys.*, **59** (1), 1–99.
- Nugent, K., Gureyev, T., Cookson, D., Paganin, D., and Barnea, Z. (1996) Quantitative phase imaging using hard X-rays. *Phys. Rev. Lett.*, **77**, 2961–2964.
- Null, C.W., Liu, C.W., Hedehus, M., Conolly, S., and Davis, R.W. (2008) High-resolution, in vivo magnetic resonance imaging of *Drosophila* at 18.8 Tesla. *PLoS ONE*, **3** (7), e2817.
- Oeffner, J. and Lauder, G.V. (2012) The hydrodynamic function of shark skin and two biomimetic applications. *J. Exp. Biol.*, **215**, 785–795.
- Ogawa, S., Lee, T.M., Kay, A.R., and Tank, D.W. (1990) Brin magnetic resonance imaging with contrast dependent on blood oxygenation. *Proc. Natl. Acad. Sci. U.S.A.*, **87**, 9868–9872.
- Olivo, A., Ignatyev, K., Munro, P.R.T., and Speller, R.D. (2011) Noninterferometric phase-contrast images obtained with incoherent x-ray sources. *Appl. Opt.*, **50** (12), 1765–1769.
- Paganin, D., Mayo, S.C., Gureyev, T.E., Miller, P.R., and Wilkins, S.W. (2002)

- Simultaneous phase and amplitude extraction from a single defocused image of a homogeneous object. *J. Microsc.*, **206** (1), 33–40.
- Pasco-Viel, E., Charles, C., Chevret, P., Semon, M., Tafforeau, P., Viriot, L., and Laude, V. (2010) Evolutionary trends of the pharyngeal dentition in cypriniformes (Actinopterygii: Ostariophysi). *PLoS ONE*, **5** (6), e11293.
- Pérez-Huerta, A., Cusack, M., McDonald, S., Marone, F., Stampanoni, M., and MacKay, S. (2009) Brachiopod punctae: a complexity in shell biomineralisation. *J. Struct. Biol.*, **167** (1), 62–67.
- Peyrin, F.C. (1985) The generalized back projection theorem for cone beam reconstruction. *IEEE Trans. Nucl. Sci.*, **32** (4), 1512–1519.
- Peyrin, F. (2009) Investigation of bone with synchrotron radiation imaging: from micro to nano. *Osteoporos. Int.*, **20**, 1057–1063.
- Pfeiffer, F., Bunk, O., David, C., Bech, M., Le Duc, G., Bravin, A., and Cloetens, P. (2007a) High-resolution brain tumor visualization using three-dimensional X-ray phase contrast tomography. *Phys. Med. Biol.*, **52**, 6923–6930.
- Pfeiffer, F., Kottler, C., Bunk, O., and David, C. (2007b) Hard X-ray phase tomography with low-brilliance sources. *Phys. Rev. Lett.*, **98** (10), 108105.
- Pfeiffer, F., Weitkamp, T., Bunk, O., and David, C. (2006) Phase retrieval and differential phase-contrast imaging with low-brilliance X-ray sources. *Nat. Phys.*, **2**, 258–261.
- Pisano, E.D., Johnston, R.E., Chapman, D., Geradts, J., Iacocca, M.V., Livasy, C.A., Washburn, D.B., Sayers, D.E., Zhong, Z., Kiss, M.Z., and Thomlinson, W.C. (2000) Human breast cancer specimens: diffraction-enhanced imaging with histologic correlation—improved conspicuity of lesion detail compared with digital radiography. *Radiology*, **214** (3), 895–901.
- Plouraboué, F., Cloetens, P., Fonta, C., Steyer, A., Lauwers, F., and Marc-Vergnes, J.P. (2004) X-ray high resolution vascular network imaging. *J. Microsc.*, **215** (2), 139–148.
- Pohlmann, A., Möller, M., Decker, H., and Schreiber, W.G. (2007) MRI of tarantulas: morphological and perfusion imaging. *Magn. Reson. Imaging*, **25** (1), 129–135.
- Poirier-Quinot, M., Ginefri, J.C., Girard, O., Robert, P., and Darrasse, L. (2008) Performance of a miniature high-temperature superconducting (HTS) surface coil for in vivo microimaging of the mouse in a standard 1.5T clinical whole-body scanner. *Magn. Reson. Med.*, **60** (4), 917–927.
- Poldrack, R.A. (2008) The role of fMRI in cognitive neuroscience: where do we stand? *Curr. Opin. Neurobiol.*, **18** (2), 223–227.
- Porro, L.B., Holliday, C.M., Anapol, F., Ontiveros, L.C., Ontiveros, L.T., and Ross, C.F. (2011) Free body analysis, beam mechanics, and finite element modeling of the mandible of *Alligator mississippiensis*. *J. Morphol.*, **272** (8), 910–937.
- Prymak, O., Tiemann, H., Sötje, I., Marxen, J.C., Klocke, A., Kahl-Nieke, B., Beckmann, F., Donath, T., and Eppe, M. (2005) Application of synchrotron-radiation-based computer microtomography (SRIC-T) to selected biominerals: embryonic snails, statoliths of medusae, and human teeth. *J. Biol. Inorg. Chem.*, **10** (6), 688–695.
- Radon J. (1917). Über die Bestimmung von Funktionen durch ihre Integralwerte längs gewisser Mannigfaltigkeiten. *Ber. Verh. Sachs. Akad. Wiss.*, **69**, 262–277 (English translation: Radon, J. On the determination of functions from their integral values along certain manifolds, *IEEE Trans. Med. Imaging*, **MI**, 5(4): 170–176).
- Ramachandran, G.N. and Lakshminarayanan, A.V. (1971) Three-dimensional reconstruction from radiographs and electron micrographs: application of convolutions instead of Fourier transforms. *Proc. Natl. Acad. Sci. U.S.A.*, **68** (9), 2236–2240.
- Richter, C.P., Shintani-Smith, S., Fishman, A., David, C., Robinson, I., and Rau, C. (2009) Imaging of cochlear tissue with a grating interferometer and hard X-rays. *Microsc. Res. Tech.*, **72**, 902–907.
- Sarnelli, A., Nemoz, C., Elleaume, H., Estève, F., Bertrand, B., and Bravin, A. (2005) Quantitative analysis of synchrotron radiation intravenous angiographic images. *Phys. Med. Biol.*, **50**, 725–740.
- Schultke, E., Fiedler, S., Nemoz, C., Ogieglo, L., Kelly, M.E., Crawford, P., Esteve, F.,

- Brochard, T., Renier, M., Requardt, H., Le Duc, G., Juurlink, B., and Meguro, K. (2010) Synchrotron-based intra-venous K-edge digital subtraction angiography in a pig model: a feasibility study. *Eur. J. Radiol.*, **73** (3), 677–681.
- Schulz, G., Weitkamp, T., Zanette, I., Pfeiffer, F., Beckmann, F., David, C., Rutishauser, S., Reznikova, E., and Müller, B. (2010) High-resolution X-ray tomography of a human cerebellum: comparison of absorption and grating based phase contrast. *J. R. Soc. Interface*, **7** (53), 1665–1676.
- Shepp, L.A. and Logan, B.F. (1974) The Fourier reconstruction of a head section. *IEEE Trans. Nucl. Sci.*, **NS-21**, 21–34.
- Silva, A.C., Lee, J.H., Aoki, I., and Koresky, A.P. (2004) Manganese-enhanced magnetic resonance imaging (MEMRI): methodological and practical considerations. *NMR Biomed.*, **17**, 532–543.
- Silva, A.C., Liu, J.V., Hirano, Y., Leoni, R.F., Merkle, H., Mackel, J.B., Zhang, X.F., Nascimento, G.C., and Stefanovic, B. (2011) in *Magnetic Resonance Neuroimaging Methods and Protocols*, Methods in Molecular Biology, Vol. 711 (eds M. Modo and J.W.M. Bulte), Series ed. J.M. Walker, Humana Press Springer Science+Business Media, LLC, pp. 281–302.
- Simaan, N., Taylor, R., and Flint, P. (2004) in High dexterity snake-like robotic slaves for minimally invasive telesurgery of the upper airway, in *Medical Image Computing and Computer-Assisted Intervention – MICCAI 2004* (eds C. Barillot, D. R. Haynor and P. Hellier), Lecture Notes in Computer Science, vol. 3217, Springer-Verlag, Berlin, pp. 17–24.
- Snigirev, A., Snigireva, I., Kohn, V., Kuznetsov, S., and Schelokov, I. (1995) On the possibilities of X-ray phase contrast microimaging by coherent high-energy synchrotron radiation. *Rev. Sci. Instrum.*, **66** (12), 5486–5492.
- Šoltészová, V., Patel, D., Bruckner, S., and Viola, I. (2010) A multidirectional occlusion shading model for direct volume rendering. *Comput. Graphics Forum*, **29** (3), 883–891.
- Soons, J., Herrel, A., Genbrugge, A., Aerts, P., Podos, H., Adriaens, D., de Witte, Y., Jacobs, P., and Dirckx, J. (2010) Mechanical stress, fracture risk and beak evolution in Darwin's ground finches (*Geospiza*). *Philos. Trans. R. Soc. London, Ser. B*, **365** (1543), 1093–1098.
- Stampanoni, M., Wang, Z., Thüning, T., David, C., Roessl, E., Trippel, M., Kubik-Huch, R.A., Singer, G., Hohl, M.K., and Hauser, N. (2011) The first analysis and clinical evaluation of native breast tissue using differential phase-contrast mammography. *Invest. Radiol.*, **46** (12), 801–806.
- Stock, S.R., Ignatiev, K.I., Dahl, T., Veis, A., and De Carlo, F. (2003) Three-dimensional microarchitecture of the plates (primary, secondary, and carinar process) in the developing tooth of *Lytechinus variegatus* revealed by synchrotron X-ray absorption microtomography (microCT). *J. Struct. Biol.*, **144** (3), 282–300.
- Tapfer A., Bech M., Pauwels B., Liu X., Bruyndonckx P., Sasov A., Kennntner J., Mohr J., Walter Marco M., Schulz J. & Pfeiffer F. (2011). Development of a prototype gantry system for preclinical X-ray phase-contrast computed tomography. *Med. Phys.*, **38** (11): 5910–5915.
- Thomson, R.C. and Shaffer, H.B. (2010) Rapid progress on the vertebrate tree of life. *BMC Biol.*, **8**, 19.
- Tsai, W.L., Hsu, P.C., Hwu, Y., Chen, C.H., Chang, L.W., Je, J.H., Lin, H.M., Groso, A., and Margaritondo, G. (2002) Electrochemistry: building on bubbles in metal electrodeposition. *Nature*, **417** (6885), 139.
- Tucciarone, J., Chuang, K.H., Dodd, S.J., Silva, A., Pelled, G., and Koretsky, A.P. (2009) Layer specific tracing of corticocortical and thalamocortical connectivity in the rodent using manganese enhanced MRI. *Neuroimage*, **44**, 923–931.
- Tuy, H.K. (1983) An inversion formula for cone-beam reconstruction. *SIAM J. Appl. Math.*, **43**, 546–552.
- Tyska, J.M., Fraser, S.E., and Jacob, R.E. (2005) Magnetic resonance microscopy: recent advances and applications. *Curr. Opin. Biotechnol.*, **16** (1), 93–99.
- Valton, S., Peyrin, F., and Sappey-Marinié, D. (2006) Analysis of cone-beam artifacts in off-centered circular CT for four reconstruction methods. *Int. J. Biomed. Imaging*, **2006**, 1–8.



- Van Cauter, S., Adriaens, D., Kannan, S., Srigiriraju, S., Praet, T., Masschaele, B., De Beule, M., and Verheghe, B. (2010) Virtual design from nature: Kinematic modeling of the seahorse tail, *2010 SIMULIA Customers Conference, Providence Road Island*, 14 pp. Available at [http://www.simulia.com/forms/world/pdf2010/VanCauter\\_SCC2010.pdf](http://www.simulia.com/forms/world/pdf2010/VanCauter_SCC2010.pdf) (accessed 18 June 2013).
- Van der Linden, A., Verhoye, M., Pörtner, H., and Bock, C. (2004) The strengths of in-vivo Magnetic Resonance Imaging (MRI) to study environmental adaptational physiology in fish. *Magn. Reson. Mater. Phys., Biol. Med.*, **17**, 236–248.
- Van Wassenbergh, S., Aerts, P., Herrel, A., and Adriaens, D. (2003) A forward dynamic model of mouth closing movements in clariid catfishes. *Integr. Comp. Biol.*, **43** (6), 825.
- Wagner, A., Sachse, A., Keller, M., Wagner, O., Aurich, M., Wetzel, W.D., Venbrocks, R.A., Wiederanders, B., Hortschansky, P., Horn, J., Schmuck, K., Lohmann, M., Reime, B., Metge, J., Arfelli, F., Menk, R., Rigon, L., Muehleman, C., Bravin, A., Coan, P., and Mollenhauer, J. (2006) Evaluation of titanium implant ingrowth into bone by Diffraction Enhanced Imaging (DEI). *Phys. Med. Biol.*, **51**, 1313–1324.
- Wang Z.T., Kang K.J., Huang Z.F., Chen Z.Q. (2009). Quantitative grating-based x-ray dark-field computed tomography, *Appl. Phys. Lett.*, **95**, 094105.
- Wang, H., Sawhney, K., Berujon, S., Ziegler, E., Rutishauser, S., and David, C. (2011) X-ray wavefront characterization using a rotating shearing interferometer technique. *Opt. Express*, **19**, 16550–16559.
- Weitkamp, T., Diaz, A., David, C., Pfeiffer, F., Stampanoni, M., Cloetens, P., and Ziegler, E. (2005a) X-ray phase imaging with a grating interferometer. *Opt. Express*, **13** (16), 6296–6304.
- Weitkamp T., Nöhammer B., Diaz A., David C., and Ziegler E. (2005b), X-ray wavefront analysis and optics characterization with a grating interferometer, *Appl. Phys. Lett.*, **86**, 054101.
- Weitkamp, T., Haas, D., Wegrzynek, D., and Rack, A. (2011) ANKPhase: software for single-distance phase-retrieval from inline x-ray phase contrast radiographs. *J. Synchrotron Radiat.*, **18**, 617–629.
- Weitkamp T., Zanette I., David C., Baruchel J., Bernard P., Bech M., Deyhle H., Donath T., Kennntner J., Lang S., Mohr J., Müller B., Pfeiffer F., Reznikova E., Rutishauser S., Schulz G., Tapfer A., and Valade J.P. (2010). Recent developments in X-ray Talbot interferometry at ESRF-ID19. *Proc. SPIE*, **7804**, 780406.
- Wen, H., Bennett, E.E., Hegedus, M.M., and Rapacchi, S. (2009) Fourier X-ray scattering radiography yields bone structural information. *Radiology*, **251** (3), 910–918.
- Wilkins, S.W., Gureyev, T.E., Gao, D., Pogany, A., and Stevenson, A.W. (1996) Phase-contrast imaging using polychromatic hard X-rays. *Nature*, **384**, 335–338.
- Wirkner, C.S. and Prendini, L. (2007) Comparative morphology of the hemolymph vascular system in scorpions – a survey using corrosion casting, MicroCT and 3D-reconstruction. *J. Morphol.*, **268**, 401–413.
- Xu, F., Helfen, L., Moffat, A.J., Johnson, G., Sinclair, I., and Baumbach, T. (2010) Synchrotron radiation computed laminography for polymer composite failure. *J. Synchrotron Radiat.*, **17** (2), 222–226.
- Yashiro, W., Terui, Y., Kawabata, K., and Momose, A. (2010) On the origin of visibility contrast in x-ray Talbot interferometry. *Opt. Express*, **18**, 16890–16901.
- Zanette, I., Bech, M., Pfeiffer, F., and Weitkamp, T. (2011a) Interlaced phase stepping in phase contrast x-ray tomography. *Appl. Phys. Lett.*, **98**, 094101.
- Zanette, I., Weitkamp, T., Lang, S., Langer, M., Mohr, J., David, C., and Baruchel, J. (2011b) Quantitative phase and absorption tomography with an X-ray grating interferometer and synchrotron radiation. *Phys. Status Solidi A*, **208**, 2526–2532.
- Zanette, I., Bech, M., Rack, A., Le Duc, G., Tafforeau, P., David, C., Mohr, J., Pfeiffer, F., and Weitkamp, T. (2012) Trimodal low-dose X-ray tomography. *Proc. Natl. Acad. Sci. U.S.A.*, **109** (26), 10199–10204.
- Zanette, I., Weitkamp, T., Donath, T., Rutishauser, S., and David, C. (2010) Two-dimensional X-ray grating interferometer. *Phys. Rev. Lett.*, **105** (24), 248102.
- Zhang, D., Donovan, M., Fajardo, L.L., Archer, A., Wu, X., and Liu, H. (2008)

- Preliminary feasibility study of an in-line phase contrast X-ray imaging prototype. *IEEE Trans. Biomed. Eng.*, **55** (9), 2249–2257.
- Zhu, P., Zhang, K., Wang, Z., Liu, Y., Liu, X., Wu, Z., McDonald, S.A., Marone, F., and Stampanoni, M. (2010) Low-dose, simple, and fast grating-based X-ray phase-contrast imaging. *Proc. Natl. Acad. Sci. U.S.A.*, **107**, 13576–13581.
- Zhou, J., Maisl, M., Reiter, H., and Arnold, W. (1996) Computed laminography for materials testing. *Appl. Phys. Lett.*, **68** (24), 3.
- Ziedses des Plantes, B.G. (1932) Eine neue Methode zur Differenzierung in der Roentgenographie. *Acta Radiol.*, **13**, 182–192.
- Ziegler, A., Faber, C., Mueller, S., and Bartolomaeus, T. (2008) Systematic comparison and reconstruction of sea urchin (Echinoidea) internal anatomy: a novel approach using magnetic resonance imaging. *BMC Biol.*, **6**, 33.







## 8

## Imaging Marine Life with a Thin Light-Sheet

*Jérémie Capoulade, Emmanuel G. Reynaud, and Malte Wachsmuth*

### Abstract

Light-sheet fluorescence microscopy (LSFM) is a non-invasive optical method for the observation of living specimens. Although this concept was established a century ago it is only during the last decade that instruments suitable for biological applications have been developed, thereby circumventing some of the limitations of established fluorescence imaging techniques such as confocal laser scanning microscopy. LSFM utilizes a sheet of laser light to illuminate only a thin slice of a fluorescently labeled sample. A wide-field fluorescence microscope, placed perpendicular to the light-sheet, serves to collect the fluorescence signal and image the observed region by means of a camera. This side-on illumination configuration features several advantages, including intrinsic optical sectioning without the need of spatial filtering as employed in confocal microscopy, excellent signal-to-noise ratio, high temporal resolution, and drastically reduced overall photobleaching and phototoxicity inside living specimens. Moreover, the non-conventional geometry of LSFM opens up a completely new way of sample mounting, enabling convenient multi-view image acquisition for 3D imaging by simple rotation of the sample within the medium-filled chamber. Although LSFM was developed originally for the observation of large organisms such as zebrafish embryos, this method can be adapted to a large range of samples from macroscopic specimens like corals or copepods to microscopic organisms like tintinnids.

## 8.1

### Introduction

Modern light microscopy provides access to the structure, arrangement, and dynamic behavior of living specimens, covering a wide range of applications from imaging of single molecules through cells and tissues to 3D imaging of complete organisms. As a non-invasive technique, optical imaging enables the study of samples while they are maintained under conditions as close as possible to their normal physiological context or the natural habitat.

Optical imaging exploits contrast, i.e., the spatial variation of the specimen's optical properties such as absorption, reflection, scattering, fluorescence, and nonlinear effects. In particular the emergence of lasers and LEDs (light-emitting diodes) as intense, stable, and convenient light sources has considerably advanced the use of fluorescent light as microscopy contrast. Moreover, for living sample observations, light sources emitting in the visible and near-infrared spectral range are especially useful because these wavelengths are not harmful at the intensity levels commonly used for microscopy, even for long-term observation (Prasad, 2003). This chapter will focus on the use of fluorescence as a microscopy contrast.

In conventional fluorescence microscopes the sample is illuminated and observed through the same objective lens, that is, along the same optical axis, referred to as epi-fluorescence microscopy. It provides quite high lateral resolution but features limited axial resolution and considerable background signal that limits the image quality. Optical sectioning strategies like confocal microscopy address these issues by suppressing the detection of out-of-focus fluorescence. Nevertheless, the out-of-focus regions remain illuminated, leading to a loss of information during image acquisition.

Light-sheet fluorescence microscopy (LSFM) (Huisken *et al.*, 2004) has been established recently to overcome these limitations comprehensively by illuminating only a thin section of the specimen perpendicular to a wide-field microscope used for fluorescence detection. It improves significantly the signal-to-noise ratio by reducing the out-of-focus fluorescence excitation, while the phototoxicity and photobleaching are drastically reduced as less energy is deposited in the sample. Moreover, this method allows free rotation of the specimen within a medium-filled chamber for convenient multi-view 3D imaging. This is also closer to physiological conditions, especially when considering marine samples. Early observations of aquatic samples with a light-sheet microscope include marine bacteria (Fuchs *et al.*, 2002), zebrafish embryos (Huisken *et al.*, 2004), and more recently copepods (Boistel *et al.*, 2011) or even coral polyps, dinoflagellates, and tintinnids. As the sample can be held in an agarose rod or hooked, it can be maintained over days and allows long-term non-invasive studies such as copepod digestion (Karaköylü *et al.*, 2009).

In this chapter, we introduce LSFM in comparison to conventional optical sectioning and epi-fluorescence microscopy and propose it as a tool that is highly suited for the imaging of marine organisms.

## 8.2

### Fluorescence Microscopy Methods

#### 8.2.1

##### Fluorescence

In optical imaging, the spatial variation of the specimen's optical properties such as absorption, reflection, scattering, fluorescence, or nonlinear response is used to generate an image contrast. Transmission microscopy techniques based on phase,

dark-field, or differential interference contrast exploit the optical properties of the entire biological matter. Fluorescence contrast, however, relies on the capability of particular molecules, so-called fluorophores, to emit fluorescence photons in a certain wavelength range after the absorption of excitation light in a blue-shifted wavelength range (Lakowicz, 1999). By specifically attaching these fluorophores to molecules or structures of interest, their distribution, and dynamic behavior can be studied selectively with very high sensitivity. In addition, some intrinsic molecules of the specimen may also exhibit fluorescence, referred to as auto-fluorescence. Although this could interfere undesirably with specifically introduced fluorophores, it could also constitute a useful signal, overcoming in some cases the need to label living samples with specific fluorescent molecules.

The energy of a molecule in an excited state is not inevitably transformed into a fluorescence photon but can also transfer the fluorophore irreversibly into a non-fluorescent state, a process called photobleaching that often involves the generation of highly reactive and thus phototoxic free radicals. In addition to phototoxicity, photobleaching depletes the pool of fluorescent molecules, therefore reducing the signal that can be recorded from the sample.

The emergence of new probes, especially the genetically encoded fluorescent proteins (Miyawaki, 2011), and the high specificity of fluorescent tagging along with the dynamic technological development of lasers, optics, cameras, and computer power over the last 20 years has rendered fluorescence microscopy an essential and powerful tool in biology.

### 8.2.2

#### Epi-Fluorescence Wide-Field Microscopy

The most widely used application of fluorescence imaging is epi-fluorescence wide-field microscopy where the sample is illuminated and observed along the same optical axis and through the same objective lens (Figure 8.1). LEDs, lasers, or mercury lamps serve as light sources for illumination, from which the desired spectral ranges are selected using filters or monochromators. The collected fluorescence photons, separated from the illumination using dichroic mirrors, may be further distributed and selected spectrally using filters and dichroic mirrors as well, and are subsequently collected with an imaging device such as CCD (charge-coupled device), EM-CCD (electron-multiplying charge-coupled device), or sCMOS (scientific grade complementary metal oxide semiconductor) cameras.

Usually, the specimen is mounted in a medium-containing dish or chamber with appropriate optical properties and fixed on a horizontal stage that allows for its lateral translation in a manual or motorized way. The sample is observed either from the top or from the bottom using a conventional upright or inverted microscope stand, respectively. To acquire microscope images of a sample in 3D, spatial series of 2D sections at consecutive planes must be recorded by moving either the objective lens or the sample along the optical axis. Modern cameras allow up to 100 frames per second to be recorded so that even a time series of 3D image stacks in several channels can be acquired to study the temporal behavior of a 3D object.

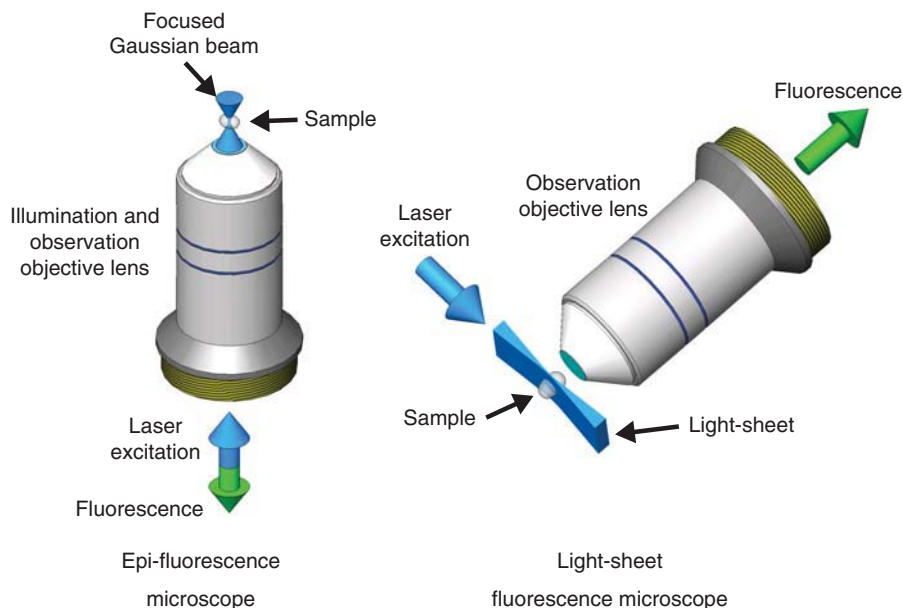


**Figure 8.1** Concepts of epi- and light-sheet fluorescence microscopy. In the epi-fluorescence configuration, the same objective lens is used for both the illumination of the sample and the detection of the fluorescence (left). In the light-sheet configuration,

a first objective (not shown here) is used to illuminate the sample from the side with a sheet of laser light, whereas the fluorescence is collected with a second objective lens placed perpendicularly to the light-sheet (right).

While providing such a good time resolution, a major drawback of epi-fluorescence wide-field microscopy is its non-isotropic spatial resolution: the lateral resolution is mostly limited by the diffraction of light whereas the resolution along the optical axis is substantially worse due to the corresponding axial symmetry of the optical path. Moreover, a significant and blurred contribution to the signal stems from sample areas outside of the focal plane and is referred to as out-of-focus fluorescence. This effect becomes even more prominent when moving the focal plane deeper into a thicker sample where both the illumination and the fluorescence light is increasingly scattered by cells, tissue, and other biological structures. Therefore, optical sectioning strategies have been developed to suppress the unwanted out-of-focus signal (Conchello and Lichtman, 2005; Fischer *et al.*, 2011; Haustein and Schwille, 2007; Stephens and Allan, 2003), as described briefly in the following paragraphs.

### 8.2.3

#### Confocal Laser Scanning Fluorescence Microscopy

To improve epi-fluorescence microscopy, the confocal laser scanning microscope (CLSM) has been devised (Pawley, 2006). Instead of illuminating and observing the complete 2D field of view at a time, the epi-fluorescence approach has been modified in such a way that only a single diffraction-limited region of the sample is illuminated with a focused laser beam. By scanning the beam in a raster-like fashion across the complete field of view, simultaneously collecting the fluorescence from the in-focus region and rejecting out-of-focus fluorescence light with a pinhole, excellent optical sectioning is achieved because, effectively, only fluorescence from a small focal volume confined in three dimensions reaches the detectors. However, the spatial resolution remains non-isotropic, although it is somewhat better than for epi-fluorescence wide-field microscopy. While the configuration of filters and dichroic mirrors is substantially the same as for epi-fluorescence wide-field microscopy, here point detectors like photomultiplier tubes, avalanche photodiodes, or hybrids of these technologies are used.

One recurrent limitation of the CLSM comes from the sequential recording scheme of single-point microscopy techniques that slows down the acquisition speed remarkably, and thus limits the time resolution for 2D or 3D imaging. In addition, out-of-focus fluorescence light continues to be excited and is only rejected when it reaches the pinhole. Therefore, photobleaching and resulting phototoxic effects may still occur in a large volume along the whole optical axis. The latter drawback can be partially overcome by using two-photon laser scanning microscopy where the excitation is confined in 3D to a diffraction-limited volume. However, two-photon excitation can be quite inefficient and may yield unexpected photo-chemical and -physical effects.

### 8.2.4

#### Other Approaches for Optical Sectioning

A solution to the speed limitation of point scanning microscopy is to parallelize the acquisition while maintaining the optical sectioning capability. The point scanner can be replaced by the typical core component of a spinning disk fluorescence microscope, a rotating disk carrying sufficiently spaced microlenses, which are illuminated with a laser beam and arranged in such a way that with one rotation of the disk the illuminated spots cover a 2D field of view exhaustively yet non-redundantly. Behind a second disk with confocally arranged pinholes, a camera catches the light during a full rotation, yielding a complete 2D image section of the sample. One of the main limitations of such a method is the light scattering that increases within increasing penetration into a thick sample, leading to spatial cross-talk between the numerous spots such that the optical sectioning and background suppression deteriorates substantially toward the quality of epi-fluorescence wide-field microscopy.

Structured illumination (and both CLSM and spinning disk fluorescence microscope can be considered as such) yet without structured detection allows to remove computationally the remaining out-of-focus and background signal post-acquisition by extracting the modulated contribution to the image and averaging over different complementary illumination patterns. Moreover, with appropriately selected pattern properties, the axial and the lateral resolution can be improved up to twofold. However, for every resulting 2D image, several acquisitions must be performed, which limits the time resolution and increases the deposited illumination energy and thus the probability of photobleaching. Being epi-illumination techniques, both spinning disk and structured illumination fluorescence microscopy are prone to out-of-focus illumination and photobleaching.

Total internal reflection fluorescence microscopy (TIRFM) is based on an epi-fluorescence wide-field microscope but provides optical sectioning and avoids out-of-focus fluorescence excitation through axially restricted illumination. This results from the remaining evanescent laser light at a cover-glass–water (or –medium) interface when it is illuminated above the critical angle for total internal reflection. Fluorescence is only excited in the vicinity of the cover-glass surface and detected in the same way as for epi-fluorescence wide-field microscopy. TIRFM, therefore, allows fast imaging and provides a high signal-to-noise ratio. However, it cannot be used for 3D imaging of large samples, as it is limited to the areas close enough to the cover-glass surface (typically cell membranes).

This list of optical sectioning techniques is far from complete and is covered more exhaustively elsewhere (Conchello and Lichtman, 2005; Mertz, 2011). Being mostly derived from epi-fluorescence wide-field microscopy, they all have their pros and cons, but are most notably either limited in spatial or temporal resolution. Light-sheet microscopy, conceived more than a century ago (Siedentopf and Zsigmondy, 1902), has only recently been identified as a very suitable approach to address the above-mentioned restrictions in fluorescence microscopy for optical sectioning, fluorescence background suppression, time resolution, and photobleaching in a very balanced way (Huisken and Stainier, 2009).

## 8.3

### Light-Sheet Fluorescence Microscopy

#### 8.3.1

##### Concept

The rationale of LSFM is to combine the advantage of optical sectioning and suppression of out-of-focus fluorescence excitation with the convenience, flexibility, and speed of wide-field fluorescence detection by uncoupling the optical paths for illumination and observation of the specimen.

Unlike most fluorescence microscopy techniques, which are based on epi-illumination and detection, an LSFM is composed of two independent optical units, the illumination unit and the detection unit, orthogonally arranged around



a medium-filled chamber containing the specimen (Figure 8.1). The illumination unit generates a light-sheet, which excites a thin section of a fluorescently tagged specimen and which coincides exactly with the focal plane of the detection unit. The fluorescence of the sample is thus only excited in and emitted from a thin slice sitting in the focus of the detection objective lens, providing the intrinsic optical sectioning capabilities of an LSM. Moreover, the illumination of the entire field of view of the detection unit at a time allows the acquisition of a 2D fluorescence image directly with a camera in a wide-field detection configuration without the need for scanning. Therefore, it speeds up substantially the acquisition of images. Of course, this also simplifies and accelerates the recording of 3D stacks of a specimen: only a single scan of the sample or the light-sheet along the optical detection axis is required.

### 8.3.2

#### Implementations and Instruments

So far, most LSM instruments used are custom-designed optical setups. The most basic configuration is the selective plane illumination microscope (SPIM) (Gieger, Swoger, and Stelzer, 2007). It is composed of the three main modules mounted horizontally on an optical table: the illumination unit, detection unit, and sample chamber (Figure 8.2).

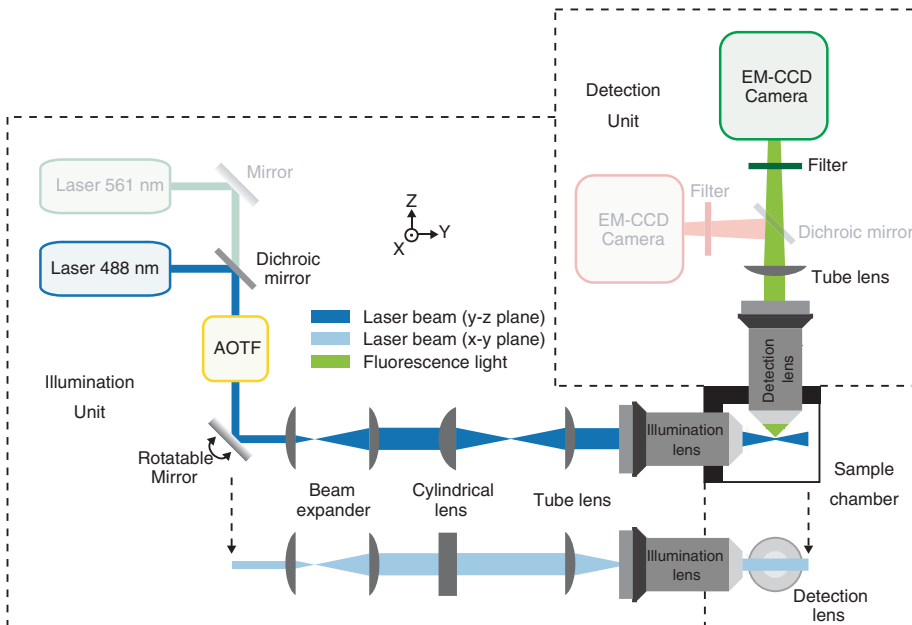


**Figure 8.2** Schematic drawing of a selective plane illumination microscope (SPIM). The main optical components required for the construction of this instrument are depicted. The optional optical paths for two-color imaging are drawn in lighter colors.

### 8.3.2.1 Illumination Unit

The wavelengths of the laser sources should be chosen to match the spectral properties of the fluorescent molecules used for labeling the sample. It is best practice to combine the beams from several laser sources into a single beam using dichroic beam splitters and mirrors in order to be as flexible as possible regarding the labeling of the sample. This is also a prerequisite for multicolor imaging. The most useful wavelengths are 488 nm (or 470, 491 nm) for the excitation of green fluorescent proteins like EGFP (enhanced green fluorescent protein) and 561 nm (or 568, 594 nm) for red fluorescent proteins like mCherry. An acousto-optical tunable filter (AOTF) placed in the optical path of the combined laser beam allows selection of the desired wavelengths, adjustment of their power, and switching of the excitation light on and off during image acquisition. The laser beam is then expanded with a telescope to fill completely the aperture of the successive optical elements.

A strikingly simple way to generate the light-sheet is to use a cylindrical lens. It focuses the beam anamorphically in the direction collinear to the optical detection axis and leaves it unaffected in the other direction. The major drawbacks of such simple optical components are firstly optical aberrations that spoil the quality of the light-sheet, and thus the optical sectioning and background suppression; in addition, their numerical aperture (NA) is rather limited, leading to relatively thick light-sheets and limiting the resulting spatial resolution along the detection axis. It is therefore advisable to couple the cylindrical lens with an objective lens. Because of mechanical fitting issues between the illumination and the detection objective, the use of a long-working distance water-dipping objective lenses that can be inserted directly into the medium is important. This will also make sample handling easier.

The focus of the light-sheet is placed in the area of interest within the sample, which lies at the same time in the focal plane of the detection objective lens.

### 8.3.2.2 Detection Unit

The detection unit, arranged at 90° with respect to the light-sheet plane, is a simple wide-field fluorescence microscope. A high NA water-dipping objective lens is used to collect the fluorescence light that stems from the illuminated plane. An emission filter rejects the remaining laser light that may be scattered or refracted by the sample, and lets only the fluorescence photons pass to the camera. The image is focused onto the camera by means of the tube lens. Different camera technologies can be used. Because of their very high quantum efficiency of more than 90%, back-thinned/back-illuminated EM-CCD cameras are a good choice for most LSFM applications. The more recent sCMOS technology is a promising alternative when the acquisition speed is an important factor. Indeed, sCMOS cameras allow to obtain 100 frames of 4 million pixels per second at a quantum efficiency of up to 70%.

The detection unit can be easily extended to two-color imaging by spectrally separating two fluorescent species with a dichroic mirror placed behind the

detection objective lens, and by focusing the two signals either onto two different parts of the same camera chip or onto two different cameras.

### 8.3.2.3 Sample Chamber and Movement Unit

The horizontal configuration of the SPIM setup requires the use of a sample chamber containing medium to keep the specimen healthy during the experiments (Figure 8.3). Holes are designed on two sides of the chamber to insert the water-dipping objective lenses into the medium, and glass windows can be placed on the two other vertical sides for convenient visualization of the sample in the chamber. Perfusion pumps allow the medium to be replaced (or replenished) and to administer media of different compositions or drugs. Heating and cooling of chamber and medium can also be easily arranged. Before the observation, the sample is embedded in a small agarose droplet or rod that permits it to be positioned in front of the objective lens (for the mounting techniques see below). The agarose droplet or rod is fixed on a motorized rotation stage, which itself is mounted on a 3D-motorized stage, the first one enabling rotation of the sample perpendicular to the optical axis of detection for multi-view imaging and the second one enabling the observer to precisely position and scan the sample across the light-sheet.

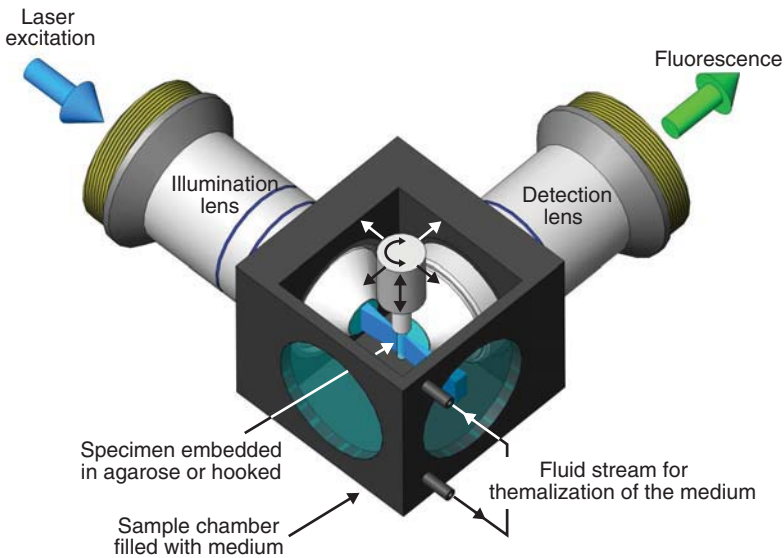


**Figure 8.3** The sample chamber: The specimen is embedded in an agarose cylinder in order to hold it in the focal plane of the detection objective lens. A rotatable motor mounted on a 3D-motorized stage allows precise placing and scanning of the sample

across the light-sheet for image stack acquisition. Tubes allow the chamber to be connected to a perfusion pump so as to control the composition and temperature of the sample medium.

### 8.3.3

#### Spatial Resolution

The spatial resolution of the LSFM depends on the optical specifications of both the illumination and the detection unit (Engelbrecht and Stelzer, 2006). The axial resolution of the LSFM is driven by the light-sheet thickness, which itself is determined by the NA of the illumination objective lens. The smaller the NA, the thicker the light-sheet is. For instance, an NA of 0.8 would result in a thin light-sheet and an axial resolution well below a micrometer, whereas an NA of 0.3 would lead to a light-sheet  $\sim 2\text{ }\mu\text{m}$  thick. The lateral resolution is determined by the NA of the detection objective lens. As in conventional microscopy, the higher the NA, the better the lateral resolution is. Here, a resolution well below a micrometer is generally achieved, since in most of the cases the detection NA is higher than 0.8.

### 8.3.4

#### Sample Mounting

As mentioned above, for typical LSFM configurations, the sample is mounted on a platform that provides a large free moving space without using any primary support such as a slide commonly used in conventional microscopy. While for many decades sample support has been mostly based on the flat and horizontal surface of slides and coverslips, such new ways of sample mounting expand our view by allowing at the same time precise translation and full rotation of the specimen as well as flexible control of the medium (temperature, gas, ions, water, chemicals) while following its temporal evolution (such as growth in embryonic development). Nevertheless, several recent LSFM implementations employed more conventional flat support (Capoulade *et al.*, 2011; Dunsby, 2008; Holekamp, Turaga, and Holy, 2008; Wu *et al.*, 2011). As a common rule for all sample mounting strategies used for fluorescence imaging, it is crucial to minimize the impact on the optical properties of the microscope.

The most obvious option to maintain the sample in the desired position is to use hooks, tweezers, or clips made of metal or plastic (Figure 8.4). This simple method features a high stability while moving the sample during image stack acquisition. However, only a few users have applied this technique for the observation of large samples such as brains (Klohs *et al.*, 2008) or fish tails (Engelbrecht *et al.*, 2007).

The second and most common mounting technique to hold the sample is to embed it in a transparent hydrogel, for example, consisting of agarose. This is facilitated by the use of a syringe or capillary to create a rod-shaped hydrogel block that can be easily adapted on a rotating platform. The hydrogel block can be tailored to the size of the sample, molded as a cup or chamber to accommodate sensitive samples such as plants or moving embryos that don't grow when spatially confined, or adapted for mounting several samples at once. However, one must be careful with the choice of the hydrogel regarding melting temperature, stiffness, optical properties, or contaminants as most of the products available on the market have not been designed for microscopy but rather for electrophoresis, spectroscopy, or

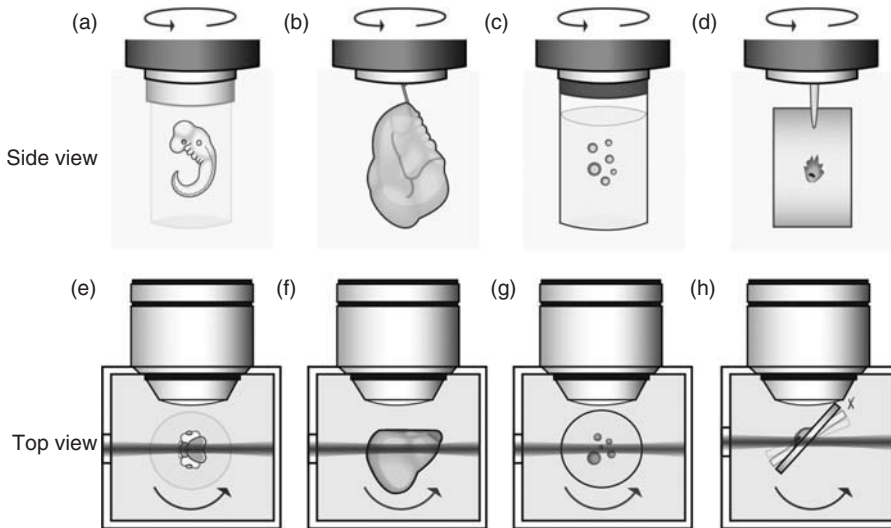


**Figure 8.4** Light-sheet fluorescence microscopy (LSFM) sample mounting: In most cases, the sample is embedded in an agarose rod suspended from above, (a) and (e). Additional mounting strategies include “hooking,” (b) and (f), mounting in containers or chambers (agarose, FEP...), (c) and (g), or flat mounting, (d) and (h).

growth support. This mounting method can be applied to hold samples ranging from entire adult organisms like mosquitoes (few millimeters) to single yeast cells (few micrometers) (Taxis *et al.*, 2006).

Small transparent containers can also be used for mounting samples. They are generally made of specific plastic Teflon foils featuring appropriate optical properties for microscopy, such as polytetrafluoroethylene (PTFE) (Keller *et al.*, 2008a) or fluorinated ethylene propylene (FEP), and can be filled with low concentrations of agarose or methylcellulose (Kaufmann *et al.*, 2012). This type of container is very useful for sensitive samples such as growing cysts and tissues, *in vitro* microtubules growth assays (Keller *et al.*, 2008a), and long-term time-lapse 3D imaging of embryonic development (Kaufmann *et al.*, 2012).

Nevertheless, more conventional mounting based on Petri dishes and other flat supports can be used for LSFM as well, especially for samples that do not require multi-view imaging like monolayer culture cells. This approach is mostly used with upright configurations and is discussed in more detail in the following subsection.

### 8.3.5

#### Upright LSFM: an Alternative Configuration with Simplified Sample Mounting

The idea of putting the light-sheet microscope into an upright position was already used in the first instrument (Siedentopf and Zsigmondy, 1902) and implemented for fluorescence imaging a few years ago (Holekamp, Turaga, and Holy, 2008). In this setup, referred to as a objective-coupled planar illumination (OCPI) microscope,

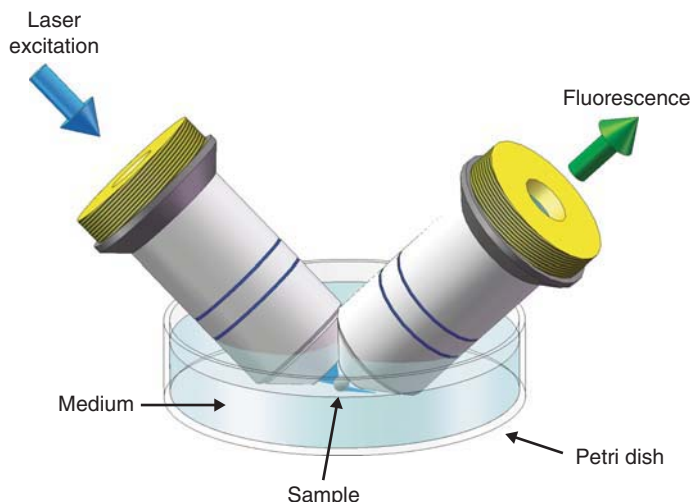


**Figure 8.5** Upright configuration of an LSFM. The illumination and detection objective lenses are directly dipped from the top into a medium-filled Petri dish containing the sample. This enables the use of conventional sample mounting protocols developed for conventional fluorescence imaging.

the optical fiber that delivers the light-sheet and the observation objective lens are dipped into the sample chamber from the top. As a major advantage, this configuration renders possible the use of classical Petri dishes as a sample chamber (Figure 8.5) (Capoulade *et al.*, 2011; Wu *et al.*, 2011). This avoids the need for more complicated sample mounting methods such as those described above. Most conventional mounting and manipulation protocols developed for imaging living specimens in Petri dishes are applicable; the Petri dish must be filled with medium, and the objective lenses are directly dipped into the medium from the top. In addition, this configuration does not suffer from optical aberrations induced, for example, by embedding the sample in agarose, especially when using a tightly focused and thin light-sheet. Although this configuration allows precise positioning of the specimen, the observation of its expansion or growth, the control of the medium regarding chemical composition and temperature, or the rotation of the sample are no longer possible or at least difficult to implement.

#### 8.4

##### Advantages of LSFM

As mentioned above, uncoupling the illumination unit from the detection unit allows to illuminate the specimen only in the relevant plane, which is the focal plane of the detection objective lens, thereby conferring LSFM with inherent optical sectioning capabilities. Therefore, since no out-of-focus fluorescence is generated, the LSFM provides high contrast images, even deep inside large objects.

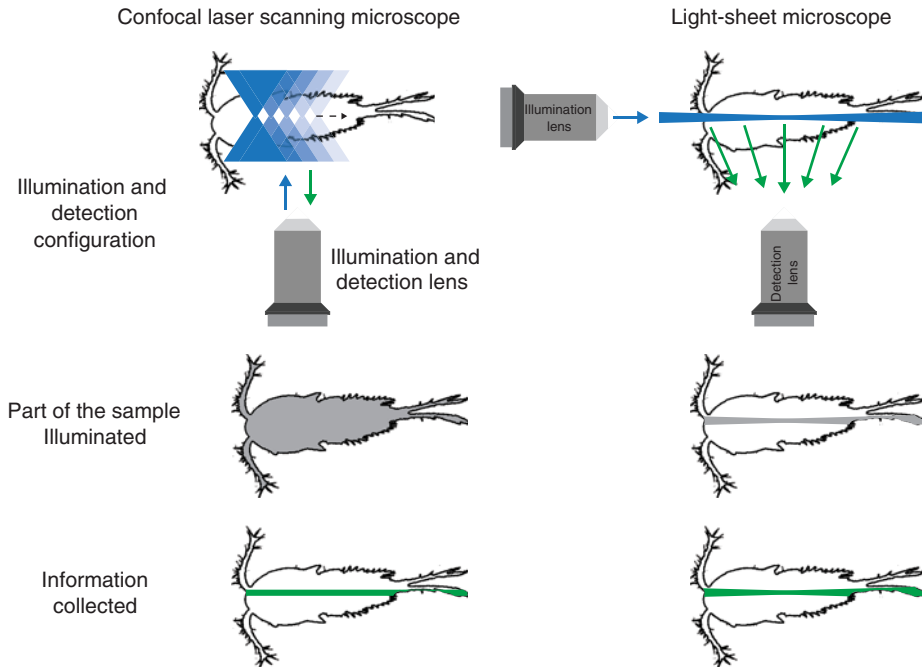


**Figure 8.6** Comparison between CLSM and LSFM: sequential versus simultaneous acquisition, and out-of-focus versus no out-of-focus illumination. In the LSFM, the overall photobleaching is lower whereas the efficiency of information collection is higher.

One important and recurrent problem in fluorescence microscopy is photobleaching of fluorescent molecules. LSFM addresses this issue in a very efficient way (Figure 8.6): since only the focal plane of the detection objective lens is illuminated, photobleaching of fluorophores outside of this plane is avoided. Thus, the overall photobleaching and the resulting phototoxicity are greatly reduced. This is a clear advantage compared to CLSM where, due to its epi-fluorescence configuration, the optical sectioning is obtained by illuminating a large volume of the specimen and by rejecting with a pinhole a large portion of the fluorescence collected, to observe just a small region in focus of the objective lens.

For the same reasons, the information collection is much more efficient with an LSFM than with a confocal microscope: a larger part of the fluorescent photons generated are collected and used efficiently for imaging, and not wasted by spatial filtering.

As another major advantage of LSFM, the wide-field configuration of the detection unit allows high-speed imaging. No scanning is required to acquire a 2D fluorescence image while optical sectioning is maintained. The speed of image acquisition is only limited by the capabilities of the camera used and by the brightness of the sample. Owing to recent advancements in camera technology, a rate of 100 frames of 4 million pixels per second can be achieved.

When mounting the sample vertically it is straightforward to perform multi-view imaging by simply rotating the hook, the agarose rod, or the plastic chamber.

LSFM is applicable to a large range of living samples, from single cells (a few micrometers) to entire adult organisms (few millimeters), by adapting the light-sheet thickness and length to the size of the specimen of interest and the spatial resolution desired. For single cells, a light-sheet thickness below a micrometer is recommended to achieve sub-cellular resolution, while a thickness of a few microns is often sufficient for 3D imaging of large specimens.

Taken together, these features make the LSFM image acquisition system very fast, enable high-resolution imaging with high contrast deep inside large biological samples, and minimize photoinduced damage of living specimen.

## 8.5

### How to Improve LSFM Imaging

Despite its advantages, especially for 3D fluorescence microscopy of large specimens, LSFM does have certain conceptual drawbacks. Long optical paths both for illumination and detection inside heterogeneously refracting, scattering, and absorbing biological samples might lead to shadowing effects and loss of intensity with increasing penetration depth. Not least due to the perpendicular illumination–observation geometry, these effects are clearly visible as stripes as well as loss of contrast, intensity, and resolution along the illumination direction. To address these two issues, the multidirectional selective plane illumination microscope (mSPIM) (Huisken and Stainier, 2007) has been devised. The mSPIM features an even light-sheet in the entire field-of-view by pivoting the light-sheet at an angle of  $\pm 10^\circ$  around the optical axis of detection. This allows to illuminate the sample from different directions and to remove the stripes in the resulting image. To overcome the loss of image intensity and contrast due to the single-side illumination configuration of the basic LSFM, the mSPIM has two facing illumination objective lenses that render it possible to illuminate the sample sequentially from two opposing directions. The two images are merged to a final image exhibiting a substantially more homogeneous contrast, intensity, and resolution.

As another drawback, a typical LSFM provides anisotropic spatial resolution: usually, the axial resolution is lower than the lateral resolution, which poses an issue for 3D image reconstruction. A solution can be found in two steps. First, one has to acquire a multi-view image stack of the sample by rotating the agarose rod embedding the specimen. Second, the multi-view image stack is transformed post-acquisition into a 3D image data set with isotropic resolution (Swoger *et al.*, 2007; Verveer *et al.*, 2007). For this purpose, it is important to rotate the sample properly to enable a correct fusion of the multi-view image stack. To account correctly for inherent deviations from an ideal rotation, the sample can be embedded in agarose together with sparsely distributed fluorescent beads as fiducial markers (Preibisch *et al.*, 2010). As part of the post-acquisition image processing, the positions of the



beads are tracked throughout the whole multi-view image series as an intrinsic coordinate system such that the multiple views can be aligned correctly. Of course, multi-view imaging limits substantially the temporal resolution when imaging larger specimens in 3D over time. As a partial remedy, multiple views can be acquired simultaneously not only by illuminating but also by observing the sample using two opposing light paths, or even by multiplexing illumination and detection light paths (Krzic *et al.*, 2012; Tomer *et al.*, 2012).

Isotropic resolution can also be obtained by using two identical objective lenses or at least the same NA both for illumination and detection (Capoulade *et al.*, 2011; Planchon *et al.*, 2011). In this configuration, no computational processing as described above is required, because the isotropic resolution is provided by the microscope hardware.

## 8.6

### Different Ways to Generate a Light-Sheet

The illumination path of an LSM is flexible, so that different ways to generate a light-sheet have been developed to further improve its imaging capabilities.

#### 8.6.1

##### Digital Scanned Light-Sheet Microscope

In a SPIM, a static light-sheet is generated using a cylindrical lens either directly or through an objective lens. While this is simple and robust, it is often difficult to maintain constant illumination intensity throughout the desired field of view. In a digital scanned light-sheet microscope (DSLM) (Keller *et al.*, 2008b), only a single line of the sample is illuminated at a time with a focused Gaussian beam (Figure 8.7). The light-sheet is generated dynamically by vertically scanning this line across the field of view during the exposure time of the camera. This confers to the DSLM several advantages over the SPIM, especially while observing larger samples. First of all, the intensity of the line remains constant while it is scanned to form the light-sheet, resulting in a more homogeneous illumination of the sample as compared to SPIM. Second, since the laser light is focused into a single line rather than spread out over an entire light-sheet, a DSLM can provide a higher illumination intensity for a given laser power. Third, instead of a cylindrical lens, only corrected optical elements (achromatic doublet, aspherical, or scan lenses) are used to create the light-sheet, which usually feature smaller optical aberrations in the illumination optical path, thus increasing the image quality.

#### 8.6.2

##### Incoherent Structured Illumination

The image quality can be further improved by combining the DSLM with incoherent structured illumination (Keller *et al.*, 2010) that has previously been developed

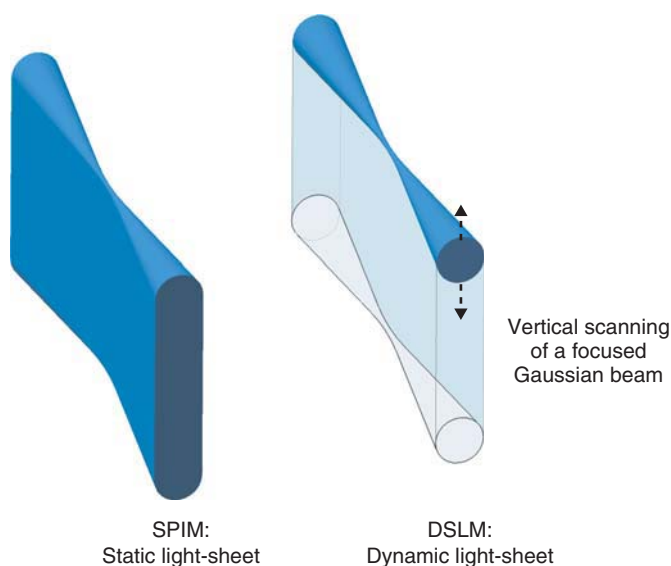


**Figure 8.7** The different ways of generating a light-sheet: in the SPIM (selective plane illumination microscope) configuration a static light-sheet is generated by a cylindrical lens, whereas in the DSLM (digital

scanned light-sheet microscope) configuration the light-sheet is dynamically generated by quickly scanning a focused Gaussian beam along the focal plane of the detection objective lens.

for epi-fluorescence wide-field microscopy to improve the optical sectioning capabilities and the image contrast (Neil, Juskaitis, and Wilson, 1997). While the sample is scanned in the DSLM fashion, the laser intensity is modulated at different frequencies and different phases. Here, for a given spatial frequency, each section of the sample is imaged at three different phases ( $0^\circ$ ,  $120^\circ$ , and  $240^\circ$ ). The computational combination of the images obtained leads to the removal of background due to scattering and out-of-focus fluorescence from the in-focus signal, therefore increasing the image contrast. This method has also been applied on a static LSFM setup using a movable grid placed before the cylindrical lens to structure the static light-sheet (Breuninger, Greger, and Stelzer, 2007).

### 8.6.3

#### Two-Photon Excitation

Two-photon excitation exploits the fact that fluorophores can be excited by the simultaneous absorption of two photons of approximately half the energy (or twice the wavelength) needed for its single-photon excitation. Because of the very low probability that a molecule absorbs two photons at a time, two-photon excitation depends on the square of the incident laser intensity. It occurs therefore just at the focus of the objective lens where the intensity is high enough, yielding intrinsic optical sectioning capabilities. Moreover, to match the absorption spectra of typical

fluorophores, near-infrared light is required, which shows significantly reduced light scattering in biological tissues and thus increased penetration depth of the incident laser light into thick heterogeneous specimens.

Recently, two-photon excitation has been implemented in LSFM both for statically (Palero *et al.*, 2010) and dynamically generated light-sheets (Truong *et al.*, 2011). Both studies show that two-photon excitation gives a slightly better axial resolution and that it allows much deeper penetration into large samples as compared to single-photon excitation LSFM.

#### 8.6.4

##### Bessel Beams

The penetration depth into the sample can also be increased by using Bessel beams instead of conventional Gaussian beams to generate the scanned light-sheet. While Bessel beams are focused, they possess two beneficial properties: they do not diffract over a certain distance and they are self-reconstructing when encountering small obstacles, thus minimizing the deformation of the illumination beam in an optically heterogeneous environment. Bessel beams were first implemented on a DSLM using one-photon excitation (Fahrback and Rohrbach, 2010). Despite their advantages mentioned above, one-photon Bessel beams thwart the conceptual advantage of LSFM because they feature pronounced side lobes and generate undesired out-of-focus illumination. To resolve this issue on the detection side, incoherent structured illumination together with image processing post-acquisition as described above (Planchon *et al.*, 2011) or a spatial filter such as a slit in an intermediate image plane of the detection unit for side lobe suppression have been used (Fahrback and Rohrbach, 2012). Alternatively, excitation side lobes can be suppressed on the illumination side by using two-photon excitation. Here as well, only the main lobe will contribute efficiently to fluorophore excitation since the illumination intensity in the side lobes remains below the threshold for two-photon excitation (Planchon *et al.*, 2011).

## 8.7

### Application Examples

LSFM applications in marine biology are discussed in more detail below. Here we give the reader an impression of some rather remarkable results obtained previously with LSFM microscopes.

One of the major goals of LSFM development was the fast and efficient 3D imaging of large fluorescently tagged specimens like embryos that could be followed over time during their development with high temporal resolution. Using SPIM, Huisken *et al.* were able to study *Drosophila melanogaster* embryogenesis for more than 15 h at two different planes inside the specimen, demonstrating that

even in relatively opaque samples, high-resolution imaging is possible (Huisken *et al.*, 2004).

The development of DSLM enabled time-lapse 3D imaging of a zebrafish embryo over the first 24 h of development (Keller *et al.*, 2008b). The DSLM-specific improvements made it possible to observe cell division processes and to track the movement (position, speed, and direction) of each single nucleus in the embryo and allowed the authors to propose a model for mesoderm formation in zebrafish embryos.

Extending the mSPIM concept to dual-color imaging, Huisken *et al.* were able to perform high-speed imaging of the beating heart in zebrafish embryos at a frame rate of up to 69 frames per second. By combining this technique with optogenetic experiments, where the heart beat rate was optically controlled, the emergence of heart function during zebrafish embryonic development could be observed and analyzed (Arrenberg *et al.*, 2010; Huisken and Stainier, 2009).

The imaging not only of larger specimens but also of subcellular structures and processes with high spatial and temporal resolution has been a goal of LSFM developments. Using high NA objective lenses for both illumination and detection allowed the creation of a thinner light-sheet as compared to previous LSFM implementations and the achievement of an isotropic resolution of only 300 nm. The use of a static light-sheet permitted quantitative study of the diffusion and binding of nuclear proteins with sub-millisecond time resolution (Capoulade *et al.*, 2011). The combination of a light-sheet generated by a scanned Bessel beam with two-photon excitation enabled 3D time-lapse imaging of chromosome dynamics during mitosis (Planchon *et al.*, 2011).

## 8.8

### LSFM Combined with Other Fluorescence Techniques

LSFM has also been used as a basis for other established fluorescence microscopy techniques, normally based on epi-fluorescence wide-field imaging or CLSM, like super-resolution microscopy (Cella Zanacchi *et al.*, 2011), fluorescence correlation spectroscopy (FCS) (Capoulade *et al.*, 2011; Wohland *et al.*, 2010), fluorescence life-time imaging microscopy (FLIM) (Greger *et al.*, 2011), and single-molecule tracking (Ritter *et al.*, 2010). All these techniques benefit from intrinsic optical sectioning deep inside the specimen and from wide-field detection using a camera to either fully parallelize the data acquisition over the entire field-of-view or to speed up the image acquisition in 3D.

## 8.9

### Light-Sheet Fluorescence Microscopy for Marine Biology

To fully benefit from the advantages of LSFM, the sample, the fluorescent labeling approach, and the mounting method must be carefully considered. The optical

properties of the sample determine both the penetration depth of the light-sheet and the transmission of the fluorescence toward the detection camera: the more transparent the specimen is the deeper the light-sheet can penetrate, and the higher is the fluorescence yield. However, if the sample is slightly opaque and diffracts or scatters the light-sheet, for example, due to lipid vesicles or dense collagen fiber arrays, the optical sectioning and the imaging quality will decrease along the illumination axis, whereas a poorly transparent sample will also affect detection of the fluorescence signal. Moreover, a fully opaque sample that blocks completely the penetration of the light-sheet, for example, due to insect cuticular structures or bone, will limit imaging to the sample surface.

The optical properties and thus the imaging quality of the sample can be optimized by choosing a suitable model organism, for example, transparent fish like medaka, particular growth conditions, for example, no phenol red in the growth medium to avoid autofluorescence, or a clearing treatment for non-transparent specimens, for example, with BABB.<sup>1)</sup> Moreover, it is important to aim for homogeneous labeling of the sample: many large molecules such as dyes and antibodies do not penetrate deeper than 100  $\mu\text{m}$  into a tissue slice or embryo so that the staining will not be evenly distributed throughout the specimen. This could result in misleading observations because central areas of the sample may look dark and “empty.”

As in any other microscopy technique, specimen preparation is crucial, as badly labeled and deformed specimens will not take full advantage of the microscope. This is especially important for LSFM, where the specimen handling is often performed in a very different way because of the need to hold the sample vertically in front of the detection objective within a medium-filled chamber. Because illumination and detection occur along different directions, LSFM provides the opportunity to revisit established sample preparation methods and to conceive completely new approaches. Ideally, they enable us to maintain the specimen much closer to its actual physiological appearance and under conditions much closer to its natural habitat.

In summary, specimen preparation for LSFM experiments must be mechanically stable, the specimen must be well supported to avoid distortion due to movement during imaging, and it must support the physiological aspects of the specimen.

The mounting system should be flexible enough to allow the specimen to develop and grow and should not change its mechanical properties during observation or dissolve in the buffer. It should feature minimal impact on the optical quality of the microscope. For example, the refractive index of the mounting medium should be as close as possible to the refractive index of the buffer filling the imaging chamber to avoid light refraction that may increase the light-sheet thickness and impair the detection resolution. Both optical and physiological aspects have to be brought together, especially in live imaging where biocompatibility has to be taken

1) BABB (also known as Murray's clear) is a 1:2 or 1:1 mixture of benzyl alcohol and benzyl benzoate.

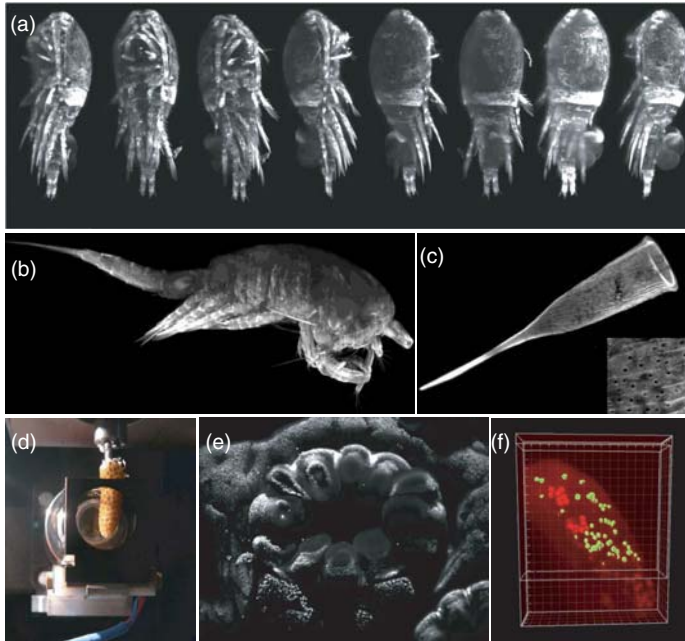


**Figure 8.8** Marine samples observed with a light-sheet fluorescence microscope. (a) A copepod (150  $\mu\text{m}$ ) observed from eight different angles that can be combined to provide a full 3D view of the animal (autofluorescence). (b) A single angular view of a *Thermocyclops consimilis* after  $\text{DiOC}_6$  staining, showing a more evenly distributed fluorescence signal and a detailed view of every appendage (250  $\mu\text{m}$ ); intensity projection of a complete stack acquired along one angle (Boistel *et al.*, 2011). (c) *Rhabdella spiralis*,

a tintinnid (120  $\mu\text{m}$ ); an enlarged view of the theca shows details of the pore distribution and size, which is below 1  $\mu\text{m}$  for each pore stained with  $\text{DiOC}_6$ . (d) A whole mount of a fixed coral stem inside the LSFM sample chamber. (e) A complete retracted polyp imaged from (d). Single zooxhantella can be counted. (f) Zooxhantella distribution (green and red dots) in the tip of a single tentacle from (e) processed using Imaris: red: low autofluorescence; green: high autofluorescence.

into consideration. Generally, the samples are maintained in their integrity in a liquid-filled chamber.

Figure 8.8 displays some images of marine samples observed with an LSFM, showing that light-sheet microscopy method is indeed well adapted to marine biology.

## 8.10

### Summary and Outlook

Fluorescence microscopy is an essential tool for biology. By labeling proteins or structures of interest with fluorescent marker molecules, it is possible to assess quantitatively biological processes *in vivo* with sub-cellular resolution. During recent decades, the ever increasing demand of biologists for higher sensitivity,

higher spatial resolution, longer as well as finer temporal sampling, and multicolor imaging has challenged the most widely used and established fluorescence imaging techniques such as confocal microscopy. This has triggered and accelerated the development of new fluorescence microscopes. In particular, developmental biologists need quantitative data acquired *in vivo* with high resolution deep inside large specimens such as embryos. Another typical application is to perform time-lapse 3D imaging over long periods (e.g., for the observation of embryogenesis).

LSFM has been devised to overcome some of the limitations of epi-fluorescence microscopy. First, by illuminating from the side only a thin section of the sample, LSFM yields high-resolution images with high contrast even deep inside large specimens. Second, the LSFM concept generically reduces photobleaching and phototoxicity. Therefore, as a non-invasive optical imaging method, LSFM is ideally suited for living specimens and allows 3D high-resolution and high-speed acquisition. LSFM can be adapted to various samples ranging from adult mosquitoes (few millimeters) to yeast cells (few micrometers).

So far, LSFM has been mostly used for cell and developmental biology applications. However, the first observations on tintinnids, copepods, zebrafishes, and even entire coral stems have demonstrated the capabilities and also the convenience of LSFM to image marine life in 3D with high resolution and in an environment that is as similar as possible to the physiological conditions and natural habitat. We believe that with an increasing number of both custom-designed and commercial instruments becoming available, LSFM bears great potential as an important imaging tool for marine biology.

## References

- Arrenberg, A.B., Stainier, D.Y.R., Baier, H., and Huisken, J. (2010) Optogenetic control of cardiac function. *Science*, **330**, 971–974.
- Boistel, R., Swoger, J., Kržić, U., Fernandez, V., Gillet, B., and Reynaud, E.G. (2011) The future of three-dimensional microscopic imaging in marine biology. *Mar. Ecol.*, **32**, 438–452.
- Breuninger, T., Greger, K., and Stelzer, E.H.K. (2007) Lateral modulation boosts image quality in single plane illumination fluorescence microscopy. *Opt. Lett.*, **32**, 1938–1940.
- Capoulade, J., Wachsmuth, M., Hufnagel, L., and Knop, M. (2011) Quantitative fluorescence imaging of protein diffusion and interaction in living cells. *Nat. Biotechnol.*, **29**, 835–839.
- Cella Zanacchi, F., Lavagnino, Z., Perrone Donnorso, M., Del Bue, A., Furia, L., Faretta, M., and Diaspro, A. (2011) Live-cell 3D super-resolution imaging in thick biological samples. *Nat. Methods*, **8**, 1047–1049.
- Conchello, J.A. and Lichtman, J.W. (2005) Optical sectioning microscopy. *Nat. Methods*, **2**, 920–931.
- Dunsby, C. (2008) Optically sectioned imaging by oblique plane microscopy. *Opt. Express*, **16**, 20306–20316.
- Engelbrecht, C.J., Greger, K., Reynaud, E.G., Krzic, U., Colombelli, J., and Stelzer, E.H.K. (2007) Three-dimensional laser microsurgery in light-sheet based microscopy (SPIM). *Opt. Express*, **24**, 6420–6430.
- Engelbrecht, C.J. and Stelzer, E.H. (2006) Resolution enhancement in a light-sheet-based microscope (SPIM). *Opt. Lett.*, **31**, 1477–1479.
- Fahrbach, F.O. and Rohrbach, A. (2010) A line scanned light-sheet microscope with phase shaped self-reconstructing beams. *Opt. Express*, **18**, 24229–24244.

- Fahrbach, F.O. and Rohrbach, A. (2012) Propagation stability of self-reconstructing Bessel beams enables contrast-enhanced imaging in thick media. *Nat. Commun.*, **3**, 632.
- Fischer, R.S., Wu, Y., Kanchanawong, P., Shroff, H., and Waterman, C.M. (2011) Microscopy in 3D: a biologist's toolbox. *Trends Cell Biol.*, **21**, 682–691.
- Fuchs, E., Jaffe, J., Long, R., and Azam, F. (2002) Thin laser light sheet microscope for microbial oceanography. *Opt. Express*, **10**, 145–154.
- Greger, K., Neetz, M.J., Reynaud, E.G., and Stelzer, E.H.K. (2011) Three-dimensional fluorescence lifetime imaging with a single plane illumination microscope provides an improved signal to noise ratio. *Opt. Express*, **19**, 20743–20750.
- Greger, K., Swoger, J., and Stelzer, E.H.K. (2007) Basic building units and properties of a fluorescence single plane illumination microscope. *Rev. Sci. Instrum.*, **78**, 023705.
- Haustein, E. and Schwille, P. (2007) Trends in fluorescence imaging and related techniques to unravel biological information. *HFSP J.*, **1**, 169–180.
- Holekamp, T.F., Turaga, D., and Holy, T.E. (2008) Fast three-dimensional fluorescence imaging of activity in neural populations by objective-coupled planar illumination microscopy. *Neuron*, **57**, 661–672.
- Huisken, J. and Stainier, D.Y.R. (2007) Even fluorescence excitation by multidirectional selective plane illumination microscopy (mSPIM). *Opt. Lett.*, **32**, 2608–2610.
- Huisken, J. and Stainier, D.Y.R. (2009) Selective plane illumination microscopy techniques in developmental biology. *Development*, **136**, 1963–1975.
- Huisken, J., Swoger, J., Del Bene, F., Wittbrodt, J., and Stelzer, E.H. (2004) Optical sectioning deep inside live embryos by selective plane illumination microscopy. *Science*, **305**, 1007–1009.
- Karaköylü, E.M., Franks, P.J.S., Tanaka, Y., Roberts, P.L.D., and Jaffe, J.S. (2009) Copepod feeding quantified by planar laser imaging of gut fluorescence. *Limnol. Oceanogr. Methods*, **7**, 33–41.
- Kaufmann, A., Mickoleit, M., Weber, M., and Huisken, J. (2012) Multilayer mounting enables long-term imaging of zebrafish development in a light sheet microscope. *Development*, **139**, 3242–3247.
- Keller, P.J., Pampaloni, F., Lattanzi, G., and Stelzer, E.H.K. (2008a) Three-dimensional microtubule behavior in *Xenopus* egg extracts reveals four dynamic states and state-dependent elastic properties. *Biophys. J.*, **95**, 1474–1486.
- Keller, P.J., Schmidt, A.D., Wittbrodt, J., and Stelzer, E.H.K. (2008b) Reconstruction of zebrafish early embryonic development by scanned light sheet microscopy. *Science*, **322**, 1065–1069.
- Keller, P.J., Schmidt, A.D., Santella, A., Khairy, K., Bao, Z., Wittbrodt, J., and Stelzer, E.H.K. (2010) Fast, high-contrast imaging of animal development with scanned light sheet-based structured-illumination microscopy. *Nat. Methods*, **7**, 637–642.
- Klohs, J., Gräfe, M., Graf, K., Steinbrink, J., Dietrich, T., Stibenz, D., Bahmani, P., Kronenberg, G., Harms, C., Endres, M. *et al.* (2008) In vivo imaging of the inflammatory receptor CD40 after cerebral ischemia using a fluorescent antibody. *Stroke*, **39**, 2845–2852.
- Krzic, U., Gunther, S., Saunders, T.E., Streichan, S.J., and Hufnagel, L. (2012) Multiview light-sheet microscope for rapid in to imaging. *Nat. Methods*, **9**, 730–733.
- Lakowicz, J.R. (1999) *Principles of Fluorescence Spectroscopy*, 2nd edn, Kluwer Academic/Plenum Publishers, New York.
- Mertz, J. (2011) Optical sectioning microscopy with planar or structured illumination. *Nat. Methods*, **8**, 811–819.
- Miyawaki, A. (2011) Proteins on the move: insights gained from fluorescent protein technologies. *Nat. Rev. Mol. Cell Biol.*, **12**, 656–668.
- Neil, M.A.A., Juskaitis, R., and Wilson, T. (1997) Method of obtaining optical sectioning by using structured light in a conventional microscope. *Opt. Lett.*, **22**, 1905–1907.
- Palero, J., Santos, S.I.C.O., Artigas, D., and Loza-Alvarez, P. (2010) A simple scanless two-photon fluorescence microscope using selective plane illumination. *Opt. Express*, **18**, 8491–8498.
- Pawley, J. (2006) *Handbook of Biological Confocal Microscopy*, 2nd edn, Springer, Berlin.



- Planchon, T.A., Gao, L., Milkie, D.E., Davidson, M.W., Galbraith, J.A., Galbraith, C.G., and Betzig, E. (2011) Rapid three-dimensional isotropic imaging of living cells using Bessel beam plane illumination. *Nat. Methods*, **8**, 417–423.
- Prasad, P.N. (2003) *Introduction to Biophotonics*, Wiley-Interscience, Hoboken, NJ.
- Preibisch, S., Saalfeld, S., Schindelin, J., and Tomancak, P. (2010) Software for bead-based registration of selective plane illumination microscopy data. *Nat. Methods*, **7**, 418–419.
- Ritter, J.G., Veith, R., Veenendaal, A., Siebrasse, J.P., and Kubitschek, U. (2010) Light sheet microscopy for single molecule tracking in living tissue. *PLoS ONE*, **5**, e11639.
- Siedentopf, H. and Zsigmondy, R. (1902) Über sichtbarmachung und größenbestimmung ultramikroskopischer teilchen, mit besonderer anwendung auf goldrubingläser. *Ann. Phys.*, **315**, 1–39.
- Stephens, D.J. and Allan, V.J. (2003) Light microscopy techniques for live cell imaging. *Science*, **300**, 82–86.
- Swoger, J., Verveer, P., Greger, K., Huiskens, J., and Stelzer, E.H.K. (2007) Multi-view image fusion improves resolution in three-dimensional microscopy. *Opt. Express*, **15**, 8029–8042.
- Taxis, C., Maeder, C., Reber, S., Rathfelder, N., Miura, K., Greger, K., Stelzer, E.H.K., and Knop, M. (2006) Dynamic organization of the actin cytoskeleton during meiosis and spore formation in budding yeast. *Traffic*, **7**, 1628–1642.
- Tomer, R., Khairy, K., Amat, F., and Keller, P.J. (2012) Quantitative high-speed imaging of entire developing embryos with simultaneous multiview light-sheet microscopy. *Nat. Methods*, **9**, 755–763.
- Truong, T.V., Supatto, W., Koos, D.S., Choi, J.M., and Fraser, S.E. (2011) Deep and fast live imaging with two-photon scanned light-sheet microscopy. *Nat. Methods*, **8**, 757–760.
- Verveer, P.J., Swoger, J., Pampaloni, F., Greger, K., Marcello, M., and Stelzer, E.H.K. (2007) High-resolution three-dimensional imaging of large specimens with light sheet-based microscopy. *Nat. Methods*, **4**, 311–313.
- Wohland, T., Shi, X., Sankaran, J., and Stelzer, E.H.K. (2010) Single plane illumination fluorescence correlation spectroscopy (SPIM-FCS) probes inhomogeneous three-dimensional environments. *Opt. Express*, **18**, 10627–10641.
- Wu, Y., Ghitani, A., Christensen, R., Santella, A., Du, Z., Rondeau, G., Bao, Z., Colón-Ramos, D., and Shroff, H. (2011) Inverted selective plane illumination microscopy (iSPIM) enables coupled cell identity lineaging and neurodevelopmental imaging in *Caenorhabditis elegans*. *Proc. Natl. Acad. Sci. U.S.A.*, **108**, 17708–17713.



## 9

### *Ex-situ* Macro Photography of Marine Life

*Mattias Ormestad, Aldine Amiel, and Eric Röttinger*

#### 9.1

##### Introduction

One of the biggest challenges facing the new generation of scientists is making an increasingly complex and technical field more accessible and understandable to the general public in order to increase scientific literacy. Being scientifically literate helps in acknowledging science as a pool of information about the world around us, and helps making appropriate decisions for both our community and ourselves. While the scientific literature is largely reserved for those active in the scientific community, beautiful images and illustrations appeal to all and are a very powerful media through which to share scientific observations with the public, and to educate future generations. In these days of web communication and fast-food information where we are overwhelmed by images on a daily basis, quality scientific images representing animals, cells, or organelles rarely seen by laymen can grab one's attention, raise questions, open eyes, and highlight important scientific issues.

Historically, scientific illustration, a time-consuming and technically challenging technique, was used to create extraordinarily detailed drawings serving as a visual record to document and describe scientific observations of not only the specimen under study but also of various biological phenomena such as biodiversity, embryonic development, and animal behavior (Dionysius Ehret, 1736; Haeckel, 1868, 1904). Today, digital photography provides a modern and widely accessible alternative to illustration that allows a greater proportion of the scientific community to quickly and accurately document natural life science. These days, the presence of photographs in all branches of science is taken for granted. However, it was not until the end of the 1890s that scientific photographs first began to be included in scientific journals, increasing progressively in numbers and significance, until they finally reached the front covers of journals only as recently as the 1970s (Wilder, 2009). These days, the presence of photographs in all branches of science is taken for granted.

All types of photography, from infrared, throughout the visual spectrum, and even into the ultraviolet and X-ray wavelengths, as well as derived digital techniques such as confocal imaging and tomographic techniques [e.g., magnetic resonance

imaging (MRI), optical projection tomography (OPT), selective plane illumination microscopy (SPIM), etc.], are currently extensively used to share complex scientific observations among the research community. These images also play an increasingly important role in reaching out to the general public and educating future generations. A good example are recent publications from the Census of Marine Life project ([www.coml.org](http://www.coml.org)) in specialized scientific journals (McIntyre, 2010; Webb, Vanden-Berghe, and O'Dor, 2010). Images taken during scientific expeditions are also often used with great success by various general public media as a way of communicating the scientific message to a broad audience.

Although sampling for immediate or subsequent detailed analysis (ecology, physiology, morphology, molecular analysis, etc.) is the main and most important aspect during scientific expeditions, it should not be forgotten that there are several other very important advantages of scientific photographic imaging:

- High-quality images can store additional important information that can be retrieved even after the samples have been processed.
- These images can be added and annotated in scientific image databases and therefore provide useful information to an even larger scientific community, for outreach and, importantly, for educational purposes.
- Imaging projects on scientific vessels may be the only commonality that connects the various scientific studies carried out onboard (from oceanographic and chemical studies to plankton and benthic sea creatures) and they also create a simple and understandable platform between scientists and the wider public.
- Images taken during scientific expeditions constitute a legacy for future generations, similar to the old scientific drawings that still amaze us today.

Technical improvements in diving techniques (e.g., SCUBA dives up to 700 ft) and underwater imaging equipment [e.g., remotely operated vehicles (ROVs) that can go even deeper (up to 15 000 ft) have opened new frontiers in marine science such that previously undescribed species can now be observed and recorded in their natural environment (Webb, Vanden-Berghe, and O'Dor, 2010; Haddock *et al.*, 2005). Nevertheless, underwater marine photography imposes constraints that may impair image quality or altogether prohibit shooting (e.g., organism size, behavior, dive time, weather, and water conditions). Technological improvements and miniaturization of imaging equipment, however, have also made it easier than ever to bring advanced imaging techniques, such as portable photographic studios and microscopes, into the field for *in vitro* imaging under a controlled environment.

In this chapter, we describe how to construct an optimized and portable photographic studio for photographing marine organisms in the laboratory, in the field, or even onboard a research vessel where space can be very limited. We focus on the photographic theory as well as photographic equipment, including the choice of lenses, lighting system, and aquaria required to capture high-quality images and video of a diversity of interstitial, free-living, sessile, benthic, or pelagic marine organisms.

## 9.2 The Exposure

First, we will introduce some basic photography terms that will be used in the following sections. Although all exposure settings in the camera are interconnected – for any given exposure the shutter speed, aperture size, and light sensitivity (ISO) of the film or sensor are all dependent on each other – we will present these terms individually and later suggest workflows that fit the needs for *ex-situ* macro photography of marine biodiversity.

The exposure, or the total amount of light that reaches the image sensor (or the film), is determined by the shutter speed in combination with the aperture of the lens. Conventionally, the exposure is measured in units of exposure value (*EV*, also called *stops*), representing a halving or doubling of the exposure. Multiple combinations of shutter speed and aperture can give the same exposure – however, shutter speed and aperture size also affects other characteristics such as movement and depth of field (*DoF*), so even if the exposure is the same with different settings the resulting images can be very different! Thus, at any given exposure, doubling the time and halving the aperture size, or vice versa, will result in the same amount of light entering the camera. For example, a shutter speed of 1/125 s and f/11 is the same as with 1/250 s and f/8, or 1/500 s and f/5.6. In the following sections we describe how changing these values affects the exposure and the image.

### 9.2.1 Shutter Speed

The shutter speed, or exposure time, is the length of time that the camera's shutter is open to allow light to reach the film or digital image sensor. In addition to its effect on exposure, the shutter speed influences the way movement is captured in the picture. Short exposure times (i.e., faster shutter speeds) can be used to “freeze” fast moving objects (Figure 9.1d) and long exposure times (i.e., slower shutter speeds) can create blurry images if the camera or the subject is moving (Figure 9.1h).

A rough estimate of the slowest shutter speed that can be used without creating blurry images due to camera movement is 1/focal length of the lens being used. For example, to handhold a camera mounted with a 100 mm lens you use a shutter speed slower than 1/100 s, and even this requires you to have a very steady hand. However, this rule usually does not apply for macro shots close to the minimum focus distance (the minimum focusing distance of a lens is the closest the lens can get to a subject while maintaining sharp focus), which often requires a much faster shutter speed than the 1/focal length ratio. Image stabilization (or vibration reduction) mechanisms integrated into either lens (e.g., Canon IS, Nikon VR) or camera (e.g., Sony) can often allow the use of shutter speeds two to four stops slower than the exposure requires. If a shutter speed is too slow for handholding, a tripod should be used to eliminate loss of focus because of camera movement. If you need to freeze movement in poor light conditions the only options are opening

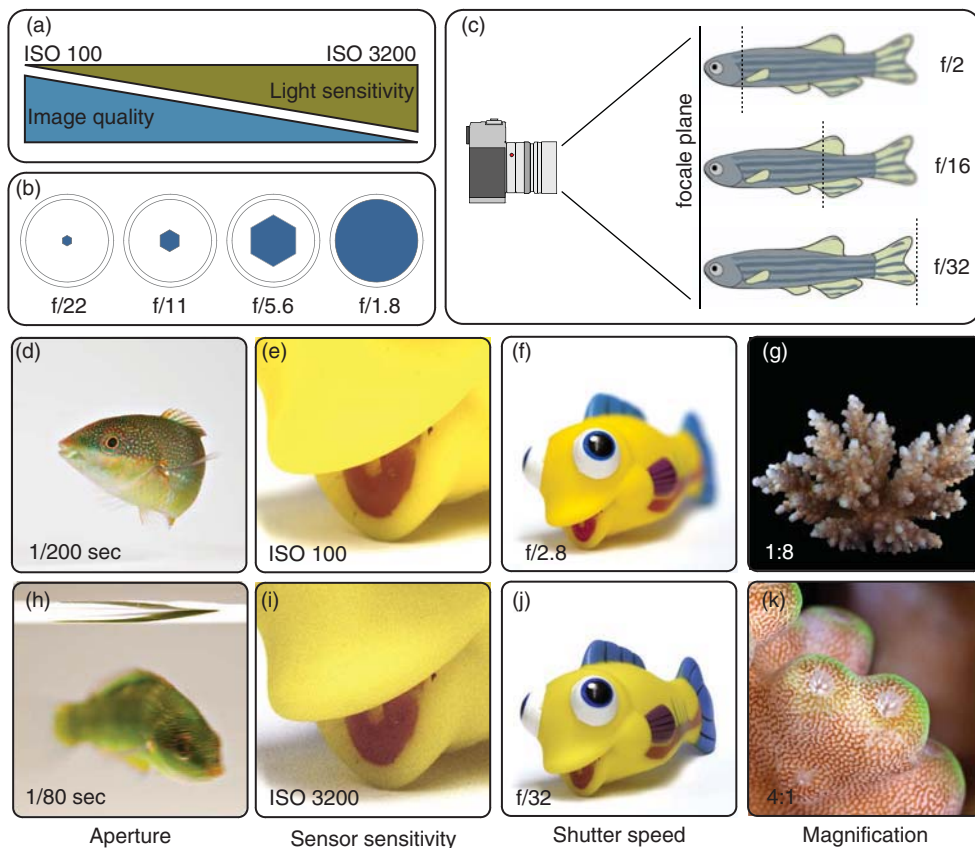


**Figure 9.1** Basics in photography: (a) Relation between light sensitivity and image quality. A low ISO value corresponds to a lower light sensitivity, which means less noise (or smaller grain size on film) and higher resolution and image quality. (b) Aperture or *f-stop*. A high *f-stop* value correlates with a small aperture size. (c) Schematic representation of the depth of field (DoF). The line in front of the fish indicates the beginning, and the dashed line the end, of the DoF in relation to the aperture value. A low value gives a narrow DoF, while a high number offers a DoF that spans the entire fish size. (d, h) Real images illustrating the DoF described in (c). At *f*/2.8 (d) the dorsal fin is already out

of the DoF, while at *f*/32 (h) the caudal fin is perfectly sharp and included in the DoF. (e, i) Sensor sensitivity: a low ISO value causes nearly no noise (e), while a high ISO value causes high noise (i). (f, j) Shutter speed: A high shutter speed (f) “freezes” the object, while a low shutter speed (j) causes a blurry image. To maintain a similar background color, the image in (f) was taken at *f*/22, ISO 200 with flashes, while (j) was taken at *f*/5.6, ISO 800 and without flash. (g, k) Magnification: 1:8 means that the object in the picture is eight times smaller than the real object while 4:1 means that the object in the picture is four times magnified compared to the real object.

up the aperture (see next section), adjusting the light sensitivity of the sensor (see later section), and/or adding flashes or fixed light sources that will provide the extra light needed for a good exposure.

### 9.2.2

#### Aperture

An aperture is a hole or an opening in the lens through which light travels before reaching the film or the image sensor. Higher aperture numbers (i.e., f-stop or f-number) correspond to smaller openings, lower aperture numbers to larger openings (Figure 9.1b). Each sequentially higher f-stop (or f-number) allows half the light to travel through its opening than the previous one. Therefore, the aperture determines how much light reaches the image sensor. For a given exposure time, the narrower the aperture (higher f-number), the darker the final image will be. Note that all lenses lose sharpness when either “closed down” or “opened up” too much—each lens always has an optimal aperture range where the image has the best sharpness from the center all the way out to the periphery. Adjusting the aperture size also affects the DoF, which corresponds to the distance range over which objects are acceptably sharp (Figure 9.1c). The DoF is explained in more detail in Section 9.2.4.

### 9.2.3

#### ISO Value

In traditional film photography, ISO (or ASA) is the indication of how sensitive a film is to light. ISO values are indicated in numbers (100, 200, 400, 800, etc.). The higher the value the greater is the sensitivity of the film, and the bigger the grain in the final image. In contrast, the lower the number is the less sensitive the film is to light and the finer the grain (Figure 9.1a). In digital photography, the term *ISO* has been conserved and indicates in a similar manner the sensitivity of the image sensor. Therefore, the same “sensitivity” principles apply as in traditional film photography but the “digital grain,” more properly called *noise*, has a completely different character than the grain on film. The noise on a digital camera is caused by random electrical charges in the sensor, and by amplifying the signal (i.e., increasing the ISO) you also amplify these random fluctuations. The appearance of this *noise* not only depends on the ISO value but also on other factors such as exposure time, sensor type, pixel density, and even the ambient temperature. The digital noise consists of both variations in pixel brightness and color. Most cameras have noise reduction built in and can for long exposures also make a dark frame exposure, which is automatically subtracted from the final image to remove sensor noise.

Low ISO settings are usually used in good light conditions and will give highly detailed images with clear colors (Figure 9.1e) while higher ISO settings are generally chosen in darker situations, but at the cost of increased image noise resulting in the loss of fine details (Figure 9.1i). The ISO setting can be used to

compensate for lack of aperture size when keeping the exposure time down in low light conditions. For example, if you are using a 200 mm lens and at ISO 100 you obtain a shutter speed of 1/100 s at  $f/2.8$  (let us say this is the largest aperture size for this lens), you will probably have a bit of camera-shake blur unless you have a tripod or a really steady hand. Turn up the ISO to 200 and you have the equivalent exposure at 1/200 s, or 1/400 s at ISO400.

Changing shutter speed, aperture, and ISO is performed in EV steps or parts thereof (usually  $\frac{1}{3}$  steps), and by understanding these basic principles you can vary and balance these three factors to create an unlimited variety of images.

#### 9.2.4

##### Depth of Field (DoF)

A given lens can precisely focus at only one distance (focal plane) and the decrease in sharpness is gradual on each side of the focused distance. Nevertheless, within the DoF, the unfocused regions are imperceptible under normal viewing conditions. In normal photography the DoF is not evenly distributed around the focal plane, rather  $\frac{1}{3}$  of the field is located in front and  $\frac{2}{3}$  behind the focal plane. In macro photography, however, the DoF is equally distributed, with  $\frac{1}{2}$  of it extending both in front of and behind the focal plane. This might be good to keep in mind when obtaining macro photographs, since focusing on the eyes might not always be the best option if you want the whole animal within the DoF.

A more scientific explanation of DoF is that the aperture size determines the cone angle of a bundle of rays that come to a focus in the image plane (e.g., image sensor), basically determining how gradual the transition to unsharpness is from the focal plane. The camera aperture (Figure 9.1b), which is adjustable in increments or f-stops (e.g.,  $f/2$ ,  $f/11$ ,  $f/22$ , etc.), determines how co-linear the admitted rays are and therefore plays an important role in the appearance of the final image. If an aperture is narrow (high value, big DoF), then only highly co-linear rays are admitted, resulting in a sharp focus at the image plane (Figure 9.1j). If an aperture is wide (low value, narrow DoF), then un-collimated rays are admitted as well, resulting in an image that is sharp at the focal plane but unsharp in all other parts of the photograph (Figure 9.1f).

An important fact to bear in mind is that the perceived DoF is not only determined by the aperture value but also by the focal length of the lens and in the case of macro photography also by the subject magnification. For a given f-number, increasing the magnification by moving closer to the subject results in a decrease in DoF and vice versa.

The progress of digital technology and image editing tools has provided additional means of controlling the extent of image sharpness. For example, Helicon Software (Helicon Soft Ltd.) allows the DoF to be extended (by merging images taken at several focal planes). Tools like this can be very useful when the imaging setup has limited control of the DoF, such as a digital camera mounted on a microscope with a fixed numerical aperture of the lens.



For most scientific images it may be desirable to adjust the setting for a large DoF in order to have the entire object sharp and to capture most of the information.

### 9.2.5

#### Camera Settings

Most current semi- or professional digital cameras offer various exposure modes, namely, P, Av, Tv, and M (or P, S, A, and M respectively for Nikon cameras):

- P** (Program) corresponds to an automatic mode. The camera selects aperture and shutter speed while trying to keep a reasonable DoF and exposure time.
- Av** (Aperture value) is the aperture (or f-stop) priority mode. The user selects the aperture and the camera adjusts the shutter speed accordingly.
- Tv** (Time value) is the shutter speed priority mode. The user selects the shutter speed and the camera will select the aperture value to obtain a correct exposure.
- M** (Manual) is a pure manual mode. The user has to set the desired aperture value and the shutter speed. This mode provides the most flexibility and full control over the shot.

Modern cameras have several ways of measuring the light falling onto the sensor, and depending on how the light is measured you will obtain different exposure settings. For our purposes, however, light metering is seldom used since we actually do not want to make the exposure based on the natural light of the scene. We are making the exposure based on the light from our flashes. Since this is a situation where the flashes usually are at a fixed position, the background does not change unless we want to, and as there is no ambient light affecting the exposure, the best way is to use the camera in manual mode making sure we get the same exposure every time. The aperture or flash intensity is only adjusted when the magnification is changed, that is, according to the distance to the subject.

### 9.2.6

#### What Is a Good Exposure?

This is of course a very difficult question and will have many different answers depending on what the photographer wants to visualize. In the context of scientifically documenting the anatomy of an animal, we could say that a good exposure would be focused on technical details such as a DoF that covers the entire animal and at the same time getting the maximum amount of color information possible with the image sensor. A good exposure in other contexts can, of course, be very different.

A good way to get an overview of the color information in an image is by looking at the histogram (either directly in the camera or in an image editing application on your computer). A histogram (Figure 9.2) is a graphical representation of the tonal distribution of an image, plotting the tonal variations on the horizontal axis

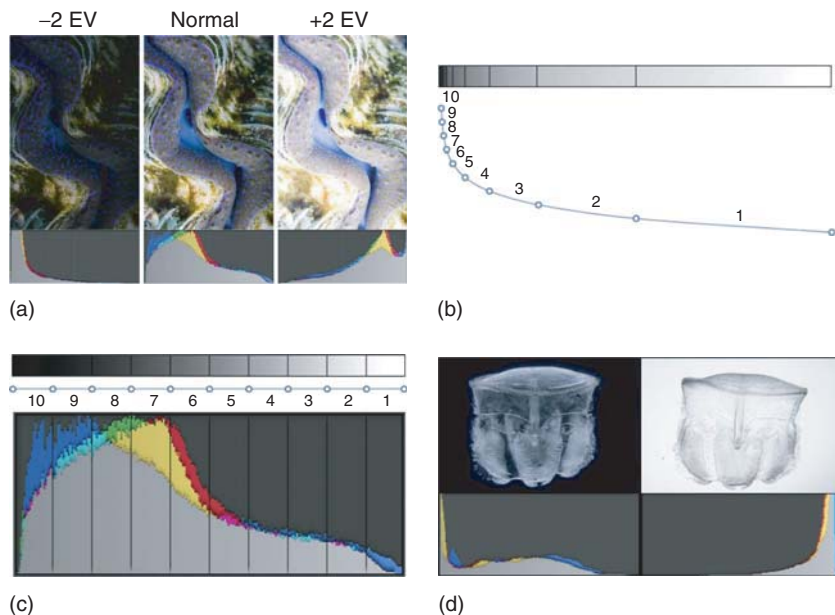


**Figure 9.2** The histogram. (a) This panel shows the sharp cutoff in the histograms when under- or over-exposing an exposure. In the middle is the original exposure, showing a nice tonal distribution over the whole histogram and to the left is an exposure underexposed by two stops, showing a cutoff in the shadow tones. To the right is an overexposed image (also by two stops), showing a sharp cutoff of the highlights in the histogram, and also areas of clipped highlights where detail is irreversibly lost. (b) A hypothetical exponential curve showing ten

stops of dynamic range of a camera sensor. Half of the total bit-depth of the sensor is used by the first f-stop, on a 12-bit sensor there are 4096 levels of each color, meaning the first f-stop is 2048 levels, the second 1024 levels, the third 512 levels, and so on. (c) After gamma correction of the raw data, the tonal range is transformed to obtain an equal distribution of levels from dark to bright. (d) Examples of images of a tonaria larva on a black and a white background.

and the number of pixels for each tone on the vertical axis. The horizontal scale ranges from dark tones on the left to light tones on the right.

Learning to interpret the histogram can be very useful when determining whether an exposure is good. Again, “good” can mean very different things, but in this case we will consider “good” to be equal to capturing the maximum amount of color information possible. For a better understanding of the histogram and how to use it we will give an example and introduce a few new terms.

First we need to have a basic understanding of how the image sensor works. A digital sensor has a completely linear relationship between the number of photons and sensor output, which is totally different to how an image is exposed on traditional film where the highlights are gradually compressed until the film saturates. Imagine each pixel as a bucket that fills up with an electrical charge as light falls on it, and when a bucket becomes full it just flows over. When a bucket

flows over – or rather when a pixel is *saturated*, all data that “flows over” is lost, resulting in loss of detail since differences in luminance between the different pixels disappears. This shows up in the image as “clipped highlights,” pure white areas where detail is abruptly and irreversibly lost. In the histogram, this looks like the pixel count for the brightest values never hits zero and there is a sharp cutoff at the right end of the histogram (Figure 9.2a). On the other extreme are regions in the image with very low light that fails to excite the pixels – or fill the buckets – above the background noise level. Similarly to the highlights, this will show up in the histogram as a cutoff in the left part (Figure 9.2a).

Dynamic range is the luminance range over which the sensor can register light and is determined by, for example, the pixel size. Think of this as the surface area of the buckets; wider buckets have a greater chance of collecting enough charges to get over the background noise in low light regions of the sensor *before* the buckets in the high light regions overflow – effectively leading to an extension of the range where variations in luminance can be detected. Dynamic range is measured as a logarithmic scale and the unit is f-stops; as we described earlier, each f-stop has half the light of the previous one. When considering the linearity of the sensor output, this has some interesting implications for signal-to-noise ratios, as discussed by Michael Reichmann on his website “The Luminous Landscape” (<http://www.luminous-landscape.com/tutorials/expose-right.shtml>). Modern digital SLR cameras usually have a dynamic range of at least 10 f-stops, which is comparable to that of black and white film. If we combine this with the color depth, or bit depth (see Section 9.6.1 for further explanation of bit-depth), of the sensor we can obtain a numerical representation of how the image data is distributed across the dynamic range of the sensor. This shows that *half* of the image bit-depth is contained within the first stop (Figure 9.2b), and about 97% of the available raw levels are contained within the five brightest stops!

Since the human eye, similar to photographic film, does not have this linear response to light – twice the amount of photons are not perceived as twice as bright – this data needs to be transformed using nonlinear encoding called *gamma compression* or *gamma correction*. This is done by the RAW converter and essentially expands the darker tones and compresses the brighter tones, resulting in an equal distribution of levels from dark to bright (Figure 9.2c). If you underexpose a photograph and afterwards want to recover detail in the shadows you will have very little data to work with, resulting in increased noise and the risk of posterization of gradients within the shadow tones (remember that 97% of the bit-depth of the sensor is in the five brightest stops). To maximize the usage of bit depth you should therefore “expose right,” meaning that you balance the histogram to the right, but very carefully so as to avoid saturation of pixels. If you get more of the available stops to describe the shadows, you obtain a better signal-to-noise ratio and more shadow details can be picked up in post-processing.

When shooting photographs against white or black backgrounds you probably want the background either as white or as black as possible (Figure 9.2d). Interpreting these histograms might be a bit tricky because you cannot know just by looking at the histogram if clipping in the highlights or shadows is just on the

background or also on the animal. In this case, most cameras have a highlight- or shadow-clipping indicator, highlighting the parts of the image that are in danger of saturation or loss of signal.

## 9.3

### Using Flashes

#### 9.3.1

##### Controlling Exposure

To be able to use the desired DoF, to avoid blurry images, and to sufficiently and evenly light the subject, macro photography often requires the use of additional light sources. Most commonly flashes are used since they provide a good way of precisely adjusting the amount of light and they have a consistent and well-defined color temperature. As we have seen in the previous section, there are basically two options to control the light exposure of the sensor, namely, by adjusting either the aperture or the exposure time. However, in flash photography we are introducing one or more variable light sources that have to be balanced together with the exposure settings on the camera.

In photography, *flash synchronization* (also called *flash sync*) is defined as the firing of the flash coinciding with the opening of the shutter allowing the light to reach the image sensor. Usually, the flash sync time can be anything down to 1/250 s. Even faster sync times are often possible when using the proprietary flashes for your camera system, but they work in a different way and significantly reduce the power of the flash.

There are many ways flashes can be used when carrying out an exposure. The most common way is to use it as a fill light to modify the ambient light of the scene. For the purpose of the macro photography described here, however, we wish to reduce the ambient light as much as possible, thereby making the light from the flashes the sole source of light, giving us total control over the exposure. In this case, when the light from the flashes is totally dominant, the shutter speed has less significance for the purpose of freezing motion since the exposure is almost completely determined by the flash itself. The duration of the actual flash is so short it will freeze even fast movements as long as the ambient light is not playing a significant part in the exposure. Most hot shoe flash units can be used in an automatic mode, *TTL* (through the lens metering), or in manual mode that allows the user to manually control the intensity of the emitted flash.

#### 9.3.2

##### Positioning and Shaping the Light

To obtain a high quality macro photograph it is important to light the subject correctly. When using flashes, you can control not only the amount of light produced by the flash but also the shape or character of the light by adding different

modifications to the light path or by moving the light source. Usually, the direct light from the flash is very “hard” and produces sharp highlights and shadows. For scientific or purely descriptive purposes it is usually important to have an even lighting of the subject with no pronounced shadows obscuring potentially important anatomical features.

For the purpose of getting even lighting with few shadows that gives a good overview of the animal, you want a large light surface that scatters the light. This can be accomplished by using a diffuser, either in the form of a softbox (a sort of “tent” placed around the flash with a white semi-transparent surface that will act as the effective light source) or a smaller variant (e.g., Omni-Bounce or the built in diffuser on the flash). This will give the light a less pronounced directionality and will produce “softer” light and shadows (Figure 9.3b,f).

Sometimes you need to direct the light in a very specific way, for example, to prevent it from illuminating a black background, or to concentrate it around a small transparent animal. To do this, a so-called snoot can be used, and it can be as simple as putting a rolled up piece of paper like a tube around the light source (Figure 9.3c,g).

Usually, two flashes are enough when lighting smaller animals that will fit in an aquarium; the setup is usually one flash on each side of the camera to minimize

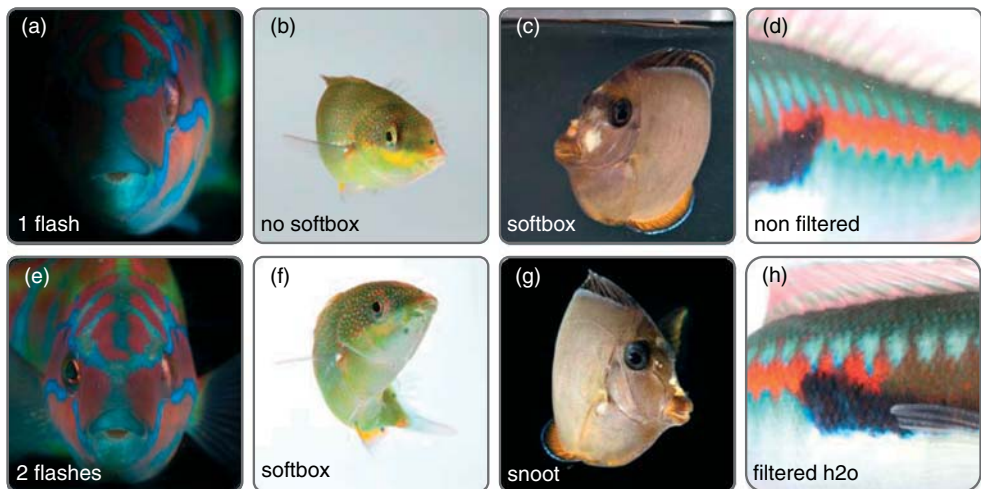


**Figure 9.3** Using the right flash accessories. (a, e) The flash: the use of only one flash (a) causes the formation of a strong shadow on one side of the object, while the use of two synchronized flashes allows a correct illumination of the photographed object (e). (b, f) The softbox: The use of a softbox helps the user to soften the light on your object and enhances the white of the background. (c, g) The snoot: The use of snoots

helps to focus the light on the object rather than on the background. The use of a softbox is recommended for white backgrounds while the use of snoots is recommended for black backgrounds. (d, h) Filtered seawater: The white dots and lines in (d) are reflections of particles from non-filtered seawater. In (h) filtered seawater was used and the particle reflections considerably reduced.

shadows. A third flash is convenient when photographing larger animals against a white background since it can be used to specifically light the background, making sure it stays completely white and eliminates shadows from the subject.

## 9.4 Equipment

### 9.4.1 Camera

Macro-photography of marine biodiversity can be realized with all sorts of camera bodies; the only requirement is that there must be some way to control a set of external flashes. However, since this work is mainly carried out in close proximity to water and often in the field, a rugged and well-sealed body is highly recommended. In addition, a full frame sensor ( $24 \times 36$  mm) may be more important than speed (frames per second) since larger pixels on the sensor gather more light and generate less noise. Presently, we are using the Canon EOS 5D mark II and Canon EOS 7D (both of which allow HD video recording).

### 9.4.2 Lenses

Macro or close-up photography is defined by the subject-to-film (or digital sensor) ratio, and not by the distance from the lens to the subject, as the name would suggest – although a relation exists. This ratio, also known as the *magnification rate*, indicates the subject's actual size compared to the size representing the subject on the digital sensor. For example, when the size of the actual subject is equivalent to the size of its image represented on the digital sensor, the magnification rate is 1:1 (also called *life size*). Therefore, a ratio of 1:8 (Figure 9.1g) indicates that the size captured on digital sensor is one-eighth of the actual size, while a ratio of 4:1 indicates a four-times magnification of the actual size (Figure 9.1k). Although no official cutoff for macro photography exists, real close-up photography usually starts at a ratio of 1:1.

The lens defines the maximum magnification that can be obtained. The minimum focusing distance of a lens is the closest the lens can get to a subject, while maintaining sharp focus. At exactly this distance the maximum magnification rate of the lens is obtained. Traditionally, macro lenses have a fixed focal length that usually ranges between 50 and 60 mm, 90 and 105 mm, and 180 and 200 mm, depending on the manufacturer. The 50–60 mm lenses have a short minimum focusing distance, while the 180–200 mm lenses have a long minimum focus distance, which might be useful when performing macro photography in the wild, allowing the photographer to get close-up photographs of animals without getting too close and risking scaring them away. The 90–105 mm lenses are widely used for their intermediate working distance. For the macro photography described in this

chapter, the 100 mm macro lens is our lens of selection, with a few exceptions made for very small (Canon EF 65 MP-E 1-5×) or bigger animals (Canon EF 24–70 mm non macro lens). You can certainly practice close-up photography without a macro lens, for example, using extension tubes, but the maximum magnification will not be as great.

### 9.4.3 Flashes

Most amateur level and semi-professional camera models have a so-called pop-up flash built directly into the camera, but flashes can also be mounted onto the lens (e.g., macro- or ring flashes arranged in a circle around the front part of the lens) or mounted on the camera via the hot-shoe connector on the top. The use of such flashes will create reflections on the front panel of the aquarium and therefore obscure the subject. Using a cord or a wireless flash trigger, the flashes can be positioned independently of the camera and therefore undesired reflections can be avoided.

For flexibility and maximum control of the lighting conditions, and also to avoid reflections in glass surfaces, we will focus on off-camera flashes synchronized with the camera either wirelessly (radio signal, IR, or by the built in flash), with a sync cable or with a TTL cable. Many flashes have built-in IR controls, so several flashes can be wirelessly connected with each other. By using a sync- or TTL-cable to a flash set as the “master,” this unit can control one or several “slave” units. When using wireless triggers there is usually a transmitter unit that needs to be put on the hot-shoe connector on the camera, with the exception of some Nikon cameras (the Nikon *CLS*, creative lighting system) and the Canon 7D, which have a built in control for remote flash triggering. An IR transmitter can be used to trigger flashes with built in IR receivers or an alternative is to use a transmitter/receiver system using radio waves, which have a much longer working distance, are not sensitive to daylight conditions, and more importantly do not require a direct line of sight between transmitter and receiver (this method however, requires you to have one radio receiver per flash). Both IR and radio systems can perform wireless TTL metering; however, most wireless TTL systems are expensive and are definitely not necessary for the purposes described in this chapter. A big drawback of TTL cables is that there are limitations in cable length; and for some strange reason they are all spiral shaped like an old phone cord. This may impede camera movements or result in the flash or the whole stand dropping to the floor. Therefore, the most flexible way of triggering your flashes is by using wireless triggers.

For lighting we prefer the flexibility of hot-shoe flashes, and our current setup consists of a Canon Speedlite 580EX II and a Canon Speedlite 430EX, remotely triggered by either a Canon ST-E2 Transmitter (infrared) or AlienBees CyberSync™ radio triggers or by the built-in trigger in the Canon 7D camera. Additional advantages of using these flashes for this type of work is that they are relatively small and battery operated with readily available alkaline batteries (or rechargeable batteries) and can easily be used when no other power source is available.

## 9.4.4

## Flash Accessories and Lighting Gear

Depending on the available space, we mount the flashes either on tripods or on flexible arms attached to a support. We also use  $38 \times 38$  cm softboxes (e.g., Lastolite™, especially made for hot-shoe flashes) that can be mounted on tripods and positioned around the tanks if enough space is available. When space is limited, we also use smaller softboxes ( $13 \times 18$  cm) or “snoots” (to direct the light from the flash) that can be mounted directly on the light-emitting part of the flash. The flashes are mounted on flexible arms (also containing a hot-shoe connector) that are screwed onto a supporting plate. We use two types of support plates, one large, which defines the workstation, and a second, smaller in size, which is used to lift up (using Styrofoam) the medium size and plankton tanks (Figures 9.4 and 9.5). For a space limiting way to handle the lighting setup we use up to four flexible arms (e.g., two for flashes and two for LED lights to help with focusing in low light conditions).

## 9.4.5

## Aquarium Setup

As marine organisms are quite diverse in their behavior as well as in their size, the use of a set of tanks in different sizes and proportions is recommended. To reproduce the true colors of the animal or the plant we portrait and to achieve maximum light transmission, we opted for front panels in ultra white glass (Starphire® or OptiWhite™, Figure 9.5f). After testing various tank formats and sizes we also opted for custom-made rimless aquariums that are more scratch resistant and cause less distortions than acrylic tanks. Table 9.1 gives the sizes of the tanks and their usage. For both plankton tanks, the side panels should be made

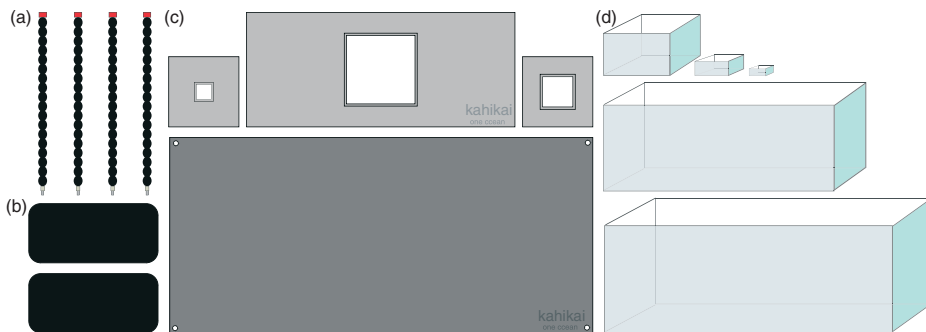


**Figure 9.4** Photography studio equipment: Schematic representation of the equipment used to set up an *ex-situ* macro-photography studio. (a) Four flexible arms hold the flashes and LED lights in the required position. (b) Two Styrofoam blocks support the plate for the small tank and the plankton

tanks to allow imaging from above on a black background. (c) Various support plates used for the tanks. The large plate contains four threads to fix the flexible arms. (d) Set of five aquariums in various dimensions. See Table 9.1 for tank sizes and suggested use for each aquarium.



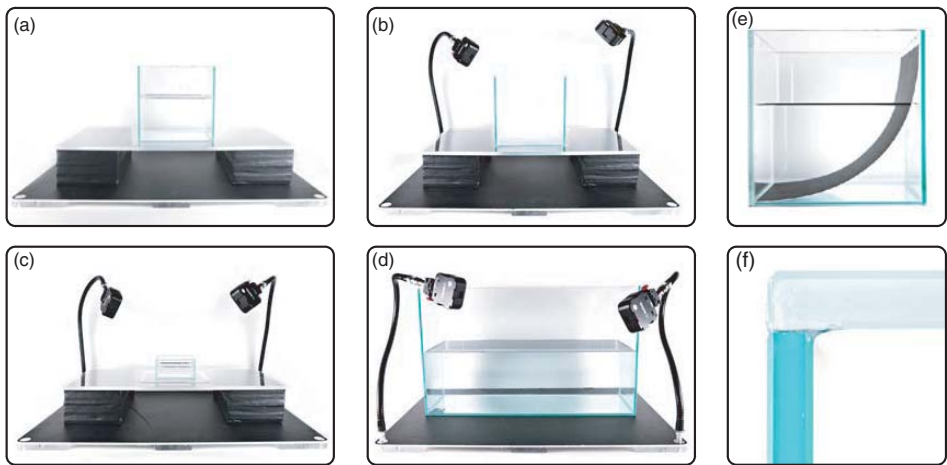


**Figure 9.5** Macro photography studio: (a, b) Set up using the bottom plate; two Styrofoam blocks lift the support plate and the small tank, allowing imaging from above. In (b) two flexible arms holding LED lights are mounted on the back of the bottom plate and the tank contains a white plastic back-ground. Note that the white background fades out the back panel of the tank. (c) Set up using the bottom plate, two Styrofoam blocks, the support plate containing

the insert to hold the large plankton tank, and two flexible arms. (d) Set up using only the bottom plate to hold a large aquarium and two flexible arms mounted on the front of the plate. (e) Profile of a small tank showing the curvature of the black plastic sheet that serves as background. (f) Detailed view of the OptiWhite<sup>®</sup> front panel (top) in contrast to the regular greenish glass side panel (to the left).

**Table 9.1** Tank sizes and usage.

Tank size (L x W x H in cm)	5 x 5 x 2.5	10 x 10 x 5	17 x 17 x 13	30 x 15 x 20	50 x 22 x 30
Usage	Small macro-plankton (2–8 mm)	Big macro-plankton (1–3 cm)	Small sea creatures (up to 8 cm)	Medium sea creatures (up to 12 cm )	Large sea creatures (up to 15 cm)

These five sizes cover most of the small to medium sized animals we imaged. Usage for these tanks may vary according to the behavior and character of the animals to be photographed.

of thick matte glass so it can act as an integrated diffuser, helping to spread the light throughout the whole tank.

9.4.6  
**Other Accessories**

To obtain a clear view of the subject, monochrome plastic backgrounds can be used as backgrounds both inside and outside of the aquarium depending on the situation.

It is usually advisable to keep a certain distance between the background and the subject, meaning that when taking photographs from above it is recommended to put the background a few centimeters outside of the tank. Backgrounds used inside the tank should cover the back and the bottom and fit tightly between the side panels so that the animals cannot hide behind them (Figure 9.5d).

For high magnification, macro lenses such as the Canon MP-E 65 mm lens are suitable; a tripod in combination with a micrometric focusing rail is very useful at the higher magnifications.

To remove particles from the water or to remove droplets from the front panel of the tank other accessories such as pipettes (various sizes), Chamois leather, or soft paper towels are very useful.

## 9.5

### Macro Photography of Marine Life

#### 9.5.1

##### Setting up the Camera

For macro photography of marine organisms from about 10 to 20 mm and bigger, using a digital camera with the two flashes is the best option. For the best possible image quality the camera should be set to take RAW images, which contain the raw image data from the sensor and gives you more flexibility during post-processing. Joint Photographic Experts Group (*JPEG*) images use a compression algorithm that actually removes data from the image and, in addition, this format contains less image data to begin with, making it harder to make adjustments during the post-processing stage. It is also good to set the color space to “Adobe RGB” since this contains more color information than the standard “sRGB.” As color handling can be complex we will not go into details here.

It is preferable to use the camera un-mounted (hand-held, rather than on a tripod), which make it easier to move around and focus on a moving animal. Since the flash will “freeze” any movement, handholding the camera will not result in unsharp images. However, if you are going to film the animal, especially at higher magnifications, it is a good idea to use a tripod to ensure that the camera is steady. For more details and information concerning camera settings see Section 9.2.

The camera mode has to be set to manual (M), and since the shortest flash sync time usually is 1/250 s this is what the shutter time will be set to. Since most of the light comes from the flashes the camera’s white balance setting can be set to “Flash.” To obtain a good exposure, you need to balance the power of the flashes with the lens aperture size and a good practice is to first set the camera to manual (M) with a shutter time of 1/250 s and an aperture of f/20. Take a test shot with the flashes at half power (refer to the flash manuals to adjust the flash settings), and if the image is overexposed you have to either stop down the aperture (how much you can close the aperture depends on what lens you are using) or lower the power of the flashes. Usually it is preferable to stop down the aperture since we usually

want a larger DoF. If the image still is too dark with the flashes at maximum you need to open up the aperture to let more light in. This will result in a shallower DoF, so an alternative is to change the light sensitivity of the camera sensor (the ISO value), but if the ISO value is too high the final image will contain more pixel noise. For a more detailed description of the ISO settings see Section 9.2. The exposure settings will be very different, depending on numerous factors such as subject magnification, distance of flashes to subject, the kind of softbox used, and so on; after a while, though, you will get a feeling for what settings to start with. Each shoot generally takes a few shots to adjust the settings to get a good exposure.

Working on a moving boat is quite different from standing on dry land—some of this type of photography may be quite difficult even if you are not moving around on the open ocean. If the boat is moving a lot you have to be careful not get splashes of water on the camera equipment, and focusing and composing the image will be a lot harder when you, the water, and the animal are moving. Using the camera's autofocus with only the center focus point activated is probably a good idea but, unless you have a state of the art autofocus system and good static lighting, manual focus is the only realistic option.

### 9.5.2

#### Positioning the Flashes

To obtain a clean background it is advisable to use a sheet of solid colored plastic (preferably neutral colors such as black or white depending on the color or transparency of the animal) behind and/or under the subject. This gives a background free of distractions, helping to emphasize focus on the subject.

Lighting small creatures is usually easier than lighting bigger objects, which is why we will deal with it first.

#### 9.5.2.1 Lighting Small Animals

Very small animals, and especially fast swimming small animals, are easier to photograph from above in a small tank or dish with a low volume of water restricting the vertical movement to a minimum. To create maximum contrast for small and transparent animals, side lighting is the key. Side lighting is preferably done using the two flashes facing each other on each side of the tank. To avoid stray light from the flashes entering the camera lens (resulting in a low contrast image), you can use so-called “snoots.” A cheap and easy method of making a snoot is to take a piece of paper (preferably dark and/or thick enough so that the light does not shine through) and roll it around the side of the flash head, thereby creating a narrow path for the light.

Small and/or transparent animals are usually better visualized on a dark background. A good way to obtain good lighting on the animal and at the same time obtain a really black background when taking photographs from above is to put the tank/dish with the animal on a stage with a piece of black paper or plastic placed about 5–10 cm directly under it. If the flashes are set up level with the animal using snoots, the background will receive little or no light and at the same time be out

of focus, ensuring a dark and homogeneous background. It is very important that there are no particles in the water since all particles will shine like little bright spots with the use of flashes (Figure 9.3d,h). If the photographs are taken from above, make sure that the bottom plate of the aquarium is clean and scratch-free.

### 9.5.2.2 Lighting Bigger Animals

Generally, you want to put one flash on each side of the camera, pointing roughly at a 45° angle toward the center of the tank. You may need to adjust the positions if reflections appear in the glass. Usually, the biggest problem is to get the animal in the right position – especially if it is swimming! What you want is to create a contrast between the animal and the background, so, for example, a transparent animal is usually best viewed on a black background, since reflections and refractions in the anatomy of the animal will easily be visible against the dark backdrop. *It is not necessarily always true that a dark animal will be best on a white background.* The contrast might sometimes be too high, so it is always good to try a few different setups.

With a white background we want it to be overexposed and washed out to pronounce the effect, but when using a dark background you do not want too much of the light falling onto it. Make sure the animal is not too close to the background and try to adjust the flashes so as to avoid the main light falling onto the background directly behind the animal. You can try to move the light so you obtain a smaller angle against the background and shield off the light going backwards by putting up pieces of paper or cardboard as a screen. If the animal is not too big and is not moving around much you can try using the snoots described in the previous section.

In addition, when setting up the background for photographing larger animals from the side it is usually easier to get a good shot if the background covers both the bottom and the backside of the tank. If you use a large sheet that is bent between the two surfaces you will get a smooth looking background (Figure 9.5e).

### 9.5.2.3 Water Quality

Regardless of the size of the animal, the purity of the water is crucial to obtaining good images. All water needs to be filtered (the best results are obtained with at least 0.2 µm pore size) to avoid the particles being lit by the flashes and appearing as dots on the final image (Figure 9.3d,h). Anything in the light path between the subject and the lens is important, so if you are taking the pictures through the glass of the tank it is of course also important to remember to clean the glass surface before you start shooting! Clean with freshwater first and finish off with some alcohol to remove any grease stains.

## 9.6

### After the Photographic Shoot

Although the main goal is to use an imaging setup that avoids extensive post-processing, factors such as the water quality can interfere with the quality of the

final image. If the lighting and camera are set up correctly and the water is filtered, you should not need to do much post-processing of the images.

### 9.6.1

#### File Formats

On most current digital camera models, two file formats (RAW and JPEG) are available. The RAW format is the raw output from the image sensor and is specific to each brand and model while JPEG is a standardized compressed format. The JPEG standard uses lossy compression, meaning that the compression algorithm removes information about the image to make it smaller. This compression, however, is done in a way that takes the sensitivity of the human eye into account, mostly removing luminance (brightness) and chroma (color) data in areas and in the ranges where the eye is less sensitive to details. This type of compression is especially suitable for photographic images where there are usually subtle gradients in color and brightness, and can achieve very high compression ratios without any major compression artifacts. This is a great image format for saving bandwidth when publishing photographs on the web and saving space when storing your family photographs, but there are several disadvantages that make this format less ideal for high quality photographs that might go through image processing and/or be used for large prints.

You may think that the most obvious reason is the compression, and while this of course is an important factor affecting the image quality there is another major technical difference between the two formats – and that is bit-depth. The JPEG standard allows 8 bits of data allocated to each color channel (red, green, and blue), meaning that there are  $2^8 = 256$  levels of luminosity per color channel (this is the single-channel nomenclature meaning that 8 bits per channel gives an image with a total color depth of  $8 + 8 + 8 = 24$  bits). Taking all three color-channels into account we end up having a total color depth of  $2^{24} = 256^3 = 16\,777\,216$  different colors. As the human eye can distinguish about 10 million different colors (Judd and Wyszecki, 2005) this might seem to be more than enough, but it actually does not give much room for adjustments. The native bit-depth of the raw output from most camera sensors is usually 12 or 14 bits per channel, meaning that a 12-bit image can address  $2^{12} = 4096$  levels of luminosity per color channel – a considerable difference from the 256 levels of an 8-bit image. Therefore, keep in mind that when shooting JPEG you trust the camera software to down-sample your image data from the native bit-depth to 256 levels in the JPEG standard, which is a reduction to only 1/16 of the levels in a 12-bit raw image. For these reasons it is recommended that all adjustments to the image are carried out at high bit-depth and down sampling to 8 bits per channel is only performed with the final image before it is printed or published on the web.

Another big difference in addition to compression and color depth is image processing. When using JPEG in the camera you let the camera software do adjustments to, for example, contrast, color saturation, and sharpness. These settings can usually be adjusted, but since this is done indiscriminately to all

images there is still a fair chance these settings will be suboptimal for many of the images. When shooting RAW you get to adjust these parameters manually and this lets you optimize each image individually.

The RAW workflow is obviously more time consuming than handling JPEG, but powerful tools such as Adobe Lightroom® or Apple Aperture make the effort of post-processing minimal while still giving you maximum flexibility.

### 9.6.2

#### Post-processing Workflow

We use Adobe Lightroom and Photoshop® for managing the images and to carry out image processing, although in most cases Adobe Lightroom is sufficient (at least from version 2 and upward). Our standard workflow is described in the following section, but should only be considered as a starting point. Each image, and especially each sea creature, has particularities that need to be taken into account both when doing the exposure and during post-processing:

- 1) Check white balance and correct if necessary. If the camera is set to auto white balance it usually works fine with few exceptions. Since you are only using flashes, you may also set the white balance camera setting to “flash.”
- 2) Sometimes cropping and/or rotation of the image are required.
- 3) Remove spots and debris, and so on, from the background.
- 4) Correct the exposure if needed, but you should make sure you get it right in the camera! If you shoot RAW images you will have far more possibilities to make exposure changes since the amount of image data in the RAW image is considerably larger than when shooting, for example, JPEG.
- 5) Carry out level and curve adjustments to enhance contrast.
- 6) Add a little more color saturation to reflect the true colors (just be careful so as not oversaturate any colors; the “Vibrance” control in Lightroom 2 is better to use than “Saturation” since it tends to be less prone to oversaturate colors). This is usually only necessary when shooting RAW since when using, for example, JPEG this is done automatically in the camera.
- 7) Apply sharpening (e.g., “Smart Sharpen” or “Unsharp mask” in Adobe Photoshop or similar features in Adobe Lightroom). This should always be the last step.

To produce lower resolution images suitable for web publication, you must remember to carry out another sharpening after resizing. In addition, if the color space of the image is “Adobe RGB,” convert the image into “sRGB.” This is because many web browsers do not take image color space into account and computer screens can usually not display all colors in the “Adobe RGB” color-space, so the image might look a bit “flat” with unsaturated colors. Adobe Photoshop, for example, reads the image color space and converts it for the computer display profile, so that the extra colors provided by the color space are only important during editing where it provides more room for making adjustments.

## 9.6.3

## Selecting Images

When carrying out the photo shoot, try to make as many variations as possible of each animal, for example, with different backgrounds and from different angles. If you have time during the shoot it is also worth experimenting a little so as to obtain more artistic images suitable for education, promotion, magazine covers, and so on. From a large selection of photographs you will have a better chance of getting the material you perhaps did not even know you needed!

Here are just a few examples of different image styles (Figure 9.6):

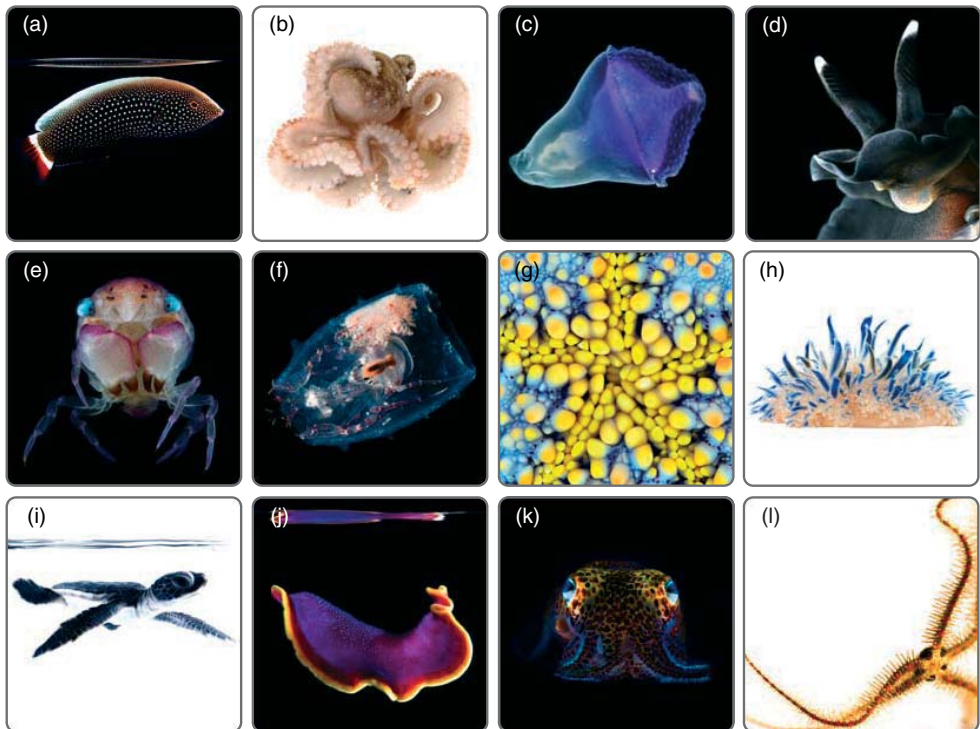


**Figure 9.6** Sample images: (a) psychedelic wrasse (*Octopus cyanea*), (b) Hawaiian day octopus (*Octopus cyanea*), (c) undefined larvae, (d) black nudibranch (*Dendrodoris nigra*), (e) undetermined juvenile crab, (f) crustacean (*Phronima*) protecting its eggs inside a salp (tunicate), (g) close-up of the mouth region of the cushion sea star *Culcita novaeguineae*, (h) upside down jellyfish (*Cassiopea andromeda*), (i) juvenile green sea turtle (*Chelonia mydas*), (j) swimming

flatworm (*Pseudoceros ferrugineus*), and (k, l) brittle star (*Ophiura fragilis*). Images (d, g) have been used to illustrate the covers of *EMBO Journal* in 2009 (volume 28, number 11) and 2010 (volume 29, number 20), respectively. Image (d) has been featured in *Burn Magazine*. Images (c, f) have been featured in the *TARA Magazine* and (c) has been used for a dress design by French fashion designer Agnes B.

- science (all in focus, characteristic behavior, etc.);
- art (movement, selective focus, creative reflections);
- education (cute, fun).

## 9.7

### Animal Care

We also place particular emphasis on the preservation of live animals in appropriate conditions after their capture, as well as the proper handling of the animals, before, during, and after the photographic session. This includes release into their original habitats directly following a photographic session, if they are not to be subsequently used for further scientific examination.

#### 9.7.1

##### Collecting

Scientists need to take buckets with them on the Zodiac (or other collecting vessels) to keep the samples that will be imaged permanently in the water and avoid additional stress for these animals. This is particularly important when the animals are exposed to high temperatures and direct sunlight. The use of a portable aerator that allows the continuous oxygenation of the samples is highly recommended. Remove only samples that actually fit in the tanks being used, and choose small to medium size samples, which are easier to handle and light.

Sampling days on scientific cruises are usually busy with a lot of different samples that need to be collected and processed. Nevertheless, if serious imaging on board is envisaged, a dedicated “imaging sampling” protocol and time set aside for doing the actual imaging and post-processing is required. The main purpose of performing macro-photography out in the field is to get photographs of live material and the time needed for this has to be taken into account when designing the sampling protocols.

#### 9.7.2

##### Handling and Imaging

Collected live animals should be kept in running seawater as long as possible, for example, in polystyrene boxes. Never keep the animals exposed to direct sunlight. Running seawater is important for animal health, oxygenation, removal of particles, and mucus from collected animals and for polyp extrusion in the case of corals. When storing several animals in the same container, make sure that they are actually compatible. Some animals, like nudibranchs, release toxic mucus that could be lethal for other animals in the tank and, therefore, they should be kept isolated.

If possible, gently rinse your samples inside the polystyrene box (and change the water in the box to remove the sediment and mucus) before depositing them inside



the imaging tanks. If the animal still releases mucus, this can be removed using a plastic Pasteur pipette.

For corals, extruded polyps are often retracted when one transfers them from the storage tank to the imaging tank, and it often takes quite a while before the polyps extrude again (if they do so). To work effectively, the use of several imaging tanks in parallel is very convenient. By doing so, the samples can be deposited simultaneously in the individual tanks, and while one sample is going to be imaged the others have time to relax and extrude their polyps.

To ensure the best possible image quality, and in many cases also the well being of the animal, it is important to have access to clean filtered seawater, preferably from a 0.2  $\mu\text{m}$  filter.

Some animals (e.g., squids and nautilus) are extremely sensitive to light, and too much stress can cause the death of the animal. If imaging such animals, reduce the flash intensity to the strict minimum, or use no flash but, instead, raise the ISO settings.

## Acknowledgements

We thank Richard Chock, for his valuable help in optimizing and making various prototypes, and Mark Q. Martindale and Elaine C. Seaver for their support. We particularly thank Patricia Murata for fruitful discussions and careful reading of the manuscript and Emmanuel Reynaud for his continuous support and for giving us the opportunity to be part of the three-year TARA expedition ([oceans.taraexpeditions.org](http://oceans.taraexpeditions.org)).

## References

- Dionysius Ehret, G. (1736) *Methodus Plantarum Sexualis in sisternate descripta*, Leiden.
- Haddock, S.H., Dunn, C.W., Pugh, P.R., and Schnitzler, C.E. (2005) Bioluminescent and red-fluorescent lures in a deep-sea siphonophore. *Science*, **309**(5732), 263.
- Haeckel, E. (1868) *Natürliche Schöpfungsgeschichte*, Georg Reimer, Berlin.
- Haeckel, E. (1904) *Kunstformen der Natur*, Bibliographisches Institut, Leipzig and Vienna.
- Judd, D.B. and Wyszecki, G. (2005) *Color in Business, Science and Industry*, Wiley Series in Pure and Applied Optics, 3rd edn, Wiley-Interscience, New York.
- McIntyre, A. (2010) *Life in the World's Oceans: Diversity, Distribution, and Abundance*, Wiley-Blackwell, Oxford.
- Webb, T.J., Vanden-Berghe, E., and O'Dor, R. (2010) Biodiversity's big wet secret: the global distribution of marine biological records reveals chronic under-exploration of the deep pelagic ocean. *PLoS ONE*, **5**(8), e10223.
- Wilder, K. (2009) *Photography and Science*, Exposure Series, University of Chicago Press.



## 10

### Automated Image Processing in Marine Biology

Robert T. Kelly\*, Maureen A. Williams\*, and Emmanuel G. Reynaud\*

#### 10.1

##### Introduction

Planktonic communities are vital to many of the earth's processes, most notably biogeochemical nutrient cycling. Plankton accounts for over 50% of global carbon fixation each year and often plays crucial roles in many marine food webs (Giovannoni and Vergin, 2012; Jardillier *et al.*, 2005). Moreover, in contrast to terrestrial ecosystems, aquatic environments contain plankton as the main form of biomass (Stingl and Giovannoni, 2005).

Planktonic communities are composed of phytoplankton, plankton that are autotrophic and can produce their own food source, bacterioplankton, free living bacteria that function within planktonic zones, and zooplankton, which are heterotrophic. A thorough analysis of the planktonic community can reveal much about the community's current status as well as its evolutionary history. It has been demonstrated that planktonic community composition can affect the optical properties of water and control nutrient dynamics in oceanic systems (Boyd and Newton, 1999; Stramski, Bricaud, and Morel, 2001). Community structure itself is affected by pH, grazing pressure, climatic variation, and seasonal variation (Klug *et al.*, 2000; Qin and Threlkeld, 1990; Sanders *et al.*, 1989; Werne *et al.*, 2000). The study of plankton is one of the few areas where major discoveries are still to be made and baseline studies are still needed. Planktonic community study is now legally required with the development of new legislation focused on whole ecosystem study, such as the Marine Framework Strategy Directive (EC, 2008). The most recent developments in the field of planktonic community analysis have been in the field of semi-automated planktonic community analysis, a field that has grown recently due to advances in computer technology.

Several methods have been developed for planktonic community analysis (Hallegraeff, Anderson, and Cembella, 1995; Sournia, 1978). Planktonic community analysis began with basic light field microscopy techniques and taxonomic classification. The first recorded planktonic community study was conducted in 1828

\* equal contribution

by Dr J. Vaughan Thompson (Fraser, 1968). Victor Hensen, a physician, then developed the popular Hensen net following much thought and study on the quantitation of planktonic analysis and coined the term “*plankton*” based on Homer’s *Odyssey* (Smetacek, 1999). In the late nineteenth century, Per Teodor Cleve began using silk nets to study the distribution of phytoplankton in the North Sea (Cleve, 1899). By this point, interest in marine fish stocks encouraged many scientists to begin examining planktonic communities and soon Hans Lohmann developed centrifugation techniques for concentrating plankton, enabling the discovery of nanoplankton (Lohmann, 1911). The first attempts to determine worldwide patterns of planktonic species distributions occurred in the mid-1950s, with Smayda’s meta-analysis (1958). Hobbie’s development of fluorescence techniques for phytoplankton identification in 1977 again revolutionized the field, allowing the analysis of this important component of the community (Hobbie, Daley, and Jasper, 1977). Silhouette photography was first used in 1979 as a way to avoid issues associated with sample preservation (Ortner *et al.*, 1979). Cameras for analysis of planktonic communities have even been included on submersibles (Wiebe and Benfield, 2009). The most recent developments have been in the field of semi-automated planktonic community analysis, a field that has grown recently due to advances in computer technology.

The importance of community analysis has thus grown and it has become increasingly important that marine scientists, legislators, and the general public understand the processes involved in planktonic community analysis. This chapter will present the current options available for analysis and the steps used to analyze these communities. There will be a focus on the current status of semi-automated planktonic community imaging and the issues associated with this type of community analysis in particular.

## 10.2

### Methods of Planktonic Community Analysis

#### 10.2.1

##### General Methods

Planktonic community analysis is a multi-step process, with the time required for analysis increasing with the complexity of analysis. The most basic method of screening is the manual method, in which a scientist looks down a microscope and can either capture an image for subsequent analysis or can directly identify what they see. This method requires the least cost. However, it is also the most time intensive and can be difficult due to the lack of availability of standard datasets. The manual identification method requires the use of high-quality microscopes and skilled taxonomists. A more efficient method involves the use of an automated imaging platform, which images all available samples and produces a large volume of images that can then be reviewed by the scientist. Current options are based on semi-automated identification, where each individual is analyzed as a geometric particle and then

classified based on its geometric measurements. The ideal system would be a semi-automated classification system in which the automated imaging is combined with an automated classification system, with machine learning allowing the system to provide a filtering mechanism, separating classes from the sample based on pre-existing datasets. This will allow for the final stage of the process to be a simple case of the scientist reviewing the choices made by the system.

### 10.2.2

#### Semi-automated Options

Newer techniques, such as high-throughput and high-content screening, allow higher replicate numbers and faster results. Semi-automated techniques allow for error estimation, which has been shown to be equivalent to error estimates of many taxonomists, and are reproducible to a higher degree (Benfield *et al.*, 2007; Culverhouse *et al.*, 2003). The current options for semi-automated planktonic community analysis include hybrid optical-net systems such as the camera-net system (Olney and Houde, 1993; Ortner, Hill, and Edgerton, 1981). More recently, stand-alone imaging systems have been developed, such as the video plankton recorder (VPR, Davis *et al.*, 1992), ZooScan (Gorsky *et al.*, 1992, 2010), *in situ* video profiler (Tiselius, 1998), shadowed image particle profiling evaluation recorder (SIPPER, Samson *et al.*, 2001; Remsen, Hopkins, and Samson, 2004), zooplankton visualization and imaging system (ZOOVIS, Benfield *et al.*, 2003; LISA, C. P. Gallienne), and the FlowCAM (Sieracki, Sieracki, and Yentsch, 1998).

All of the semi-automated planktonic community analysis options treat the individuals as particles, only examining geometric parameters such as the ones shown in Figure 10.1, which inherently reduces the information associated with each image. The morphology, taxonomy, and geometry are separated in geometric classification, reducing the potential for interesting and informative analysis. By classifying solely on geometry and size parameters, it is possible for two members of the same species of different size to be classified as different taxa. Separating geometric, morphological, and taxonomic information reduces the power of the analysis and further introduces bias into classification systems.

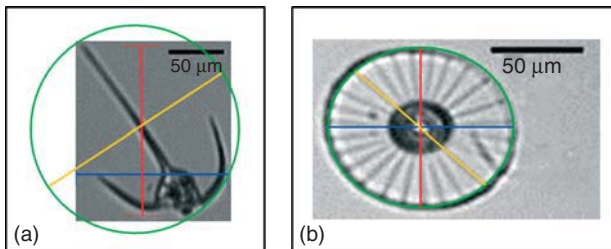


**Figure 10.1** Geometry of two planktonic organisms. The measured parameters of a dinoflagellate (a) and a diatom (b) are shown. The height of each is shown in red, with the width in blue, and the spherical diameter in yellow. Morphological differences, such as the flagella of the dinoflagellate, are ignored, leading to issues with classification.

## 10.3

## Semi-automated Planktonic Community Analysis

## 10.3.1

## Work Flow of Analysis

Semi-automatic analysis of plankton is based on an adaptable workflow from capture to classification (Figure 10.2). The general process involves community sampling and pretreatment, image capture, data importation, preprocessing of images and data *in silico*, development of a classifier, classification of geometric particles, and final analysis of results (Figure 10.2).

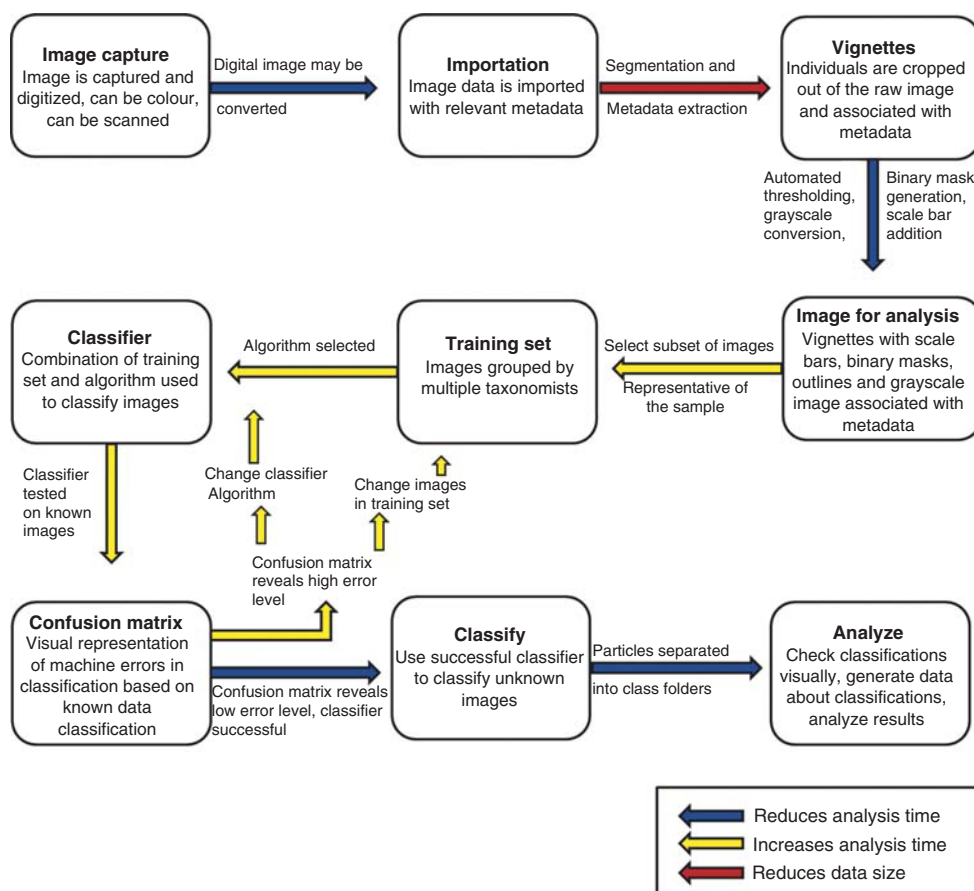


**Figure 10.2** Workflow of semi-automated planktonic imaging. The steps taken from image capture to final analysis are shown.

#### 10.3.1.1 Sample Collection

Plankton community analysis always begins with the selection of a sampling method, most of which are time and labor intensive and generally involve the use of plankton nets. Following sampling, plankton can be analyzed in two different ways, via direct live imaging or fixation. The amount of time between sampling and analysis often dictates whether live imaging is possible. It is generally more informative to study live plankton species, as there are no fixatives, no cell shrinking, and color is maintained. Time constraints make live imaging difficult and therefore fixation can allow for more long-term observation. Difficulties arise rapidly with fixation, as cells can shrink and swell and samples degrade over time, impacting on taxonomic analyses (Deuer, Lessard, and Satterberg, 2001). Furthermore loss of cells can introduce bias into the system as some species may be more susceptible than others to degradation, with some species experiencing cell loss of up to 70% (Leakey, Burkill, and Sleigh, 1994).

#### 10.3.1.2 Image Capture

The ability to create a suitable large reference dataset of images for plankton screening is strongly affected by the imaging platform used. For plankton, there are three primary locations in which an image may be taken, in the laboratory setting, on a boat with a dedicated imaging system, or using an underwater camera system. Each system of capture has specific positive and negative aspects and method selection should be carefully considered relative to the goals of each study.

An early example of a high content method of screening came with the development of the VPR (Davis *et al.*, 1992). This system used the principles of forward light scattering to image the nearly transparent specimens. Several cameras are used in the imaging system to observe several different size scales at once. This method provides high-resolution imaging and does so without handling the species themselves, allowing imaging of delicate or gelatinous species with impunity. However, this early method was limited in its ability to define plankton at the species level and therefore is unsuitable for the current need for qualitative high content screening (HCS).

The downside to these underwater imaging platforms is that they are normally expensive and highly specialized, meaning that they are unavailable to many researchers. Therefore laboratory based fluorescence microscopes and high-resolution bright-field microscopes are more commonly used in plankton imaging. Wide-field microscopes can be useful in plankton studies due to their high resolution. Wide field microscopes enables retention of information at much higher magnification on individual wells, whereas lower resolution systems, such as the binocular, are better at imaging entire plates. However, in classification analyses, the binocular fails to provide the required resolution, and is therefore unsuitable for studies requiring such detailed qualitative information.

The use of these types of imaging systems highlights the need for automation analysis as it is not only the capturing of images that is important in classification but the subsequent preprocessing of the image, which will usually take up most of the sampling time.

Digital images can reveal a wide variety of important information about suspended particles, such as abundances, size spectra, and distribution of planktonic biomass (Sieracki *et al.*, 2010). Different intensities of light are converted into discrete points known as *pixels*, which vary in values known as *gray levels*, which in turn give contrast to the image (Cardullo and Hinchcliffe, 2007; Sieracki *et al.*, 2010).

Regardless of the technical quality or expense of the system, the production of an image is usually accompanied by the formation of noise in the image, or variations in these gray levels, usually caused by uneven illumination due to scattering of light that can be observed as blurred or darkened samples (Uddin *et al.*, 2011). Noise is particularly prevalent in plankton analysis due to the large quantity of particle samples in the images, which allows for more noise to form due to the packed nature of these particles. Preprocessing of the image is therefore an important step as this seeks to correct transformations that either the optics or electronics impose on the image, distorting the necessary information (Wolf, Samarasekera, and Swedlow, 2007).

#### 10.3.1.3 Importation and Segmentation

Analysis with semi-automated planktonic techniques requires significant image preprocessing, the general steps of which are shown in Figure 10.3. After the images are taken, they must be imported into the analysis software. Importation can alter the images, reducing their size and making them easier to analyze.

Generally, filters are used to enable quick and simple analysis and improve the image quality. One of the principal methods of image preprocessing is the process of adding filters to the image to attempt to remove noise. Several filters exist and many specialize in a particular task. In the ImageJ platform, common examples are mean and median filters, and the Gaussian blur filter. In median filtering, the neighboring pixels are assessed by intensity and the median value becomes the new value for the central pixel. This allows much of the noise to be phased out with respect to the surrounding environment and is particularly adept at limiting the influence of pixels with extreme values. It also contains various levels of precision, allowing a large degree of specificity.

However, irrespective of the filtering technique used, one must acknowledge that any preprocessing technique will have a detrimental effect on the quality of the image. For example, using the median filter can drastically affect the number of pixels present in the image (Senel, Peters, and Dawant, 2002). In essence, it is better to take a good image first than to require the use of filtering at all. This also means that the quality of the camera used can be lost when using these techniques. The huge resolutions of some of the more expensive models will essentially be wasted upon subsequent preprocessing of the image.

In most cases, an image is imported and a threshold established to generate a binary mask. This removes the image of the particle from the background. An outline can then be generated for further analysis. These steps introduce a bias, as thresholding values can significantly alter the particle's shape and later classification. Many software options will turn color images into grayscale images



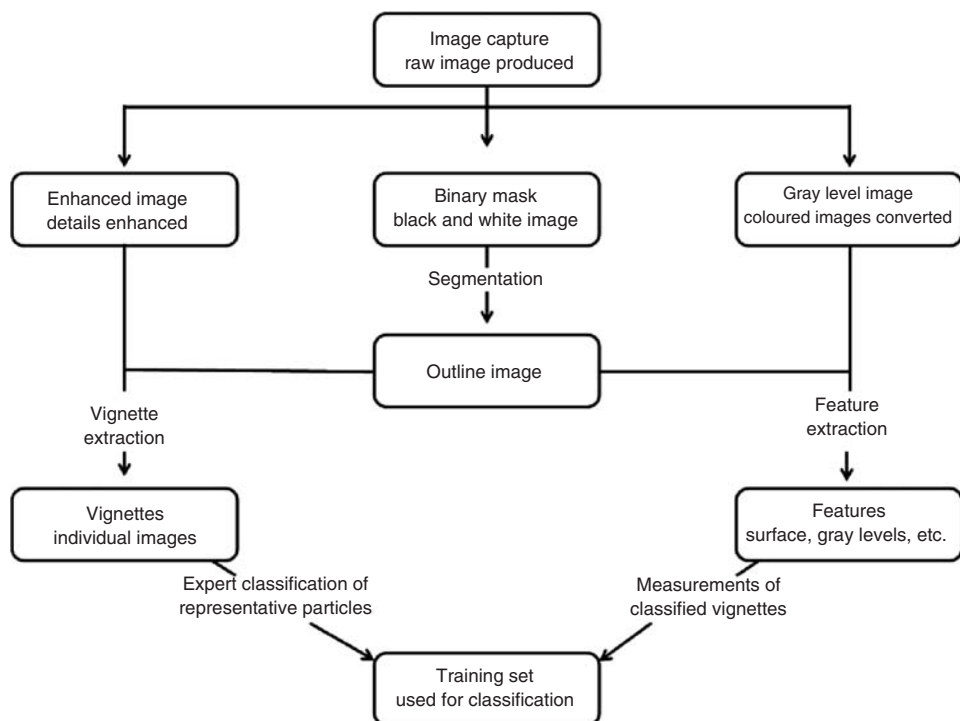


**Figure 10.3** Image processing overview. The common steps in creating a classifier are shown. Following capture, all steps are completed in analysis software. There are many options for analysis, though most follow these general principles.

to reduce the overall size of the image, though this again introduces bias and provides a source of variation in analysis. The way images are imported into the software can thus introduce a bias and care should be taken throughout.

Particles are identified in the raw image in a process known as *segmentation*. Segmentation can cause issues when individual plankton are not segmented out of raw images in one piece (Figure 10.4). This issue is avoided when the image capture device captures only single images of each individual, though this increases the time associated with analysis. This is the step where the greatest bias can be introduced, as some particles are segmented out multiple times and some particles are not segmented out at all.

#### 10.3.1.4 Classifier Generation

At this point, a taxonomist applies several filters to enable the software to recognize specific individuals that are representative of each taxon being studied. Representative plankton must be identified and sorted by an expert taxonomist into their taxa, a process that requires time, expertise, and money. Expert identification and sorting introduces variation into the analysis at two points, reducing the ability of scientists to repeat the analysis and gain identical results. The images chosen to compose the

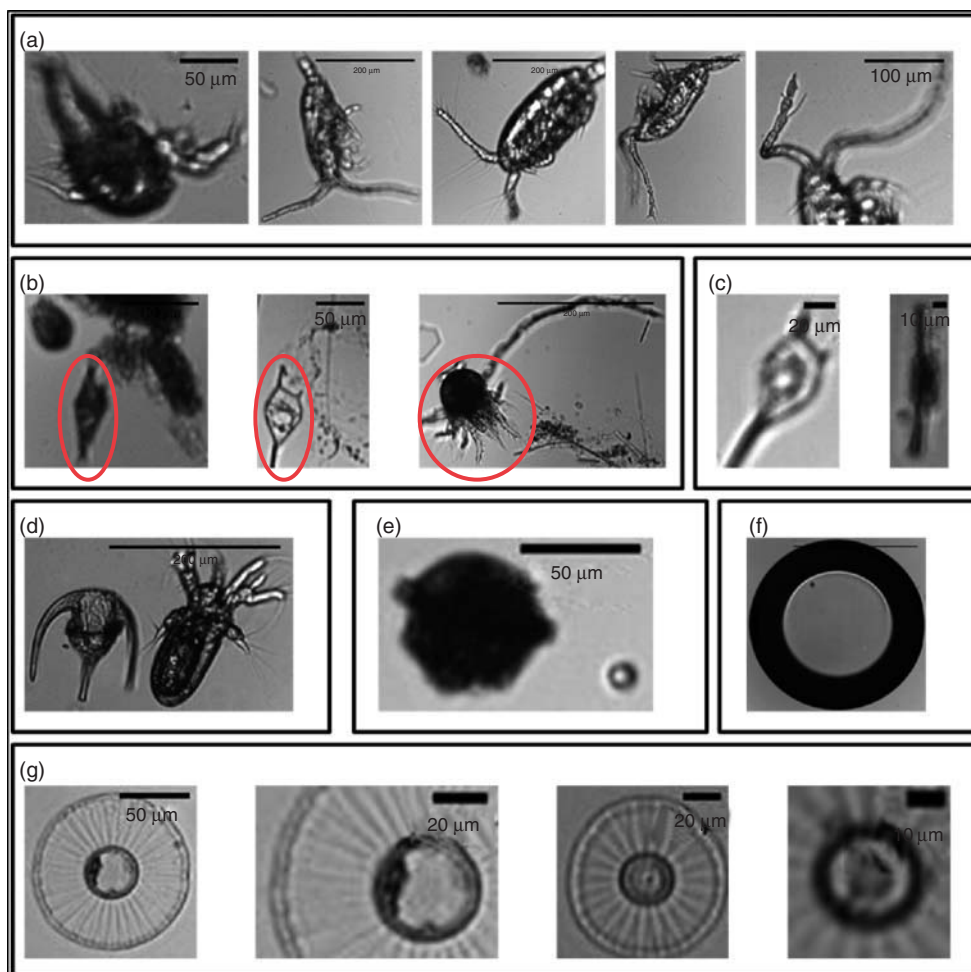


**Figure 10.4** Common issues encountered in semi-automated planktonic community imaging. These FlowCAM® images, taken following processing in ZoolImage and Image J, demonstrate the wide variety of issues encountered in analysis. (a) Multiple angles of the same taxon are commonly captured due to the use of flowing fluid, as seen with the copepod in (b), where individuals captured in aggregates are typically left unclassified, as seen with the encircled copepod

and dinoflagellates. (c) Plankton movement, as well as movement of the capturing apparatus, can lead to blurry images, shown in the dinoflagellates. (d) Segmentation can capture multiple planktons in one image, treating them as one particle for analysis, or (g) can capture only part of an individual. (e, f) Issues with debris and bubbles occur commonly, as seen in the detritus in (e) and the bubble in (f).

**Table 10.1** Common algorithms used in classifier development.

Algorithm	Source
*Learning vector quantization ( <i>LVQ</i> )	Kohonen (1987) and Tang <i>et al.</i> (1998)
*Random forest ( <i>RF</i> )	Breiman (2001)
5-Nearest neighbor ( <i>5-NN</i> )	Peters, Hothorn, and Lausen (2002)
C 4.5	Quinlan (1993)
NBC	Ye, Chang, and Hsieh (2011)
DINN	Falchi <i>et al.</i> (2007)
DKLL	Demers <i>et al.</i> (1992)
*Linear discriminant analysis ( <i>LDA</i> )	Hastie, Tibshirani, and Buja (1994)
*K-nearest neighbor ( <i>KNN</i> )	Peters, Hothorn, and Lausen (2002)
*Tree	Breiman (2001)
*Neural network ( <i>NN</i> )	Simpson <i>et al.</i> (1992)

Several algorithms have been developed for machine learning and classifier development. Most software packages will include multiple algorithm options when creating a training set. Asterisks indicate algorithm options in the FlowCAM software.

training set affect the final results, as the angle from which the individual is viewed, the clarity of the image, and the background debris in the image can all affect the machine's interpretation of how the taxon is identified, though these issues are less likely to impact a taxonomist. Each taxonomist also introduces variation, as his or her classification impacts the machine's learning and the specific training of the taxonomist can bias classification. The use of several taxonomists helps avoid many of the issues associated with machine learning, though the matter should be considered in any analysis.

The classifiers of most software utilize algorithms with the images of the plankton and the parameters to form a working model. Table 10.1 shows several algorithms commonly used.

#### 10.3.1.5 Classification

Once the machine has been taught to recognize characteristics of the parameters associated with each particle class being studied, classification of unknown plankton images can occur. Particle characterization is automated and is the step that saves the most time for analyzers, in addition to eliminating the issues of taxonomist fatigue. However, there is much bias introduced by algorithm selection, image selection for the training set, individual taxonomists used, and the ability of the taxonomist to use the software.

There are many software options available for analysis, though most are inextricably linked to the capture method used. Each piece of software has positive aspects, though many are not inherently user friendly and often require interactions with developers and some code troubleshooting. Often, solutions to common problems are addressed in online forums and blogs, where supplementary codes can be shared (Alvarez, Lopez-Urrutia, and Nogueira, 2012). There are many highly

taxonomically specialized software options, including *DiCANN* (Dinoflagellate Categorization by Artificial Neural Network) (Toth and Culverhouse, 1999). *DiCANN* can analyze and classify dinoflagellates with neural network algorithms with up to 72% accuracy. This taxon-specific software is accurate and used globally, though its high specificity is limiting. More general software options include *REFLICS* (REal FLOW Imaging and Classification System), which allows for the real-time automated recognition of fish eggs by using a nearest-neighbors algorithm, though it has a higher demonstrated error rate (Iwamoto, Checkley, and Trivedi, 2001). *VisualSpreadsheet*© is linked with the *FlowCAM* and is capable of extracting features and creating size spectra of particles. *VisualSpreadsheet* can also recognize plankton according to their similitude and easily links to *Zoo/PhytoImage* and *ImageJ* for further analysis (Grosjean and Denis, 2007; Schneider, Rasband, and Eliceiri, 2012; Spaulding, 2011). *Plankton Visual Analyzer (PVA)* is a free program which counts, sizes, and classifies particles of digital images (Harris *et al.*, 2000). *PVA* is somewhat time consuming but has recently been developed to analyze images from *VPR*. *ZooProcess* is a free piece of software designed to process images from *ZooScan* but does not allow automatic recognition of particles, though *Plankton Identifier*, a free piece of software, can be used with *ZooProcess* to identify plankton (Gorsky *et al.*, 2010).

The automated classification of planktonic community images yields valuable data about the plankton, though there are high percentages of “unclassified” images in many analyses – up to 80% of all images in some samples (Duffy, 2012). Examples from the *FlowCAM* of the main issues associated with automatic classification can be seen in Figure 10.4. There have been complications with identifying and avoiding marine snow, detritus, bubbles, and other non-plankton particles in captured images (Benfield *et al.*, 2007). The presence of aggregates, groups of multiple individuals sometimes associated with detritus or organic matter, can also complicate analysis. Some individuals may be visible in the aggregate and can be identified by manual counting but not semi-automated counting (Figure 10.4b). Aggregates reduce the overall number of plankton identified and can skew the relative proportions of each taxon present, as some taxa aggregate more frequently than others. Most tools for semi-automated planktonic community analysis capture 2D images, though the plankton move in three dimensions in moving fluid. As such, plankton can be imaged from any angle, making it difficult for the machine to recognize the geometry associated with each taxon (Culverhouse *et al.*, 2006). Movement during capture in the three-dimensional fluid also causes some images to contain blurs, which further impede the classifier’s ability to correctly identify plankton (Figure 10.4c) (Culverhouse *et al.*, 2006). Additional problems have been encountered due to the use of length and width to separate out different taxa, as larger and smaller forms of the same species can then be incorrectly classified as different taxa (Bell and Hopcroft, 2008). Though there are many issues with classification, community analysis has been largely successful using current semi-automated classification tools.

## 10.4

### Future Directions

While there have been many advances in semi-automated planktonic community imaging, there are still many directions for future research. The standardization of protocols and references, though not complete, should be prioritized. Standardization of capture methods is not possible, due to the wide variety of sampling methods and purposes that currently exist in semi-automated planktonic imaging. Standardization of analysis is also not totally possible, but future work should aim to unite current options and ensure cross-compatibility in analysis formats. This will require the development of open source software that is easily and readily accessible. The software would need to be easily adaptable and extremely user friendly, a major issue with current software. Future collaboration should focus on this area to make sure analyses are useful in future research.

The high degree of variability in machine learning methods leads to a lack of repeatability in many analyses. The bias introduced by taxonomists, the type and quality of images used for machine learning, and the various algorithms used to develop classifiers cause incompatibility among groups of studies and complicates analysis. Comprehensive, global training sets for machine learning should be compiled and made readily available for comparison. These would reduce the variability of analysis and, if kept online in an easily accessible database, could be updated with the discovery of new taxa and species. Future work should also focus on developing databases of images collected by planktonic community imagers, as these images could allow for interesting and innovative secondary analysis.

The use of morphology should be the main focus for future classification systems. By analyzing morphology, as opposed to simply geometry, more accurate classification could be made. Classifications could also reveal much more about the current status of populations within the community and further enable comparison through time (Naselli-Flores, Padisák, and Albay, 2007). Morphology analysis could be conducted using many of the same techniques as current facial recognition software. As morphology based analysis becomes common, research should focus on the development of open source, universal 3D standard models. These would allow recognition of the morphology of any taxon from any angle, eliminating some of the issues associated with capture in fluids.

## 10.5

### Conclusion

Semi-automated planktonic community classification has enabled many important studies on global communities. Semi-automated classification systems reduce the time and cost associated with whole community studies, enabling a greater number of researchers to study more systems in greater detail than previously thought. Each study requires a sampling, capture, importation, and analysis method, each

of which should be considered before beginning study. There are several options for analysis in each step from sampling to final classification and choices should be tailored to the goals and limitations of the study proposed. Close collaboration between planktonic community scientists and computer scientists should be encouraged throughout the process to ensure compatibility. As computer and photographic technology advances and international collaboration is encouraged, semi-automatic community analysis may finally become fully automated with a focus on morphology, not just geometry and taxonomy.

## References

- Alvarez, E., Lopez-Urrutia, A., and Nogueira, E. (2012) Improvement of plankton biovolume estimates derived from image-based automatic sampling devices: application to FlowCAM. *J. Plankton Res.*, **34**, 454–469.
- Bell, J.L. and Hopcroft, R.R. (2008) Assessment of ZooImage as a tool for the classification of zooplankton. *J. Plankton Res.*, **30**, 1351–1367.
- Benfield, M.C., Grosjean, P., Culverhouse, P.F., Irigoien, X., Sieracki, M.E., Lopez-Urrutia, A., Dam, H.G., Hu, Q., David, C.S., Hansen, A., Pilska, C.H., Riseman, E.M., Schultz, H., Utgoff, P.E., and Gorsky, G. (2007) RAPID: research on automated plankton identification. *Oceanography*, **20**, 172–187.
- Benfield, M.C., Schwehm, C.J., Fredericks, R.G., Squyres, G., Keenan, S.F., and Trevorrow, M.V. (2003) in *Handbook of Scaling Methods in Aquatic Ecology: Measurement, Analysis Simulation* (eds P. Strutton and L. Seuront), CRC Press, Boca Raton, FL, pp. 17–30.
- Boyd, P.W. and Newton, P. (1999) Does planktonic community structure determine downward particulate organic carbon flux in different oceanic provinces? *Deep Sea Res. Part I*, **46**, 63–91.
- Breiman, L. (2001) Random forests. *Mach. Learn.*, **45**, 5–32.
- Cardullo, R.A. and Hinchcliffe, E.H. (2007) Digital manipulation of brightfield and fluorescence images: noise reduction, contrast enhancement, and feature extraction. *Methods Cell Biol.*, **81**, 285–314.
- Cleve, P.T. (1899) Plankton collected by the Swedish expedition to Spitzbergen in 1898. *Kongliga Sven. Vetenskaps-Akad. Handlingar*, **3**, 1–51.
- Culverhouse, P.F., Williams, R., Benfield, M., Flood, P.R., Sell, A.F., Mazzocchi, M.G., Buttino, I., and Sieracki, M. (2006) Automatic image analysis of plankton: future perspectives. *Mar. Ecol. Prog. Ser.*, **312**, 297–309.
- Culverhouse, P.F., Williams, R., Reguera, B., Herry, V., and González-Gil, S. (2003) Do experts make mistakes? *Mar. Ecol. Prog. Ser.*, **247**, 17–25.
- Davis, C.S., Gallagher, S.M., Berman, M.S., Haury, L.R., and Strickler, J.R. (1992) The video plankton recorder (VPR): design and initial results. *Arch. Hydrobiol. Beih. Ergeb. Limnol.*, **36**, 67–81.
- Demers, S., Kim, J., Legendre, P., and Legendre, L. (1992) Analysing multivariate flow cytometric data in aquatic sciences. *Cytometry*, **13**, 291–298.
- Deuer, S.M., Lessard, E.J., and Satterberg, J. (2001) Effect of preservation on dinoflagellate and diatom cell volume and consequences for carbon biomass predictions. *Mar. Ecol. Prog. Ser.*, **222**, 41–50.
- Duffy, B. (2012) *FlowCAM Analysis of Plankton Communities of the Mediterranean Sea*. Bachelor thesis, University College Dublin.
- EC (2008) Directive 2008/56/EC of the European Parliament and of the Council of 17 June 2008 establishing a framework for community action in the field of marine environmental policy (Marine Strategy Framework Directive). *Off. J. Eur. Union*, **L164**, 19–40.
- Falchi, F., Gennaro, C., Rabitti, F., and Zezula, P. (2007) A distributed incremental nearest neighbor algorithm, in *Proceedings of the 2nd International Conference on Scalable Information Systems*,

- Institute for Computer Sciences, Social-Informatics and Telecommunications Engineering, Brussels, Article 82, pp. 10 ISBN: 978-1-59593-757-5
- Fraser, J.H. (1968) *Zooplankton Sampling*, UNESCO Monographs on Oceanographic Methodology II, UNESCO Publishing, Paris, pp. 11–18.
- Giovannoni, S.J. and Vergin, K.L. (2012) Seasonality in ocean microbial communities. *Science*, **335**, 671–676.
- Gorsky, G., Aldorf, C., Kage, M., Picheral, M., Garcia, Y., and Favole, J. (1992) Vertical distribution of aggregates determined by a new underwater video profiler. *Ann. Inst. Oceanogr.*, **68**, 275–280.
- Gorsky, G., Ohman, M.D., Picheral, M., Gasparini, S., Stemann, L., Romagnan, J.B., Cawood, A., Pesant, S., Garcia-Comas, C., and Prejger, F. (2010) Digital zooplankton image analysis using the ZooScan integrated system. *J. Plankton Res.*, **32**, 285–303.
- Grosjean, P. and Denis, K. (2007) *Zoo/PhytoImage Users Manual*, <http://www.sciviews.org/zooimage/docs/ZooPhytoImageManual.pdf> (accessed 21 June 2013).
- Harris, R., P., Wiebe, J., Lenz, H.R., Skjoldal, and M., Huntley (eds) (2000) *ICES Zooplankton Methodology Manual*, London, Academic Press, <http://www.azti.es/>. 2005. Plankton Visual Analyser (PVA) Software.
- Hallegraeff, G.M., Anderson, D.M., and Cembella, A.D. (eds) (1995) *The Manual on Harmful Marine Microalgae*, UNESCO Publishing, Paris, pp. 793.
- Hastie, T., Tibshirani, R., and Buja, A. (1994) Flexible discriminant analysis by optimal scoring. *J. Am. Stat. Assoc.*, **89**, 1255–1270.
- Hobbie, J.E., Daley, R.J., and Jasper, S. (1977) Use of nucleopore filters for counting bacteria by fluorescence microscopy. *Appl. Environ. Microbiol.*, **33**, 1225–1228.
- Iwamoto, S., Checkley, D.M., and Trivedi, M.M. (2001) REFLICS: real-time flow imaging and classification system. *Mach. Vis. Appl.*, **13**, 1–13.
- Jardillier, L., Boucher, D., Personnic, S., Jacquet, S., Thénot, A., Sargos, D., Amblard, C., and Debroas, D. (2005) Relative importance of nutrients and mortality factors on prokaryotic community composition in two lakes of different trophic status: microcosm experiments. *FEMS Microbiol.*, **53**, 429–443.
- Klug, J.L., Fischer, J.M., Ives, A.R., and Dennis, B. (2000) Compensatory dynamics in planktonic community responses to pH perturbations. *Ecology*, **81**, 387–398.
- Kohonen, T. (1987) *Self Organization and Associative Memory*, Springer-Verlag, Berlin.
- Leakey, R.J.G., Burkill, P.H., and Sleight, M.A. (1994) A comparison of fixatives for the estimation of abundance and biovolume of marine planktonic ciliate populations. *J. Plankton Res.*, **16**, 375–389.
- Lohmann, H. (1911) Über das nannoplankton und die zentrifugierung kleinster wasserproben zur gewinnung desselben in lebendem zustande. *Int. Rev. Gesamten Hydrobiol.*, **4**, 1–38.
- Naselli-Flores, L., Padisák, J., and Albay, M. (2007) Shape and size in phytoplankton ecology: do they matter? *Hydrobiologia*, **578**, 157–161.
- Olney, J.E. and Houde, E.D. (1993) Evaluation of in situ silhouette photography in investigations of estuarine zooplankton and ichthyoplankton. *Bull. Mar. Sci.*, **52**, 845–872.
- Ortner, P.B., Cummings, S.R., Aftiring, R.P., and Edgerton, H.E. (1979) Silhouette photography of oceanic zooplankton. *Nature*, **277**, 50–51.
- Ortner, P.B., Hill, L.C., and Edgerton, H.E. (1981) In-situ silhouette photography of Gulf stream zooplankton. *Deep Sea Res. Part A*, **28**, 1569–1576.
- Peters, A., Hothorn, T., and Lausen, B. (2002) Ipred: improved predictors. *R News*, **2**, 33–36.
- Qin, J. and Threlkeld, S. (1990) Experimental comparison of the effects of benthivorous fish and planktivorous fish on plankton community structure. *Arch. Hydrobiol.*, **119**, 121–141.
- Quinlan, J.R. (1993) *C4.5: Programs for Machine Learning*, Morgan Kaufman, San Francisco, CA.
- Remsen, A., Hopkins, T.L., and Samson, S. (2004) What you see is not what you catch: a comparison of concurrently collected net, optical plankton counter, and shadowed image particle profiling evaluation recorder data from the northeast Gulf of Mexico. *Deep Sea Res. Part I*, **51**, 129–151.



- Samson, S., Hopkins, T., Remsen, A., Langebrake, L., Sutton, T., and Patten, J. (2001) A system for high-resolution zooplankton imaging. *IEEE J. Oceanic Eng.*, **26**, 671–676.
- Sanders, R.W., Porter, K.G., Bennett, S.J., and DeBiase, A.E. (1989) Seasonal patterns of bacterivory by flagellates, ciliates, rotifers, and cladocerans in a freshwater planktonic community. *Limnol. Oceanogr.*, **34**, 673–687.
- Schneider, C.A., Rasband, W.S., and Eliceiri, K.W. (2012) NIH image to ImageJ: 25 years of image analysis. *Nat. Methods*, **9**, 671–675.
- Senel, H.G., Peters, R.A., and Dawant, B. (2002) Topological median filters. *IEEE Trans. Image Process.*, **11**, 89–104.
- Sieracki, M.E., Benfield, M., Hanson, A., Davis, C., Pilskaln, C.H., Checkley, D., Sosik, H.M., Ashjian, C., Culverhouse, P., Cowen, R., Lopes, R., Balch, W., and Irigoien, X. (2010) Optical plankton imaging and analysis systems for ocean observation, in *Proceedings of OceanObs'09: Sustained Ocean Observations and Information for Society* (eds J. Hall, D.E. Harrison, and D. Stammer), ESA Publication WPP-306, vol. 2, European Space Agency, on CD ROM.
- Sieracki, C.K., Sieracki, M.E., and Yentsch, C.S. (1998) An imaging-in-flow system for automated analysis of marine microplankton. *Mar. Ecol. Prog. Ser.*, **168**, 285–296.
- Simpson, R., Williams, R., Ellis, R., and Culverhouse, P.F. (1992) Biological pattern recognition by neural network. *Mar. Ecol. Prog. Ser.*, **79**, 303–308.
- Smetacek, V. (1999) Diatoms and the ocean carbon cycle. *Protist*, **150**, 25–32.
- Smayda, T.J. (1958) Bio-geographical studies of marine phytoplankton. *Oikos*, **9**, 158–191.
- Sournia, A. (1978) *The Phytoplankton Manual*, UNESCO Publishing, Paris, pp. 337.
- Spaulding, B. (ed.) (2011) *FlowCAM® Manual, Version 3.0*, Fluid Imaging Technologies, Yarmouth, MA.
- Stingl, U. and Giovannoni, S.J. (2005) Molecular diversity and ecology of microbial plankton. *Nature*, **437**, 343–348.
- Stramski, D., Bricaud, A., and Morel, A. (2001) Modeling the inherent optical properties of the ocean based on the detailed composition of planktonic community. *Appl. Opt.*, **40**, 2929–2945.
- Tang, X., Stewart, W.K., Vincent, L., Huang, H., Marra, M., Gallagher, S.M., and Davis, C.S. (1998) Automatic plankton image recognition. *Artif. Intell. Rev.*, **12**, 177–199.
- Tiselius, P. (1998) An in situ video camera for plankton studies: design and preliminary observations. *Mar. Ecol. Prog. Ser.*, **164**, 293–299.
- Toth, L. and Culverhouse, P.H. (1999) 3D object recognition from static 2D views using multiple coarse data channels. *Image Vision Comput.*, **17**, 845–858.
- Uddin, M.S., Lee, H.K., Preibisch, S., and Tomancak, P. (2011) Restoration of uneven illumination in light sheet microscopy images. *Microsc. Microanal.*, **4**, 607–613.
- Werne, J.P., Hollander, D.J., Lyons, T.W., and Peterson, L.C. (2000) Climate-induced variations in productivity and planktonic ecosystem structure from the Younger Dryas to Holocene in the Cariaco Basin, Venezuela. *Paleoceanography*, **15**, 19–29.
- Wiebe, P.H. and Benfield, M.C. (2009) in *Encyclopedia of Ocean Sciences* (eds J.H. Steele, S.A. Thorpe, and K.K. Turekian), Academic Publishing, London, pp. 3237–3253.
- Wolf, D.E., Samarasekera, C., and Swedlow, J.R. (2007) Quantitative analysis of digital microscope images. *Methods Cell Biol.*, **81**, 365–396.
- Ye, L., Chang, C.Y., and Hsieh, C. (2011) Bayesian model for semi-automated zooplankton classification with predictive confidence and rapid category aggregation. *Mar. Ecol. Prog. Ser.*, **441**, 185–196.



## Index

### a

absorption 27  
 absorption imaging  
   – natural contrast 151–152  
   – staining contrast 152, 153–155  
 acousto-optical tunable filter (AOTF) 194  
 additive volume rendering 169  
 Adobe Lightroom® 230  
 agarose 103  
 Airy disk 72, 73  
 algae 107  
 analyzer-based imaging (ABI) 160–161  
   – applications 161–162  
 anatomical MRI 129  
   – Aristotle 6–7  
 animalcules 10, 111  
 aperture 215  
 Apple Aperture® 230  
 auto-fluorescence 189  
   – for detailed three-dimensional  
     morphological imaging 76–80  
 automated image processing. *See* planktonic  
   community analysis  
 autonomous underwater vehicles (AUVs)  
   23–25, 34, 35, 38, 40–42, 44

### b

backscatter 26  
 Beer–Lambert law 140  
 benzyl alcohol to benzyl benzoate (BABB)  
   103  
 Bessel beams 203

### c

camera 222  
   – setting 217, 226–227  
 casper zebrafish 107  
*Challenger Deep* 16

color-coded height maps 87–88  
 Compton scattering 140  
 computational 3D segmentation 170  
 computed laminography 147  
 3D cone beam geometry 145–146  
 cone-beam tomography 133  
 confocal laser scanning microscopy (CLSM)  
   69, 101, 102, 191  
   – fluorescence dyes application 80–85  
   – prerequisites for high quality micrographs  
     generation 73–74  
   – surface topography analyses 85–88  
   – technical and methodological aspects  
     69–73  
 Congo red fluorescent dye 83–84  
 continuous plankton recorder (CPR) 112  
 copepods 206  
 corals 187, 206, 207

### d

dark-field imaging 162, 163  
 depth of field (DoF) 216–217, 219  
 diatoms 80  
 differential phase-contrast techniques 156  
 diffraction enhanced imaging. *See*  
   analyzer-based imaging (ABI)  
 diffusion tensor imaging (DTI) 129–131  
 digital in-line holographic microscopy  
   (DIHM) 50, 54–55  
   – image examples 58–61  
   – image reconstruction 56–58  
   – instruments 55–56  
   – resolution 60–62  
   – volume imaging challenges 63–64  
 digital scanned light-scanned microscope  
   (DSLM) 201–202  
 digital tomosynthesis 147  
 dinoflagellates 81

direct volume rendering (DVR) 169  
dynamic range 219

**e**

efficacy 30–31  
eHoloCam 54  
electron microscopy techniques 111–112  
– collecting and processing specimens 112–113  
– scanning electron microscopy 116–120  
– sediment cyst surveys 113–114  
– transmission electron microscopy 114–116

emission optical projection tomography (EOPT) 94, 96, 97

– illumination unit 98

epi-fluorescence microscopy 188

– wide-field microscopy 189–190

**f**

Feldkamp algorithm (FDK) 145

field emission scanning electron microscope (FESEM) 112

2D filtered back-projection 142–144

filtered back-projection (FBP) 143–146

finite element analysis (FEA) 172

flashes 223

– accessories and lighting gear 224

– controlling exposure 220

– light positioning and shaping 220–222

– positioning 227

– – lighting bigger animals 228

– – lighting small animals 227–228

– – water quality 228

flash synchronization 220

flow-OPT 107–108

fluorescence 188–189

fluorescence dyes application 80–85

focal layer 70

forward scatter 26

Fourier slice theorem 143, 149

free-space propagation methods (holotomography) 157–160

Fresnel diffraction pattern 159

Fresnel propagator 159

fringe scanning 163

Fugu vision system 40–43

functional MRI 129

**g**

Gabor filter bank 170

gamma compression 219

GIRONA-500 vehicle 25, 41–43

green fluorescent protein (GFP) 94

**h**

*H.M.S. Challenger Expedition* 11–14

halogens 31

Hamming and Han windows 144

Helicon Software® 216

high density discharge (HID) lamps 31

high intensity fluorescent (HIF) systems 31

HoloCam 52–53

HoloCamera 52–53

holographic microscopy 49

– advantages 50

– past attempts for microplankton imaging 51–54

– point source digital in-line holographic microscopy 54–55

– – image examples 58–60

– – image reconstruction 56–58

– – instruments 55–56

– – resolution 60–62

– – volume imaging challenges 63–64

hydrargyrum medium-arc iodide (HMI) lamp 31

**i**

3D image reconstruction 145–146

image weighting 128

infinity-corrected objective lens 96, 98

infrared 31–32

interactivity 168

inverse Radon transform function 95

iso-surface extraction technique 167

ISO value 215–216

**k**

K-edge digital subtraction imaging (KES) 154–155

Kirchhoff-Helmholtz transform 56, 63

**l**

LabVIEW 104

lambda scans 77

laminography 146–149

– example applications 151

– image construction 149–151

laser line scan (LLS) methods 33

laser range-gating (LRG) methods 32–33

lasers 32

lenses 222–223

light emitting diodes (LEDs) 28, 31, 99

light microscopy 113

light-sensitive sensor 138

light-sheet fluorescence microscopy (LSFM) 188, 207

– advantages 198–200

- alternative configuration with simplified sample mounting 197–198
- application examples 203–204
- Bessel beams 203
- combined with fluorescence techniques 204
- concept 192–193
- detection unit 194–195
- digital scanned light-scanned microscope (DSLM) 201
- illumination unit 194
- imaging improvement 200–201
- implementation and instruments 193
- incoherent structured illumination 201–202
- for marine biology 204–206
- sample chamber and movement unit 195
- sample mounting 196–197
- spatial resolution 195–196
- two-photon excitation 202–203
- light stripe range scanning (LSRS) 28
- local tomography 144

## m

- macro photography (*ex-situ*) 211–212
  - after photographic shoot 228–229
  - file formats 229–230
  - image selection 231–232
  - post-processing workflow 230
- animal care 232
  - collecting 232
  - handling and imaging 232–233
- camera setting 226–227
- equipment 225–226
  - aquarium setup 224–225
  - camera 222
  - flash accessories and lighting gear 224
  - flashes 223
  - lenses 222–223
- exposure 213
  - aperture 215
  - camera setting 217
  - depth of field 216–217
  - good exposure 217–220
  - ISO value 215–216
  - shutter speed 213–215
- flashes
  - controlling exposure 220
  - light positioning and shaping 220–222
- flash positioning 227
  - lighting bigger animals 228
  - lighting small animals 227–228
  - water quality 228

- magnetic resonance imaging (MRI) 124
  - applications 129–132
  - contrast 128–129
  - experimental setup 124–128
  - hardware improvements 128
- magnification rate 222
- manganese-enhanced magnetic resonance imaging (MEMRI) 131
- marine phytoplankton. *See* electron microscopy techniques, for imaging marine phytoplankton
- marine snow 26
- maximum intensity projection (MIP) 169
- multibody dynamics 172
- multidirectional selective plane illumination microscope (mSPIM) 200
- Murray's Clear. *See* benzyl alcohol to benzyl benzoate (BABB)

## n

- Nessie-VI vehicle 42–43
- nuclear magnetic resonance (NMR) 127
- Nyquist-Shannon sampling theorem 73, 74

## o

- objective-coupled planar illumination (OCPI) microscope 197
- optical projection tomography (OPT) 93
  - history 93–94
  - image processing and analysis 104
  - marine biology applications 104–108
    - illumination sources 99
    - system assembly 98
    - system capabilities and limitations 99–100
  - sample preparation 102–104
- optical sectioning 70
  - approaches 191–192
- out-of-focus fluorescence 190

## p

- Paganin's formula 160
- 2D parallel beam geometry 142
- 3D parallel beam CT 145
- partial volume effect 170
- Phalloidin 84
- phase-contrast imaging 155–157
  - analyzer-based imaging (ABI) 160–162
- free-space propagation methods (holotomography) 157–160
- X-ray grating interferometry 162–166
- phase-locked loop (PLL) 33
- phase retrieval 159

phase-stepping technique 162  
 photobleaching 189  
 photoelastic effect 37  
 photoelectric absorption 140  
 photometric stereo (PS) 28  
 pixels 97  
 plankton. *See* holographic microscopy  
 planktonic community analysis 235–236  
 Polynesian seafarers  
 – ocean currents masters 5–6

**q**

quantitative phase-contrast techniques 156  
 quantitative sampling 112

**r**

Ram–Lak filter 144  
 range gated systems 28  
 RAW file format 229  
 Rayleigh criterion 72  
 refraction contrast 160  
 region-of-interest (ROI) tomography. *See* local tomography  
 remotely operated vehicles (ROVs) 23, 24, 31, 34–35, 44  
 resilin 79  
 resulting surface 168

**s**

scanning electron microscopy (SEM) 78–79, 112, 116–120  
 scattered light rejection, using modulation/demodulation techniques 33  
 scientific volume visualization 167  
 sediment cyst surveys 113–114  
 segmentation 241  
 – and importation 240–241  
 – visualization methods  
 – – classification 166–172  
 – – main visualization methods 167–170  
 selective plane illumination microscope (SPIM). *See* selective plane illumination microscope (SPIM)  
 semi-automatic techniques 171  
 shading 168  
 Shepp–Logan filter 144  
 shutter speed 213–215  
 single-plane illumination microscopy (SPIM) 100–101  
 sinogram 143  
 spin-lattice relaxation time 127  
 spin–lattice relaxation time 125  
 spin–spin relaxation time 125

stick charts 6  
 structured illumination 191  
 – incoherent 201–202  
 surface topography analyses 85–88  
 synchronous scanning systems 28  
 synchrotron-radiation computed laminography (SR-CL) 146–149  
 SYTO<sup>®</sup> dyes 85

**t**

Talbot interferometry. *See* X-ray grating interferometry (XGI)  
 telecentric illumination lens 107  
 telecentric objective lens 107  
 thresholding 170  
 tintinnids 187, 206  
 tomosynthesis 146  
 total internal reflection fluorescence microscopy (TIRFM) 192  
 TOTO<sup>®</sup> dyes 85  
 transmission electron microscopy (TEM) 112, 114–116  
 transmission optical projection tomography (TOPT) 94, 96  
 – illumination unit 98  
 Trident (European project) 25  
 tube lens 98  
 two-photon excitation 202–203  
 two-photon microscopy 102

**u**

ultramicroscopy 101  
 underwater imaging and vision systems 23–25  
 – applications and vision system 39–40  
 – – Fugu vision system 40–43  
 – illuminating systems 30–32  
 – illumination sources 27–28  
 – improvement, via polarization 35–36  
 – – experimental evaluation 37–39  
 – – extended range using polarization 36  
 – – housing 36–37  
 – infrastructures 34–35  
 – laser-based techniques 32  
 – – laser line scan (LLS) methods 33  
 – – laser range-gating (LRG) methods 32–33  
 – – scattered light rejection using modulation/demodulation techniques 33  
 – light source position selection 28–30  
 – optical image formation 25–27  
 unsupervised classifiers 171

**v**

veiling light 26

**w**

wide-field microscopes 239–240

**x**

xenon lamps. *See* high density discharge  
(HID) lamps

xenon light 99

X-ray grating interferometry (XGI) 162–165

– performance characteristics and applications  
162–166

X-ray microtomography

– detector 131–140

– forward problem (contrast formation)  
131–142

– sample stage 137–138

– sources

– – laboratory-based setups 133–135

– – synchrotron-based setups 135–137

– tomographic reconstruction

– – 2D filtered back-projection 142–144

– – 3D image reconstruction 145–146

– – image quality and artifacts 144–145

xenon light 99

**z**

zebrafish 107